Title
Hierarchical Nanoparticle Assemblies in Thin Films of Supramolecular Nanocomposites

Author
Kao, Joseph

Publication Date
2014

Peer reviewed|Thesis/dissertation

Hierarchical Nanoparticle Assemblies in Thin Films of Supramolecular Nanocomposites

By

Joseph Kao

A dissertation submitted in partial satisfaction of the
requirements for the degree of
Doctor of Philosophy
in
Engineering – Materials Science and Engineering
in the
Graduate Division
of the
University of California, Berkeley

Committee in charge:

Professor Ting Xu, Chair
Professor Andrew Minor
Professor Phillip Geissler

Spring 2014

Hierarchical Nanoparticle Assemblies in Thin Films of Supramolecular Nanocomposites

by

Joseph Kao

Abstract

Hierarchical Nanoparticle Assemblies in Thin Films of Supramolecular Nanocomposites

By

Joseph Kao

Doctor of Philosophy in Materials Science and Engineering

University of California, Berkeley

Professor Ting Xu, Chair

This dissertation focuses on the co-assembly of nanoparticles (NPs) and block copolymer (BCP)-based supramolecules in thin films for the generation of functional nanocomposites that may find applications in next-generation nanodevices. Nanocomposites, composed of organic and inorganic building blocks, can combine the properties from the parent constituents and generate new properties to meet current and future demands in functional materials. Recent developments in NP synthesis provide a plethora of inorganic building blocks, laying the foundation for constructing hybrid nanocomposites with unlimited possibilities. The properties of nanocomposite materials depend not only on those of individual NPs, but also on their spatial organization at different length scales. Block copolymer-based supramolecules, which microphase separate into various hierarchical nanostructures, have shown their potential for organizing inorganic NPs in bulk. For practical applications and device fabrication, it is requisite to translate the NP assemblies in bulk to thin films, which has yet to be realized due to the complicated energy landscape and assembly kinetics in thin film configurations.

Here, the thermodynamics and kinetics of the NP assemblies in supramolecular thin films were systematically investigated to achieve desirable and, potentially, functional NP assemblies over multiple length scales. In particular, the complicated interplay between the entropic and enthalpic contribution in the co-assembly was explored by tuning the chain architecture of the supramolecules and the NP loading. The delicate balance among the thermodynamic driving forces was further manipulated by changing NP size, leading to a rich library of multidimensional assemblies of not only a single kind, but also mixtures of NPs in thin films. In addition, the assembly kinetics of the NPs was studied during solvent annealing. By varying the solvent volume fraction and small molecule loading in the film, the mobility, the activation energy barrier for inter-domain diffusion, and the thermodynamic driving force for defect elimination can be precisely tailored to manipulate the kinetic pathway. The results not only enable precise control over the macroscopic morphology of the supramolecular nanocomposite, but also optimize the processing conditions for the fabrication of functional nanocomposites.

Preliminary optical property results demonstrate strong wavelength dependence optical anisotropy in the supramolecular nanocomposites, showing the promise of this new family of

materials for light manipulation and information transmission. To manipulate the coupling in the NP arrays over multiple length scales, faceted and lithographically patterned surfaces were employed to direct the macroscopic 2-D alignment as well as the 3-D structure in supramolecular nanocomposites. This work demonstrates that the hierarchically structured supramolecular nanocomposite thin films are fundamentally intriguing as well as technologically relevant. The fundamental knowledge gained lays a solid foundation for future studies on the investigation of structure-property correlations, which may enable the realization of novel functional nanocomposites for a wide range of applications including, but not limited to, nanoscopic energy waveguides, optical coatings, and nanoelectronics.

Hierarchical Nanoparticle Assemblies in Thin Films of Supramolecular Nanocomposites

Table of Contents

Chapter 3: Nanoparticle Assemblies in Thin Films of Supramolecular Nanocomposites: Effect of Nanoparticle Volume Fraction

Chapter 4: Size-Dependent Nanoparticle Assemblies in Thin Films of Supramolecular Nanocomposites

Chapter 5: Assembly Kinetics in Supramolecular Nanocomposite Thin Films during Solvent Annealing

Acknowledgments

First off, I am grateful for the guidance and support that Ting has given me throughout my years in grad school. The work described in this dissertation would not have been possible without her. I appreciate the time she invested in training me to become a scientist and independent researcher. The opportunities she has given me to attend conferences and to establish collaborations with researchers from different fields have helped me broaden my horizon and develop personal qualities that will accompany me throughout my entire life. Much thanks to her.

Thank you to the collaborators, Dr. Zhang Jiang, Dr. Peter Ercius, Prof. Cheng Sun, Zhen Zhang, Prof. Caroline Ross, and Dr. Karim Aissou, all of whom have helped me tremendously with the work in this dissertation. Special thanks also go to Jesus Guardado, Nick Jose, and Nate Nuntaworanuch, who have assisted me to synthesize the nanoparticles used throughout this dissertation. Without them, this work would not have been successful.

To all the current and former members of my lab, I seriously doubt that there are many research groups in the world that get along as well as we have, and I am immensely grateful for that. In particular, the camaraderie built and fruitful discussions during those long weeks and nights at the beamline with Dr. Ben Rancatore, Kari Thorkelsson, and Peter Bai. They made the work in Chapter 5 possible! I'm also thankful for the guidance and moral support offered to me by Dr. Vivian Chuang, Dr. Seong-Jun Jeong, Dr. Dong Hyun Lee, Dr. Myung Im Kim, and Dr. Marta Kocun during the early years of my time in grad school. The nature of this project would not have been the same and the progress not as quick without them. Thank you all.

I'd like to recognize all of the valuable friends that I've made in my time at Berkeley, especially Peter Bai, Beverly Zhang, Dr. He Dong, Mong-han Huang, Nikhil Dube, and Dr. Yun-feng Qiu. There are ups and downs in my Ph.D. study and I really want to thank these people for always being at my side, sharing all the happiness, sadness, tears, smiles, laughter and other emotions with me more closely than anyone else. I don't know if I could have made it without your support, entertainment, and love.

I cannot thank my family enough for what they have done for me over the last five years, and for the 22 before that. Thank you so much for encouraging me to pursue a Ph.D. degree in materials science and facing the challenges in my life. Your love makes me strong in times of adversity. I would not have become who I am today without you. With your support, I am ready to step out of grad school and begin a new chapter of my life!

Chapter 1
Opportunities of Block Copolymer-based Supramolecular Nanocomposites

§ 1.1 Introduction

The work described in this dissertation focuses on gaining a fundamental understanding of the co-assembly of block copolymer (BCP)-based supramolecules and spherical nanoparticles (NPs) in thin films. The insights into the thermodynamics and kinetics of the hierarchical NP assembly in supramolecular thin films will lay down a solid foundation for rationally designing theoretical and experimental platforms for the investigation of structure-property correlations and, potentially, the realization of next-generation nanodevices based on functional nancoomposites. Since thousands of years ago, NPs, particles a few to tens of nanometers in size, have been used by humans due to their unique structural and optical properties without fully understanding the underlying causes.[1] More recently, NPs were discovered to act like artificial atoms, demonstrating unique physical properties due to quantum confinement effects that have found applications in a wide variety of fields such as life science, energy, electronics, and environmental science.[2,3] With the developments in NP synthesis, NPs of controlled size, shape, chemical composition, and surface ligands can be readily prepared.[4-8] Just as a hydrogen molecule has properties distinct from two uncoupled hydrogen atoms, ensembles of nanoscopic building blocks may exhibit properties different from those of the individual building blocks due to coupling and exchange phenomena.[2,9-19] By spatially organizing NPs into nanostructured arrays over multiple length scales, especially when the nanoscopic building blocks are in close proximity, say less than 10 nm apart, collective properties of NPs can be realized to enable not only a full understanding of structure-property correlations, but also the fabrication of a plethora of next-generation NP-based devices including, but not limited to, plasmonic waveguides, photonic crystals, optical lenses, memory storage devices, nanoelectronic circuits, photovoltaics, and batteries.[20]

The spatial organization of NPs on the scale of a few hundred nanometers can be obtained using "top-down" techniques, which have been progressively developed toward greater integration densities and smaller feature sizes.[21,22] At the tens of nanometers scale, however, conventional lithographic processes are approaching their practical and theoretical limits, making it challenging to manipulate sub-10 nm inter-particle ordering/coupling. On the other hand, "bottom-up" self-assembly approaches provide opportunities to overcome these limitations. Using "bottom-up" approaches, not only NPs, but also functional organic small molecules and polymers with well-defined physical and chemical properties can be readily incorporated into hybrid organic-inorganic nanocomposites. Nevertheless, it remains non-trivial to obtain macroscopic assemblies of either small molecules or NPs at low cost using existing fabrication infrastructure. In contrast, polymers can be readily synthesized with controlled molecular weight and architecture and are amenable to various processing techniques. In particular, BCPs, which self-assemble into a rich library of nanostructures, provide useful tools to manipulate the assemblies of nanoscopic building blocks at multiple length scales. However, generating molecular level assemblies using BCPs alone is not trivial. One route to overcome the deficiencies of BCPs is to employ supramolecular approaches to assemble selected functional small molecule and NP building blocks in BCP structural frameworks to construct

technologically important nanocomposites in bulk or in thin films to expand the horizon of nanoscience (Figure 1.1).

In this chapter, the assemblies of inorganic spherical NPs, with a focus on the guided assemblies of these functional building blocks in BCPs toward functional hybrid materials will be discussed in detail. The discussion first focuses on BCP-based nanocomposites where NPs are either synthesized *in situ* within BCP microdomains or pre-synthesized *ex situ*. The supramolecular approach combines polymers and small molecules and adds versatility to precisely control NP assemblies over multiple length scales in comparison to BCPs alone. To establish the foundation for understanding supramolecular nanocomposites, the phase behaviors of BCP-based supramolecules containing simple alkyl small molecules will be discussed. With the aid of hierarchically structured supramolecules, NPs form a broader range of assemblies in nanoscopically confined geometry. By manipulating the spatial organization of each building block in the multicomponent nanocomposites, the coupling effects between each functional nanomaterial can be precisely tuned to access interesting collective properties that may be useful for various NP-based devices.

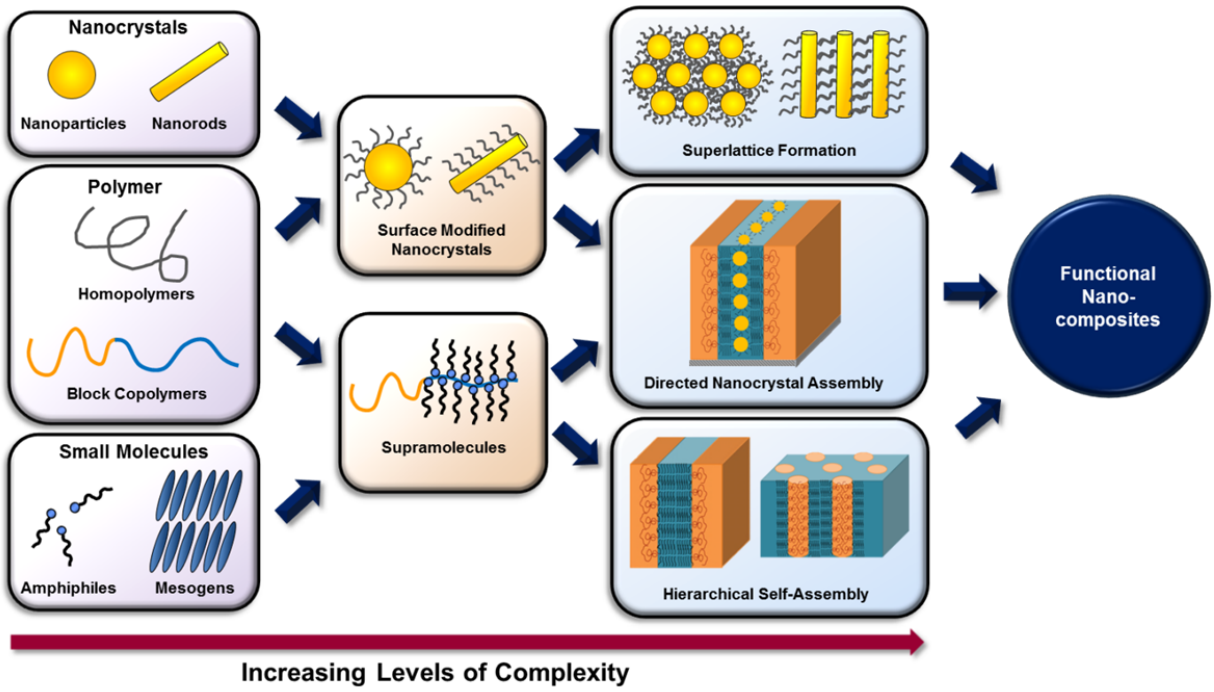

Figure 1.1. Hierarchical co-assemblies of nanocrystals, polymers, and small molecules toward functional nanocomposites.

§ 1.2 Block copolymer-based nanocomposites

Nanoparticles exhibit interesting optical, electrical, and magnetic properties, and the controlled spatial organization of these building blocks into multidimensional arrays with precise inter-particle ordering will build a structural foundation for many applications.[20,23-25] BCPs microphase separate into a rich library of well-defined and well-ordered arrays of microdomains, tens of nanometers in dimension, comparable to the size of NPs, that can be used to direct the assemblies of NPs.[26-33] In thin films, BCP microdomains can be macroscopically aligned by balancing interfacial interactions or by applying external fields.[34-38] Thus, BCPs are commonly employed as structure-directing templates for NP assemblies. Two major strategies have been explored to generate NP arrays within BCP microdomains: *in situ* synthesis of NPs and assemblies of preformed NPs in selected BCP microdomains.[39,40]

§ 1.2.1. *In situ* synthesis of NPs in BCP microdomains

For *in situ* NP synthesis, a range of NPs can be incorporated into BCP nanostructures *via* a reduction of NP precursors selectively incorporated in one of the BCP microdomains.[39,40] The options range from chemical reduction to, photoreduction and thermal decomposition, to vapor deposition methods and sputtering.[41] Cohen's group first employed chemical reduction to generate metal or semiconductor nanoclusters in microphase-separated BCP microdomains.[42-47] They conducted extensive studies on the syntheses of semiconductor nanoclusters within microphase-separated BCPs prepared by ring-opening metathesis polymerization.[42,43,47] Chan *et al*. reported the syntheses of metal nanoclusters (Au, Ag, and Pd) by decomposing metal complexes attached selectively to one BCP block (Figure 1.2).[44-46] These approaches led to nanoclusters of different species and particle sizes in confined geometry. The *in situ* NP synthesis approach is limited to certain families of BCPs where polymers favorably interact with cations. Hashimoto *et al*. employed the one-step "dispersion route", in which the solutions of the metal precursor (Pd^{II}) and the protective polyisoprene-*b*-poly(2-vinylpyridine) (PI-*b*-P2VP) were combined, and the reduction is subsequently performed in solution at elevated temperature, resulting in nanocomposite films containing Pd NPs exclusively localized around the center of the P2VP microdomains.[48]

Wiesner's group developed a sol-gel "dispersion route" to generate inorganic materials in the poly(ethylene oxide) blocks of a poly(isoprene-*b*-ethylene oxide) (PI-*b*-PEO) BCP.[49-52] The metal alkoxide precursors, which contain a polymerizable organic moiety and preferentially swell the hydrophilic PEO block as a result of hydrogen bonding, underwent a sol-gel process in the PEO microdomains. After high-temperature oxidation of the polymer matrix, a mesoporous ceramic material with unprecedented morphology control on the nanoscale was generated. A similar approach has been used to generate SiO_2 and TiO_2 nanostructures with reverse morphology and mesoporous TiO_2 thin films using nanostructured BCP films as templates.[53-55]

Russell's group showed that alkali halide or metal salts complexed with the poly(ethylene oxide) (PEO) blocks in thin films of PS-*b*-PEO, on the order of a few ions per chain.[56] They demonstrated large flexibility in the choice of salt used, including gold or cobalt salts such that well-organized patterns of NPs can be generated inside the PEO microdomains upon exposure to the electron beam.

Recently, many groups have demonstrated that *in situ* synthesis methods can be used to generate nanostructured organic/inorganic nanocomposites for catalysis,[57] dye-sensitized solar cells,[58,59] and energy conversion/storage.[49] One of the major limitations using *in situ* synthesis methods is that the size of the NP and the inter-particle ordering inside the domains cannot be precisely controlled. Mirkin's group has provided advances in NP size distribution, demonstrating that monodisperse sub-5 nm single crystalline Au NPs could be produced by reducing the metal ions associated with one blocks in BCP micelles patterned by dip pen nanolithography.[60] The *in situ* methods hold great promise for the fabrication functional nanocomposites as they usually yield a homogeneous distribution of NPs in the polymer matrix and ultra-high volume fractions of the *in situ* synthesized NPs in the BCP microdomains. However, it remains a challenge to control NP size and inter-particle ordering in the interior of BCP microdomains in a scalable manner using existing *in situ* synthesis methods, which poses limitations on the fabrication of nanocomposites with tunable functionalities.

§ 1.2.2. Nanocomposites based on preformed NPs in bulk

In the past decades, there have been great successes in controlled NP synthesis. People have been developing new methods to synthesize a rich library of monodisperse NPs with tunable shapes, and sizes.[3] Ion exchange reactions allow for the variation of the chemical composition of NPs without significantly affecting the size or morphology of the particle.[3,61] In addition, new surface chemistry has been explored to exchange the ligands on the surface of the NPs for uniform dispersion in different solvents.[3] Scientists have also strived to modify the existing NP syntheses for scalable nanomanufacturing. With the state-of-the-art NP synthesis methods, people began to seek for alternative methods by using "bottom-up" approaches to achieve multidimensional nanostructured arrays of preformed NPs with controlled inter-particle ordering toward functional nanocomposites.[18,20] To this end, directed self-assemblies of NPs using DNA linkers, carbon nanotubes or macromolecular templates, have been extensively studied to achieve multidimensional assemblies of NPs with nanoscale resolution.[18] Among template-assisted approaches, DNA-mediated self-assemblies of NPs have shown great promise to generate not only 1-D and 2-D, but also 3-D nanostructures of NPs with precisely controlled inter-particle distance.[18] However, one of the most prominent obstacles using DNA to direct the assemblies of NPs is the current high cost of synthetic DNA and its low yields, which make the approach not suitable for large-scale device fabrication. As a result, there is an interest in the development of complementary template-assisted strategies that are economically feasible to enable scalable fabrication. Over the past decade, BCPs, which have a rich library of

nanostructures, the cost effectiveness, and the solution-processability for scale-up manufacturing, have been extensively utilized as templates for directed assemblies of NPs.[18,39,40,62,63] Many NP-based devices such as plasmonic waveguides, plasmonic photonic crystals, photovoltaics, and sensors require precise control over the inter-particle ordering (coupling effects). Using BCPs to control the spatial arrangement of NPs of different sizes, shapes, and compositions may enable one to generate nanocomposites for next-generation nanodevices that may not be fabricated using *in situ* synthesis methods.

The co-assembly of NPs with BCPs relies on a delicate balance of the interactions between the ligands attached to the NPs and the segments of the BCPs, and the influence of the size of the NPs on the chain configuration of the BCPs.[27,30,31,33,63-65] For example, surface modified NPs can interact favorably with specific blocks of a BCP such that the NPs can be preferentially sequestered in the domains.[39,40] Upon incorporation of solid NPs into BCPs, the polymer chains must stretch around these obstacles, causing a loss in conformational entropy that increases with particle radius.[62] In bulk BCP nanocomposites, the change in free energy upon incorporation of NPs can be written qualitatively as:

$$\Delta G = (\Delta H_{ligand/polymer}) - T(\Delta S_{con} + \Delta S_{trans}) \quad (1)$$

where $\Delta H_{ligand/polymer}$ describes the enthalpic contribution from ligand/polymer interactions; ΔS_{con} refers to the change in conformational entropy of the polymer chains; and ΔS_{trans} accounts for the entropic contribution due to the number of physical arrangements of the NPs in the nanocomposites. Understanding the thermodynamics of the co-assemblies of NPs and BCPs allows one to precisely control the 3-D spatial organization of NPs and inter-particle distance, leading to hierarchically structured nanocomposites.

Lauter-Pasyuk *et al*. first incorporated unmodified γ-Fe_2O_3 NPs into the PS microdomains in thin films of lamellar polystyrene(deuterated)-*b*-polybutyl methacrylate (d-PS-*b*-PBMA) and studied the spatial organization of the NPs by neutron scattering.[66,67] They determined that the ~4 nm NPs concentrated close to d-PS-*b*-PBMA interfaces while larger NPs (~6 nm) localized in the center of PS domains. The results successfully demonstrated that the particle distribution inside the host domains could be controlled in BCP-based composite materials. Bockstaller *et al*. achieved co-assemblies of unmodified Au and SiO_2 NPs in a bulk system consisting of a symmetric poly(styrene-*b*-ethylene propylene) (PS-*b*-PEP) BCP and focused the entropic effects on the co-assemblies of NPs and BCPs.[27] In both studies, the NPs are covered by alkyl ligands that have favorable interactions with one BCP block. Experimentally, the enthalpic contribution from polymer/ligand interactions can be tailored by modifying the surface chemistry on the NPs.[68] One of the most well established approaches is to modify the surface of the NPs by polymers to tailor $\Delta H_{ligand/polymer}$ *via* van der Waals interactions to prevent macrophase separation between polymer and NPs and obtain dispersion of NPs in the polymer matrix.[39,40,69,70] To this end, Lin *et al*. incorporated poly(ethylene glycol) (PEG)-tagged ferritin bio-NPs into lamella-forming P2VP-*b*-PEO thin films.[30] The BCPs were found to form perpendicular and parallel lamellae in thin films with and without ferritin-PEG, respectively. The results suggested that only the bio-NPs modified by PEG could be incorporated into PEO microdomains, mediating interfacial interactions and reorient the microdomains to be normal to

the surface. Extensive studies have been performed on the assemblies of polymeric ligand coated Au NPs in PS-*b*-P2VP in bulk.[29,31,71,72] Au NPs can be selectively localized within the PS and P2VP microdomains by modifying the surface of the NPs with PS and P2VP homopolymers, respectively (Figure 1.2).[31,72,73] To localize particles at the interfaces between the blocks, particles are coated with a mixture of PS and P2VP homopolymers[31,72,73] (Figure 1.2) or PS-*b*-P2VP random copolymers.[72] Additionally, the surface coverage of the polymer ligands on the NP is a critical parameter that determines the spatial organization of NPs in BCPs.[71] PS-coated gold NPs with PS chain areal density higher than a critical value were found to be well dispersed in PS domains of PS-*b*-P2VP while the NPs were segregated along the interface between PS and P2VP domains of PS-*b*-P2VP when the areal density of the polymer ligand was small.[71]

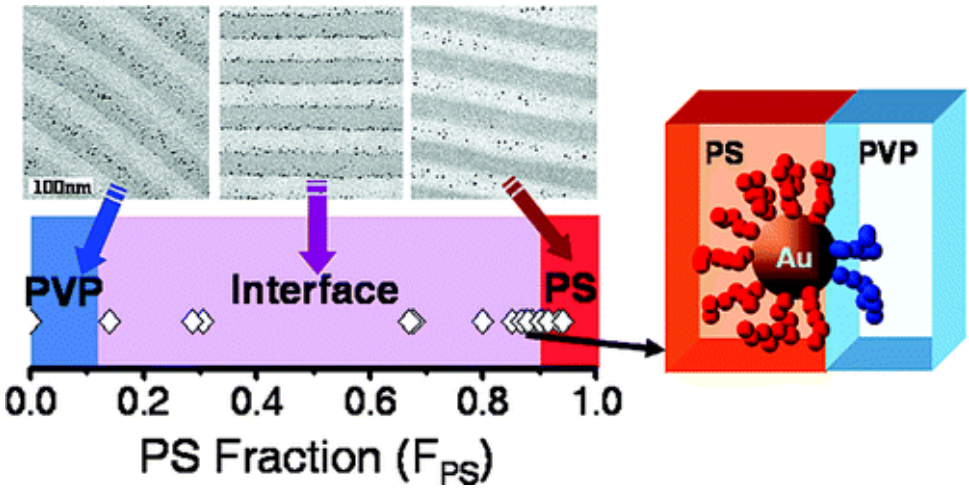

Figure 1.2. Kramer *et al*. have shown that the spatial organization of Au NPs coated by a mixture of low molecular weight thiol end-functional PS/P2VP can be controlled in PS-*b*-P2VP. Varying the PS and P2VP surface compositions (F_{PS}) on the Au NPs allows one to place the NPs into PS or P2VP microdomains or at the interface. Adapted with permission from B. J. Kim, J. Bang, C. J. Hawker, et al., *Langmuir*, 2007, **23**, 12693-12703. Copyright 2007 American Chemical Society.

Simulation and computational studies have also been reported to explore the spatial organization of polymer modified NPs in polymer matrices. Sides *et al*. presented a fluid model for investigating the equilibrium structure of mesostructured polymeric fluids with embedded NPs.[74] The simulation results were consistent with the experimental ones conducted on PS-functionalized Au NPs in a PS-*b*-P2VP melt. The method can be used for polymers of arbitrary chemical and architectural complexity, along with particles of all shapes, sizes, and surface treatments. Akcora *et al*. demonstrated theory and simulations on self-assemblies of spherical NPs uniformly grafted with macromolecules into a variety of anisotropic superstructures in homopolymer matrix.[75] The computational results suggested the balance between the energy gain

when particle cores approach and the entropy of distorting the grafted polymers in the NP self-assembly. Recently, Jayaraman *et al*. have shown simulation studies that the inter-particle attraction/repulsion in a polymer matrix can be tuned by controlling the grafting density of polymer ligand on the NPs, which may provide opportunities for one to generate NP clusters with controlled inter-particle distance in polymer domains.[76-78] Some other works illustrate how copolymer functionalization and the sequence of the grafted copolymer ligands could be a new route experimentalists can take to tailor self-assembly of NPs into nanoclusters with tunable shape and size in the polymer matrix.[77,78] The theoretical results may potentially help the experimentalists gain further control over the NP assemblies in BCPs.

For all the cases discussed above, the enthalpic contributions are relatively small since they rely on weak van der Waals interactions between NP ligands and BCP block. To achieve better solubility of NPs selectively in one BCP block, NP incorporation should be driven by stronger enthalpic interactions between the block and the NP ligands through ionic interactions, dipole-dipole interactions, and hydrogen bonding. Wiesner's group pioneered in the approach by introducing dipole–dipole interactions and hydrogen bonding between the ligands on the NPs and the PEO blocks in PS-*b*-PEO (Figure 1.3).[79] They showed that Pt NPs modified with ionic liquid ligands, N, N-di-2-propoxyethyl-N-3-mercaptopropyl-N-methylammonium chloride, could be preferentially driven into one of the domains in poly(isoprene-*b*-dimethylaminoethyl methacrylate) (PI-*b*-PDMAEMA) *via* ionic interactions.[79] Using this approach, the Pt NPs had high solubility in the PDMAEMA blocks and the NP loading could reach as high as 74 wt% in

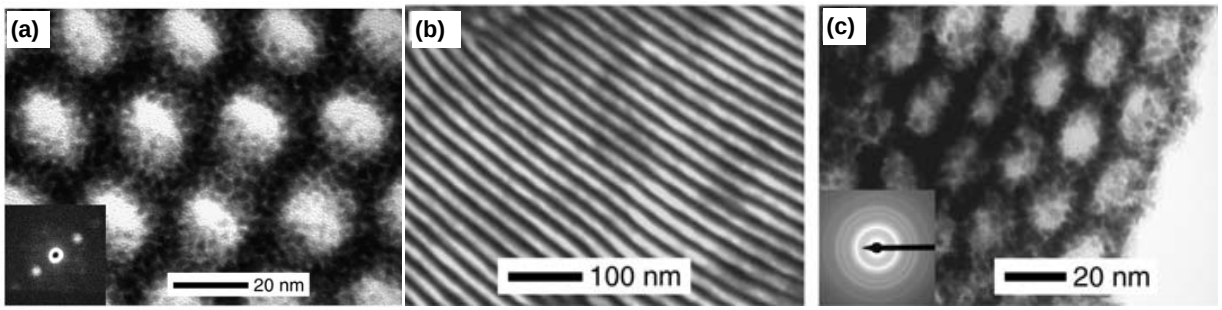

Figure 1.3. Warren *et al*. showed that Pt NPs modified with ionic liquid ligands, N, N-di-2-propoxyethyl-N-3-mercaptopropyl-N-methylammonium chloride, could be preferentially driven into one of the domains in poly(isoprene-*b*-dimethylaminoethyl methacrylate), PI-*b*-PDMAEMA *via* ionic interactions. (a) Examination of the nanocomposite at higher magnification resolved individual Pt NPs, seen as dark spots in the bright-field image of TEM. (Inset) A typical convergent-beam electron diffraction pattern (seen with an ultra–high-vacuum scanning transmission electron microscope) from a single Pt NPs, demonstrating its crystallinity. (b) An annealed lamellar hybrid. (c) Pyrolysis of an annealed inverse hexagonal hybrid yields a mesoporous Pt-C composite. (Inset) Selected area electron diffraction, showing Pt expected face-centered cubic scattering profile. From S. C. Warren, L. C. Messina, L. S. Slaughter, M. Kamperman, Q. Zhou, S. M. Gruner, F. J. DiSalvo and U. Wiesner, *Science*, 2008, **320**, 1748-1752. Reprinted with permission from AAAS.

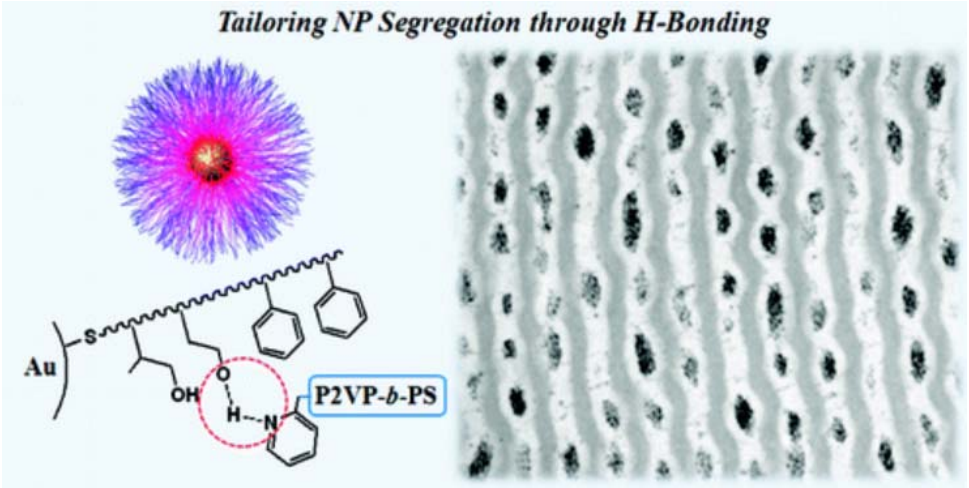

Figure 1.4. Jang *et al*. reported a facile strategy to synthesize amphiphilic Au NPs functionalized with an inner hydroxylated polyisoprene (PIOH) layer and an outer PS shell. The spatial organization of the Au NPs can be precisely contolled by varying the number of the PIOH groups in the ligand. To prove this conclusion, they added small molecule additives that can hydrogen bond with the hydroxyl groups within the PIOH shell of the NP and compete with the P2VP chains. Interestingly, as the volume fraction of the small molecule reaches a critical value, no NPs were found at the interface with the majority of NPs being present in pea-pod-like nanoaggregates within the PS domains. Adapted with permission from S. G. Jang, E. J. Kramer and C. J. Hawker, *J. Am. Chem. Soc.*, 2012, **133**, 16986-16996. Copyright 2012 American Chemical Society.

the nanocomposites. After pyrolysis of the film, a nanostructure containing 97 wt% of Pt was generated. In addition to ionic interactions, hydrogen bonding between NP ligands and one block of the BCP can be formed to enhance the enthalpic contributions, which allows one to tailor the spatial organization of NPs in BCPs. Recently, Jang *et al*. reported a synthetic strategy to synthesize amphiphilic Au NPs functionalized with an inner hydroxylated polyisoprene (PIOH) layer and an outer PS shell (Figure 1.4).[80] When the number of the PIOH groups increased, the P2VP chains had more access to the hydroxyl groups in the inner shell. The energy gain due to the hydrogen bonding between the PIOH groups and the P2VP chains offset that from the adsorption of P2VP chains on Au-core surfaces and the energy penalty of mixing PS brushes into P2VP domains. This results in selective segregation of NPs in the P2VP domains. Small molecule additives that can hydrogen bond with the hydroxyl groups within the PIOH shell of the NP were used to compete with the P2VP chains to further tailor NP-polymer interactions. Interestingly, as the volume fraction of the small molecule reached a critical value, no NPs were found at the interface with the majority of NPs being present in pea-pod-like nanoaggregates within the PS domains. Similar approaches have been used to achieve the assemblies of the Au NPs modified by hydroxylated ligands, in PS-*b*-P2VP.[81,82] Due to the formation of hydrogen bonds between the hydroxyl groups in the ligands and the polymer chains, the Au NPs were

strongly localized in P2VP domains with a very high volume fraction of NPs around 0.53.[81] Using stronger interactions such as ionic interactions and hydrogen bonding between the NP ligands and the polymer chains can strengthen the enthalpic contributions from $\Delta H_{ligand/polymer}$. This gives one not only a useful tool to manipulate the spatial organization of NPs in BCPs, but also a strategy to achieve high NP loading in BCP microdomains to generate a rich library of inorganic nanostructures.

Besides the enthalpic contributions, the entropic contributions in Equation 1 also play important roles in the co-assemblies of NPs and BCPs in bulk. Upon incorporation of NPs in polymers, the polymer chains must stretch around these obstacles, causing a loss in conformational entropy ΔS_{con}. This entropic contribution may sometimes become a dominant driving force especially when $\Delta H_{ligand/polymer}$ relies on weak enthalpic interactions and the particle radius is relatively large compared with the radius of gyration of the polymer. The entropic effects on the NP assemblies have been extensively studied theoretically.[62,65,83] The pioneering work by Balazs' group has combined density functional theory and self-consistent field theory to simulate the behavior of NPs of diameter d in BCP domains of period L.[62,64,84,85] They showed that the interfacial segregation of NPs with neutral ligands (*i.e.*, $\chi = 0$) occurs for small particles ($d/L < 0.2$).[62] However, when $d/L > 0.3$, the NPs become more localized toward the center of the appropriate domains to minimize the conformational entropic penalty as chain stretching becomes significant to accommodate the NPs.[62] In this case, the entropic cost of stretching the polymer chains in order to accommodate the particles is greater than that offset by the translational entropy of the particles, which is maximized by distributing particles homogenously throughout the domain. To systematically study the entropic effects, experimentalists have investigated the effect of d/L ratio on the assemblies of NPs in BCPs by varying the NP size, ligand size, and the molecular weight of the BCP.[39,40] Bockstaller *et al*. investigated the effect of entropy on the spatial distribution of Au and SiO_2 NPs of different sizes (Figure 1.5).[27] They observed that the larger SiO_2 NPs ($d/L = 0.26$) resided in the center of the domain while the smaller Au NPs ($d/L = 0.06$) located along the inter-material dividing surface. The experimental results agreed with the simulation, suggesting that the self-assembly process was predominantly determined by entropic contributions. For large particles, the decrease in conformational entropy of the respective polymer chains upon particle sequestration is dominant, whereas for smaller particles, the decrease in entropy is offset by the particle's translational entropy. Similar results were observed in a system containing triblock copolymers and Au NPs of different sizes.[86] These studies not only elucidated the entropic effects on the co-assemblies of NPs and BCPs, but also showed the potential of using BCPs to achieve hierarchical nanostructures of different kinds of NPs in a ternary nanocomposite. Another strategy to investigate the effect of d/L ratio on the self-assemblies of NPs in BCPs is to vary the molecular weight of the BCP, thereby varying L while keeping the particle size d unchanged. Chiu *et al*. observed that the NPs localized near the center of the microdomains when the d/L ratio was changed to be from 0.13 to 0.44 by varying the molecular weight of the BCP, which is consistent with the simulation.[73] As the d/L ratio decreased to be smaller than 0.1, the conformational entropic penalty became less significant and the particles were more dispersed in the microdomain as the molecular weight of the BCP increased. However, as the volume fraction of the NP increased, the increase in stretching

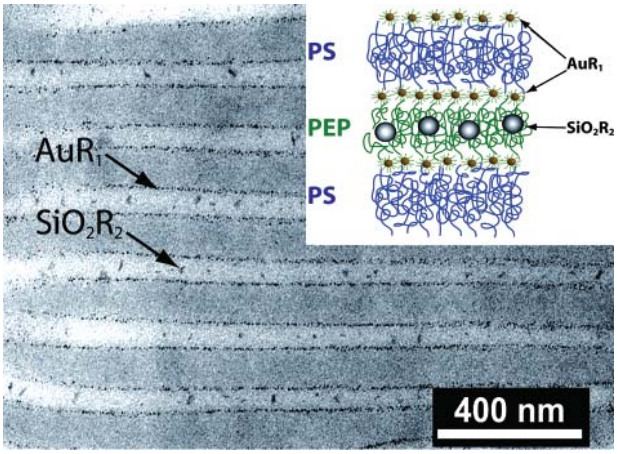

Figure 1.5. Bright field TEM micrograph of a ternary blend of PS-*b*-PEP, ~3.5 nm Au NPs, and ~21.5 nm SiO_2 NPs with the volume fraction of the NPs around inorganic filling fraction φ = 0.02. In the TEM image, the Au NPs appear as dark spots along the intermaterial dividing surface and the silica nanocrystals reside in the center of the PEP domains. Inset: Schematic of the particle distribution (size proportions are changed for clarity). Adapted with permission from M. R. Bockstaller, Y. Lapetnikov, S. Margel and E. L. Thomas, *J. Am. Chem. Soc.*, 2003, **125**, 5276-5277. Copyright 2003 American Chemical Society.

penalty could no longer be offset by translational entropy, resulting in a more localized spatial organization of the NPs in the middle of the domains.

§ 1.2.3. Nanocomposites based on preformed NPs in thin films

Multidimensional NP arrays can be readily generated in bulk BCPs by balancing the entropic and enthalpic contributions. For many practical applications, the nanostructured arrays of NPs need to be in thin film configurations. Controlling the 3-D spatial organization of NPs, especially in a thin film form of BCPs, opens up the routes toward the fabrication of functional materials with unique optical, mechanical, and electrical properties.

In thin films of BCPs, however, the thermodynamics that governs the NP assemblies becomes more complex because the surface to volume ratio is large and the interfacial interactions at the air/film and the film/substrate interfaces begin to come into play.[65,83] Similar to that in bulk, the assembly of NPs upon blending with BCP in thin films is determined by a combination of enthalpic and entropic contributions.[39,40,63,84] In thin BCP films, the change in free energy upon incorporation of NPs can be written as:

$$\Delta G = (\Delta H_{ligand/polymer} + \Delta H_{ligand/air} + \Delta H_{ligand/substrate}) - T(\Delta S_{con} + \Delta S_{trans}) \quad (2)$$

where $\Delta H_{ligand/air}$ accounts for the change in enthalpy due to ligand/air interactions and $\Delta H_{ligand/substrate}$ accounts for the energetic change due to the interfacial interactions between the ligands on the NPs and the substrate.

BCP thin films have been used as templates to guide the 1-D/2-D assemblies of NPs at the air/polymer interface.[26,87] Lopes and Jaeger showed that the deposited Au atoms preferentially wet the top of the PS microdomains through hydrophobic interactions in an ultra-thin film containing PS-*b*-PMMA BCPs.[26] The BCP film formed a regular scaffold of highly anisotropic, stripe-like domains. Differential wetting guided diffusing metal atoms to aggregate selectively along the scaffold, producing highly organized 1-D and 2-D metal nanostructures on the surface of the film. In another approach, Binder *et al*. reported binding Au NPs onto the surface of one of the blocks in microphase-separated BCPs in thin films via hydrogen bonds.[88] Another approach is to produce a nanotemplate wherein NPs could be sequestered using thin films of cylindrical BCPs.[38,89,90] Hexagonally ordered cylindrical pores were used to host NPs with appropriate sizes and surface ligands.[90] In addition, external fields can be used to deposit NPs in BCP nanoporous films. Zhang *et al*. showed the controlled placement of CdSe NPs in PS-*b*-PMMA based nanoporous film using electrophoretic deposition.[91] Varying the deposition time, the NP concentration, and the strength of the applied electric field allowed them to easily tune the degree of deposition.

To precisely control the 3-D spatial organization of NPs in BCP thin films, many reports have successfully tailored $\Delta H_{ligand/polymer}$ by modifying the surface chemistry on the NPs. Li *et al*. demonstrated that Au NPs could be functionalized with a mixture of hydrophilic and hydrophobic ligands by ligand exchange (Figure 1.6).[92] The variation of NP ligands and processing methods allowed them to disperse the Au NPs either within one of the microdomains, or at the interface between the microdomains, in PS-*b*-P2VP BCP thin films. Moreover, thermal annealing caused coarsening of the NPs in the P2VP microdomain and further heating led to an expulsion of the particles from the interior of the film. Similarly, Kang *et al*. showed that tetradecyl phosphonic acid (TDPA)-capped CdSe NPs (CdSe-TDPA) preferentially segregated near the center in the PS microdomains in PS-*b*-PMMA BCP thin films.[93] In this case, due to the strong repulsion between the PMMA chains and the TDPA ligands on the NPs, the energy penalty of mixing CdSe-TDPA into PMMA blocks was too high. As a result, CdSe-TDPA NPs were sequestered in PS microdomains. Park *et al*. showed that PEO modified Au NPs were preferentially sequestered in PMMA cylinders in poly(styrene-*b*-methyl methacrylate) (PSt-*b*-PMMA) thin films.[94] During the solvent annealing process, the PEO capped Au NPs interacted with the water vapor, thereby a significant number the NPs were segregated to the top surface of of the film, where water vapor was condensed. As the solvent was removed rapidly from the film, the PMMA cylinders containing the Au NPs began to grow vertically and induce the perpendicular orientation of the microdomains. This work shows that surface modification on the NPs can tailor ligand/polymer and ligand/surface interactions, allowing one to control the orientation and spatial organization of the NP arrays simultaneously in thin films. Li *et al.* utilized the approach of tailoring ligand/polymer interactions to create responsive polymer/NP nanocomposites by modifying Au NP with P4VP homopolymer ligands and assembling the NPs

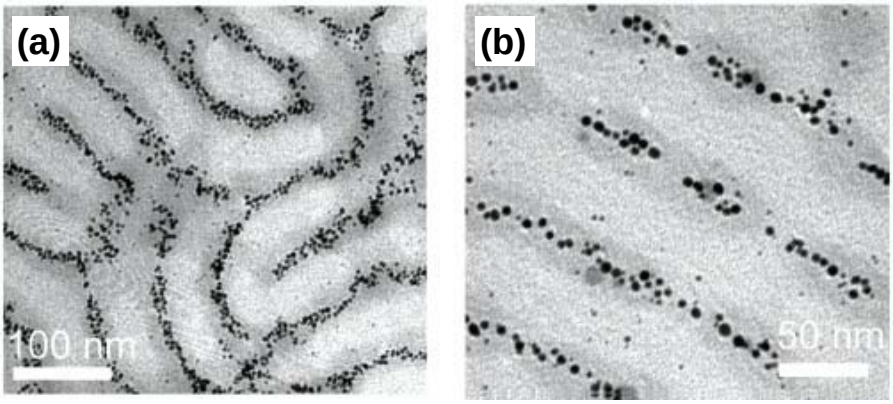

Figure 1.6. (a) and (b) show the TEM images of PS-*b*-P2VP/Au NPs A (1:1) and NP B (3:1) mixtures, respectively. NPs with ratios of dodecanethiol to 11-mercapto-1-undecanol ligand of 1:1 and 3:1 were used in this study, referred as NP A (1:1) and B (3:1), respectively. The samples were prepared on silicon wafers and solvent annealed, followed by thermal annealing on a hot stage under vacuum at 170 °C for 30 min and then quenched to room temperature in the nitrogen flow. Adapted with permission from Q. Li, J. He, E. Glogowski, X. Li, J. Wang, T. Emrick and T. P. Russell, *Adv. Mater.*, 2008, **20**, 1462-1466. Copyright 2008 Wiley-VCH.

into a PS-*b*-P4VP thin film.[95] The nanocomposite demonstrated variable localized surface plasmon resonance bands and morphologies during solvent annealing due to the spatial reorganization of the NPs.

In addition to the enthalpic contributions originating from $\Delta H_{ligand/polymer}$, $\Delta H_{ligand/air}$ and $\Delta H_{ligand/substrate}$ in Equation 2 also significantly influence the NP assemblies in BCP thin films. In thin films, the component that has relatively lower surface energy wets the air/polymer interface to minimize surface tension of the film. For example, Lin *et al*. showed that tri-n-octylphosphine oxide-(TOPO)-covered CdSe NPs covered the top of the P2VP microdomains and segregated at P2VP/substrate interface in thin films of PS-*b*-P2VP/CdSe nanocomposites (Figure 1.7).[30] Usually, the preferential interaction of P2VP with the substrate and the lower surface energy of PS forced an orientation of the cylindrical microdomains parallel to the substrate. However, the segregation of the NPs at the interfaces mediated the interfacial interactions, resulting in the perpendicular orientation of the microdomains regardless of the nature of the substrate or the film thickness. The favorable interactions between the substrate and the ligands on the NPs also determined the spatial arrangement of the NP in BCP thin films. For instance, Meli *et al*. reported that the majority of the PS capped Au NPs in a thin film consisting of polystyrene-*b*-poly(1,1',2,2'-tetrahydroperflurooctyl methacrylate) (PS-*b*-PFOMA) micellar BCPs segregated at film/substrate interface.[96] Furthermore, near the substrate (silicon nitride), the PS capped Au NPs that had an average size comparable to the radius of gyration of the polymer chain located at the interface between the two blocks. This result indicates that the enthalpic interactions between the substrate and the ligands may overcome that between the favorable ligand/polymer enthalpic

interactions and the conformational entropy of the host chains, which provides one a useful tool to control the spatial organization of NPs in thin films of BCPs.

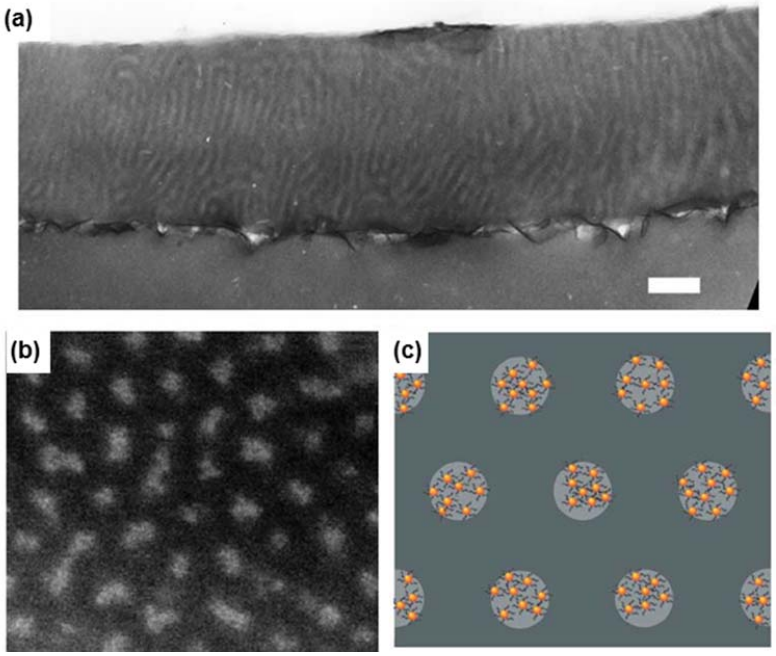

Figure 1.7. (a) and (b) show the cross-sectional TEM and secondary electron SEM images of the nanocomposite thin film containing PS-*b*-P2VP BCP and TOPO capped CdSe NPs, respectively. The CdSe NPs were found to cover the P2VP cylinders at the air/polymer and polymer/substrate interfaces. The sample was thermally annealed at 170 °C for 2 days. (c) Schematic representation of the assembly of CdSe NPs on top of the P2VP cylinders. Reprinted by permission from Macmillan Publishers Ltd: Nature. Y. Lin, A. Boker, J. B. He, K. Sill, H. Q. Xiang, et al., *Nature*, 2005, **434**, 55-59, copyright 2005.

As in bulk, besides the enthalpic contributions, the entropic ones in Equation 2 also affect the co-assemblies of NPs and BCPs in thin films significantly. In homopolymer/NP systems, Green's group has done extensive studies on the spatial organization of the NPs in polymer matrix as a function of the NP size.[97-99] In a NP/PMMA nanocomposite, Gupta *et al*. found that the larger PEO-modified CdSe NPs that had average diameter comparable to the radius gyration of the PMMA matrix were driven to the exposed crack area, whereas the smaller CdSe NPs tended to be homogeneously distributed in the film.[100] Expelling the larger NPs to the free surface resulted in an entropic gain as the PMMA chains must extend and stretch around the NPs to achieve a uniform dispersion. The result indicates that the entropic penalty imposed on the PMMA chains owing to the presence of the particles can be a dominant factor affecting the spatial organization of the NPs in polymer films.

There are also reports that focus on the entropic effects on the NP assemblies in BCP thin films. Lauter-Pasyuk *et al*. used neutron reflection to determine the spatial distributions of Fe_2O_3 NPs (4 and 6 nm in diameter) in the films containing d-PS-*b*-PBMA BCPs.[66,67] They observed that the small NPs (4 nm) concentrated close to d-PS-*b*-PBMA interfaces while the larger NPs (6 nm) localized in the center of PS domains, which is consistent with that observed in bulk. Kim *et al*. studied the spatial organization of PS-modified Au NPs in thin films of PS-*b*-PnBMA (Figure 1.8).[101] Large Au NPs preferentially segregated to the core of edge dislocations in the parallel lamellar structure to minimize the loss in conformational entropy in the matrix and relax the chain stretching from the polymer chains surrounding the core of the dislocations (Figure 1.8a and 1.8b). However, when the NPs were small, they located throughout the PS domains because the gain in translational entropy of the NPs offsets this cost in entropic energy (Figure 1.8c). The work emphasizes the dominant role of dislocations in determining the spatial organization of sufficiently large NPs and the entropic contributions to the NP assemblies in BCP thin films. Recently, Yoo *et al*. showed that the neutral Au NPs were mainly located near the substrate with some near the top surfaces in a thin film of perpendicular lamellae of PS-*b*-PMMA.[102] Their self-consistent field theory simulations show that neutral Au NPs NPs at the PS/PMMA interface moved to the film/substrate interface to reduce the entropic penalty of the polymer chains. The consistent field theory simulations show that neutral Au NPs NPs at the PS/PMMA interface moved to the film/substrate interface to reduce the entropic penalty of the polymer chains. The

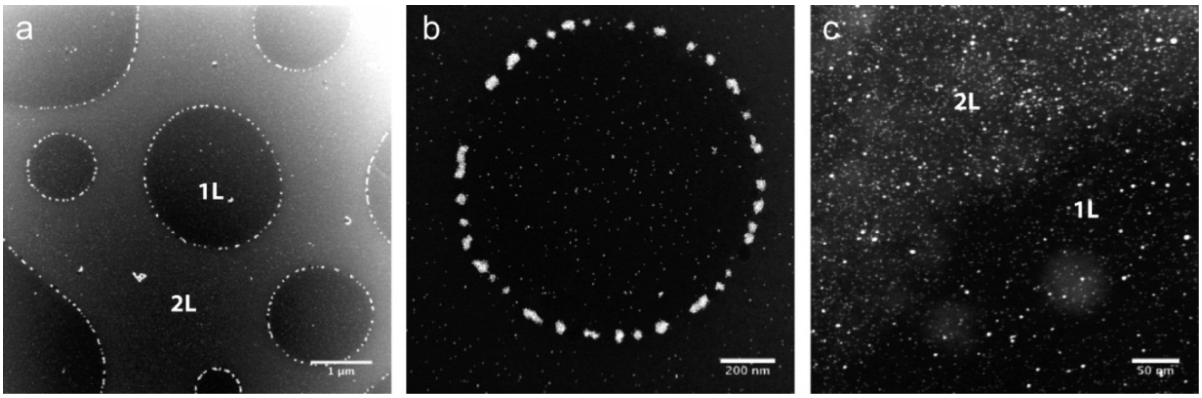

Figure 1.8. STEM images of the lateral distribution of NPs in BCP (PS-*b*-PnBMA) thin films containing 3 wt% NPs. (a) The image of a film containing PS capped Au NPs of average diameter 5.1 nm is shown and the NPs are found to be localized at the core of the edge dislocation. (b) A magnified image of (a). (c) The edge of a hole in a film containing Au NPs of average diameter 1.8 nm. It is clear that the smaller Au NPs were more homogeneously distributed in the film. Adapted with permission from J. Kim and P. F. Green, *Macromolecules*, 2010, **43**, 10452-10456. Copyright 2010 American Chemical Society.

results, again, suggest that the location of the NP within BCP templates in thin films can be greatly influenced by the entropic contributions.

It has been demonstrated that the 3-D spatial organization of a single kind of NP can be precisely controlled by tailoring the surface chemistry and the size of the NPs. Moreover, by modifying the surface chemistry of the NPs, stimuli-responsive nanocomposites may be generated. For example, Li *et al*. showed that Au NPs decorated with P4VP and poly(N-isopropylacrylamide) (PNIPAM)/poly(methoxy-oligo(ethylene glycol) methacrylate) (PMBAA) mixture ligands could be used to construct pH[103,104] and temperature[105,106] sensitive nanocomposites, respectively. For next-generation NP-based devices, however, the nanocomposite thin films may need to demonstrate multiple and tunable functionalities that originate from the coupling effects between the NP arrays of different species. To this end, people have been seeking the possibility of creating hybrid arrays of NPs in thin film configurations. For example, monodisperse metal, semiconductor, and magnetic NPs of different sizes can self-assemble into 2-D binary NP superlattices *via* controlled solvent evaporation, yielding multifunctional hybrid nanocomposites.[107,108] To self-assemble two different types of NPs using a BCP template, Sohn *et al*. incorporated Au NPs physically around hexagonally ordered micelles composed of PS-*b*-P4VP (P4VP in the core) in a monolayer film (Figure 1.9).[109] Hydrophobic Au NPs were preferentially sequestered in the intermicelle nonpolar PS corona regions energetically favorable with the minimum entropic packing penalty. Iron oxide NPs were then *in situ* synthesized in the core area of the ordered micelles (P4VP), resulting in iron oxide NPs surrounded by gold NPs. A similar approach has been used by Kim's group to fabricate hybrid NP arrays in which the preformed Au and *in situ* synthesized Ag NPs were in the core and corona regions of the micelles in the 2-D arrays, respectively.[110] This led to a controlled inter-particle distance between different plasmonic NPs in a uniform and homogeneous thin film with tunable surface plasmon resonance band. Using the same method,

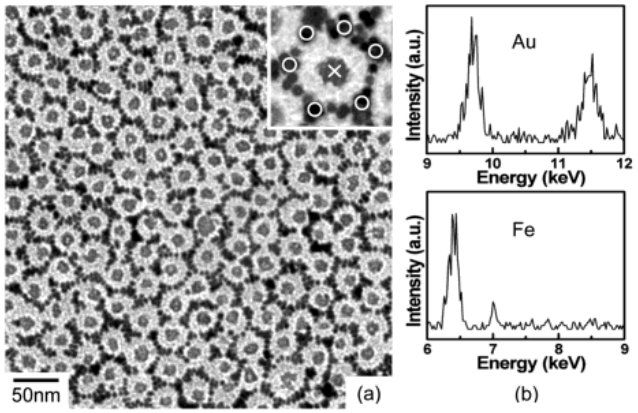

Figure 1.9. (a) TEM image of an array of iron oxide NPs surrounded by gold NPs; (b) EDX spectra on gold and iron NPs marked by circles and a cross in the enlarged TEM image, respectively. Adapted with permission from B. H. Sohn et al. *J. Am. Chem. Soc.*, 2003, **125**, 6368-6369. Copyright 2003 American Chemical Society.

Acharya *et al*. fabricated hybrid 2-D arrays of anisotropic TiO_2 nanocrystals and Ag NPs in thin films of inverse PS-*b*-P4VP micelles using the same technique.[111] The Ag NP-decorated TiO_2 2-D networks demonstrated enhanced photocatalytic activity by approximately 27 and 44% over that of Ag-free TiO_2 networks and randomly deposited TiO_2 NPs, respectively.

To control the 3-D spatial organization of hybrid arrays of NPs, one of the recent efforts done by Haridas *et al*. showed the potential of using BCPs to guide the assemblies of binary mixtures of NPs in thin films.[112,113] In their work, thin films of hybrid arrays of pyridine modified CdSe quantum dots and PS grafted Au NPs were successfully prepared using PS-*b*-P4VP template. Specifically, the preferential interactions between pyridine and P4VP localized the CdSe quantum dots exclusively into the P4VP cylinders while the PS capped Au NPs resided inside the PS matrix. Controlling the dispersion and location of the respective NPs allowed them to tune the exciton–plasmon interaction in the hybrid arrays and hence control the optical properties of the nanocomposite thin film.

§ 1.3 Block copolymer-based supramolecular nanocomposites

In the previous section, the efforts made to generate multidimensional nanostructured arrays of NPs in conventional coil-coil BCPs in bulk/thin films have been discussed. Manipulating the balance between the enthalpic and entropic contributions provides one the opportunities to precisely control the spatial distribution of NPs in BCPs. However, it still remains challenging to achieve precise control over the inter-particle ordering in NPs assemblies using BCPs that have coil-coil chain configurations. Supramolecules can be readily constructed by attaching small molecules to polymer backbones *via* secondary interactions such as hydrogen bonding and ionic interactions. Attaching small molecules that favorably interact with the NP ligands to the polymer side chains can effectively tailor NP/polymer interactions. This eliminates the need to conduct NP surface chemistry. In addition, the unique architecture of BCP-based supramolecules allows one to tailor the balance between ΔS_{con} and ΔS_{trans}, which depends on not only the d/L ratio, as discussed previously, but also the entropic spring constant k of the polymer chain. The k of the comb-like segments in coil-comb supramolecules deviates from the expression ($k = 3kT/(Nb^2)$) for conventional Gaussian polymer chains, which makes the system to be more sensitive to the change in conformational entropy upon NP incorporation and enhance the entropic contributions in the co-assembly process. This provides a unique handle to direct NP assembly at a single polymer chain level. The small molecules in the comb blocks can order on the molecular level within the BCP microdomains, resulting in hierarchical assemblies that can further guide the spatial distribution of the NPs with a precision akin to that seen when using DNA.

To make coil-comb BCPs, one can either synthesize BCPs with a block containing rigid moieties covalently bonded to the back bones or attach rigid small molecules to the blocks through secondary interactions to form BCP-based supramolecules. Using secondary interactions eliminates the need to modify polymer chains and the strength of the non-covalent linkage

between the small molecules and BCP can be varied by external stimuli. Therefore, the architecture of the supramolecules and the spatial distribution of the NPs can be tailored using external fields. In addition, using a supramolecular approach allows one to incorporate functional small molecules into the supramolecules to tune the physical properties of the nanocomposites. The supramolecular approach allows one to precisely control the spatial organization of NPs at multiple length scales to generate functional/stimuli responsive nanocomposites. In this section, we will focus on the constructions and the phase behaviors of the BCP-based supramolecules containing various kinds of small molecules and the directed assemblies of spherical/anisotropic NPs in supramolecular templates in bulk or in thin films.

§ 1.3.1. Phase behaviors of BCP-based supramolecules in bulk/thin films

The phase behavior of BCP-based supramolecules in bulk has been extensively studied by ten Brinke and Ikkala, which provide useful information to guide initial studies in co-assemblies of NPs and BCP-based supramolecules in bulk.[114-121] They demonstrated a simple supramolecular way of constructing self-organizing comb-coil BCPs with two length scales by combining BCPs with hydrogen-bonding amphiphiles.[114,115] The most extensively studied supramolecular system contains PS-*b*-P4VP with 3-pentadecylphenol (PDP) small molecules attached to the 4VP groups through hydrogen bonding, leading to self-assembly at two different length scales.[114,115,122,123] The larger length scale corresponds to the microphase separation of BCP in tens to a few hundred nanometers, and the shorter length scale, typically only a few nanometers, is determined by the length of the repulsive side chains within the comb block. The concept allows a rich variety of morphologies and phase transitions by modifying the block lengths, the amount of the amphiphiles, their alkyl chain lengths, and the strength of the hydrogen bonding.[123] The side chains, typically low molecular weight amphiphilic compounds, can also be attached to the P4VP backbones through ionic interactions. For instance, Ikkala and ten Brinke *et al*. showed that the 4VP groups could be protonated with methanesulfonic acid (MSA) such that the MSA small molecules were strongly attached to the P4VP blocks through ionic interactions and the comb-like blocks became charged.[121,123]

In addition to the phase behavior of the supramolecules, Ikkala and ten Brinke *et al*. also investigated the stimuli responsiveness of the BCP-based supramolecules.[118,119,124] They first reported the influence of large amplitude oscillatory shear on the macroscopic orientation of the PS-*b*-P4VP(PDP)$_r$ supramolecules and the pathways toward macroscopic orientations.[124] In one case, they found that oscillatory shear orientation of hierarchically-ordered PS-*b*-P4VP(PDP)$_r$ of a cylinder-within-lamellar morphology resulted in parallel alignment of the PS cylinders with the (10) plane parallel to the shear plane and transverse alignment of the matrix layers.[119] Their results suggested that PS-*b*-P4VP nanorods of up to 10 μm length can easily be prepared using the shear flow procedures.

To prepare the supramolecular approach for nanofabrication and nanotemplating, it is necessary to study the phase behavior of the BCP-based supramolecules in thin films. In thin films of BCPs, the interfacial interactions at air/polymer and polymer/substrate interfaces have strong impacts on the morphology of the BCPs.[125] Van Zoelen *et al*. first reported that the P4VP(PDP) blocks wet the surface and the silicon oxide layer on the substrate due to the low surface energy of the PDP small molecules and the favorable interactions between the P4VP blocks and the silicon oxide on the substrate.[126] As opposed to pure PS-*b*-P4VP BCPs, which exhibit asymmetric wetting conditions (PS wets the surface and P4VP the substrate), the PS-*b*-P4VP(PDP) supramolecules have symmetric boundary conditions in thin films. Tung *et al*. showed that the interfacial interactions could be modified by the PDP small molecules.[127] They found that increasing the weight fraction of the P4VP(PDP) blocks not only affected the morphology of the supramolecules, but also resulted in the perpendicular orientation of the microdomains in thin films. The PDP in the P4VP(PDP) microdomains and a trace amount of PDP in the PS domains were found to mediate the interfacial interactions between the polymer chains and the underlying substrate. Kao *et al*. further continued the study by modifying the polarity of the underlying substrate by using PS coated substrate.[128] With the weight fraction of the comb block > 0.5, the macroscopic orientation of the supramolecules was still perpendicular to the surface. The main reason was that the PDP small molecules near the polymer/substrate interface changed their orientation to mediate the unfavorable interfacial interactions between P4VP and the PS modified substrate. Thus, the macroscopic orientation of the supramolecules could be preserved on non-polar substrate.

In addition to PDP, the solvent used during solvent annealing also mediate the interfacial interactions, affecting the morphology and the macroscopic orientation of the supramolecules in thin films. Because of the selectivity of chloroform toward PS, the morphology of the supramolecules could be changed by annealing at different vapor pressures, which, for a specific strongly segregated system that was on the boundary between lamellar and cylindrical, resulted in terraces of metastable perpendicular lamellae.[129] During annealing, the P4VP(PDP) comb blocks underwent an order–to-disorder transition and PS and P4VP microphase separated in the normal parallel structures. After solvent evaporation, the combs crystallized and formed parallel layers within the terraces of the parallel microdomains. Recently, Stamm *et al*. found that the orientation of cylindrical microdomains of P4VP(HABA) in thin films of PS-*b*-P4VP(HABA) depended on the selectivity of the solvent as well as on the degree of swelling.[130] In a nonselective solvent like chloroform, the cylinders were found to lie parallel to the substrate as long as the swelling ratio allowed the system to be in the cylindrical region of the phase diagram. At high swelling ratio, the cylinders transforms into spherical domains, and drying of the solvent resulted in perpendicular orientation due to the coalescence of the spherical microdomains. In a selective solvent like 1, 4-dioxane, the cylinders were found to be always oriented perpendicular to the substrate. The solvent preferentially swell the PS domains and the system easily went into spherical morphology which ultimately resulted in perpendicular cylinders.

§ 1.3.2. Nanoparticle assemblies in BCP-based supramolecules in bulk

Using supramolecular templates (PS-*b*-P4VP(PDP)$_r$), Zhao *et al*. directed the assemblies of NPs to generate stimuli-responsive hierarchically structured nanocomposites in bulk (Figure 1.10).[131] Compared with the BCPs with random coil configuration, BCP-based supramolecules have small molecules that effectively tailor the interactions between BCP and NPs, direct inter-particle ordering and generate responsive NP assemblies. In blends of PS(40 kDa)-*b*-P4VP(5.6 kDa)(PDP)$_1$ and various kinds of NPs of different sizes, the native alkyl ligands capped NPs were selectively incorporated into the lamellar P4VP(PDP)$_1$ microdomains due to the favorable PDP/alkyl ligand interactions (Figure 1.10a). In cylindrical supramolecules where PS cylinders were embedded in P4VP(PDP)$_3$ matrix, 7 vol% of ~5.4 nm PbS NPs were arranged in a hexagonal grid (Figure 1.10b and 1.10c). Because of the unique architecture of the supramolecule, the increase in entropic penalty arising from the polymer chain deformation on the incorporation of the NPs is greater than that in coil-coil BCPs. To minimize the loss in conformational entropy due to chain deformation, the NPs formed a single layer, only one particle diameter in thickness, in the center of the P4VP(PDP)$_1$ blocks (Figure 1.10a). In cylindrical nanocomposites, the PbS NPs were preferentially sequestered in the corners of the hexagons when the NP loading was decreased (Figure 1.10c). This, again, suggested that the

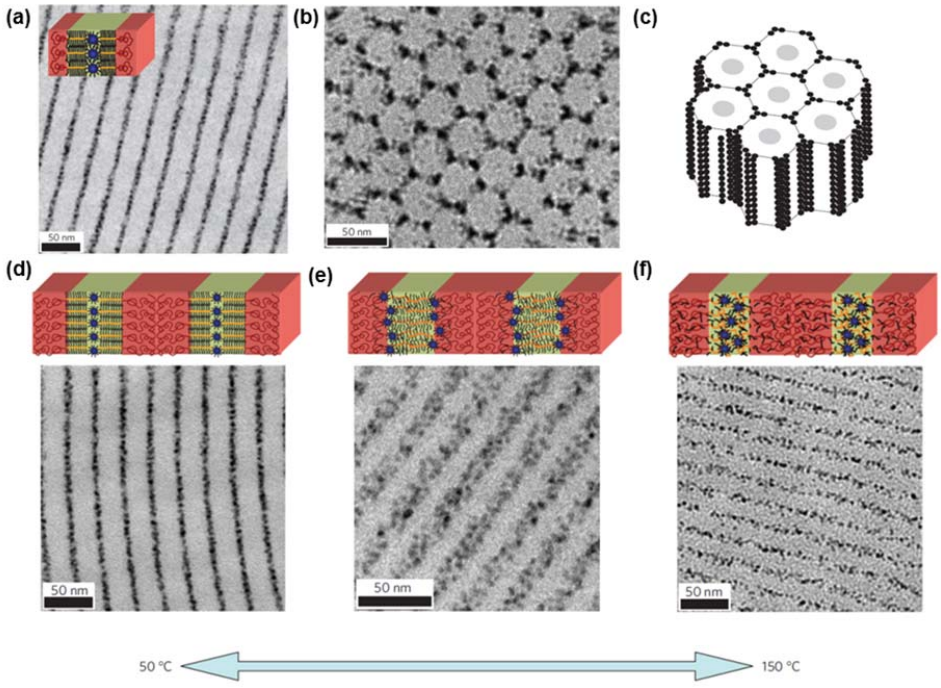

Figure 1.10. (a) TEM image of a blend of PS(40)-*b*-P4VP(5.6)(PDP)$_2$ and ~4 nm CdSe (2 vol%) NPs. The NPs were well confined in the middle of the P4VP(PDP)$_2$ blocks and formed NP sheets in the lamellae. (b) TEM image of a blend of PS(40)-*b*-P4VP(5.6)(PDP)$_3$ and ~5.4 nm PbS NPs, showing the PbS NPs arranged in a hexagonal grid. (c) Schematic diagram showing that the PbS

NPs were preferentially sequestered in the corners of the hexagons as shown in (b). (c-e) TEM images and schematic drawings of the blend of PS(40)-*b*-P4VP(5.6)$(PDP)_2$ and ~4 nm CdSe (2 vol%) NPs quenched from (c) 50 °C, (d) 110 °C, and (e) 150 °C, during the heating and cooling cycles. The blend was heated from 50 to 160 °C and cooled down to 50 °C at a heating/cooling rate of 10 °C min^{-1}. The NPs were assembled in the center of P4VP$(PDP)_2$ lamellae from 50 to 100 °C, at the interfaces between the polystyrene-rich and P4VP$(PDP)_2$ lamellae at 110 °C and randomly distributed in the P4VP$(PDP)_2$ lamellae at 150 °C once the population of the hydrogen bonding between PDP and 4VP decreased. Adapted from Y. Zhao et al. *Nat. Mater.*, 2009, **8**, 979-985. Copyright 2009 Nature Publishing Group.

conformational entropy may be the dominant driving force that directed the NP assemblies in the supramolecular system. The nanocomposites were also found to be thermal and light responsive. Zhao *et al*. found that the NPs were assembled in the center of P4VP$(PDP)_r$ lamellae from 50 to 100 °C, at the interfaces between the polystyrene-rich and P4VP$(PDP)_r$ lamellae at 110 °C and randomly distributed in the P4VP$(PDP)_r$ lamellae at 150 °C as the population of the hydrogen bonding between PDP and 4VP decreased (Figure 1.10c-e). They also attached OPAP small molecules to the supramolecules and the X-ray scattering results suggested that the *trans–cis* isomerization of OPAP induced a 12% change in the periodicity of the NP assemblies in lamellar morphology. Overall, the supramolecular method enables precise control over the spatial distribution of the NPs over multiple length scales due to the coil-comb architecture of the supramolecules, and the hierarchically structured nanocomposites are responsive to heat and light.

Most of the existing studies on supramolecular systems focus on alkyl-based small molecules. The supramolecular approach makes it synthetically trivial to incorporate functional small molecules without synthesizing new polymers. Considering the diversity of small molecules available in terms of molecular packing and built-in functionalities, there are tremendous technological potentials for these supramolecules alone or their blends with NPs. Thorkelsson *et al.* successfully generated PS-*b*-P4VP supramolecules based on organic semiconductors and high dielectric small molecules, in addition to PDP and OPAP, and used the functional supramolecules to effective direct the assembly of a variety of NPs.[132] Liquid crystal smolecules have also been non-covalently attached to the backbone of BCPs to achieve mesogenic phases in BCP microdomains and photo-/magneto-responsive nanostructures.[133-141] In addition, organic semiconductors have been successfully incorporated into BCP frameworks via secondary interactions to generate electronically-active BCP-based supramolecules. This approach not only circumvents some of the synthetic challenges inherent to the preparation of conjugated BCPs, but also solves the dewetting issues of organic semiconductors.[142-144] The crystallization of the organic semiconductors in BCPs microdomains may not only provide percolative pathways for electron/hole charge transfer,[143,144] but also induce stimuli-responsive hierarchical assemblies of small molecules in BCP nanostructures.[145] These results demonstrate

that the supramolecular approach is applicable to a wide range of functional small molecules and NPs, opening new routes for device fabrication based on composite materials.

§ 1.4 Perspective and outlook

Nanocomposites have opened up processing pathways to readily incorporate the properties offered by traditional hard materials without the commonly required high temperature, high vacuum processing conditions. This chapter has highlighted some of the more recent progress in the field of BCPs and BCP-based supramolecules as templates for nanostructured polymer–inorganic hybrid nanocomposites. It is evident from the research over the last fifteen years that powerful design criteria are emerging for the generation of BCP-based nanocomposites with exquisite control over NP spatial organization. Using the supramolecular approach discussed in section 1.3, 3-D nanostructured NP arrays with controlled inter-particle ordering at the molecular level can be achieved in bulk regardless of NP composition. For practical applications, the fabrication process should produce 3-D NP assemblies in thin film configurations that are suitable for device fabrication over macroscopic distances using existing fabrication infrastructure. Yet, it remains challenging as various studies have shown that the thermodynamics and the assembly kinetics governing the phase behavior of BCP-based nanocomposite thin films can be quite different from that in bulk.

The first and perhaps the most important area is establishing a fundamental understanding of the thermodynamics, *i.e.*, the enthalpic and entropic contributions that take place during the co-assembly of BCPs and NPs in thin films. It is requisite to tailor the delicate balance among surface energy, conformational entropy, and polymer/NP enthalpic interactions to achieve 1-D, 2-D, and even 3-D NP assemblies in BCP thin films. For nanocomposites containing preformed NPs, particular emphasis should be devoted to modifying BCP chain architecture, NP surface chemistry, and NP size to modulate the thermodynamic driving forces in the assembly process. Certain applications including nanoelectronics, photovoltaics, catalysis, and energy storage devices require nanocomposites with appropriate 3-D nanostructures of NPs with high volume fractions of inorganic component. However, varying the NP loading perturbs the energy minimum in the system. To generate organic-inorganic hybrid materials with a rich variety of morphologies and compositions, the effect of NP loading on the phase behavior of the nanocomposite also needs to be fully understood.

In addition to thermodynamics, the kinetics of the co-assemblies needs to be further investigated to not only optimize the processing parameters for processing-friendly techniques, but also precisely control the morphologies in equilibrium/kinetically-trapped states to expand the possibility of these nanocomposites to be technologically relevant. Solvent annealing is considered a more advantageous processing technique than thermal annealing as the solvent molecules effectively plasticize the BCP chains to improve the mobility in BCP thin films. However, hours of annealing under high solvent vapor pressure is usually required to achieve

ordered BCP nanostructures. To facilitate the kinetics in BCP-based nanocomposite thin films, the complicated interplay among the diffusion coefficient, activation energy barrier for inter-domain diffusion, and the thermodynamic driving force needs to be elucidated. The fundamental kinetic studies will lay down a solid foundation for the rational design of manufacturing-friendly roll-to-toll processing techniques for scalable fabrication of functional nanocomposite thin films.

Lastly, the macroscopic alignment of the NP arrays in BCP-based nanocomposite thin films needs to be precisely controlled for the investigation of structure-property correlations and the realization of practical nanocomposite-based devices. A much sought after solution is to guide the assembly of the nanocomposite via faceted or lithographically patterned surfaces over macroscopic distances. To achieve the goal, in-depth understanding on the effects of incommensurability and film thickness on the NP assembly in confined geometry is requisite. Addressing these fundamental challenges may bridge the gap between NP self-assembly and application and lead to the development of functional nanocomposite thin films suitable for a wide range of devices. As we approach these milestones, and as the system becomes more complex and the number of controllable variables escalate, experimentalists will face even greater challenges in manipulating these multiple component systems. Computational design and simulation to provide insights into the assembly process will be more important than ever. It is my hope that the readers take the work described in this dissertation as an inspiration to further advance this rising field and implement it in the fabrication of advanced functional materials.

§ 1.5 General approach and synopsis of subsequent chapters

The work described in this dissertation focuses on answering fundamentally intriguing questions in the field of BCP-based supramolecular nanocomposites, starting with the thermodynamics in the co-assembly in Chapter 2, 3, and 4, to the assembly kinetics in Chapter 5, to finally a demonstration of a versatile platform for structure-property correlation studies, in Chapter 6. The fundamental studies on the model systems containing alkyl ligand capped spherical NPs and lamellar/cylindrical BCP-based supramolecules led to 3-D hierarchical NP assemblies in thin films. Moreover, the supramolecular nanocomposite thin films were found to demonstrate strong wavelength dependence optical anisotropy that can potentially be applied in optical applications. This then motivated us to conduct in-depth fundamental investigation to fully understand the thermodynamics as well as kinetics in the co-assemblies of supramolecules and NPs in thin films, which can be tailored as desired to yield various NP assemblies of interest. Chapter 2 through 4 are the focus of systematic studies upon variance of the architecture of the supramolecules, NP volume fraction, and NP size. In Chapter 5, the assembly kinetics in the nanocomposites was studied by *in situ* GISAXS during solvent annealing. By changing the solvent volume fraction, small molecule loading, and the molecular weight of the supramolecule, the annealing condition was optimized that allows rapid fabrication of nanocomposite thin films in minutes. The fundamental understanding and the processing method developed in the earlier chapters pave the way for macroscopically aligned NP arrays with tunable 3-D structures on

faceted or lithographically patterned surfaces. This opens a new avenue for not only the investigation of structure-property correlations, but also the fabrication of next-generation nanodevices for light manipulation, information transmission, energy harvesting, catalysis, and sensing.

Chapter 2
Nanoparticle Assemblies in Thin Films of Supramolecular Nanocomposites

Nanocomposite thin films containing hierarchically ordered 3-D nanoparticle (NP) arrays exhibit new properties to meet the growing material demands for advanced technology. However, translating NP assemblies in bulk nanocomposites to thin films is not trivial because NPs tend to segregate on the film surface to minimize entropic penalty from polymer chain deformation and the surface tension. We recently overcame the difficulties of NP surface segregation in thin films using a block copolymer (BCP)-based supramolecular approach. The non-covalently bonded small molecules on the polymer chains effectively modulate NP/polymer enthalpic interactions and the chain architecture of BCPs. The NPs form 2-D NP lattices in the middle of the microdomains stacked parallel to the surface and hexagonally packed in-plane NP chains in the interstitial sites in lamellar and cylindrical nanocomposite thin films, respectively. Different from that observed previously in thin films of coil-coil BCPs, the coil-comb chain conformation of the supramolecule magnifies the entropic contributions, overcoming the differences in the surface tension between NP and supramolecule to stabilize 3-D NP assemblies with sub-10 nm inter-particle distances in cylindrical nanocomposites. In lamellar nanocomposites, the NPs are kinetically trapped in the microdomains as the activation energy barrier is too high for the NPs to migrate to the film surface due to the high entropic loss associated with the deformation of the rigid comb block. Lastly, the hexagonally packed 3-D Au NP arrays in cylindrical supramolecular nanocomposite thin films demonstrate a drastic, wavelength-dependent isotropic-to-anisotropic transition of complex refractive indices and a rapid switch of polarization states in the visible light regime, highlighting their potential applications for optical coating, light manipulation and potential information transmission. The present work is one of the first studies that overcome major challenges in generating 3-D hierarchical NP assembly in thin films over macroscopic distances. The supramolecular approach provides not only a powerful platform to test theoretical predictions of nanocomposite properties but also a versatile method to precisely tailor the coupling between 3-D NP arrays containing a wide range of elements on the periodic table for next-generation devices.

§ 2.1 Introduction

Nanoparticles (NPs) are viewed as artificial atoms and exhibit unique optical, electrical, and mechanical properties. Similar to the synthesis of new compounds, organizing NPs into ordered arrays can lead to additional interesting properties due to synergistic inter-particle coupling.[1-11] Numerical simulations[12,13] and experimental studies[14] have shown that electromagnetic waves can be transported along 1-D chains of closely spaced metal NPs. 2-D hexagonally-packed metal NP arrays demonstrate strong collective surface plasmon resonance that provides surface-enhanced Raman scattering.[15-17] While the unique physical behaviors of 1-D and 2-D NP arrays have been investigated; the collective properties of 3-D NP assemblies have been rarely explored. Development of a fabrication platform to generate 3-D ordered arrays of NPs will not only enable basic understanding of this new family of materials, but also the fabrication of a wide range of next-generation nanodevices including, but not limited to, optical

lenses, optical polarizers, memory storage, nanoelectronic circuits, photovoltaics, and batteries. Various approaches have been explored to this end. DNA linkers or controlled solvent evaporation have been used to generate suprelattices of a single type or mixtures of NPs.[1-3,18-21] Lithographically patterned surfaces are also effective in generating NP assemblies.[22-24]

For practical applications, the fabrication process should produce 3-D NP assemblies in forms suitable for device fabrication over macroscopic distances using existing fabrication infrastructure. Nanocomposites based on polymers meet these requirements and are well suited for scalable nanomanufacturing.[25-28] In comparison to *in situ* synthesis of NPs in polymeric matrix,[29-31] co-assembling preformed NPs with block copolymers (BCPs) have several advantages.[25,32,33] In the past two decades, there have been extensive studies and many successes in the co-assemblies of NPs and BCPs. With the co-assembly approaches, the cyrstallinity, composition, size, shape and surface passivation of NPs can be readily tailored. In addition, different types of NPs with complementary properties can also be used to take advantage of synergistic effects when the NPs are electronically or optically coupled. However, there are only limited successes to obtain 3-D assemblies of NPs with the precision at single particle level in thin films.

In bulk, the phase behavior of BCP-based nanocomposites is mainly governed by the enthalpic interactions between the NP ligands and the polymer matrix; and the entropy associated with polymer chain conformation upon NP inclusion.[25,33] Favorable ligand-polymer interactions are key to obtain dispersion of NPs in polymer matrix without macrophase separation. The NP ligand-polymer interactions can be modified to precisely control the selective spatial distribution of NPs in one BCP microdomains or at the interface between two blocks.[27,34-37] Upon incorporation of NPs, the polymer chains experience conformational changes, resulting in conformational entropy. The entropic effects on the NP assemblies have been extensively studied theoretically[38-43] and experimentally.[44,45] Coil-comb BCP-based supramolecules offer more advantages to guide NP assemblies in comparison to coil-coil BCPs. The small molecules in the comb block effectively mediate NP-BCP interactions and the entropic effects upon NP incorporation become more dominant as the spring constant of the comb block increases. We recently showed that both spherical NPs and nanorods can be assembled with highly precise control over their spatial distributions within BCP microdomains in bulk.[28,46]

Many NP-based devices require 3-D ordered arrays of NPs to be fabricated in thin film configurations. Hypothetically, if one can directly translate the assemblies of preformed NPs in bulk into thin films with high fidelity, the present bottleneck in NP-based nanodevices would be overcome. However, various studies have shown that the thermodynamics and the assembly kinetics governing the phase behavior of BCP-based nanocomposites in thin films can be quite different from that in bulk.

In thin films of BCP-based nanocomposites, the favorable ligand-block interactions and the conformational entropy of the polymer chains upon NP incorporation are still the critical factors that determine the spatial distribution of NPs.[47-49] However, the entropic effect becomes more prominent. When the diameter of NP is larger than the radius of gyration, R_g, of the polymer, the NPs were shown to be expelled to the air-polymer or polymer-substrate interface

and the edge dislocations to relieve the cost in conformational entropy in homopolymer and BCP thin films.[50-52] This is quite different from the observation in bulk nanocomposites where the NPs are sequestered in the middle of BCP microdomain.[44] There are additional factors that need to be taken into consideration including the surface tension of each component and the interfacial interactions at the nanocomposite-substrate interface.[53-56] NPs capped with organic alkyl ligands have lower surface tension than many polymers and may localize at the air-polymer interface to lower the surface tension.[57] Depending on the chemical nature of the substrate, NPs can also localize at the nanocomposite-substrate interface to maximize NP ligand-substrate interactions.[49,58] Together, the low surface energies of the NPs, preferential interfacial interactions, and the entropic penalties associated with the deformation of the polymer chains lead to NP segregations at the air-polymer and polymer-substrate interfaces as seen in thin films of nanocomposites. Thermodynamically, to directly translate hierarchical assemblies of NPs in bulk into thin films requires a delicate balance among all the energetic contributions mentioned above.

Kinetically, there are also additional considerations depending on the method used to fabricate nanocomposite thin films. Solvent annealing is routinely used to implement chain mobility at ambient temperature and is particularly useful for BCP-based supramolecules due to the possible thermal evaporation of small molecules.[59,60] The presence of solvent may lead to changes in surface tension, interfacial interactions, the conformation of polymer chains and Flory-Huggin's segmental interaction parameter between two BCP blocks.[61] The solvent annealing conditions such as swelling and deswelling rates can be readily manipulated to obtain equilibrium morphologies or kinetically trapped states.[59,62,63] These aspects become particularly complicated for selective solvents.[64,65] There is still no effective approach to fabricate 3-D ordered nanostructures of NPs in thin films with high precision in terms of the spatial distribution of the NPs.

Here, we investigated the co-assemblies of spherical NPs and BCP-based supramolecules forming two common morphologies, *i.e*. lamellae and hexagonally packed cylinders, in thin films with the film thickness ranging from 100 – 200 nm. We demonstrated that the 3-D assemblies of NPs observed in bulk can be readily translated into thin films. In lamellar nanocomposites, the NPs form 2-D sheets stacked parallel to the surface. Within the 2-D NP sheet, the NPs form hexagonally packed ordered arrays, akin to that obtained using DNA linker or solvent evaporation. In thin films of NPs/cylindrical supramolecule blends where BCP cylinders are oriented parallel to the surface, the hexagonal lattice of parallel cylindrical microdomains are distorted upon solvent removal. Different from that observed previously in thin films of coil-coil BCPs, the entropic contributions from polymer chain conformation upon NP incorporation favor the incorporation of NPs in the interior of thin films. However, our results showed that the mechanisms to obtain 3-D NP assemblies in thin films of lamellar and cylindrical nanocomposites may be different. For lamellar nanocomposites, the solvent annealing condition is optimized such that lamellae are oriented parallel to the surface before the NPs migrate to the surface. The activation energy barrier is too high for the NPs to migrate to the surface of the film due to the high entropy associated with the rigid comb block deformation.

Hence, the parallel lamellar nanocomposite thin films may be in a kinetically trapped state. For cylindrical nanocomposites, however, the NPs act as filler, localizing in the interstitial regions between cylindrical microdomains to effectively release the comb block deformation. Energetically, the entropy gain overcomes the differences in the surface tension between NP and supramolecule and stabilizes 3-D NP assemblies within the film. Furthermore, upon formation of 3-D ordered arrays of gold NPs, nanocomposite thin films exhibit a wavelength dependent optical anisotropy and a rapid switch of polarization states in the visible light regime, confirming the feasibility to generate new functional materials by forming hierarchically structured nanocomposites. Present studies clearly demonstrate a simple and robust approach to direct NP assemblies in thin films with exceptional precision and build the foundation for one to manipulate these assemblies to meet demands in NP-based device fabrication and optimize macroscopic properties of nanocomposites.

§ 2.2 Results and discussion

The supramolecules, poly(styrene)-*b*-poly-(4-vinylpyridine)(3-pentadecylphenol)$_r$ (PS-*b*-P4VP(PDP)$_r$) (the subscript *r* denotes the ratio of PDP to 4VP unit), are constructed by attaching PDP small molecules to the 4VP units of the P4VP block via hydrogen bonding (Schematic 1).[66] Two PS-*b*-P4VP BCPs with PS/P4VP blocks of 40 kDa/5.6 kDa and 19 kDa/5.2 kDa, respectively, were used. PS(40k)-*b*-P4VP(5.6k)(PDP)$_1$ forms lamellae-within-lamellae morphology in bulk and the NPs are sequestered in the middle of the P4VP(PDP)$_1$ comb blocks as schematically shown in Figure 2.1.[28] In thin films, PS(40k)-*b*-P4VP(5.6k)(PDP)$_1$ form parallel lamellar morphology with periodicity ~22 nm as shown in the AFM and cross-sectional TEM images in Figure 2.2a-b. The lamellae-within-lamellae hierarchical structure in the film is further confirmed by the structure factor at $q_y \sim 0.14$ Å^{-1} in the GISAXS pattern (Figure 2.2c). The other supramolecule, PS(19k)-*b*-P4VP(5.2k)(PDP)$_{1.7}$, forms cylinders-within-lamellae hierarchical assembly where the hexagonally-packed PS cylinders are embedded in the P4VP(PDP)$_{1.7}$ matrix (Figure 2.2d-f). In bulk, the NPs are localized at the interstitial areas between three PS cylinders and form a single chain of NPs at each corner, resulting in hexagonally-packed NP chains, as depicted in Figure 2.1.[28] Gold (Au) NPs were synthesized using an established method.[67] The average diameters of the two gold NPs used were determined to be ~6 nm and ~4.9 nm by TEM image analysis (see A.1.1). To fabricate thin films of nanocomposites, solutions of the supramolecules and the Au NPs were mixed and spun cast onto Si wafer with native SiO_x layer. The films were subsequently solvent annealed under chloroform atmosphere in a sealed glass jar. The nanocomposite thin films were swollen to ~145-150% of their original thicknesses to achieve nanostructures shown here. After solvent annealing, the glass jar was opened and the chloroform solvent was allowed to freely evaporate.

Figure 2.3a shows the AFM phase image of a ~150 nm thin film of a PS(40k)-*b*-P4VP(5.6k)(PDP)$_1$/Au NP blend with 1.5 vol% of Au NPs. Small clusters of NPs can be readily observed on the film surface. The NPs are hexagonally packed in each cluster. Figure 2.3b shows

the cross-sectional TEM image of the same film. Seven layers of NP sheets oriented parallel to the surface can be clearly seen. Each layer of NP sheet is around one NP in thickness. Based on the cross-sectional TEM, the lamellae periodicity of the nanocomposite, *L*, is measured to be ~22 nm under this sample treatment condition. The *d/L* ratio is 0.22. According to studies in blends of NP and coil-coil BCP, this *d/L* value is in the range where NPs are expelled to the surface due to the entropic penalty with NP incorporation. With this particle loading at this film thickness,

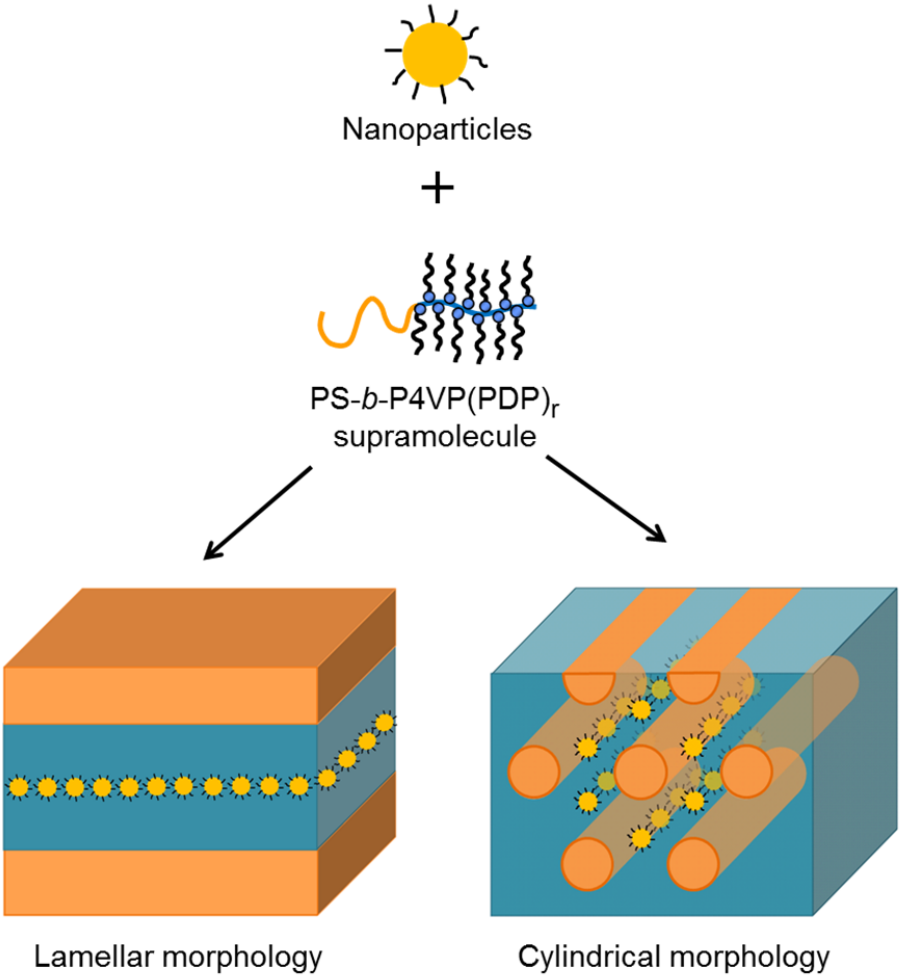

Figure 2.1. The PS-*b*-P4VP(PDP)$_r$ coil-comb supramolecules are constructed by attaching PDP small molecules to the 4VP groups via hydrogen bonding. In bulk samples of lamellar and cylindrical nanocomposites, the alkyl-capped NPs form a single 2-D NP sheet in the middle of each P4VP(PDP)$_r$ block and 1-D chains at the interstitial sites of hexagonal close-packed PS cylinders in P4VP(PDP)$_r$ matrix, respectively.

there are enough Au NPs to completely cover the air-film interface if all the NPs reside on the surface. However, the surface of the film is not fully covered by the Au NPs, different from previously reported observations.[57] The intensity profile of the cross-sectional TEM image shows

that the concentrations of Au NPs in each NP sheet are fairly uniform throughout the entire film thickness.

Figure 2.4a shows the AFM phase image of a ~150 nm thin film of PS(40k)-*b*-P4VP(5.6k)$(PDP)_1$ blended with 2.9 vol% Au NPs. The complete surface coverage of NPs was observed. Hexagonal close-packed 2-D ordered arrays of Au NPs can be clearly seen and the grain spans over a few hundred of nanometers, much larger than that shown in Figure 2.3a. Figure 2.4b shows the cross-sectional TEM of the same film. Seven layers of NP sheets can be clearly seen. The in-plane ordering of the Au NPs inside the comb blocks in the interior of the film cannot be imaged directly. Grazing incidence small angle X-ray scattering (GISAXS) was used to probe internal NP structures. Figure 2.4d shows the GISAXS pattern of a film similar to

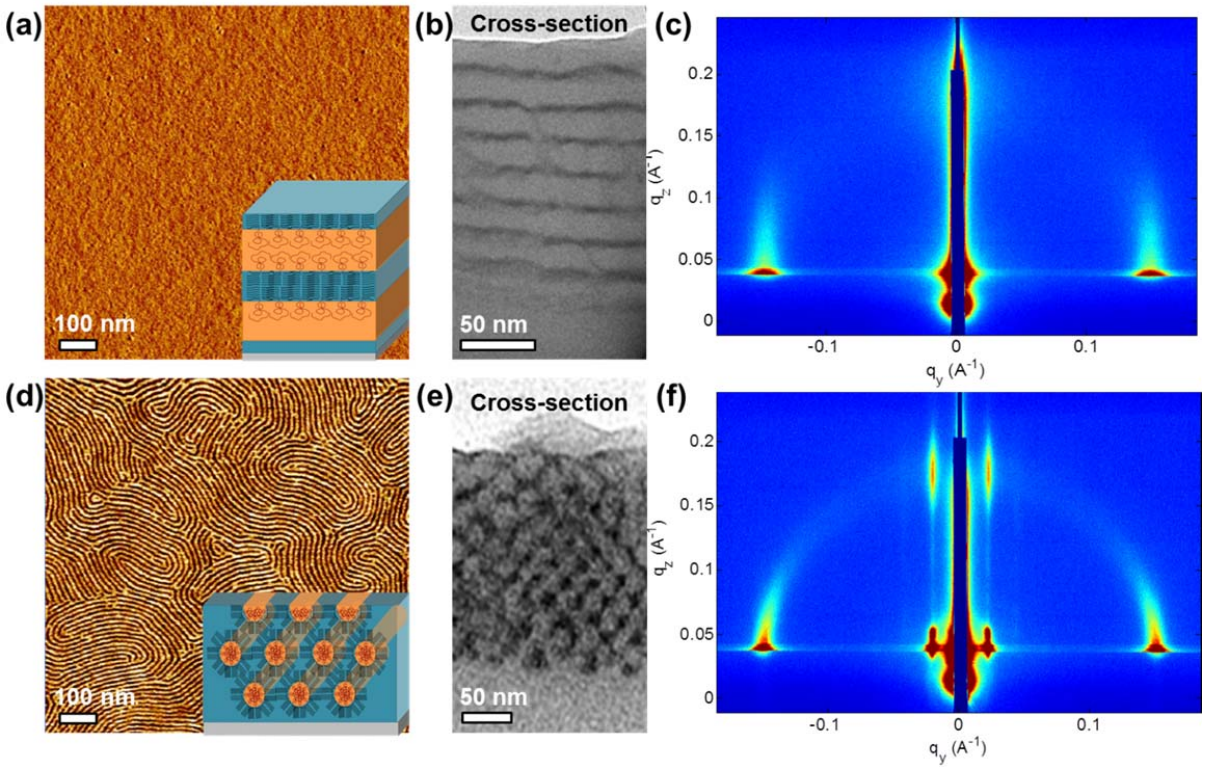

Figure 2.2. The AFM, cross-sectional TEM, and GISAXS images of a ~200 nm thick PS(40k)-*b*-P4VP(5.6k)$(PDP)_1$ thin film are shown in (a), (b), and (c), respectively. I_2 was used to stain the P4VP$(PDP)_1$ domains to create contrast under TEM. Parallel lamellar morphology is observed in the film with the P4VP$(PDP)_1$ domains wetting the air-polymer and polymer-substrate interfaces. The lamellae-within-lamellae hierarchical structure is present in the supramolecular thin film as evidenced by the GISAXS result. (d-e) show the AFM, cross-sectional TEM, and GISAXS data of a ~200 nm PS(19k)-*b*-P4VP(5.2k)$(PDP)_{1.7}$ thin film. Hexagonally packed in-planes PS cylinders are seen in the P4VP$(PDP)_{1.7}$ matrix. The cylinders are arranged into a distorted hexagonal lattice, leading to one interstitial site among four PS cylinders.

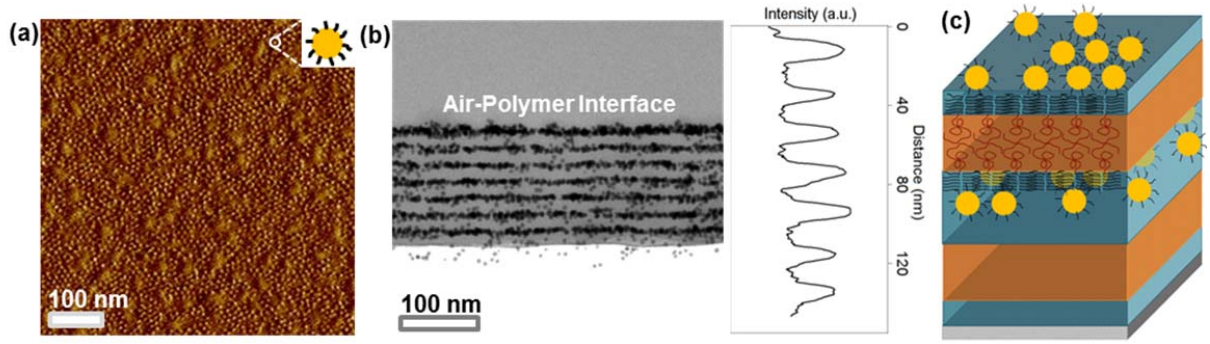

Figure 2.3. The AFM phase image and the cross-sectional TEM image of a ~150 nm thick PS(40k)-*b*-P4VP(5.6k)$(PDP)_1$/1.5 vol% Au NPs thin film are shown in (a) and (b), respectively. Each spherical dot in the AFM image represents an individual Au NP. At 1.5 vol% NP loading, the Au NPs formed clusters at the air-polymer interface and they were hexagonally-packed locally. The cross-sectional TEM image and the image analysis (intensity vs. film thickness profile) suggest that the NPs formed a NP sheet in the middle of P4VP$(PDP)_1$ lamellae and the concentration of NPs in each NP sheet is similar throughout the entire thickness of the nanocomposite thin film. The schematic drawing in (c) depicts the spatial distribution of NPs in thin films with this particle loading.

that in Figure 2.3a at incident angle $\alpha = 0.1°$. The incident angle was selected to probe only the in-plane structure of NPs at the film surface. In-plane diffraction peaks of up to the 7^{th} order can be clearly seen, corresponding to highly-ordered 2-D lattice domains of hexagonally-packed NPs. The vertical GISAXS intensity modulations along the q_z direction on the in-plane diffraction peaks, *e.g.* the (10), (11), and (20) peaks, arise from the form factor of individual NPs, indicating that the NPs on the surface formed a monolayer. These observations are consistent with the AFM result shown in Figure 2.4a. To probe NP assemblies in the interior of the film, GISAXS patterns were collected at six incident angles below and above the critical angle of the film from 0.1° to 0.2° with an increment of 0.02°. Figure 2.4e shows the horizontal (q_y) linecuts of the GISAXS patterns at the six different incident angles. In Figure 2.4e, the scattering profiles along the q_y direction that corresponds to the 2-D in-plane NP assemblies remain similar at each incident angle, confirming that the NPs formed hexagonally-packed ordered arrays with similar grain sizes not only at the air-polymer interface, but also in the interior of the film.

In parallel, we studied the assemblies of Au NPs blended with cylindrical supramolecule, PS(19k)-*b*-P4VP(5.2k)$(PDP)_{1.7}$, in thin films. Using similar solvent annealing treatments, thin films of PS(19k)-*b*-P4VP(5.2k)$(PDP)_{1.7}$ formed parallel hexagonally-packed PS cylinders with a lateral periodicity of ~30 nm embedded in P4VP$(PDP)_{1.7}$ matrix. The parallel orientation of cylindrical morphology in thin film is similar to that previously shown by ten Brinke *et al.* [68,69] except that we never observed the brush layer on the film surface. Figure 2.5a shows the AFM phase image of a ~120 nm thick thin film of a PS(19k)-*b*- P4VP(5.2k)$(PDP)_{1.7}$/Au NP blend

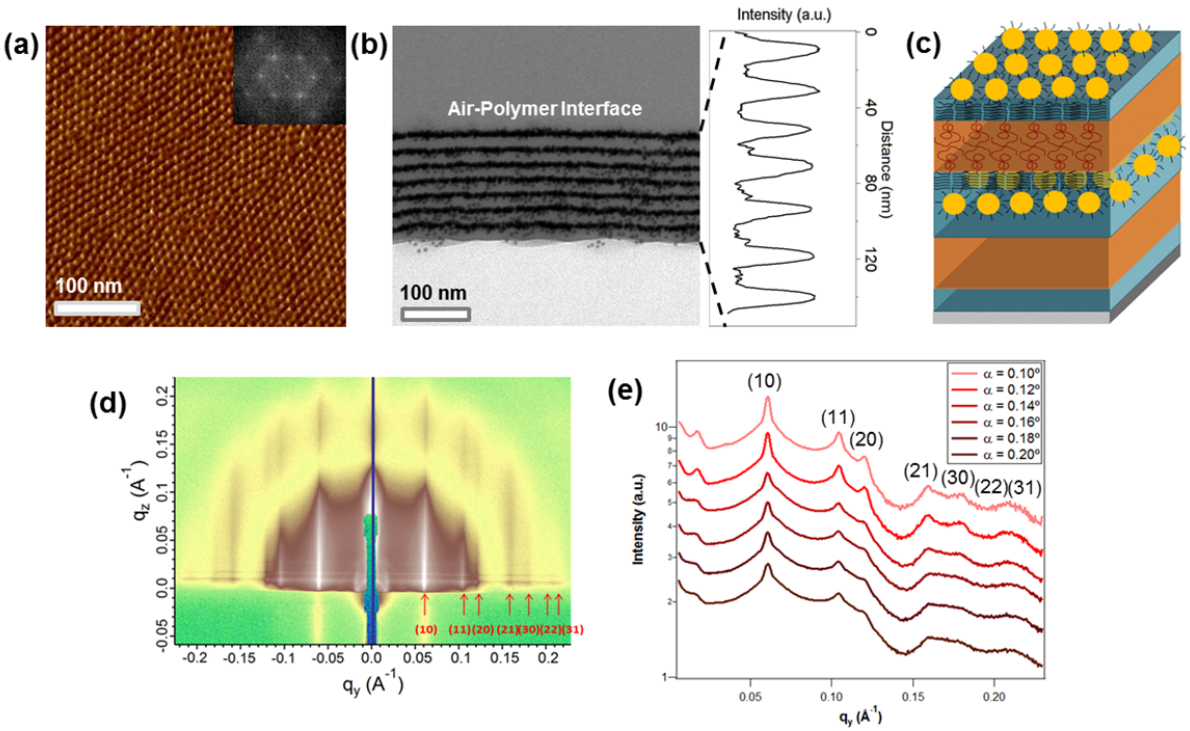

Figure 2.4. The AFM phase image and the cross-sectional TEM image of a ~150 nm thick PS(40k)-*b*-P4VP(5.6k)$(PDP)_1$/2.9 vol% Au NPs thin film are shown in (a) and (b), respectively. At 2.9 vol% NP loading, the Au NPs covered the entire air-polymer interface and form 2-D hexagonally-packed NP arrays. The inset of (a) shows the Fourier transform of a single grain of 2-D NP array at the film surface, confirming that the NPs are hexagonally packed with an inter-particle distance of ~10 nm. The cross-sectional TEM image and the image analysis suggest that the NPs formed a 2-D NP sheet in the middle of P4VP$(PDP)_1$ lamellae and the concentration of NPs in each NP sheet is uniform throughout the entire thickness of the nanocomposite thin film. The schematic drawing in (c) depicts the spatial distribution of NPs in this particular sample. (d) shows the GISAXS pattern of the nanocomposite thin film at an incident angle α of 0.1°, confirming the NPs form hexagonally packed ordered arrays on the film surface. (e) shows the horizontal (q_y) line cuts of the GISAXS patterns of the same film at 6 different incident angles. As the incident angle went from below to above the critical angle of the film, the scattering profiles along the q_y direction remain similar, confirming that the hexagonally-packed 2-D NP lattice is present at the air-polymer interface as well as the interior of the film. The plots were shifted vertically for clarity.

containing 2.9 vol% Au NPs. A single chain of Au NPs can be clearly observed in the trenches ($(PDP)_{1.7}$ microdomains) and the distance between NP chains is ~30 nm (Figure 2.5a). Figure 2.5b shows the in-plane TEM image of a ~120 nm thin film of a PS(19k)-*b*-P4VP(5.2k)$(PDP)_{1.7}$/Au NP blend containing 2.9 vol% of Au NPs. Lines of Au NPs with similar particle densities are observed with inter-array distances of around 15 nm, which is half of the lateral periodicity of the supramolecule (Figure 2.5b). Figure 2.5b only shows the 2-D projection

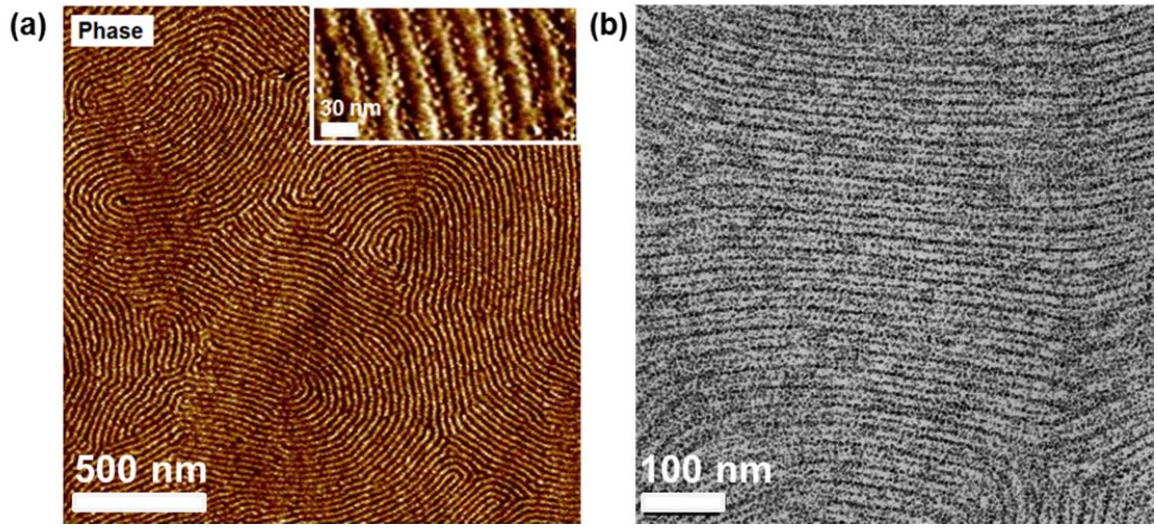

Figure 2.5. AFM phase image and the top-view TEM image of ~120 nm thin film of PS(19K)-*b*-P4VP(5.2K)$(PDP)_{1.7}$ with 2.9 vol % Au NPs are presented in (a) and (b), respectively. The inset in (a) is a close-up view of a small section of the AFM image, showing that the NPs formed a single NP array in each P4VP$(PDP)_{1.7}$ microdomains with one particle in width. The lateral interarray spacing is ~30 nm.

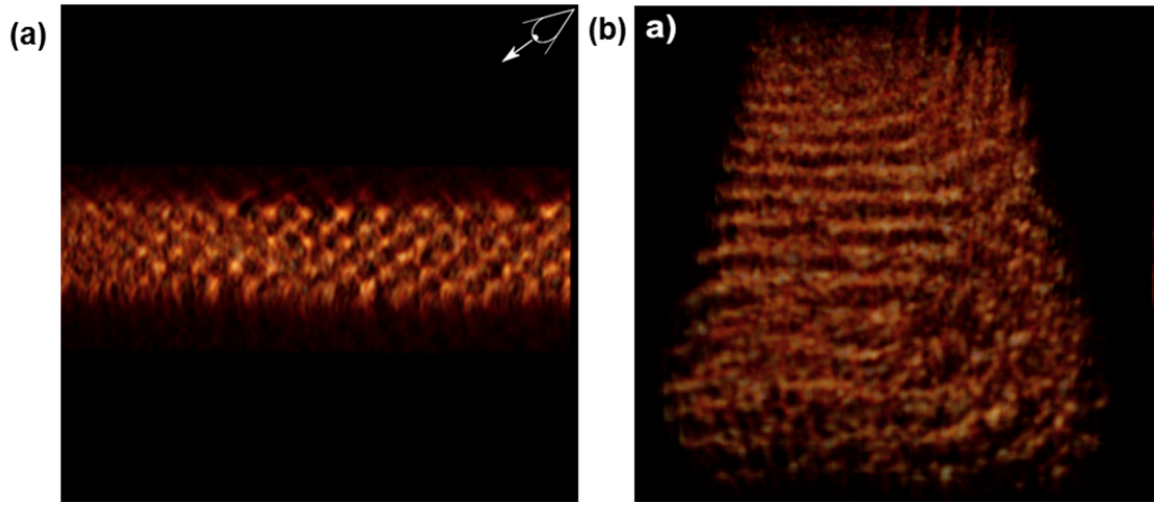

Figure 2.6. (a, b) Perspective images of a three-dimensional representation of a subset of the reconstruction of the same film in Figure 2.5b. (a) is a perspective view of the thin film's cross section showing the Y−Z plane, while (b) is the image of the separated [110] planes 54° from the film normal. The eye graphic in (a) indicates the relative perspective viewing direction in (b).

of the NP arrays. To characterize the 3-D spatial organization of the NPs in the nanocomposite thin film, TEM tomography was conducted on the sample shown in Figure 2.5b.

Figure 2.6a shows the cross-sectional projection (normal to the film surface) of the 3-D tomographic reconstruction of the nanocomposite thin film. A snap shot of the reconstruction tilted at 54° is shown in Figure 2.6b, showing that the NPs formed parallel lines of NP chains, one particle in width with a well-defined inter-particle distance. Six layers of NP chains aligned parallel to the film surface in registry with each other can be clearly seen. The Au NP chains were arranged in a distorted hexagonal lattice with an average in-plane spacing of 29.3 nm and an inter-layer spacing of 21.0 nm. The film thickness decreases during the solvent removal process, which leads to compression of the hexagonal lattice in the vertical direction.

The internal structure of the nanocomposite thin film was further quantified using GISAXS. Figure 2.7a shows the GISAXS pattern of a similar thin film of a PS(19k)-*b*-P4VP(5.2k)$(PDP)_{1.7}$/2.9 vol% Au NPs blend taken with 10 keV x-rays at an incident angle of 0.15°, greater than the critical angle of the nanocomposite but less than that of the silicon substrate to characterize the average morphology inside the film. The ring of scattering (centered at the white dotted line at a scattering wave vector q = 0.757 nm^{-1}) is characteristic of an inter-particle distance of 8.3 nm. To fit the GISAXS pattern, the real space basis wave vectors for a centered rectangular lattice, or equivalently distorted hexagonal lattice, of cylinder micro-domains parallel to surface are written as $\mathbf{a}=\{a,0,0\}$, $\mathbf{b}=\{0,\infty,0\}$, and $\mathbf{c}=\{0,0,c\}$. The positions of scatters (cylinder cross sections as indicated in the inset of Figure 2.7a) in each unit cell are given by $\mathbf{r_j}=x_j\mathbf{a}+ y_j\mathbf{b}+ z_j\mathbf{c}$, where j=1,2 with $(x_1, y_1,z_1)=(0,0,0)$ and $(x_2, y_2,z_2)=(1/2,0,1/2)$. The reciprocal lattice vectors are then given by $\mathbf{a}^*=2\pi(\mathbf{b}\times\mathbf{c})/(\mathbf{a}\cdot(\mathbf{b}\times\mathbf{c}))$, $\mathbf{b}^*=2\pi(\mathbf{c}\times\mathbf{a})/(\mathbf{b}\cdot(\mathbf{c}\times\mathbf{a}))$, $\mathbf{c}^*=2\pi(\mathbf{a}\times\mathbf{b})/(\mathbf{c}\cdot(\mathbf{a}\times\mathbf{b}))$. The diffraction is allowed when scattering structure factor $S(\mathbf{q})=\Sigma_{j=1,2}\exp(-\mathbf{q}\cdot\mathbf{r})$ is non-zero, where scattering wave vector transfer is $\mathbf{q}=h\mathbf{a}^*+k\mathbf{b}^*+l\mathbf{c}^*$, and h, k, l are the Miller indices. Due to the reflection and refraction effects at the grazing-incidence angle from a thin film surface, the diffraction peaks split into two sets which correspond to transmission and reflection geometries with diffraction angles.[70-72] The fitting results indicate that the NP arrays were arranged into a distorted hexagonal lattice parallel to the substrate with lattice spacings a and c around 33.7 nm and 44.4 nm, respectively. The vertical inter-layer spacing, c, is ~25% less than the corresponding spacing for a non-distorted hexagon.

Experimentally, we were unable to visualize the arrangement of PS cylindrical microdomains. Based on the TEM tomography and lattice constants obtained from GISAXS fitting, Figure 2.7b schematically shows the proposed spatial organization of cylindrical supramolecule and NPs in thin films after solvent annealing. Figure 2.7c shows the schematic of the same nanocomposite in bulk for comparison. It is apparent that the spatial distribution of NPs in thin films of cylindrical nanocomposite is different from those in bulk. In bulk, the PS cylinders are hexagonally close-packed, the NPs are selectively localized in the dented-triangular interstitial sites among three PS cylinders to relieve chain deformation of the P4VP$(PDP)_{1.7}$ block that is required to fill the cavity otherwise.[28] Similarly, in thin films, the NPs also act as nanofillers and preferentially segregate to the interstitial sites. However, the interstitial sites are

between four PS cylinders as shown in Figure 2.7b and can be attributed to the compression of hexagonal lattice in the vertical direction.

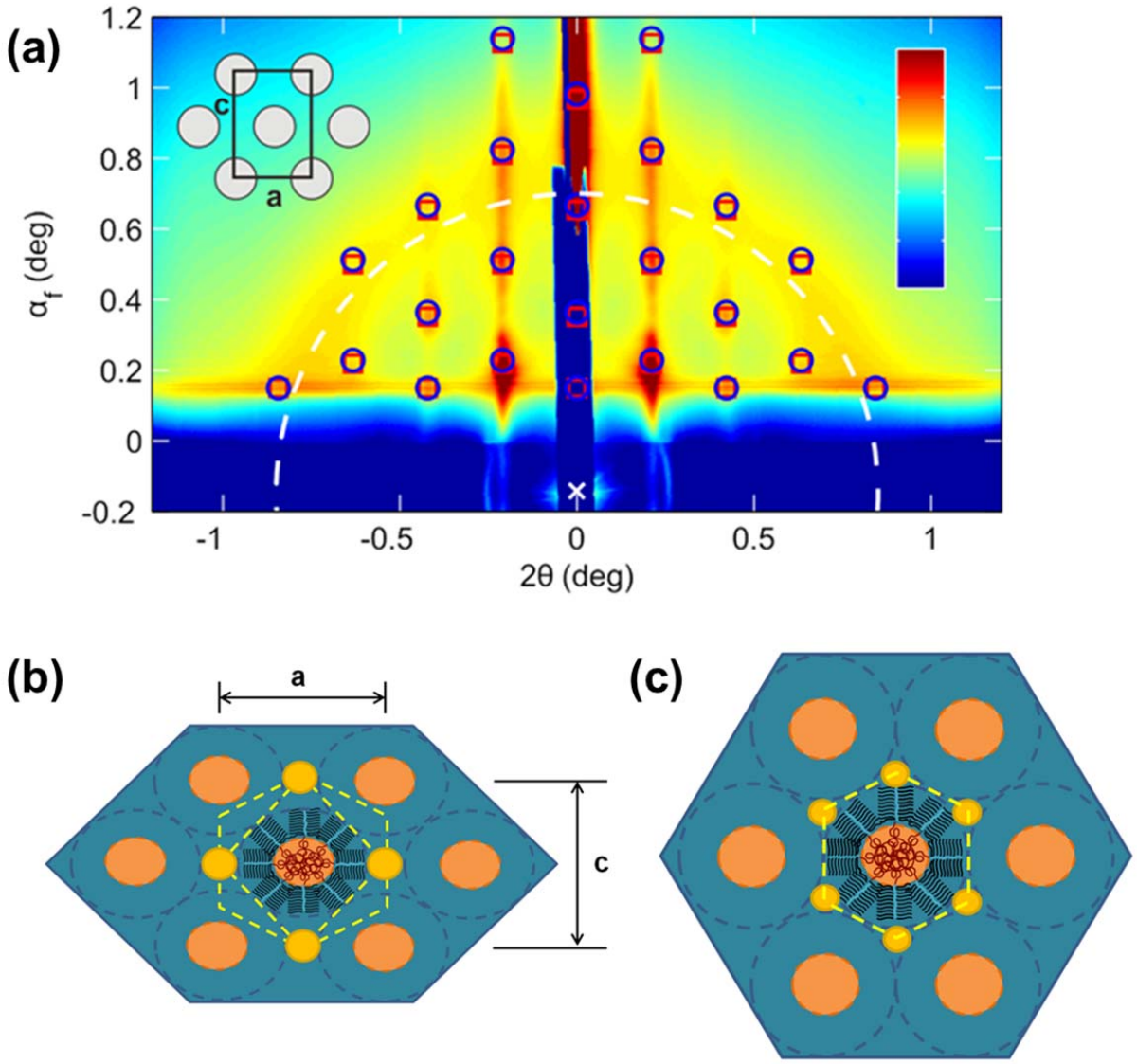

Figure 2.7. (a) GISAXS pattern of a ~120 nm thin film of a PS(19)-b-P4VP(5.2)$(PDP)_{1.7}$/Au NP (2.9 vol %) blend at an incident angle of 0.15°. The ring of scattering (centered at the white dotted line at a scattering wave vector q = 0.757 nm^{-1}) is characteristic of an interparticle distance of 8.3 nm. The diffraction peaks in the GISAXS pattern are best fit to a distorted face-centered rectangular lattice of PS cylinders parallel to the film surface with a = 33.7 nm and c = 44.4 nm, as schematically depicted in (b). The schematic drawing in (b) shows the distorted hexagonal lattice of in-plane PS cylinders in thin films as a result of the solvent removal. The NPs localize at the dented-rectangular interstitial sites among four PS cylinders to relieve the deformation of $P4VP(PDP)_r$ chains to minimize the loss in conformational entropy. In bulk, the PS cylinders form hexagonal close-packed lattice and the NPs are observed to assemble at the

dented-triangular interstitial sites to form hexagonally packed NP chains as schematically shown in (c).

The observations confirmed that 3-D assemblies of spherical NPs in thin films upon blending with lamellar and cylindrical supramolecules, respectively, can be readily obtained by balancing various energetic contributions and kinetic control. Under the experimental condition used here, the presence of surface and interface macroscopically orients BCP microdomains parallel to the surface. The entropic penalty to deform rigid P4VP(PDP)$_r$ comb block to incorporate Au NP, ~5 nm in size, can be quite significant.[73] This, in conjunction with the low surface tension of alkyl ligand, should provide strong driving force for the NPs to migrate to the surface. On the contrary, NPs are present both on the air-film interface and in the interior of the film for both lamellar and cylindrical nanocomposites and form fairly uniform 3-D NP assemblies through the entire film thickness. In both cases, the favorable interactions between the PDP and the ligands on the surface of the NPs are important enthalpic driving forces for the preferential sequestration of NPs in the P4VP(PDP)$_r$ blocks in thin films. However, the mechanisms behind the observed 3-D NP assemblies may be quite different for the two cases investigated here.

Figure 2.3b shows the slightly higher concentration of the Au NPs at the air-film interface, indicating that alkyl-passivated Au NPs have lower surface tension than the PS-*b*-P4VP(PDP)$_1$ supramolecule. The observed layered NP sheet morphology may very likely be a kinetically trapped state and may have strong dependence on the solvent annealing condition and the assembly pathway. Experimentally, the solvent annealing condition is selected such that the NPs are trapped in the P4VP(PDP)$_1$ microdomain in the film and the mobility of the NP is quite limited during assembly process. Detailed studies on the effect of solvent annealing condition will be reported in an upcoming contribution. Once the BCP lamellae are oriented parallel to the surface, there is no percolation pathway for the NPs to travel to the free surface. Due to the rigidity of the P4VP(PDP)$_1$ block and nonfavorable interactions between the NP ligands and PS block, it is energetically costly for the NPs to penetrate the P4VP(PDP)$_1$ lamellae to migrate to the film surface. In addition, as the solvent is removed from the nanocomposite thin film, the P4VP(PDP)$_1$ chains stiffen. The Au NPs, ~5 nm in size, are locally expelled from the P4VP(PDP)$_1$ lamellae and form a 2-D NP sheet in the middle of P4VP(PDP)$_1$ microdomains in the film.[28] This process may effectively reduce the conformational entropic penalty due to the NP incorporation and the driving force for the surface migration of NPs.[38-40,50]

In the cylinder-forming supramolecular thin film, the favorable enthalpic interactions between PDP and the ligands on the NPs localize the NPs in the P4VP(PDP)$_{1.7}$ blocks. Unlike the previous case, the P4VP(PDP)$_{1.7}$ matrix provides pathways for the NPs to migrate to the air-polymer interface. However, we did not observe a layer of NP at the free surface after solvent annealing. In fact, both the PS and the P4VP(PDP)$_{1.7}$ blocks are on the film surface. The reason may be that the presence of solvent mediates the surface tension of each component and reduces differences in surface tension. However, the results from the lamellar nanocomposites shown in

Figure 2.3 and 2.4 and the fact that Au NPs are still observed on the top of P4VP(PDP)$_1$ microdomain indicate that the Au NPs have lower surface tension albeit the difference may be quite small. Thus, the experimental results show that it is more energetically favorable to sequester the NPs in the interstitial regions between PS cylinders than to have the Au NP cover the surface to lower surface tension. The entropic gain from positioning the nanofillers at the interstitial regions is higher than the enthalpic gain of the surface tension. It needs to be noted that the NPs are not homogenously distributed in the P4VP(PDP)$_{1.7}$ blocks and localize to the interface of the two blocks since the conformational entropy is more dominant than the translational entropy as d/L is larger than 0.15 in this case. In addition, at the PDP:4VP ratio, r = 1.7, the free PDP molecules not hydrogen bonded to the 4VP are also expected to concentrate in the interstitial regions to relieve the packing frustration of the comb block. The favorable interactions between the locally enriched unbounded PDP small molecules and the alkyl ligands of NPs provide an enthalpic driving force to further localize the NPs at the interstitial sites in the interior of the film. Together, the enthalpic and entropic contributions balance the surface tension differences for surface aggregation of Au NPs to achieve 3-D NP arrays in thin films.

Once the nanocomposite is ordered, the inter-particle distance and the inter-particle coupling are defined, leading to new properties unique to ordered arrays of NPs (Figure 2.8). For the cylindrical nanocomposites studied here, after solvent annealing, the in-plane inter-particle distance is 9.6 nm, smaller than that of out-of-plane (26 nm), thus, to the first approximation, a stronger inter-particle plasmonic coupling. Indeed, a wavelength-dependent optical anisotropy was observed and the optical birefringence, Δn, is close to -0.05 between 400 to 600 nm (Figure 2.8b). In contrast, the as-cast nanocomposite or the as-cast/annealed supramolecular thin films mainly are fairly optically isotropic (see A.1.2). Different from other materials with optical anisotropy, the refractive indices of the ordered nanocomposite have strong wavelength dependence. The highest Δn is -0.087 at 544 nm, comparable to that of lithium niobate (Figure 2.8c). The complex reflectivity ratio ($\rho = r_p/r_s = tan(\Psi) \cdot e^{i\Delta}$) was measured, where r_p and r_s are the complex reflection coefficients for *p*- and *s*- polarized light and $tan(\psi)$ and Δ are the changes in amplitude and phase between *p* and *s* components of polarized light reflected from the film as shown in Figure 2.8d and 2.8e as a function of wavelength, respectively. When the incident angle was close to the Brewster angle, 55° in this case, the reflection from the film of supramolecule alone is *s*-polarized over a broad range of wavelength as expected. For nanocomposites, the presence of Au NPs leads to large changes in both $tan(\psi)$ and Δ (Figure 2.8c). The wavelength dependent polarization was clearly seen between 400 to 550 nm for the nanocomposite thin films before and after solvent annealing. Notably, there is a strong blue shift from 457 to 472 nm (~15 nm) when Au NPs are rearranged from disordered to ordered arrays. The Au NP used here is only 5 nm in size and the edge-to-edge distance between two particles is ~3-4 nm. Thus, the plasmonic coupling between the NPs is fairly weak as can be seen in the UV-vis spectra of the nanocomposite thin films (see A.1.3). However, simply by varying the NP assemblies in thin films via the solvent treatment demonstrated here, the macroscopic optical properties of the nanocomposites can be tailored along different directions. It is worthwhile to note that the dimensions of the NP arrays are at least one order of magnitude smaller than that of

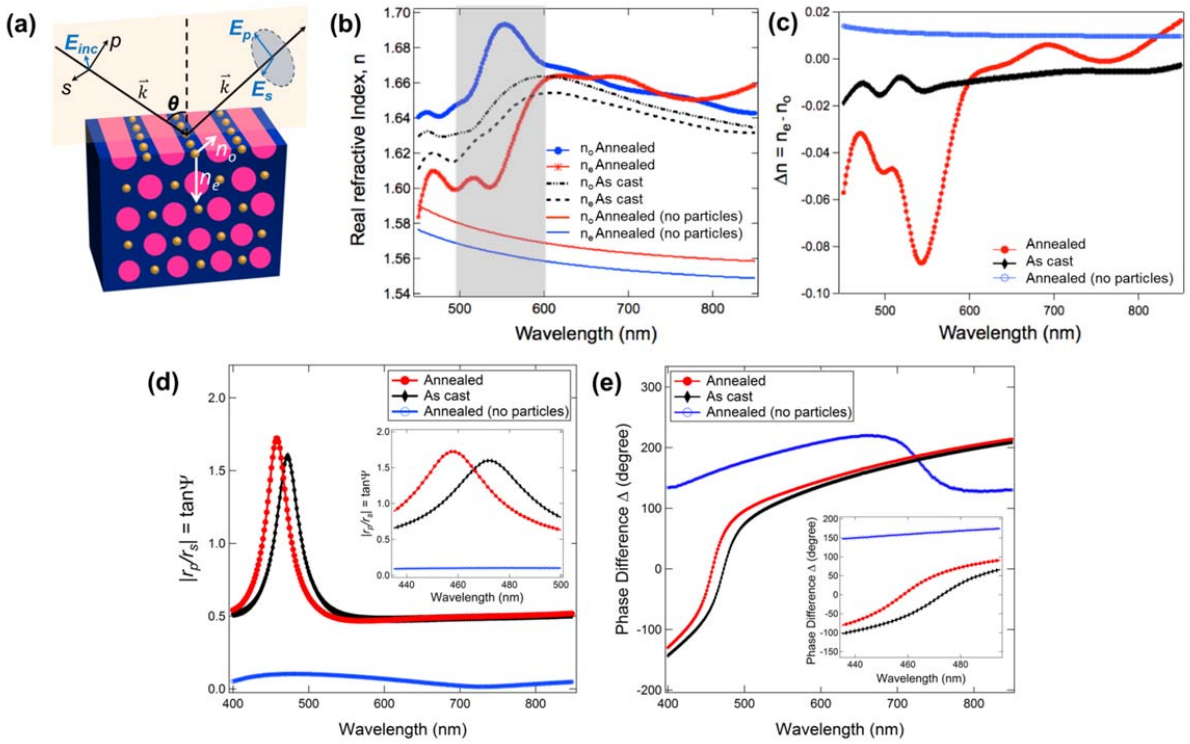

Figure 2.8. Optical properties of nanocomposite films containing disordered and ordered arrays of NPs. (a) Schematics of the ellipsometry measurements for the characterization of the in-plane $(n_o + ik_o)$ and out-of-plane $(n_e + ik_e)$ components of the complex refractive indices of the supramolecular nanocomposite thin film and the polarization state of the reflected light before and after solvent annealing. (b) Unlike that in the as-cast film, n_o shows a strong peak near λ = 545 nm due to the strong interaction between the incident electromagnetic wave and the collective plasmonic coupling of the ordered NP chains parallel to the surface. This leads to a wavelength dependence optical birefringence of the film (Δn ~ -0.05 at 545 nm) for light manipulation applications as shown in (c). Moreover, the nanocomposite thin film's anisotropic property changes the polarization state of the incident light at the Brewster angle (θ = 55°) from linear to elliptical as evidenced by the wavelength dependence of the reflectivity ratio and the phase difference shown in (d) and (e), respectively. The functional wavelength range of the polarization anomaly can be blue shifted by controlling the spatial arrangements of the NPs. The preliminary optical property data demonstrates the potential supramolecular nanocomposite thin films as a new family of optical coatings.

visible wavelength. However the nanocomposite still exhibits quite large optical anisotropy, clearly demonstrating the potential of using supramolecular nanocomposites as metamaterials. More importantly, the spatial arrangement of NPs after annealing leads to anisotropic collective properties with strong wavelength dependence even though the inter-particle coupling is rather

weak. Thus, the nanocomposite films presented here open an opportunity to manipulate how light of different wavelength interacts with the film to tune the functional wavelength range of the optical coating. Nevertheless, the optical results are very intriguing and require further in-depth investigation.

§ 2.3 Conclusion

In summary, we have demonstrated a simple yet versatile supramolecular approach to precisely control 3-D spatial organization of NPs with single particle precision over macroscopic distances in thin films. The NPs formed hexagonally-packed 2-D NP arrays in the middle of each comb block stacked parallel to the surface in thin films of lamellar nanocomposites. This is the first time that 2-D NP assembly, similar to those obtained using DNA linkers and controlled solvent evaporation, can be clearly observed in supramolecule-based nanocomposite thin films. In cylindrical nanocomposite thin films, the 1-D NP chain with single particle width in each interstitial site was packed into a distorted hexagonal lattice, forming 3-D NP arrays with well-defined lattice spacings parallel to the substrate. These results indicate that there are possibilities to generate highly-ordered lattices of NPs within BCP microdomains and obtain 3-D hierarchical assemblies of NPs with structural control spanning from a single particle to macroscopic distances. For both cases, the inter-particle distance is ~8 to 10 nm, as determined by the size of the NP and the ligand length. The 1-D chains and 2-D arrays of Au NPs with sub-10 nm inter-particle spacings may demonstrate strong plasmonic coupling along the chain and in the NP sheet, respectively. This is confirmed by the wavelength dependent anisotropic optical properties of the 3-D Au NP arrays in the cylindrical nanocomposite thin film that demonstrated the potential and feasibility for engineering nanocomposites for light manipulation. The physical properties of nanocomposite thin films depend on the properties of individual NP and equally importantly, well defined inter-particle distance along different directions. Since the supramolecular approach is compatible with NPs of different chemical compositions and can lead to a library of NP assemblies, present studies clearly open a viable approach to generate a new family of materials that provide a powerful platform to study structure-property correlations and to build a wide range of NP-based devices for light manipulation, information transmission, memory storage, energy harvesting, energy storage, sensing, and catalysis.

§ 2.4 Experimental section

2.4.1 Sample preparation

PS(19,000)-*b*-P4VP(5,200) (PDI = 1.09) and PS(40,000)-*b*-P4VP(5,600) (PDI = 1.10) were purchased from Polymer Source, Inc. 3-*n*-pentadecylphenol (95%) was purchased from Acros. Chloroform was purchased from Fisher. All chemicals were used as received. Blends of supramolecules and NPs were prepared as described previously. Thin films were prepared by spin-coating the mixed solutions onto silicon wafers or polystyrene brush modified silicon wafer at spinning speeds ranging from 1000 to 3000 rpm. Sample thicknesses were measured using a Filmetrics F20 interferometer. For solvent annealing, samples were annealed using 300 μL of $CHCl_3$ injected inside a 250 mL top-capped jar at 22.5°C. Once the film thickness of the nanocomposite thin film reached 145-150% of its original thickness, the jar was opened and the $CHCl_3$ vapor inside the jar was allowed to freely evaporate.

2.4.2 Atomic force microscopy

Atomic force microscopy was performed on a Veeco Dimension 3100 with a Nanoscope III controller and a Quadrex extension box. The spring constant of the cantilever was 10 − 130 N m^{-1} with a resonant frequency in the range of 300–500 kHz. The set point for auto tune was ~1.5 V. The set-point amplitude was 90% of the free vibration value.

2.4.3 Grazing incidence small angle X-ray scattering

GISAXS experimental measurements were made at beamline 7.3.3 at the ALS in Lawrence Berkeley National Laboratory and at beamline 8-ID-E the APS in Argonne National Laboratory. X-ray wavelengths of 1.687 Å and 1.240 Å were used at APS, and ALS, respectively. The scattering intensity distribution was captured by a Pilatus 1M detector at ALS and APS. The intensities (I) are plotted with respect to q, where $q = (4\pi/\lambda)\sin(\theta/2)$, λ is the wavelength of the incident X-ray beam, and θ is the scattering angle.

2.4.4. Analysis of GISAXS results

The real space basis wave vectors for a centered rectangular lattice, or equivalently distorted hexagonal lattice, of cylinder micro-domains parallel to surface is written as $\mathbf{a}=\{a,0,0\}$, $\mathbf{b}=\{0,\infty,0\}$, $\mathbf{c}=\{0,0,c\}$ (Figure 2.9a). The positions of scatters (cylinder cross sections) in each unit cell are given by $\mathbf{r_j}=x_j\mathbf{a}+ y_j\mathbf{b}+ z_j\mathbf{c}$, where j=1,2 with $(x_1, y_1,z_1)=(0,0,0)$ and $(x_2, y_2,z_2)=(1/2,0,1/2)$. The reciprocal lattice vectors are then given by $\mathbf{a}^*=2\pi(\mathbf{b}\times\mathbf{c})/(\mathbf{a}\cdot(\mathbf{b}\times\mathbf{c}))$, $\mathbf{b}^*=2\pi(\mathbf{c}\times\mathbf{a})/(\mathbf{b}\cdot(\mathbf{c}\times\mathbf{a}))$, $\mathbf{c}^*=2\pi(\mathbf{a}\times\mathbf{b})/(\mathbf{c}\cdot(\mathbf{a}\times\mathbf{b}))$. The diffraction is allowed when scattering structure factor $S(\mathbf{q})=\Sigma_{j=1,2}\exp(-\mathbf{q}\cdot\mathbf{r})$ is non-zero, where scatter wave vector transfer $\mathbf{q}=h\mathbf{a}^*+k\,\mathbf{b}^*+l\,\mathbf{c}^*$, and h, k, l are the Miller indices. Due to the reflection and refraction effects at the grazing-incidence angle from a thin film surface, the diffraction peaks split into two sets which correspond to transmission and reflection geometries with diffraction angles given by $(2\theta_f,\alpha_f)$

$$\alpha_f = \arccos\sqrt{n^2 - \left[(q_z/k_0) \pm \sqrt{n^2 - \cos^2\alpha_f}\right]^2}$$

$$2\theta_f = \arccos\left(\frac{\cos^2\alpha_i + \cos^2\alpha_f - \left(q_c^{\|}/k_0\right)^2}{2\cos\alpha_i \cos\alpha_f}\right)$$

where n is the average refractive index of the film, k_0 is the wave vector of the x-ray in air, q_z is the component the wave vector transfer q normal to the film surface, $q_c^{\|}$ is the in-plane component of the wave vector transfer at the critical angle (Figure 2.9b).

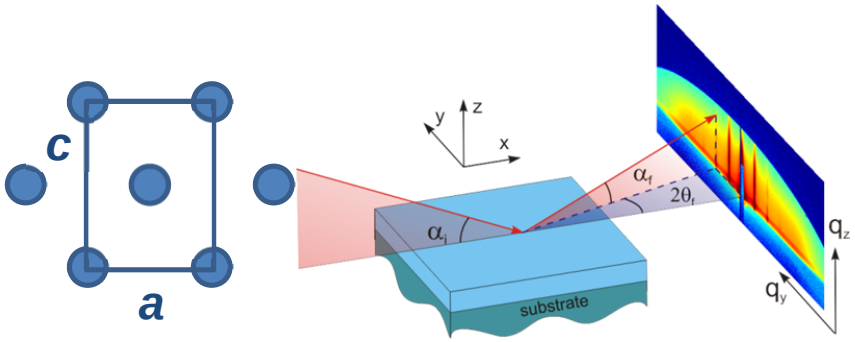

Figure 2.9. (a) Cross-section of the real space lattice of a centered rectangular lattice of cylindrical microdomain parallel to surface. (b) GISAXS experiment geometry.

2.4.5 Transmission electron microscopy

PS-*b*-P4VP(PDP)$_r$ thin films were spun cast on polystyrene-coated sodium chloride (NaCl) disks in a manner similar to those on silicon substrates. After solvent annealing, films were floated off the substrate onto a pool of water. Thin films were retrieved with carbon film coated copper grids. The top-view TEM images were collected on a FEI Tecnai 12 transmission electron microscope at an accelerating voltage of 120 kV. To prepare the cross-section of a nanocomposite thin film, the sample was first prepared on NaCl disk. Then, the thin film was floated off from the substrate on the surface of a pool of water. An epoxy block (Araldite 502, Electron Microscopy Sciences) was used to catch the film such that the sample is on top of the epoxy block with the air-polymer interface in contact with the top of the epoxy block. The epoxy along with the sample were cured at 60°C for at least 4 hours to ensure good contact between the epoxy and the nanocomposite thin film. Thin sections, ~60 nm in thickness, were microtomed using an RMC MT-X Ultramicrotome (Boeckler Instruments) and picked up on copper TEM grids on top of water. Again, the cross-sectional TEM images were collected using a FEI Tecnai 12 transmission electron microscope at an accelerating voltage of 120 kV.

2.4.6 Transmission electron microscopy tomography

TEM tomography was collected using an FEI ultra-twin Tecnai F20 operated at 200 kV and a Hummingbird Scientific high-tilt tomography holder. The tilt-series was acquired from -70° to 74° with 1° tilt step increments and pixel resolution of 0.43 nm. Custom scripts developed in IDL were used for post-processing alignment via automatic cross-correlation and manual adjustment. The weighted back-projection reconstruction method was employed to reconstruct the particles, and the Amira 5.2 software package was used for visualization.

2.4.7 Optical property measurements

Reflection ellipsometry experiment was conducted using a spectroscopic ellipsometer (M2000U®, J. A. Woollam) to measure the complex refractive index of the as-cast and annealed supramolecular nanocomposite thin films. The white light source used had a broad spectrum of wavelength ranging from 250 to 1000 nm. When the light source is perpendicular to the sample, the diameter of the incident light spot was around 2 mm. At incident angle 75°, the spot size increased to 6 mm in the projection direction. Biaxial model was used to retrieve the refractive index of the samples. The fitting had small mean square error, which confirms the reliability of the retrieved data. Information about the 3 measured samples is listed in Table 2.1. The complex reflectivity ratio of the light reflected from supramolecular nanocomposite thin film coated on the silicon substrate was characterized experimentally using a linearly polarized light incident at the angle of 55°. It polarizes along 45° in respect with both *s*- and *p*-polarization axes. Therefore, the incident *s*- and *p*-polarization components are in phase and have the same amplitude.

Table 2.1

Samples	Fitting Model	Nominal Thickness	Retrieved Thickness	Mean Square Error
PS(19 kDa)-*b*-(5.2kDa)$(PDP)_{1.7}$ with 0 vol% Au (as cast)	Biaxial	294 nm	280 nm	1.6
PS(19 kDa)-*b*-(5.2kDa)$(PDP)_{1.7}$ with 6 vol% Au (as cast)	Biaxial	268 nm	252 nm	4.8
PS(19 kDa)-*b*-(5.2kDa)$(PDP)_{1.7}$ with 6 vol% Au (annealed)	Biaxial	256 nm	242 nm	5.3

Chapter 3
Nanoparticle Assemblies in Thin Films of Supramolecular Nanocomposites: Effect of Nanoparticle Volume Fraction

Block copolymer-based supramolecules provide versatile routes to direct multidimensional hierarchical nanoparticle assemblies in thin films for various applications. Besides the spatial arrangement of the incorporated nanoparticles, the utility of functional nanocomposites also significantly relies on the nanoparticle volume fraction of the active inorganic constituent. Here, we present a systematic study to understand the phase behavior of cylindrical as well as lamellar supramolecular nanocomposite thin films as a function of nanoparticle loading. A surface-directed nanoparticle assembly is observed upon incorporation of nanoparticles. 3-D nanoparticle networks form in the matrix throughout the entire film thickness as more nanoparticles are loaded in the nanocomposites. Without any synthetic modification of the nanoparticle surface and polymer backbone, 15 vol% (53 wt%) of nanoparticles can be incorporated in the film before jamming of nanoparticles occurs. Instead of inducing a cylinder-to-sphere morphological transition, macrophase separation of NPs occurs above the thermodynamic limit of nanoparticle volume fraction. This phenomenon is further found to be nanoparticle size dependent in lamellar supramolecular nanocomposite with smaller nanoparticles. Lastly, at ultra-high nanoparticle loadings, GISAXS results reveal the break-down of the co-assembly and a uniform dispersion of supramolecules in 3-D nanoparticle lattices. Present studies demonstrate a versatile approach to tailor the morphology and, potentially, the physical properties of functional nanocomposites by simply varying the nanoparticle volume fraction in the film. The comprehensive investigation narrows the gap between NP solids and self-assembled nanocomposites, opening new avenues for the fabrication of functional nanodevices.

§ 3.1 Introduction

Nanoparticle (NP) solids present opportunities to exploit both the collective physical phenomena due to inter-particle coupling and the properties of individual NPs for various applications.[1-7] Recent advances in ligand chemistry have enabled surface modification of long alkyl ligands capped NPs by short functional ligands to enhance inter-particle coupling in solution or in thin-film solids without sacrificing the solution dispersibility of the NPs.[8-11] Polymer nanocompoistes hold promise to combine the unique properties of NP solids and the outstanding solution processability of macromolecules. Among many polymeric materials, block copolymers (BCPs), which microphase separate into various nanostructures, offer scalable and processing-friendly routes to direct hierarchal NP assemblies that demonstrate novel macroscopic responses.[12,13] In order to resemble the inter-particle coupling in NP solids, the percolation threshold needs to be reached to ensure improved physical properties in BCP-based nanocomposites. For example, in nanocompoite-based electronics or photovoltaics, efficient electron transport occurs only when the NP loading, ϕ_{NP}, is close to the percolation threshold, which can be as large as 17 vol% based on 3-D continuum models for spherical NPs.[14,15] Toward this end, NPs have been generated in BCP microdomains with high ϕ_{NP} via *in situ* synthesis methods.[1,2,16,17] However, it remains challenging to control NP size and inter-particle

ordering/coupling in the BCP microdomains using existing *in situ* synthesis approaches. Alternatively, ordered nanocomposites can be achieved via the co-assembly of BCPs and pre-formed NPs.[12,13] Nevertheless, ϕ_{NP} is usually low (< 2 vol%) to ensure synergistic co-assembly of BCPs and NPs in these nanocomposites, which limits their potential for certain applications. By simultaneously controlling NP spatial organization and ϕ_{NP} in BCP-based nanocomposites, the gap between NP solids and self-assembled nanocomposites may be narrowed to open new avenues for the fabrication of functional nanodevices.

The realization of ordered BCP nanocomposites containing preformed NPs results from an energy balance between enthalpic and entropic contributions.[12,13,18-20] Upon NP incorporation, the polymer chains stretch around the NPs to accommodate them in the microdomains, leading to an entropic penalty from chain deformation. This can be offset by the favorable BCP/NP ligand enthalpic interactions to sequester NPs in selective microdomains.[20] At intermediate ϕ_{NP}, the NPs may induce morphological transitions in the nanocomposites depending on the relative magnitudes of the enthalpic and entropic contributions.[21-24] As ϕ_{NP} reaches a loading threshold, it becomes too entropically costly to accommodate NPs in the domains, resulting in particle aggregation/macrophase separation or loss of order. Kinetically, the nanocomposites may become kinetically trapped as the jamming of NPs occurs at high ϕ_{NP}.[25,26] To overcome this challenge, hydrogen bonding[27-30] and ionic interactions[31] have been employed to strengthen the NP/BCP enthalpic interactions to generate nanostructured nanocomposites with 79 and 53 vol% of NPs in bulk, respectively. Yet, little success has been achieved in the thin film counterparts as the NPs tend to segregate at defects or the air/polymer interface to minimize the surface energy and the entropic penalty arising from chain deformation, limiting the applicability of BCP-based nanocomposites as technologically relevant devices.[32,33]

We recently introduced a supramolecular approach to achieve hierarchical 3-D NP assemblies in thin film configurations.[34,35] The small molecules non-covalently attached to the backbone of the BCPs not only effectively mediate the NP/BCP enthalpic interactions, but also alter the chain architecture to modulate the entropic contributions. At low ϕ_{NP}, the enthalpic contribution is sufficient to compete with the magnified entropic terms arising from the conformation of the comb block to stabilize NP assemblies in thin films.[35,36] The delicate balance of the various energetic contributions leads to hexagonally packed in-plane 1-D NP chains and alternating layers of 2-D NP lattices with defined inter-particle ordering in the interior of cylindrical and lamellar supramolecular nanocomposite thin films, respectively.[35] Due to the complicated entropic contributions in the system, the spatial organization of the NPs in the supramolecular nanocomposite strongly relies on NP size regardless of the chemical composition of the NPs.[36] However, as shown in previous chapters, ϕ_{NP} is always smaller than 3 vol%. For different applications, ϕ_{NP} needs to be increased, which may induce large energy perturbations in the system and bring about the following questions that await answers: 1) How does surface energy affect the NP assembly with small ϕ_{NP}? 2) Do the NPs induce morphological transition as ϕ_{NP} increases? 3) What is the thermodynamic limit of ϕ_{NP} in supramolecular nanocomposite thin films? 4) Do the NPs macrophase separate from the film at high ϕ_{NP}? To answer these

fundamentally and technologically important questions, it is requisite to study the phase behavior of the supramolecular nanocomposite thin film as a function of ϕ_{NP}.

Here, using a model system containing cylindrical supramolecules and ~4.9 nm Au NPs, we present a systematic investigation of the morphology in supramolecular nanocomposite thin films with ϕ_{NP} ranging from 0.4 to 45 vol%. Upon incorporation of small amounts of NPs, a surface-directed NP assembly is observed. The NPs begin occupying the interstitial sites near the air/polymer interface, followed by those in the interior of the film. At intermediate ϕ_{NP}, 3-D NP networks form in the matrix, maximizing the translational entropy and the comb block/NP interfacial area to alleviate the entropic penalty associated with chain deformation. Jamming of NPs is observed at high ϕ_{NP} (ϕ_{NP} > 15 vol%), leading to a poorly ordered perpendicular morphology in the film. As the entropic penalty from comb block deformation becomes dominant, some NPs macrophase separate to form NP lattices at the film surface. No cylinder-to-sphere morphological transition is observed since it is energetically unfavorable for the NPs to stabilize spherical curvature at the interface between the two blocks. In addition, the domain spacing of the nanostructure decreases as ϕ_{NP} increases. The incorporated NPs disrupt the crystalline comb blocks, resulting in a decrease of the domain spacing with increasing ϕ_{NP}. As ϕ_{NP} reaches above 30 vol%, the co-assembly breaks down and the NPs dominate the assembly. Two *h.c.p.* NP packing configurations with different inter-particle distances are observed near the surface and in the interior of the film. The present studies elucidate the thermodynamics in various hierarchical NP assemblies in supramolecular nanocomposite thin films as a function of ϕ_{NP}. This will potentially enhance the versatility of the approach, expanding the potential applications of functional supramolecular nanocomposites for a wide range of devices.

§ 3.2 Results and discussion

3.2.1 Morphology of cylindrical supramolecular nanocomposite thin films as a function of nanoparticle volume fraction

The supramolecules are constructed by attaching 3-pentadecylphenol (PDP) small molecules to the 4VP groups in PS(19 kDa)-*b*-P4VP(5.2 kDa) at a PDP/4VP molar ratio of 1.7 via hydrogen bonding. In bulk, PS(19 kDa)-*b*-P4VP(5.2 kDa)$(PDP)_{1.7}$ form hexagonally packed PS cylinders in P4VP$(PDP)_{1.7}$ matrix in equilibrium. The 1-dodecanethiol capped Au NPs are synthesized by a reported method and the average diameter of the NPs is found to be 4.9 nm by the particle analysis of the TEM images (see A.2.1). Supramolecular nanocomposite thin films with ϕ_{NP} ranging from 0.4 to 45 vol% were prepared by spin casting a solution containing PS(19 kDa)-*b*-P4VP(5.2 kDa)$(PDP)_{1.7}$ and different amounts of 4.9 nm Au NPs. All films were solvent annealed together under $CHCl_3$ vapor and the films swell to 145% of their original film thicknesses during annealing. The estimated wt% of the NPs is calculated using the information obtained from thermal gravimetric analysis (TGA). According to the TGA results, the gold core and 1-dodecanethiol ligand contribute to 76 and 24 wt% of the contents in the NP solution,

respectively (see A.2.2). In a supramolecular nanocomposite blend containing 62.6 wt% of the supramolecules, for example, the weight percentage of gold and 1-dodecanethiol are 28.4 and 9 wt%, respectively. Assuming the density of gold, supramolecules and 1-dodecanethiol are 19.3, 1, and 0.85 g/cm^3, the volume fraction of gold is calculated to be 1.44 vol% in the supramolecular nanocomposite. To characterize the actual volume fraction of gold in the film experimentally, TGA is conducted on the nanocomposite. The experimental result shows that the gold NPs make up 22.3% of the compound, which is equivalent to 1.47 vol% of NPs in the film (Figure 3.1). In the calculation converting weight fraction to volume fraction, the average density of the organic component (the supramolecules and the ligands) is assumed to be around 1. This leads to an overestimation of the actual ϕ_{NP}, resulting in a slightly larger value of the experimental ϕ_{NP} (1.47 vol%) than the computed one (1.44 vol%). For consistency, we use the experimental values to address the supramolecular nanocomposites with different Au NP volume fractions throughout the chapter which are listed in the table in Figure 3.1. In the following sections, the phase behavior of the supramoelcular nanocomposite thin film will be discussed in five NP loading regimes: Regime I (0 vol% < ϕ_{NP} < 3 vol%), Regime II (3 vol% < ϕ_{NP} < 15 vol%), Regime III (15 vol% < ϕ_{NP} < 20 vol%), Regime IV (20 vol% < ϕ_{NP} < 30 vol%), and Regime V (ϕ_{NP} > 30 vol%).

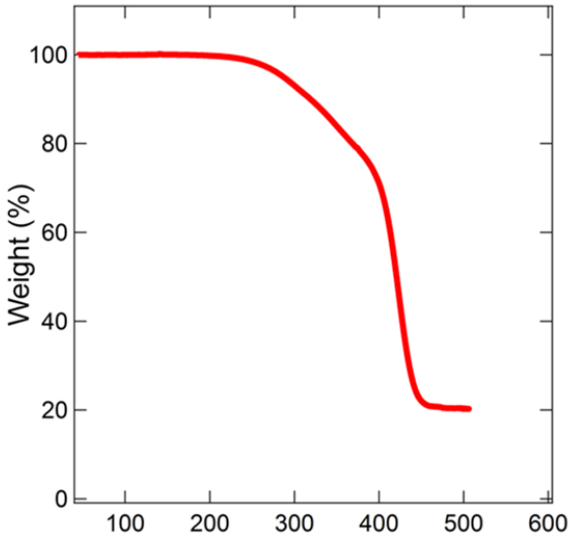

Calculated NP vol%	Actual NP vol%	Actual NP wt%
0.48 vol%	0.49 vol%	9.7 wt%
1.44 vol%	1.47 vol%	22.3 wt%
2.89 vol%	2.93 vol%	32.9 wt%
4.33 vol%	4.40 vol%	39.2 wt%
7.22 vol%	7.33 vol%	46.1 wt%
14.45 vol%	14.65 vol%	53.2 wt%
21.67 vol%	21.98 vol%	56.1 wt%
28.90 vol%	29.31 vol%	57.7 wt%
36.12 vol%	36.63 vol%	58.6 wt%
43.35 vol%	43.96 vol%	59.3 wt%

Figure 3.1. Thermal gravimetric analysis of the supramolecular nanocomposite containing 98.6 vol% of PS(19 kDa)-*b*-P4VP(5.2 kDa)(PDP)$_{1.7}$ and 1-dodecanethiol ligands and 1.4 vol% of 4.9 nm Au NPs. According to the TGA result, the Au content in the nanocomposite is 22.3 wt%, leading to an actual volume fraction of Au NPs around 1.5 vol%. This data point is used to calibrate the actual ϕ_{NP} of all the other nanocomposites, which are shown in the table on the right.

3.2.1.1 Regime I: Surface-directed nanoparticle assembly in cylindrical supramolecular nanocomposite thin film (0 vol% < ϕ_{NP} < 3 vol%)

Figure 3.3 shows the AFM, top-view TEM, and cross-sectional TEM images of a ~200 nm supramolecular nanocomposite thin film containing PS(19 kDa)-*b*-P4VP(5.2 kDa)$(PDP)_{1.7}$ and only 0.4 vol% of Au NPs. In the AFM image, it is clearly observed that the Au NPs form a single 1-D NP chain in the middle of each P4VP$(PDP)_{1.7}$ block at the air/polymer interface (Figure 3.2a). The top-view TEM image shows fingerprint patterns of NP chains with inter-array spacing ~30 nm, which is the lateral periodicity of the supramolecular thin film (Figure 3.2b).

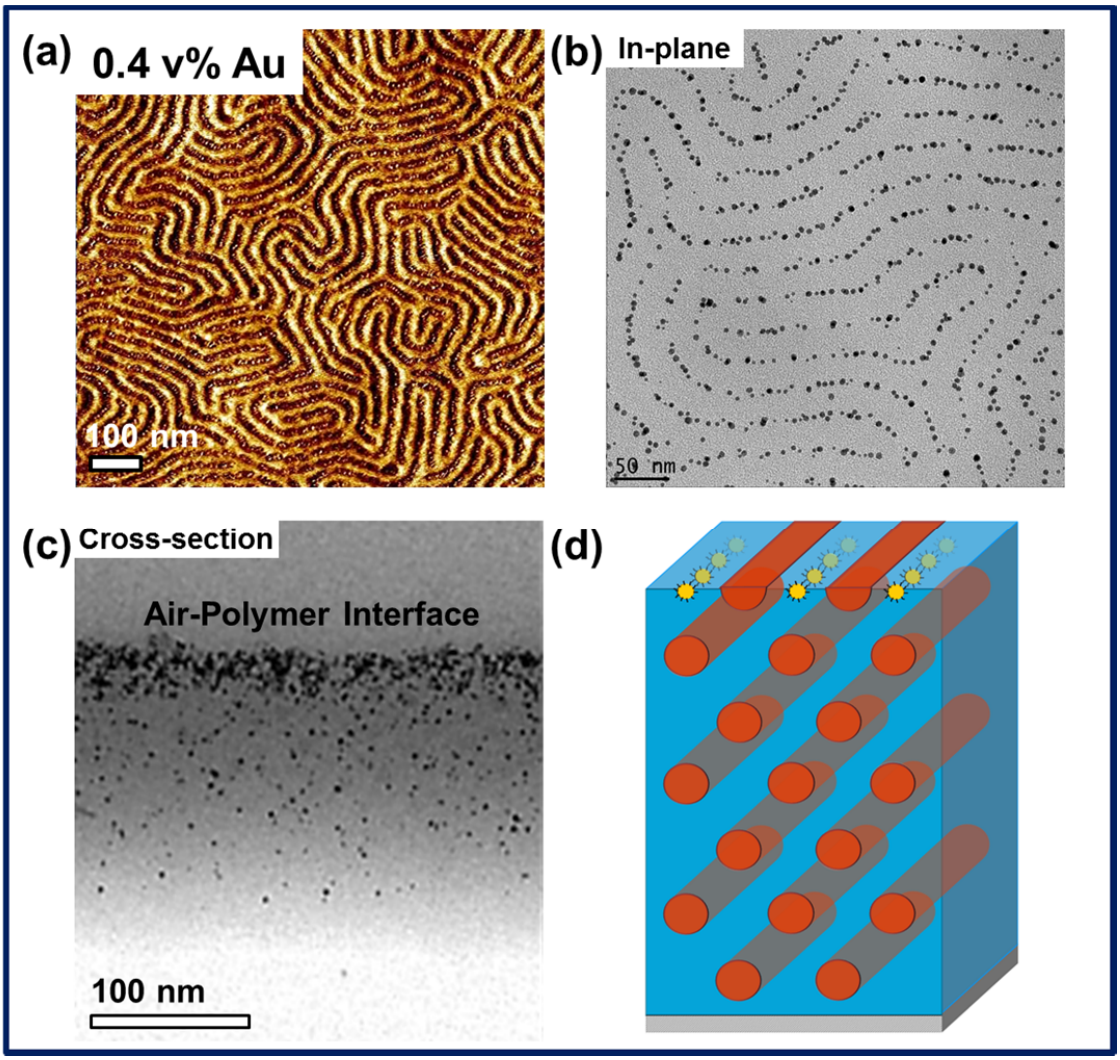

Figure 3.2. (a) AFM, (b) top-view TEM, and (c) cross-sectional TEM images of a ~200 nm supramolecular nanocomposite thin film containing PS(19 kDa)-*b*-P4VP(5.2 kDa)$(PDP)_{1.7}$ and only 0.4 vol% of Au NPs. The NPs mainly segregate to the P4VP$(PDP)_{1.7}$ microdomains at air/film interface as illustrated in (d).

No NPs are observed beneath the NP arrays on the film surface. Figure 3.2c shows the cross-sectional TEM image of the film, which further confirms a higher concentration of Au NPs at the air/film interface and the nanocomposite morphology is schematically illustrated in Figure 3.2d. Similar morphology is observed in the nanocomposite with ϕ_{NP} = 0.7 vol% as shown in Figure 3.3a. However, in many regions, an extra 1-D NP chain appears in the middle of the NP chains in the fingerprint patterns as indicated by the white arrow in the zoomed-in top-view TEM image. When ϕ_{NP} reaches 1.5 vol%, the morphology of the film becomes homogeneous across the surface (Figure 3.3b). The NP arrays assume alternating packing density with periodicity half of that of the supramolecule (~15 nm) as shown in Figure 3.3b. The cross-sectional TEM image of the sample further demonstrates that the majority of the NP chains locate at the first 5 layers of interstitial sites near the surface, allowing us to discern 3-D morphology of the nanocomposite. In the top-view TEM image, the darker-colored NP array is the projection of 2 to 3 NP chains residing in the 1st, 3rd, and 5th layers of interstitial sites from the surface and the lighter-colored region represents the NP chains in the interstitial sites in the 2nd and 4th layers (Figure 3.3b). The results show that the NP assembly is surface-directed when ϕ_{NP} < 1.5 vol%. At ϕ_{NP} = 2.9 vol%, there are enough NPs that occupy all the interstitial sites in the interior of the film, resulting in a 3-D NP array consisting of hexagonally packed in-plane NP chains (Figure 3.3c).

The morphology of each supramolecular nanocomposite thin film is also characterized using grazing incidence small angle X-ray scattering (GISAXS) at an incident angle larger than the critical angle, α_c, of the film (see A.2.3). Bragg rods corresponding to the lateral periodicity of the nanocomposite can be clearly seen in the q_y direction when ϕ_{NP} = 0.5 vol%. However, no structure factor arising from the 3-D NP assembly in the interior of the film can be observed in the q_z direction, confirming that the NPs arrays are on the surface of the film. When ϕ_{NP} reaches 1.5 vol%, strong Bragg spots corresponding to the hexagonally packed in-plane NP arrays show up in the 2-D GISAXS pattern due to the 3-D NP assembly near the air/film interface. The intensity of the Bragg spots become stronger and higher order peaks begin to appear in the q_z direction as ϕ_{NP} increases to 2.9 vol%. This indicates that more layers of hexagonally packed NP chains are present in the interior of the film. The GISAXS q_y linecuts of the samples with ϕ_{NP} = 0, 0.5, 1.5, and 2.9 vol% of Au NPs are plotted in Figure 3.4. The lateral periodicity remains to be around 32.6 nm as the 1st order Bragg peaks lie at the same position when ϕ_{NP} increases.

Upon incorporation of NPs into supramolecular nanocomposites, the alkyl ligand capped Au NPs reside in the P4VP(PDP)$_{1.7}$ domains due to the enthalpic contribution from ligand–polymer interactions, $\Delta H_{ligand/polymer}$. In the supramolecular nanocomposite, the surface tension of the NP ligand is 25 mN/m, which is smaller than that of PS (33 mN/m), P4VP (42 mN/m), and PDP (27 mN/m). When the NP loading is only 0.4 vol%, the NPs segregate to the surface of P4VP(PDP)$_{1.7}$ blocks to maximize the energetic gain in surface energy, $\Delta H_{surface}$, after solvent annealing. To minimize the entropic penalty from chain deformation, ΔS_{con}, the NPs reside in the middle of each P4VP(PDP)$_{1.7}$ domain and form a 1-D NP chain with well-defined inter-particle distance. During spin casting, the strong vertical solvent field biases the perpendicular orientation of the microdomains. Kinetically, the NPs in the P4VP(PDP)$_{1.7}$ blocks at film surface act as the growth front for NP assembly. To minimize loss in ΔS_{con} and maximize the energetic

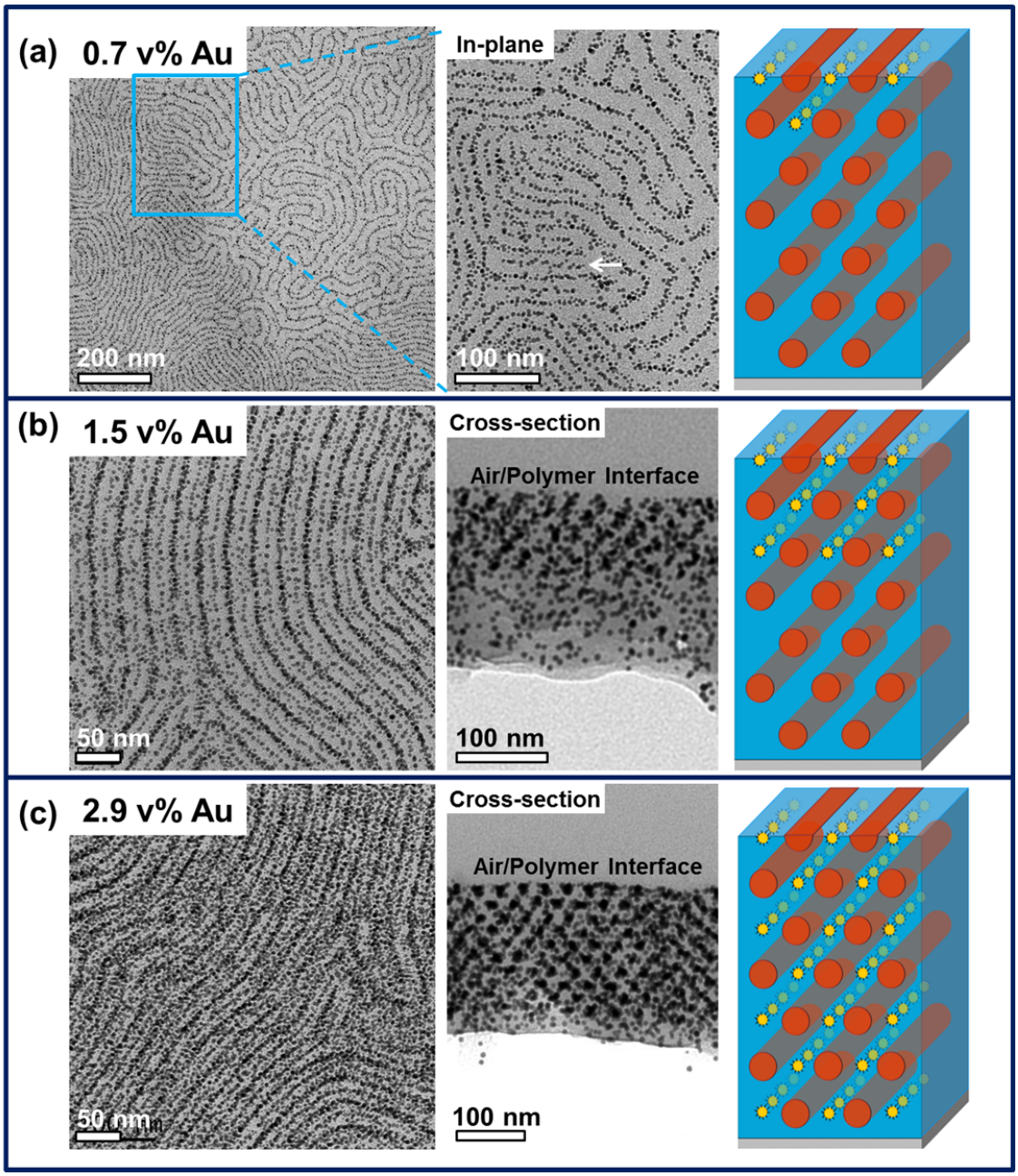

Figure 3.3. Top-view and cross-sectional TEM images of ~200 nm supramolecular nanocomposite thin films containing PS(19 kDa)-*b*-P4VP(5.2 kDa)$(PDP)_{1.7}$ and (a) 0.7, (b) 1.5, and 2.9 vol% of Au NPs. The surface energy plays an important role in the NP assembly, driving the NPs to segregate to the P4VP$(PDP)_{1.7}$ domains starting from the interstitial sites at the surface. The surface-directed assembly then propagates into the film as ϕ_{NP} increases. The morphology of the nancoomposite becomes homogeneous at ϕ_{NP} = 2.9 vol% when the hexagonally packed in-plane NP chains is observed throughout the entire film thickness.

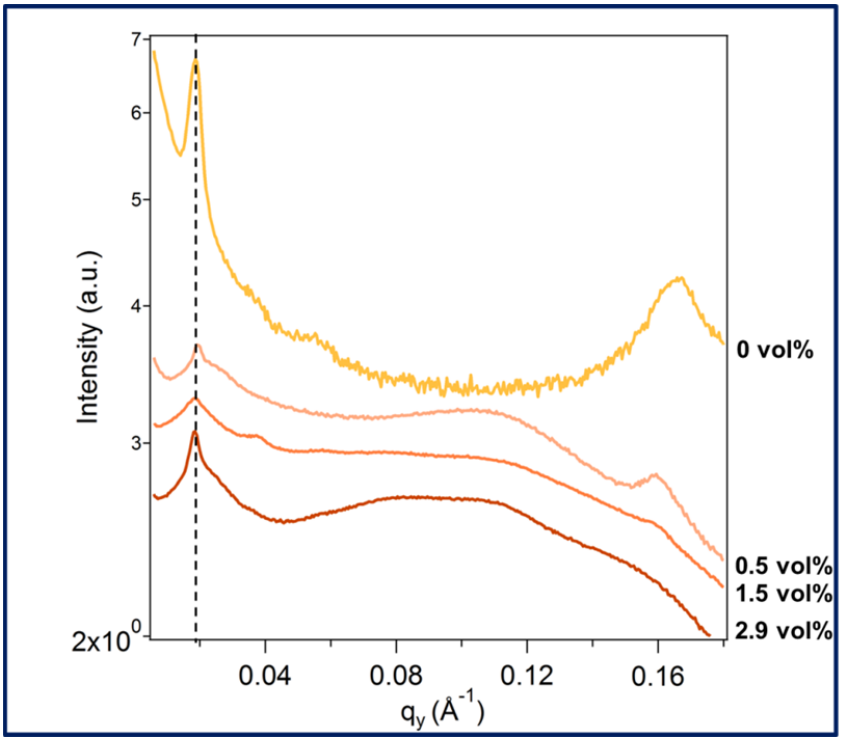

Figure 3.4. q_y lincuts of the GISAXS patterns at q_z = 0.04 Å^{-1} for the ~200 nm supramolecular nanocomposite thin films containing PS(19 kDa)-*b*-P4VP(5.2 kDa)(PDP)$_{1.7}$ and 0, 0.5, 1.5, and 2.9 vol% of ~4.9 nm Au NPs. Upon NP incorporation into the supramolecular thin film, the position of the 1st order Bragg peak stays unchanged. The lateral periodicity of the nanocomposite remains at ~32.6 nm as ϕ_{NP} increases from 0.5 to 2.0 vol%.

gain in $\Delta H_{ligand/polymer}$, the NPs pack in the middle of the P4VP(PDP)$_{1.7}$ domains starting from the surface, resulting in a higher NP concentration near the air/film interface. Solvent annealing then allows a reorientation of the perpendicular domains to reach the ordered in-plane morphology in a local energy minimum. During this process, the NPs segregate to the closest interstitial sites among cylindrical domains to maximize entropic gain in S_{con}, leading to the surface-directed NP assembly observed in Figure 3.3. When ϕ_{NP} reaches 2.9 vol%, there are sufficient NPs that pack densely in the P4VP(PDP)$_{1.7}$ domains throughout the entire film thickness after spin casting. The NPs diffuse locally to the nearest interstitial regions as the cylinders undergo the reorientation process during solvent annealing, leading to hexagonally packed in-plane NP chains with homogeneous NP concentration in the interior of the film.

In addition to the morphology, the GISAXS results demonstrate that the lateral periodicity of the supramolecular nanocomposite thin films remains constant from 0 to 2.9 vol%. With ~4.9 nm NPs residing in the middle of the P4VP(PDP)$_{1.7}$ blocks, a slight increase in the lateral periodicity is expected. In addition, the chain ends of the comb blocks need to deform around the NPs, which may lead to a decrease of the contour length of the P4VP(PDP)$_{1.7}$ chains.

The two effects may decouple, resulting in an unchanged lateral periodicity of the supramolecular nanocomposite ~32.6 nm when ϕ_{NP} is varied between 0 and 2.9 vol%.

3.2.1.2 Regime II: Formation of 3-D nanoparticle networks in cylindrical supramolecular nanocomposite thin film (3 vol% < ϕ_{NP} < 15 vol%)

The AFM and cross-sectional TEM images of ~200 nm PS(19 kDa)-*b*-P4VP(5.2 kDa)$(PDP)_{1.7}$ supramolecular thin films containing and 4.4 and 7.3 vol% of ~4.9 nm Au NPs are shown in Figure 3.5a and 3.5b, respectively. The AFM images confirm that both samples have in-plane cylindrical morphology. When the NP loading is 4.4 vol%, the majority of the NPs still reside in the interstitial sites (Figure 3.5a). Some of the particles, on the other hand, are observed in the P4VP$(PDP)_{1.7}$ matrix, conforming to the distorted hexagonal framework of the supramolecules and forming homogeneous 3-D NP networks throughout the entire film thickness (Figure 3.5a). As ϕ_{NP} reaches 7.3 vol%, more NPs are dispersed in the matrix, resulting in NP networks with a mixture of distorted and undistorted hexagonal structures (Figure 3.5b). In addition to AFM and TEM, GISAXS was also used to characterize the morphology of these two nanocomposite thin films (A.2.3). Bragg spots corresponding to the hexagonally packed NP chains can still be observed in both GISAXS patterns since the majority of the NPs are located in the interstitial sites. The arcs near the base of the Bragg rods and the smeared Bragg spots with larger angular widths indicate that the NPs are not just confined in the interstitial sites in the film. In addition, the q_y scan of the two GISAXS patterns reveals a shift of the 1st order Bragg peak to higher q values as ϕ_{NP} increases. The lateral periodicities of the nanocomposites with 4.4 and 7.3 vol% of NPs are around 31.8 and 29.6 nm, respectively.

At ϕ_{NP} = 2.9 vol%, the interstitial sites are fully occupied. Accommodating more NPs into the interstitial regions requires significant deformation of the comb blocks, which is entropically unfavorable. Dispersion of NPs in the matrix results in an entropic gain due to the new configurations of the NP arrangements in the nanocomposites, ΔS_{trans}, an enthalpic gain in $\Delta H_{ligand/polymer}$, but a drop in S_{con} as a result of the deformation of P4VP$(PDP)_{1.7}$ chains. Overall, $\Delta H_{ligand/polymer}$ and ΔS_{trans} may offset $\Delta H_{surface}$ and ΔS_{con} to set the 3-D NP networks as the local equilibrium in the system. Kinetically, the solvent molecules effectively modify the chain conformation of the comb blocks during solvent annealing, lowering the activation energy barrier for the diffusion of the NPs into the middle of the P4VP$(PDP)_{1.7}$ matrix. When the P4VP$(PDP)_{1.7}$ chains become less rigid during annealing, it is less energetically costly for the NPs to diffuse into the comb blocks. Once a NP gets into the matrix, it lowers the activation energy barrier for diffusion and acts as a nucleation site for the NP assembly. As solvent annealing progresses, small grains of NP assemblies grow into 3-D NP networks in the matrix. When the solvent escapes the film, the comb blocks crystallize around the NP networks and freeze in the assemblies. Depending on the NP loading in the film, the NP networks may assume different shapes that do not conform exactly to that of the supramolecule framework. This results in a disruption of the hierarchical structure of the supramolecules during solvent removal, which may potentially lead to a decrease in the lateral periodicity of the supramolecular nanocomposite, which will be discussed in detail in the next section.

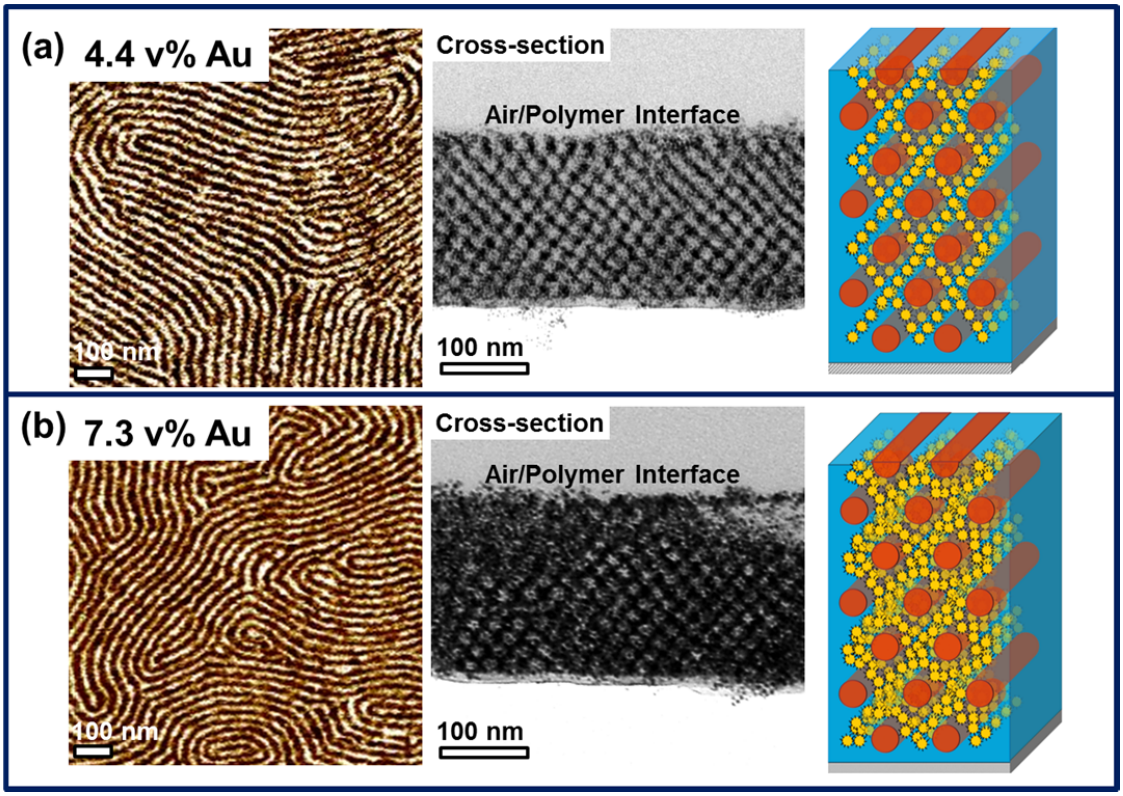

Figure 3.5. AFM and cross-sectional TEM images of ~200 nm supramolecular nanocomposite thin films containing PS(19 kDa)-*b*-P4VP(5.2 kDa)$(PDP)_{1.7}$ and (a) 4.4 and 7.3 vol% of ~4.9 nm Au NPs. The NPs are driven to the interstitial sites as well as the P4VP$(PDP)_{1.7}$ matrix by $\Delta H_{ligand/polymer}$ and ΔS_{trans}, leading to 3-D NP networks in the interior of the films.

3.2.1.3 Regime III: Kinetically-trapped nanoparticle assembly in supramolecular nanocomposite thin film near the thermodynamic limit of ϕ_{NP} (15 vol% < ϕ_{NP} < 20 vol%)

Drastic change of the orientation of the NP arrays and the microdomains is observed when ϕ_{NP} reaches 14.7 vol%. AFM, top-view TEM, and cross-sectional TEM images of a ~200 nm supramolecular nanocomposite thin film containing PS(19 kDa)-*b*-P4VP(5.2 kDa)$(PDP)_{1.7}$ and 14.7 vol% of ~4.9 nm Au NPs are shown in Figure 3.6a, 3.6b, and 3.6c, respectively. The AFM image of the sample shows the perpendicular orientation of the hexagonally packed cylindrical domains (Figure 3.6a). The NPs in the P4VP$(PDP)_{1.7}$ matrix form honeycomb-like assemblies (Figure 3.6b). The cross-sectional TEM image further reveals that the NP arrays prevail throughout the entire film thickness but are not perfectly normal to the surface. Figure 3.6c shows that the perpendicular cylindrical domains assume a finite distribution of tilt angles with respect to the air/film interface. The strong Bragg rods in the q_y direction in the GISAXS pattern confirm the overall perpendicular orientation of the morphology in the film (see A.2.3). According to the q_y linecut of the GISAXS pattern, the lateral periodicity and the average inter-particle distance are around 27.1 and 5.8 nm, respectively. Figure 3.7 summarizes the q_y scans of

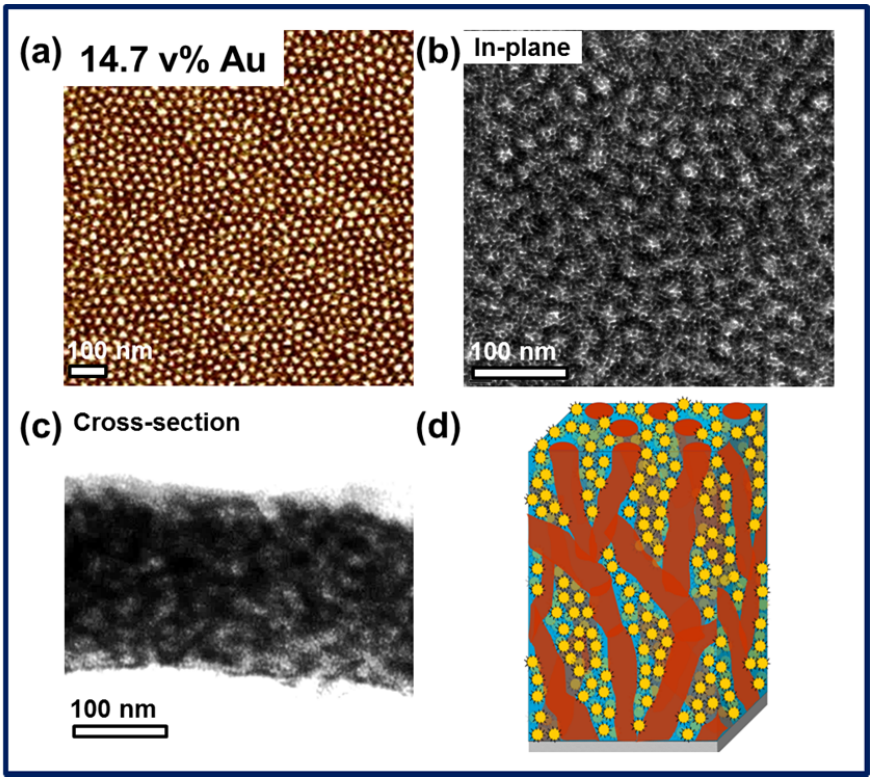

Figure 3.6. (a) AFM, (b) top-view TEM, and (c) cross-sectional TEM images of a ~200 nm supramolecular nanocomposite thin film containing PS(19 kDa)-*b*-P4VP(5.2 kDa)$(PDP)_{1.7}$ and 14.7 vol% of ~4.9 nm Au NPs. Jamming of NPs in the interior of the film leads to a long-lived kinetically-trapped perpendicular cylindrical morphology in the nanocomposite.

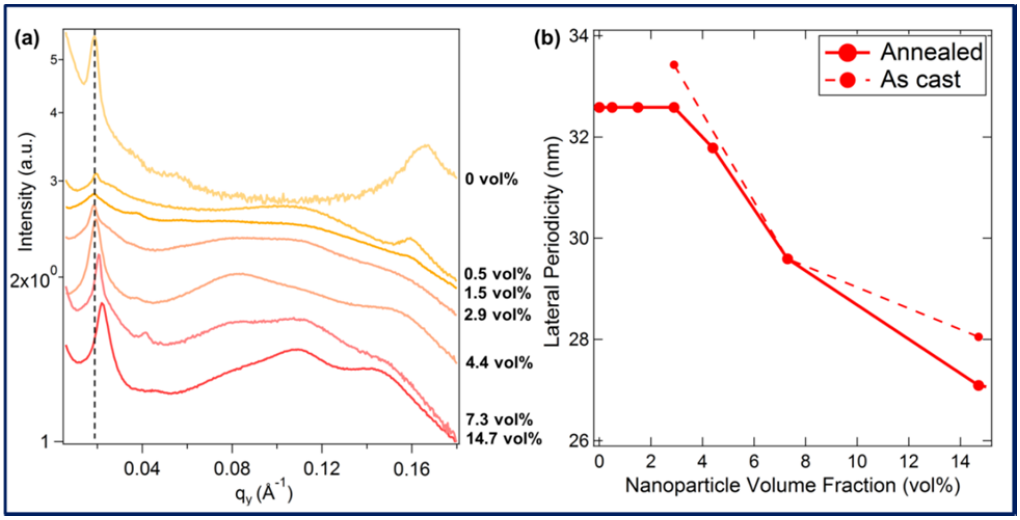

Figure 3.7. (a) q_y lincuts of the GISAXS patterns at $q_z = 0.04$ Å^{-1} for the ~200 nm PS(19 kDa)-*b*-P4VP(5.2 kDa)$(PDP)_{1.7}$ supramolecular thin films containing 0, 0.5, 1.5, 2.9, 4.4, 7.3, and 14.7 vol% of ~4.9 nm Au NPs. A clear trend of a shift of the peak to higher q values can be observed

as ϕ_{NP} goes above 2.9 vol%. (b) summarizes the lateral periodicity of the nanocomposites as a function of ϕ_{NP} and it decreases to 27.1 nm when ϕ_{NP} reaches 14.7 vol%. At high NP loadings, the NPs occupy the entire P4VP(PDP)$_{1.7}$ domain, which alters the hierarchical structure of the comb blocks, and therefore the conformation of the PS chains near the interface. This may lead to a decrease of the lateral periodicity of the nanostructure.

all the supramolecular nanocomposites that have been discussed so far and it demonstrates a decrease of the lateral periodicity of the nanostructure as a function of ϕ_{NP}.

During spin casting, the vertical solvent field biases the microdomains to orient perpendicular to the surface. The coalescence of neighboring cylinders leads to a poorly ordered perpendicular morphology in the as-cast film. Usually, solvent annealing provides sufficient mobility that allows the supramolecular nanocomposite to overcome the activation energy barrier to escape the kinetically trapped state and form ordered parallel morphology. At high ϕ_{NP}, however, the majority of the NPs occupy the entire P4VP(PDP)$_{1.7}$ domains and some NPs may even locate near the interface between the two blocks, resulting in jamming of NPs and the comb blocks.[26] This stabilizes the non-equilibrium perpendicular morphology in the nanocomposite thin film generated during spin casting, similar to that observed in the cases of immiscible polymer blends or immiscible liquids.[25,37,38] Therefore, neither the lateral nor the vertical ordering of the nanostructure can be improved even after prolonged solvent annealing. During spin casting, some of the NPs may pack in the comb blocks, disrupting the crystallization of the small lamellae in the P4VP(PDP)$_{1.7}$ domains as schematically depicted in Figure 3.8. As a result, the P4VP(PDP)$_{1.7}$ chains no longer have comb-like architectures and may assume bottlebrush-like conformations. This further induces a larger cross-sectional mismatch at the interface between the two blocks than that in a coil-comb supramolecule framework. The PS chains need to change their conformations near the interface to accommodate the change in the cross-sectional area at the interface, which leads to a decrease in their end-to-end distance in the lateral direction (Figure 3.8). This conformational change of the chain architecture is not alleviated when the solvent enters the film during solvent annealing. Kinetically, the jamming of the NPs significantly decreases the diffusion coefficient of the system and increases the activation energy barrier for inter-domain diffusion. Moreover, the solvent molecules further disrupt the hierarchical structure in the P4VP(PDP)$_{1.7}$ domains. Thus, the lateral periodicity of the nanocomposite decreases with increasing ϕ_{NP}. Unlike those in highly loaded supramolecular nanocomposites, the NPs in the films with relatively small ϕ_{NP} locate in the middle of the P4VP(PDP)$_{1.7}$ domains, preserving the highly crystalline comb blocks with large contour lengths. Thus, the lateral periodicity in the supramolecular nanocomposites with low ϕ_{NP} (*a*) is larger than that with high ϕ_{NP} (*b*) as shown in Figure 3.8.

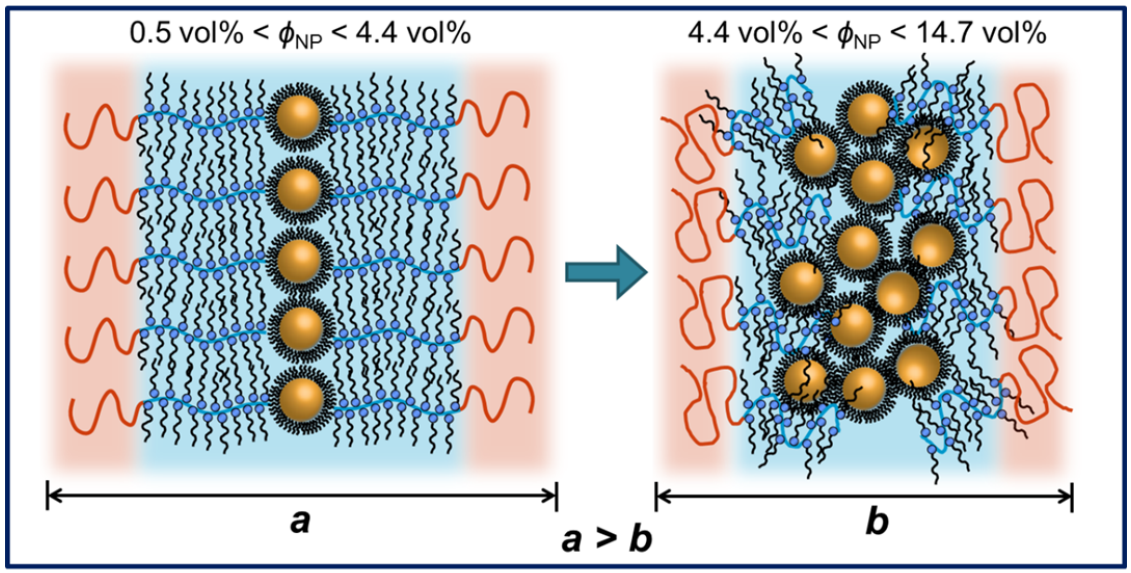

Figure 3.8. Schematic drawings of the chain conformations of PS and P4VP(PDP)$_{1.7}$ chains and the spatial distribution of NPs at relatively low and high NP loadings. When ϕ_{NP} is high, the NPs in the P4VP(PDP)$_{1.7}$ domains may get into the comb blocks and disrupt the crystallization of the small lamellae. This leads to a bottlebrush-like architecture of the P4VP(PDP)$_{1.7}$ chains and a change of the PS conformation to accommodate the cross-sectional mismatch at the interface between the two blocks. The lateral periodicity of the microdomains, therefore, may decrease as a result of the altered chain architecture of the supramolecules.

3.2.1.4 Regime IV: Macrophase separation of nanoparticles in cylindrical supramolecular nanocomposite thin film (20 vol% < ϕ_{NP} < 30 vol%)

With 14.7 vol% of NPs in the P4VP(PDP)$_{1.7}$ domains, the total volume fraction of the matrix becomes 77 vol% since the volume fraction of the comb block is 62 vol% in PS(19 kDa)-*b*-P4VP(5.2 kDa)(PDP)$_{1.7}$. In bulk, the supramolecules form spherical morphology when f_{comb} reaches above 82 vol%.[39] To investigate if the supramolecular nanocomposite undergoes morphological transition at high ϕ_{NP} and to test the thermodynamic limit of ϕ_{NP} in the film, we further increase the NP loading to > 20 vol%. Figure 3.9a shows the AFM and top-view TEM images of a ~200 nm PS(19 kDa)-*b*-P4VP(5.2 kDa)(PDP)$_{1.7}$ supramolecular nanocomposite thin film containing 22.0 vol% of ~4.9 nm Au NPs. The upper half and the bottom half of the AFM image, which are separated by a blue dashed line, show the surface morphology of the film under a weaker and a stronger tapping force, respectively. When the tapping force is small, hexagonally packed 2-D NP lattices can be observed whereas the feature of the microphase-separated cylindrical morphology is only seen when the tapping force is large. The top-view TEM image of the sample further corroborates this observation as NP lattices are seen in many regions on the surface of the film as shown in the zoomed-in image. The GISAXS result of the sample shows one Bragg peak corresponding to the perpendicular cylindrical morphology with a

lateral periodicity ~26 nm (Figure 3.10a). Interestingly, two peaks representing inter-particle distances ~5.7 and ~5.0 nm are present on the q_y linecut. As ϕ_{NP} increases to 29.3 vol%, the AFM image only shows NP lattices on the film surface regardless of the tapping force (Figure 3.9b). The GISAXS pattern of the sample shows a Bragg peak corresponding to a lateral periodicity ~26 nm. Two inter-particle distance peaks (5.5 and 5.0 nm), again, appear on the q_y scan (Figure 3.10a). To further characterize the internal structure of the film, GISAXS was conducted on the 29.3 vol% sample at different incident angles (α) (Figure 3.10b). When α is smaller than the critical angle of the film (α = 0.15°), only the peak corresponding to a 5.5 nm inter-particle distance can be observed. As α is increased from 0.15° to 0.34°, the Bragg peaks corresponding to the lateral periodicity of the nanocomposite and the inter-particle distance ~5.0 nm begin to show up. The intensity of the two peaks becomes stronger and stronger as a function of α. This indicates that the surface of the film is mainly covered by NP assemblies with average inter-particle distance ~5.7 nm. In the nanocomposite thin film, the morphology is similar to that at ϕ_{NP} = 14.7 vol% but with a smaller lateral periodicity. Moreover, the inter-particle distance in the nanocomposite (5.0 nm) is smaller than that in the NP lattices on the film surface (5.7 nm).

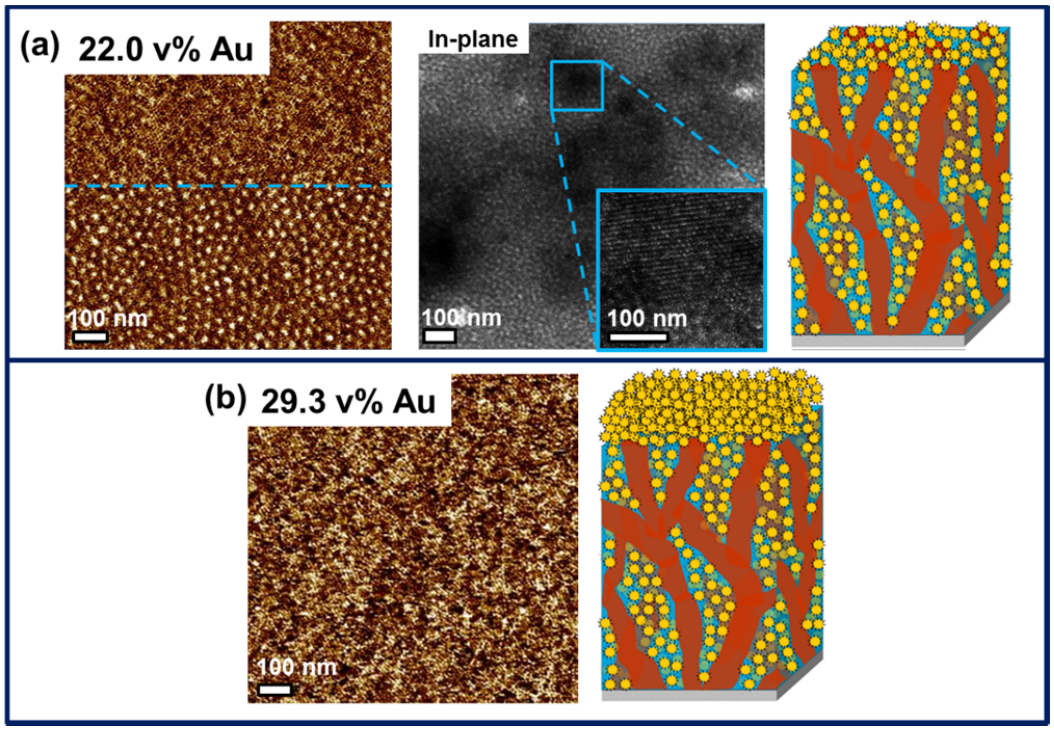

Figure 3.9. AFM and top-view TEM images of the ~200 nm PS(19 kDa)-*b*-P4VP(5.2 kDa)(PDP)$_{1.7}$ supramolecular thin films containing (a) 22.0 and (b) 29.3 vol% of ~4.9 nm Au NPs. At ϕ_{NP} = 22.0 vol%, some NPs are expelled from the interior of the film and form a monolayer of hexagonally packed 2-D NP lattices at the air/film interface. The film surface becomes completely covered by multiple NP layers at ϕ_{NP} = 29.3 vol% as no microphase-separated nanostructure can be observed in the AFM image in (b).

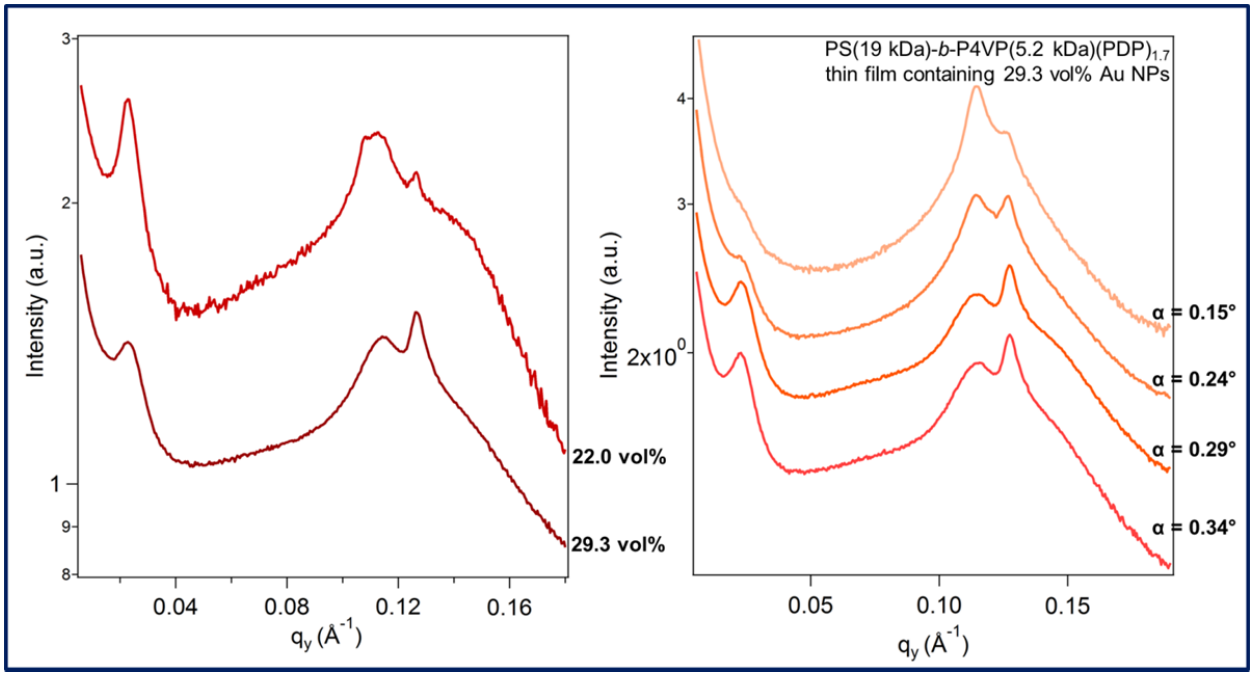

Figure 3.10. (a) q_y lincuts of the GISAXS patterns at q_z = 0.04 Å^{-1} for the ~200 nm PS(19 kDa)-*b*-P4VP(5.2 kDa)(PDP)$_{1.7}$ supramolecular thin films containing 22.0 and 29.3 vol% of ~4.9 nm Au NPs. The 1st order Bragg peak seen at high α corresponds to the microphase-separated supramolecule framework and shifts to higher q values as ϕ_{NP} increases. Additionally, the relative intensity of the inter-particle distance peak at a higher q value becomes stronger as α rises, which is indicative of a smaller inter-particle distance (~5.0 nm) in the microphase-separated nanocomposite film than that in the macrophase-separated NP lattices on the film surface (~5.5 nm) as shown in (b).

The cylindrical supramolecular nanocomposite is in the spherical morphology regime in the phase diagram when volume fraction of the P4VP(PDP)$_{1.7}$ domains reaches 84.0 vol% at ϕ_{NP} = 22 vol%. The results, however, demonstrates no sign of cylinder-to-sphere order-order transition in the film, which is usually observed when the matrix is significantly swollen by the incorporated NPs. Usually, the increase in the effective volume of the matrix may bend the interface and the NPs can stabilize the curvature of the spheres to induce morphological transformation. However, in this case, the threshold ϕ_{NP} for cylinder-to-sphere transition is above the thermodynamic limit of ϕ_{NP} in the film. Between 15 and 20 vol%, the nanocomposite reaches a ϕ_{NP} limit at which it becomes too entropically costly to deform the polymer chains to accommodate more NPs in P4VP(PDP)$_{1.7}$ domains. Therefore, ΔS_{con} can easily offset $\Delta H_{ligand/polymer}$, which only relies on weak van der Waals interactions. In addition, as more and more NPs get close to the PS/P4VP(PDP)$_{1.7}$ interface, more energy loss needs to be compromised due to the unfavorable ligand/PS enthalpic interactions. Thus, no morphological transition is observed and the macrophase separation of NPs occurs above the thermodynamic

limit of NP loading and the excess amounts of NPs are expelled from the interior of the film to the air/film interface. Once 2-D NP lattices form at the film surface, the particle-particle interactions and $\Delta H_{surface}$ may offset the unfavorable ligand/PS interactions at the NP/film interface. This induces a growth of the macrophase separated NP lattices as ϕ_{NP} increases. Decreasing NP size and enhancing $\Delta H_{ligand/polymer}$ via hydrogen bonding or ionic interactions may suppress ΔS_{con} and allow higher NP loadings in the film, which requires further investigation in the future. At this point, it is not fully understood why the inter-particle distance in the NP-only layer is larger than that in the nanocomposite. Our speculation is that the supramolecule framework imposes a 3-D confinement on the NPs in the nanocomposite thin film. This may result in a smaller inter-particle distance in the film when the supramolecules rapidly shrink during fast solvent removal. To further elucidate the underlying physical reasons for the observed phenomenon, in-depth investigation involving *in situ* GISAXS experiments may be required, which is not the focus of this chapter.

3.2.1.5 Regime V: Nanoparticle dominant assembly at high ϕ_{NP} (ϕ_{NP} > 30 vol%)

Although some NPs macrophase separate when ϕ_{NP} > 22.0 vol%, most of the NPs still co-assemble with the microphase-separated supramolecules beneath the NP lattices in the top layer. At even higher ϕ_{NP}, it is questionable if the co-assembly and the NP assembly can coexist. Figure 3.11a-c show the AFM and GISAXS data of the ~80 nm films containing PS(19 kDa)-*b*-P4VP(5.2 kDa)$(PDP)_{1.7}$ supramolecules and 36.6, 44.0, and 100 vol% of ~4.9 nm Au NPs, respectively. All three AFM images show only NP lattices at the film surface and no microphase-separated nanostructure can be seen (Figure 3.11). GISAXS is used to characterize the internal structures of the nanocomposites. In all GISAXS patterns, no Bragg peak corresponding to the supramolecule framework is observed at low q at different incident angles (see A.2.4 and A.2.5). In addition, a strong inter-particle distance doublet at ~0.12 $Å^{-1}$ is observed in the q_y scans, which can be separated into two single peaks by deconvolution and the exact peak positions are listed in Table 3.1. The NP assemblies in the 36.6 and 44.0 vol% samples assume larger inter-particles distances (5.4 and 4.9 nm) than those in the NP-only film (5.1 and 4.8 nm) (Figure 3.11a).

To further characterize the crystal structures of the NP assemblies in the highly-loaded nanocomposite thin films, the positions of the structure factor on the q_y linecut for the 44.0 vol% sample are compared to those for *f.c.c.*, *h.c.p.*, and *b.c.c.* crystal structures (Figure 3.12b). There are four peaks on the q_y scan at $\alpha = 0.15°$ and the normalized peaks positions are located at $q/q_o \approx$ 1, 1.10, 1.73, and 1.92, identifying neither of the combination tabulated in Table 3.2. Careful observation of the profiles in Figure 3.12b reveals two sets of peaks with varying intensity and full width at half maximum (FWHM) as a function of α. The 1st and 3rd peaks gradually weaken whereas the 2nd and the 4th ones become stronger as α increases. Moreover, the two sets of peaks both have $q/q_o \approx 1.73$, which is indicative of the *h.c.p.* structure. This demonstrates that the NP assemblies near the surface and in the interior of the film both possess *h.c.p.* packing configuration but different average inter-particle distances around 5.1 and 4.8 nm, respectively. When ϕ_{NP} reaches 36.6 vol%, the NP-NP interactions becomes dominant and offsets the thermodynamic driving force for the microphase separation of the cylindrical supramolcules. As

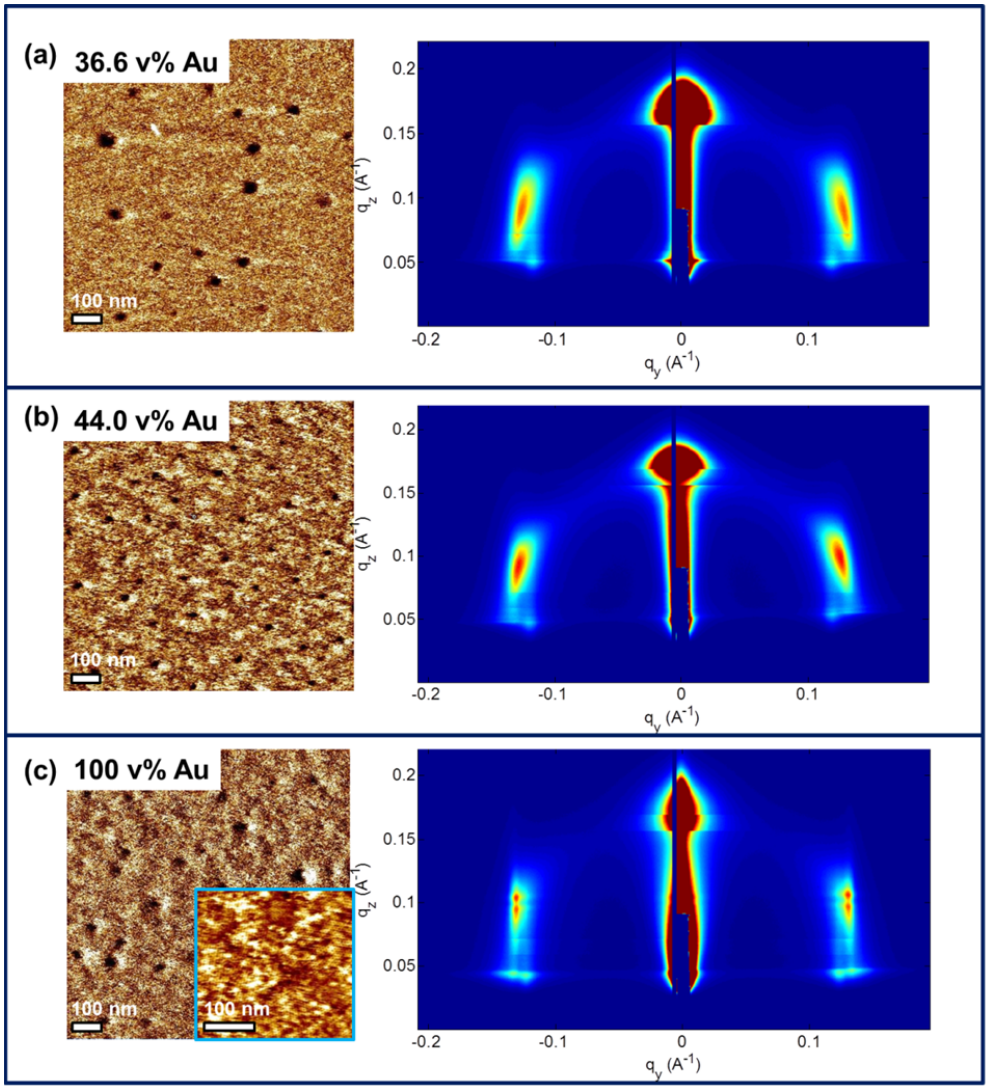

Figure 3.11. AFM and GISAXS images of the ~80 nm PS(19 kDa)-*b*-P4VP(5.2 kDa)$(PDP)_{1.7}$ supramolecular thin films containing (a) 36.6, (b) 44.0, and (c) 100 vol% of ~4.9 nm Au NPs. The results show no sign of microphase-separater supramolecular framework in the films. Only the Bragg peaks corresponding to the inter-particle ordering in the film are observed in the GISAXS patterns at different incident angles. The supramolecules may form work-like micelles dispersed in the NP assemblies.

the supramolcule concentration drops below a critical value, they can no longer hold the nanostructure to direct NP assembly. Instead, the $P4VP(PDP)_{1.7}$ blocks may encapsulate the PS blocks to form worm-like micelles to maximize the interfacial area between the NP ligands and the PDP small molecules. According to the results shown in Figure 3.11, we speculate that these worm-like micelles are uniformly dispersed in the NP lattices. They may mediate the inter-

particle ordering in the films that have small amounts of supramolecules, making the average inter-particle distance larger than that in the NP solids. In addition, the surface field and the solvent annealing may alter equilibrium inter-particle distance at the film surface, leading to a larger inter-particle distance near the surface of the film. The competition between the packing density preferred at the surface with that preferred in the interior of the film results in two *h.c.p.* structures with slightly different inter-particle distances.

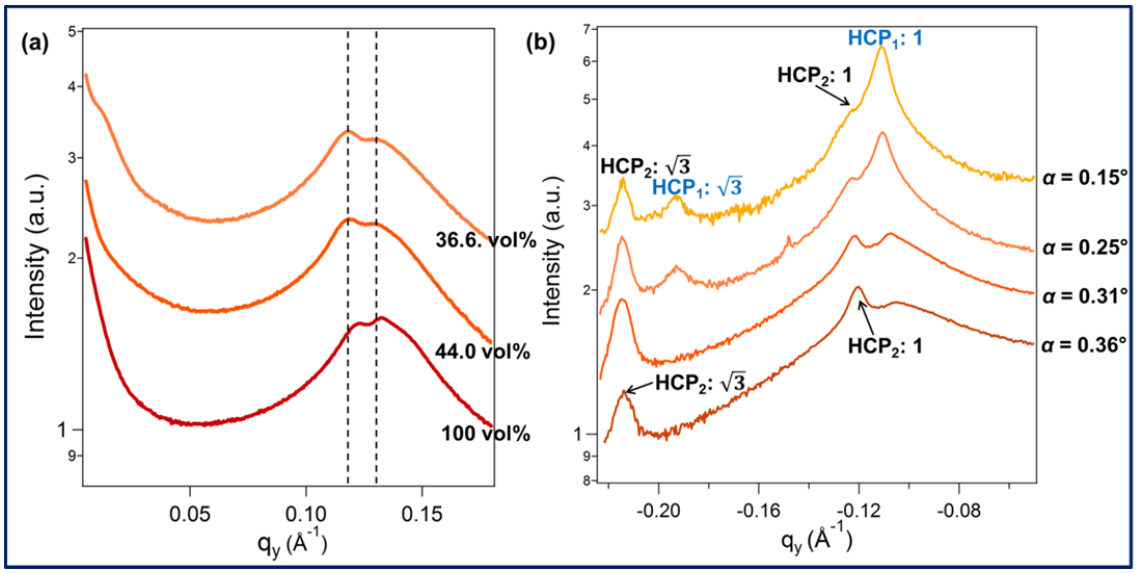

Figure 3.12. (a) q_y lincuts of the GISAXS patterns at q_z = 0.04 Å^{-1} for the samples in Figure 3.13. The inter-particle distances in the films with small amounts of supramolecules are larger than that in the NP-only film. The supramolecules may act like surfactants to mediate particle-particle interactions when they become the minority component in the composite. (b) shows the q_y scans of the GISAXS patterns for the film with 44 vol% of NPs at 4 different incident angles. Fitting the peaks reveals two sets of *h.c.p.* NP lattices with inter-particle distances ~5.4 and ~4.9 nm near the surface and in the interior of the film, respectively.

Table 3.1

	ϕ_{NP} = *36.6 vol%*	ϕ_{NP} = *44.0 vol%*	ϕ_{NP} = *100 vol%*
Inter-particle distance **near the surface**	5.4 nm	5.4 nm	5.1 nm
Inter-particle distance **in the film**	4.9 nm	4.9 nm	4.8 nm

Table 3.2

	1st order peak (q/q_o)	*2nd order peak* (q/q_o)	*3rd order peak* (q/q_o)	*4th order peak* (q/q_o)
h.c.p.	1	$\sqrt{3} = 1.73$	2	$\sqrt{7} = 2.65$
f.c.c.	1	$\sqrt{4/3} = 1.15$	$\sqrt{8/3} = 1.63$	$\sqrt{11/3} = 1.91$
b.c.c.	1	$\sqrt{2} = 1.41$	$\sqrt{2} = 1.73$	2

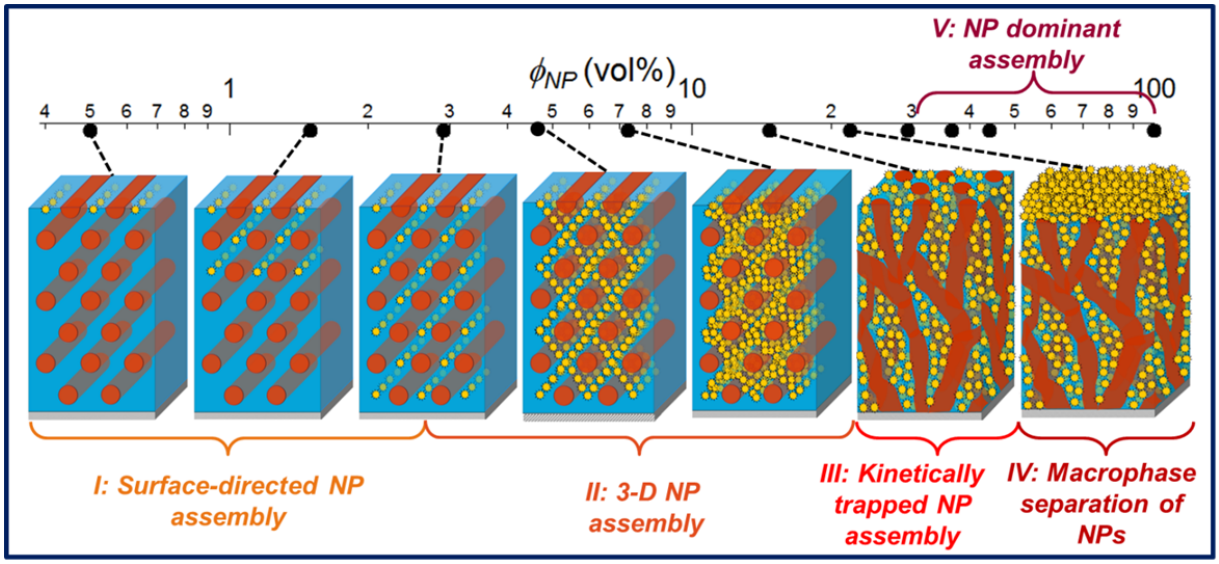

Figure 3.13. Summary of the morphologies in the supramolecular nanocomposite thin films with different NP volume fractions ranging from 0.4 to 45 vol%.

So far, the morphology of the cylindrical supramolecular nanocomposite thin film has been systematically investigated as a function of ϕ_{NP}. The enthalpic and the entropic contributions reach delicate balances in different regimes of ϕ_{NP}, resulting in various multidimensional hierarchical NP assemblies in the system (Figure 3.13). In Regime I, $\Delta H_{ligand/polymer}$, $\Delta H_{surface}$, and ΔS_{con} drive the surface-directed NP assembly in the film. As ϕ_{NP} reaches Regime II, ΔS_{trans} and $\Delta H_{ligand/polymer}$ become the dominant driving forces, dispersing the NPs in P4VP(PDP)$_{1.7}$ matrix, resulting in 3-D NP networks throughout the entire film thickness. The importance of the kinetics surfaces in Regime III, where jamming of NPs in the film leads to long-lived non-equilibrium perpendicular NP arrays in the nanocomposites. Above 20 vol% (Regime IV), it becomes too entropically costly for the polymer chains to accommodate more NPs, resulting in macrophase separation of NPs on the film surface. Finally, in Regime V, the co-assembly breaks down. The supramolecules become dispersed in the NP lattices as the NP

assemblies dominate. The systematic study on the phase behavior of the cylindrical supramolecular nanocomposite thin film as a function of ϕ_{NP} gives us insights into the thermodynamics of the co-assembly of NPs and BCP-based supramolecules. It lays a solid foundation for us to further investigate the effect of NP loading on the morphology of lamellar supramolecular nanocomposites and to fully understand the fundamentals in the system in the following section.

3.2.2 Morphology of lamellar supramolecular nanocomposite thin films as a function of nanoparticle volume fraction

To further understand the phase behavior in supramolecular nanocomposite thin film as a function of NP loading, we next study a model system containing a lamellar supramolecule, PS(40 kDa)-*b*-P4VP(5.6 kDa)(PDP)$_1$, and different amounts of ~3.5 nm Au NPs. The supramolecule has a volume fraction of P4VP(PDP) block, f_{comb}, around 0.35. With ϕ_{NP} varied between 0 and 6 vol%, the total volume fraction of the comb block in the supramolecular nanocomposite may reach above 0.42 and the system can get close to lamella-cylinder phase boundary at high ϕ_{NP}.

Figure 3.14a-c show the AFM, cross-sectional TEM, and GISAXS images of a ~200 nm PS(40 kDa)-*b*-P4VP(5.6 kDa)(PDP)$_1$ supramolecular thin film containing 0.5 vol% of ~3.5 nm Au NPs. Local clusters of hexagonally packed NPs on the film surface are seen in the AFM image. The cross-sectional TEM image demonstrates a higher NP concentration at the air/polymer interface (Figure 3.14b). In the interior of the film, the NP concentration in each P4VP(PDP)$_1$ domain is homogeneous throughout the film thickness. The GISAXS pattern of the sample shows a weak peak in the q_y direction corresponding to the inter-particle distance ~9.5 nm. No structure factor from the in-plane lamellar morphology in the q_z direction is observed. These results indicate that the NPs mainly segregate to the air/polymer interface and there is insufficient amount of NPs for the formation of a complete layer of close-packed 2-D NP lattices as illustrated in Figure 3.14d. When ϕ_{NP} reaches 1.5 vol%, a complete hexagonally packed NP sheet can be seen at the film surface (Figure 3.15a). The Bragg peaks up to the 3rd order appear in the GISAXS pattern (Figure 3.15b), which is indicative of the presence of the NP sheets in the middle of each P4VP(PDP)$_1$ microdomain as shown in Figure 3.15c. The inter-particle ordering peak becomes sharper and shifts to a higher q value in the GISAXS pattern, confirming that the NPs become more closely packed in the microdomains. At ϕ_{NP} = 2.9 vol%, 2-D NP sheets can be, again, clearly seen on the surface of the lamellar supramolecular nanocomposite thin film (Figure 3.16a). The cross-sectional TEM image of the film shows a NP sheet with thickness ~7.5 nm in each P4VP(PDP)$_1$ block (Figure 3.16b). In fact, the image analysis indicates that there are at least two layers of NPs in every NP sheet. Moreover, in some regions of the TEM image, the two layers of NPs are observed to be spatially coordinated in the vertical direction, forming NP

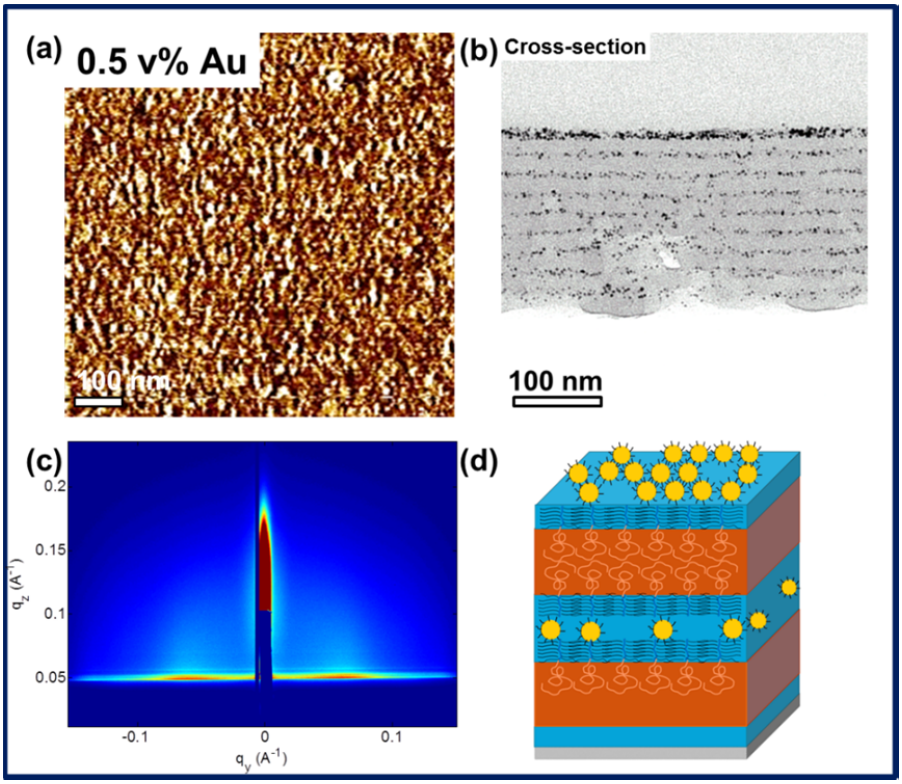

Figure 3.14. (a) AFM, (b) cross-sectional TEM, and (c) GISAXS images of a ~200 nm PS(40 kDa)-*b*-P4VP(5.6 kDa)$(PDP)_1$ supramolecular thin film containing 0.5 vol% of ~3.5 nm Au NPs. The majority of the NPs form small cluster of 2-D NP assemblies at the film surface. Unlike that in cylindrical supramolecular nanocomposites with the same NP loading, kinetically trapped NPs can be observed in each P4VP$(PDP)_1$ microdomains in the interior of the film. The layered structure imposes large activation energy barrier for the NPs to diffuse through to reach the air/polymer interface.

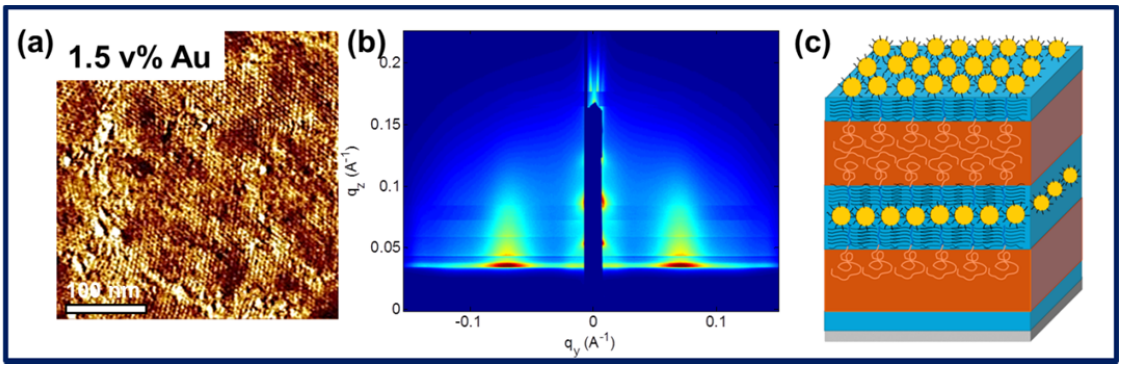

Figure 3.15. (a) AFM, (b) cross-sectional TEM, and (c) GISAXS images of a ~200 nm PS(40 kDa)-*b*-P4VP(5.6 kDa)$(PDP)_1$ supramolecular thin film containing 1.5 vol% of ~3.5 nm Au NPs.

The results confirm that the NPs assemble in the middle of each P4VP(PDP)$_1$ block throughout the entire film thickness.

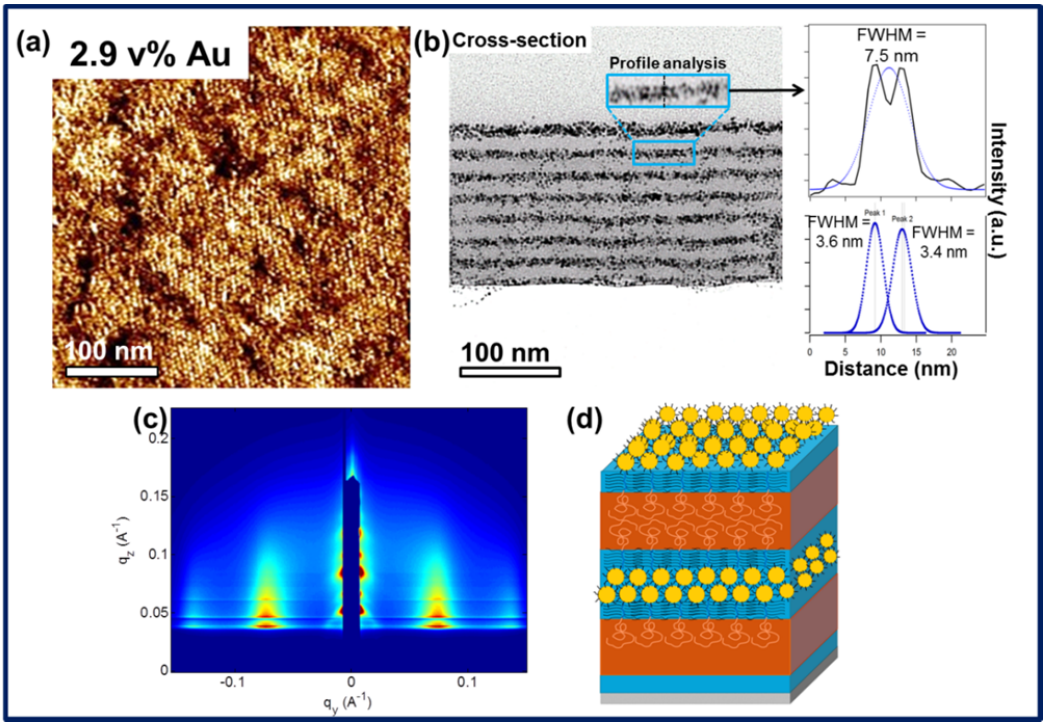

Figure 3.16. (a) AFM, (b) cross-sectional TEM, and (c) GISAXS images of a ~200 nm PS(40 kDa)-*b*-P4VP(5.6 kDa)(PDP)$_1$ supramolecular thin film containing 2.9 vol% of ~3.5 nm Au NPs. The image analysis of the TEM data and the enhanced scattering of the P4VP(PDP)$_1$ lamellar structure in the GISAXS patterns are indicative of hierarchical NP assemblies in the P4VP(PDP)$_1$ microdomains. Two layers of NPs form in the domains with characteristic lateral periodicity.

assemblies in the middle of P4VP(PDP)$_1$ small lamellae with characteristic lateral periodicity similar to that of the comb block (~3-4 nm). In the GISAXS pattern of the sample, the Bragg peak in the q_z direction, confirms the lamellar structure in the nanocomposite thin film. The inter-particle distance becomes smaller than that in the 1.5 vol% sample, suggesting closed packed NP assemblies in the P4VP(PDP)$_1$ domains. Interestingly, the structure factor corresponding to the periodicity of the P4VP(PDP)$_1$ small lamellae can be seen at q_y = 0.14 Å^{-1} in the GISAXS pattern. In cylindrical supramolecular nanocomposite, the intensity of this peak gradually weakens as a function of ϕ_{NP} due to the scattering from the high-electron-density gold NPs. In this case, however, the scattering intensity of the P4VP(PDP)$_1$ lamellar structure increases as ϕ_{NP} rises (see A.2.6). Combining with the TEM result, we conclude that the 3.5 nm Au NPs may

reside in the middle of P4VP(PDP)$_1$ lamellae at high ϕ_{NP}, resulting in hierarchical NP assemblies in the P4VP(PDP)$_1$ domains as shown in Figure 3.16.

When there is little amount of NPs in the film, most of the NPs segregate to the air/polymer interface to minimize the entropic penalty from polymer chain deformation and the surface energy of the film. Some NPs are not rejected to the film surface as they are kinetically trapped in the P4VP(PDP)$_1$ domains during spin casting. Since it is energetically unfavorable for these NPs to diffuse to the film surface during solvent annealing, they form local clusters of NP assemblies in the middle of the P4VP(PDP)$_1$ domains to minimize the reduction in S_{con}. As ϕ_{NP} increases, more NPs are trapped in the comb blocks during the film formation process. These NPs form a single 2-D NP sheet in the middle of the P4VP(PDP)$_1$ blocks to reach a local thermodynamic minimum. At ϕ_{NP} = 2.9 vol%, it appears that many NPs are located in the P4VP(PDP)$_1$ lamellae. Although this spatial organization of NPs can maximize the interfacial area between the NP ligands and the PDP small molecules, it is extremely entropically unfavorable as the P4VP(PDP)$_1$ chains need to undergo significant change of their conformations to accommodate the NPs. Thermodynamically, ΔS_{con} may offset $\Delta H_{ligand/polymer}$, making it energetically unstable for the NPs to reside in the P4VP(PDP)$_1$ lamellae. We, hence, speculate that the morphology is in a kinetically trapped state. During solvent annealing, the solvent molecules may disrupt the crystalline structure of the comb blocks and modulate the chain conformations of the P4VP(PDP)$_1$ chains. This significantly lowers the activation energy barrier for the 3.5 nm NPs to diffuse into the P4VP(PDP)$_1$ lamellae. When the solvent is removed from the film rapidly, the comb blocks crystallize and the NPs are confined in the middle of the P4VP(PDP)$_1$ lamellae, resulting in the hierarchical NP assemblies observed in Figure 3.17. This may only hold true when the NP size is smaller than the periodicity of the P4VP(PDP)$_1$ lamellae, which is usually around 4 to 5 nm. When the NPs become larger than 5 nm, it is too entropically costly for the polymer chains to deform around the NPs and accommodate them in the P4VP(PDP)$_1$ comb blocks. Thus, 5-6 nm NPs tend to assemble just in the middle of the P4VP(PDP)$_1$ domains as shown in the previous chapter. This is corroborated by the GISAXS results of ~200 nm lamellar supramolecular thin films with different amounts of ~6.0 nm Au nanoparticles (see A.2.7). No lamella-to-cylinder morphological transition is induced in the film even at high NP loadings.

Next, we further increase ϕ_{NP} to 5.8 vol% and the AFM, GISAXS, and cross-sectional TEM images of the ~200 nm lamellar nanocomposite thin film are shown in Figure 3.17a-c, respectively. The AFM and the GISAXS data confirm an in-plane cylindrical morphology in the film. The cross-sectional TEM image, however, shows that the hexagonally packed in-plane NP chains are only present near the film surface (Figure 3.17c). Parallel lamellar morphology appears in the interior of the film near the polymer/substrate interface. More than two sheets of NPs in each P4VP(PDP)$_1$ domain and undulation of the interface between the two blocks are observed. Moreover, the concentration of NPs is not homogeneous in each P4VP(PDP)$_1$ domain, resulting in clusters of NPs in the assemblies that may be a sign of lamella-to-cylinder morphological transition in the interior of the film.

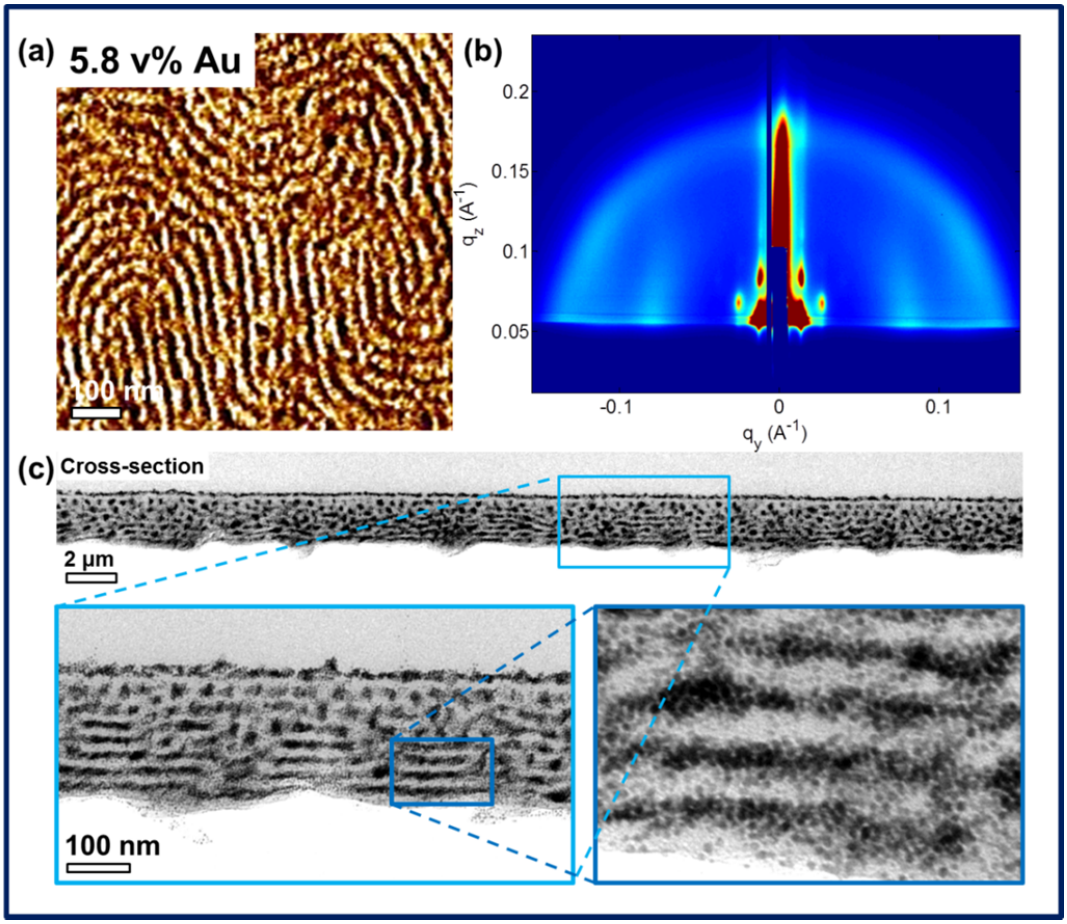

Figure 3.17. (a) AFM, (b) GISAXS, and (c) cross-sectional TEM images of a ~200 nm PS(40 kDa)-*b*-P4VP(5.6 kDa)$(PDP)_1$ supramolecular thin film containing 5.8 vol% of ~3.5 nm Au NPs. Cylindrical and lamellar morphologies are observed near the film surface and in the interior of the film, respectively. At this NP loading, the NPs occupy the entire blocks, resulting in a fluctuation of the interface between the two blocks. This further leads to a NP-induced lamella-to-cylinder morphological transition starting from the film surface due to the concentration gradient of solvent in the film during solvent annealing.

When ϕ_{NP} > 5.8 vol%, the 3.5 nm Au NPs occupy the entire P4VP$(PDP)_1$ domains. This results in a change of the chain conformation of the P4VP$(PDP)_1$ chains from comb-like to bottlebrush-like, leading to a larger cross-sectional mismatch between the two blocks. To accommodate this change in the interfacial area, the PS chains need to adjust their chain conformations, resulting in a change of the thickness of the microdomains. As a result, the bending modulus of each block fluctuates accordingly. The undulation of the interface then leads to local clusters of NPs with characteristic periodicity in the P4VP$(PDP)_1$ domains, which force the supramolecules to change their spatial organization. Thus, a lamella-to-cylinder morphological transition is induced, which starts from the air/polymer interface due to the

concentration gradient of solvent in the film. Each PS, P4VP(PDP)$_1$, and NP layer acts as a geometric diffusion barrier for the solvent molecules, resulting in a higher solvent concentration and a faster kinetics near the film surface during solvent annealing.[40] During the transition, the NP chains in each layer assume alternating positions due to the undulation of the interface, leading to a distorted hexagonal lattice of parallel NP chains when the film reaches a local thermodynamic equilibrium.

§ 3.3 Conclusion

In summary, the phase behavior of supramolecular nanocomposite thin films was systematically investigated as a function of NP loading. The complicated interplay between the thermodynamic and kinetic considerations significantly influences the morphology of the nanocomposites in different ϕ_{NP} regimes. In cylindrical supramolecular nanocomposite thin films, a delicate balance among $\Delta H_{surface}$, ΔS_{con}, and $\Delta H_{ligand/polymer}$ drive the surface-directed NP assembly in Regime I (ϕ_{NP} < 3 vol%). The NPs occupy the first few layers of interstitial regions in the cylindrical morphology starting from the ones at the surface as NP loading increases. In Regime II (3 vol% < ϕ_{NP} < 15 vol%), ΔS_{trans} and $\Delta H_{ligand/polymer}$ offset ΔS_{con}, leading to NP assemblies in not only the interstitial sites, but also the 3-D NP networks in the P4VP(PDP) matrix throughout the entire film thickness. When the thermodynamic limit of ϕ_{NP} is reached in Regime III (15 vol% < ϕ_{NP} < 20 vol%), kinetically trapped perpendicular morphology is observed in the nanocomposite. As ϕ_{NP} reaches Regime IV (20 vol% < ϕ_{NP} < 30 vol%), no NP induced cylinder-to-sphere morphological transition is observed as the NPs begin to macrophase separate to form NP lattices on top of the film. Eventually, the co-assembly breaks down as the NPs dominate the assembly in the system at high ϕ_{NP} (Regime V).

Similar studies were conducted on the lamellar supramolecular nanocomposite thin films but with NPs of smaller sizes. Unlike that in cylindrical nanocomposite, the layered structure in parallel lamellae significantly increases the activation energy barrier for the NPs to diffuse to the surface of the film. Kinetically trapped NP assemblies are observed in every P4VP(PDP) microdomains even at low ϕ_{NP}. As ϕ_{NP} increases, the NPs disrupt the crystalline structure of the comb blocks, forming hierarchical assemblies with characteristic periodicity in the microdomains. This induces the fluctuation of the interface between the two blocks and a lamella-to-cylinder morphological transition at ϕ_{NP} above 7 vol%. The results suggest that NP size plays an important role in the co-assembly of NPs and the supramolecules in thin films.

These systematic studies extend our fundamental understanding on the thermodynamics and kinetics in the co-assembly of spherical NPs and BCP-based supramolecules in thin films. The rich library of multidimensional NP assemblies in supramolecular thin films provide a great platform for structure-property correlation study to eventually harness various collective properties of supramolecular nanocomposites for applications including optical coatings, plasmon-enhanced photovoltaics, high-energy-density thin film capacitors, and catalysis. Present

studies also lay a solid foundation for a full understanding of the thermodynamics in the co-assemblies. By simply changing the NP size, the conformational entropy can be precisely modulated to achieve various hierarchical NP assemblies over multiple length scales in supramolecular thin films, which will be further discussed in detail in the next chapter.

§ 3.4 Experimental

3.4.1 Sample preparation

PS(19,000)-*b*-P4VP(5,200) (PDI = 1.09) and PS(40,000)-*b*-P4VP(5,600) (PDI = 1.10) were purchased from Polymer Source, Inc. 3-*n*-pentadecylphenol (95%) was purchased from Acros. Chloroform was purchased from Fisher. All chemicals were used as received. Blends of supramolecules and nanoparticles were prepared as described previously. Thin films were prepared by spin-coating the mixed solutions onto silicon wafers or polystyrene brush modified silicon wafer at spinning speeds ranging from 1000 to 3000 rpm. Sample thicknesses were measured using a Filmetrics F20 interferometer. For solvent annealing, samples were annealed using 300 μL of $CHCl_3$ injected inside a 250 mL top-capped jar at 22.5°C. Once the film thickness of the nanocomposite thin film reached 145-150% of its original thickness, the jar was opened and the $CHCl_3$ vapor inside the jar was allowed to freely evaporate.

3.4.2 Atomic force microscopy

Atomic force microscopy was performed on a Veeco Dimension 3100 with a Nanoscope III controller and a Quadrex extension box. The spring constant of the cantilever was 10 − 130 N m^{-1} with a resonant frequency in the range of 300–500 kHz. The set point for auto tune was ~1.5 V. The set-point amplitude was 90% of the free vibration value.

3.4.3 Grazing incidence small angle X-ray scattering

GISAXS experimental measurements were made at beamline 7.3.3 at the ALS in Lawrence Berkeley National Laboratory and at beamline 8-ID-E the APS in Argonne National Laboratory. X-ray wavelengths of 1.687 Å and 1.240 Å were used at APS, and ALS, respectively. The scattering intensity distribution was captured by a Pilatus 1M detector at ALS and APS. The intensities (I) are plotted with respect to q, where $q = (4\pi/\lambda)\sin(\theta/2)$, λ is the wavelength of the incident X-ray beam, and θ is the scattering angle.

3.4.4 Transmission electron microscopy

PS-*b*-P4VP$(PDP)_r$ thin films were spun cast on polystyrene-coated sodium chloride (NaCl) disks in a manner similar to those on silicon substrates. After solvent annealing, films were floated off the substrate onto a pool of water. Thin films were retrieved with carbon film coated copper grids. The top-view TEM images were collected on a FEI Tecnai 12 transmission

electron microscope at an accelerating voltage of 120 kV. To prepare the cross-section of a nanocomposite thin film, the sample was first prepared on NaCl disk. Then, the thin film was floated off from the substrate on the surface of a pool of water. An epoxy block (Araldite 502, Electron Microscopy Sciences) was used to catch the film such that the sample is on top of the epoxy block with the air-polymer interface in contact with the top of the epoxy block. The epoxy along with the sample were cured at 60°C for at least 4 hours to ensure good contact between the epoxy and the nanocomposite thin film. Thin sections, ~60 nm in thickness, were microtomed using an RMC MT-X Ultramicrotome (Boeckler Instruments) and picked up on copper TEM grids on top of water. Again, the cross-sectional TEM images were collected using a FEI Tecnai 12 transmission electron microscope at an accelerating voltage of 120 kV.

3.4.5 Thermogramimetric analysis

Thermogravimetric analysis (TGA) was performed on a TGA 500 thermogravimetric analyzer heating at a rate of 10 °C/min from room temperature to 550°C under a continuous purge of nitrogen.

Chapter 4
Size-Dependent Nanoparticle Assemblies in Thin Films of Supramolecular Nanocomposites

The results in the previous chapter reveal that the supramolecules and the nanoparticles co-assemble as a result of a delicate balance between the enthalpic and entropic contributions. In this chapter, we focus on tuning the entropic terms via varying the nanoparticle size to gain further insights into the thermodynamics of the system. We discover that 3-D spatial organization of nanoparticles in cylindrical supramolecular thin films is dependent on the ratio of the NP size to the periodicity of the block copolymer-based supramolecule (*d/a*), which is simply tailored by using nanoparticles of different diameters. When *d/a* is larger than 0.28, the nanoparticles are expelled from the interior of the film to the air/polymer interface to minimize the entropic penalty from chain deformation and surface energy. When the nanoparticle size becomes similar to that of the interstitial sites, 6 nm in this case, the nanoparticles predominantly segregate to the interstitial regions, acting as fillers to relax the chain stretching from the comb blocks. As *d/a* becomes smaller than 0.17, the translational entropy becomes the dominant driving force, leading to 3-D distorted rectangular network of nanoparticles throughout the entire film thickness. These results demonstrate that the rigidity of the comb block significantly magnifies the entropic contributions, resulting in the size-dependent assemblies in supramolecular thin films. This gives us a useful tool to achieve hybrid nanoparticle arrays regardless of the chemical composition of the nanoparticles. By changing the size and mixing ratio of the nanoparticles of different chemical compositions, various 3-D co-assemblies of semiconducting quantum dots and plasmonically active gold nanoparticles are successfully generated in thin films. This opens a new avenue for the fabrication of hierarchically structured hybrid nanoparticle arrays with tunable functionality for a wide range of nanodevices.

§ 4.1 Introduction

Controlled co-assemblies of nanoparticle (NP) mixtures with different chemical compositions can not only combine the properties of individual components, but also lead to properties arising from the coupling effects between the NPs.[1] The fluorescence, optical absorption, and photocurrent of semiconductor NPs can be significantly affected by electromagnetic interactions in the vicinity of the metallic materials via the excitation of surface plasmon resonances.[1-9] 2-D and -3D binary NP superlattices have been obtained by co-assembling monodispersed metal, semiconductor, and magnetic NPs of different sizes via controlled solvent evaporation. These studies led to NP solids with unique properties.[10, 11] 2-D arrays of metals or semiconductor NPs have been used to investigate their optical and/or electronic properties.[12, 13] Functional hybrid nanocomposites can also be prepared by blending NPs and block copolymers (BCP) or BCP-based supramolecules.[14, 15] Enthalpically, NP ligands were chemically modified to tailor NP-polymer interactions so as to control the spatial distribution of different types of NPs in BCP/NP blends.[15] Entropically, the penalty to deform polymer chains upon NP incorporation depends on the relative size ratio between the NP and the polymer.[16] Simulations[16-18] and experimental studies[19] have shown that the size-dependent

spatial organization of different types of NPs in lamellar nanocomposites. NPs of different sizes can be selectively sequestered at the interface between two BCP lamellae or in the middle of the lamellar microdomains with good precision.[19] Many NP-based devices are based on thin films. However, it is not trivial to directly extrapolate size-dependent, entropy-driven particle assemblies from bulk to thin films of nanocomposites since NPs tend to aggregate to the film surface to reduce entropic deformation of polymer chains and to lower surface tension.[20, 21] There is no straightforward route to direct co-assemblies of different types of NPs in thin films to tailor the inter-particle coupling and exchange phenomena.

We recently overcame the difficulties of surface aggregation of NPs in thin films using a BCP-based supramolecular approach.[22] Alkyl ligand capped NPs self-assemble into 3-D hierarchical nanostructures in thin films where BCP cylindrical microdomains are oriented parallel to the surface. Energetically, the observed 3-D NP assemblies are entropically driven and can be attributed to the rigidity of the supramolecular comb block that significantly enhances the entropic contribution from the NPs. The NPs selectively localized in the interstitial regions between BCP cylinders (Figure 4.1) act as nanofillers to release the chain deformation of the rigid comb block. Here, the entropy-driven supramolecular approach is applied to obtain directed co-assemblies of NP mixtures in thin films. Different NP assemblies ranging from 3-D interstitial localization, to 3-D network, to 2-D monolayer on the surface, can be readily obtained simply by varying the NP size (d) relative to BCP periodicity (a). Furthermore, this approach can be applied to co-assemble NP mixtures to obtain hybrid arrays of semiconductor and metallic NPs in thin films. Present studies open a new avenue to achieve structural control toward NP-based devices of different chemical compositions and will provide powerful platforms to experimentally test theoretical predictions of nanocomposite properties based on various coupling and exchange phenomena between the NP arrays.

§ 4.2 Results and discussion

The assembly of NPs upon blending with BCP in thin films is determined by a combination of enthalpic and entropic contributions.[14, 15, 23] Qualitatively, the change in free energy upon incorporation of NPs can be described as:

$$\Delta G = (\Delta H_{surface} + \Delta H_{ligand/polymer}) - T(\Delta S_{con} + \Delta S_{trans} + \Delta S_{geometric}),$$

where $\Delta H_{surface}$ originates from the difference in surface tension of each component. Alkyl ligand capped NPs tend to preferentially segregate to the air/film interface to lower surface tension.[21] To incorporate NPs into BCP microdomains in thin films, the NP ligands need to interact favorably with at least one of the BCP blocks, *i.e.* the enthalpic driving force, $\Delta H_{ligand/polymer}$.[20, 22, 24] Functional groups can be included in the NP ligands to strengthen the polymer-NP interactions to increase energetic contribution from $\Delta H_{ligand/polymer}$.[25, 26] ΔS_{con} refers to the change in

conformational entropy of the polymer chains upon NP incorporation. Due to the geometric packing of the hexagonal lattice of cylindrical morphology, there is additional entropic contribution from the polymer chains surrounding the interstitial sites upon NP incorporation, $\Delta S_{geometric}$. This has been shown in homopolymer/BCP blends theoretically[27] and experimentally where homopolymers are selectively localized in the interstitial region.[28] ΔS_{trans} accounts for the entropic contribution due to the number of physical arrangements of the NPs. Present studies mainly focus on the effects of various entropic contributions. The enthalpic contributions, $\Delta H_{ligand/air}$ and $\Delta H_{ligand/polymer}$, were kept constant. Entropically, important parameters include the spring constant, *k*, *i.e.* the rigidity of the polymer chain, and the *d/a* ratio, where *d* is the particle diameter including ligand length and *a* is the lateral periodicity of the supramolecule.

The BCP-based supramolecules, called "PS-*b*-P4VP(PDP)$_{1.7}$" were constructed by hydrogen bonding small molecules 3-pentadecylphenol (PDP) to the 4-vinylpyridine groups in PS(19 kDa)-*b*-P4VP(5.2 kDa) at a molar ratio of PDP to 4VP, r = 1.7. It is expected to be entropically costly to deform rigid P4VP(PDP)$_{1.7}$ chains.[22] All the NPs were passivated with alkyl ligands and preferentially solubilized within P4VP(PDP)$_{1.7}$ matrix. Thin films of PS(19 kDa)-*b*-P4VP(5.2 kDa)(PDP)$_{1.7}$ supramolecular nanocomposites form distorted hexagonal lattice after solvent annealing with lattice constants *a* and *c* being ~33 nm and ~44 nm, respectively (Figure 4.1).[22] The lateral dimension of an interstitial site *x* is 0.167**a*, i.e. 5.5 nm. The *d/a* ratio was varied by using NPs of different sizes, larger or smaller than the interstitial sites. The NP sizes were selected based on the lattice constants of cylindrical supramolecules. PbS (4.5, 6.2, and 8.1 nm), gold (4.2 and 6.1 nm) and PbSe (7.7 nm) NPs were used as listed in Table 4.1. Different from that in the previous chapters, the NP sizes here are calculated as the sum of the NP core diameter and the ligand shell thickness as determined from TEM images (see A.3.1).

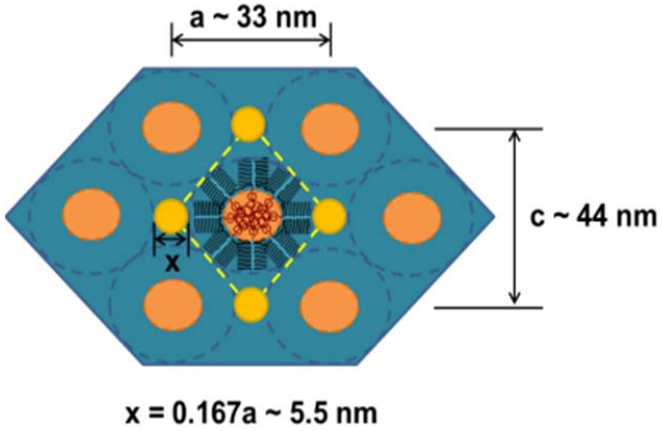

Figure 4.1. Schematic drawing of distorted hexagonal lattice of PS(19 kDa)-*b*-P4VP(5.2 kDa)(PDP)$_{1.7}$ thin films after solvent annealing. The lattice constants *a* and *c* are 33 nm and 44 nm, respectively. The lateral dimension of each interstitial site *x* is 0.167**a*, i.e. 5.5 nm.

Table 4.1

Measure NP Core Size	Measured NP Size (*d*)	*d/a* Ratio
3.3 nm Au	5.7 nm	0.173
5.2 nm Au	7.4 nm	0.224
3.4 nm PbS	5.5 nm	0.167
5.1 nm PbS	7.4 nm	0.224
6.9 nm PbS	9.3 nm	0.282
6.5 nm PbSe	9.0 nm	0.273

Figure 4.2a and 4.2b are the top-view and cross-sectional transmission electron microscopy (TEM) images of a ~180 nm thin film of PS(19 kDa)-*b*-P4VP(5.2 kDa) blended with 5 vol% of ~9.3 nm PbS NPs (*d/a* = 0.28). The PbS NPs formed ordered arrays located at air/polymer interface, one NP in width, conforming to the contours of the fingerprint-like pattern of the cylindrical supramolecular morphology (Figure 4.2a). Upon increasing the NP loading to *f* = 10 vol%, the ~9.3 nm PbS NPs formed multiple grains of 2-D NP hexagonal-close-pack lattices on the film surface (Figure 4.2b). This is in contrast to thin films of supramolecular nanocomposites where the NP size is comparable to the interstitial sites. As shown in Figure 4.2c and 4.2d for comparison, the 7.4 nm PbS NPs preferentially locate in the interstitial area to form 3-D NP arrays and no surface aggregation of nanoparticles was seen.[22] Positioning the 7.4 nm NPs at the interstitial regions relaxes the comb-like chains from stretching into the interstitial sites, leading to an entropic gain in S_{con} and $S_{geometric}$. Similar results are also observed in a ~200 nm thin film of lamellar nanocomposite containing PS(40 kDa)-*b*-P4VP(5.6 kDa)(PDP)$_1$ and 10 vol% of 9.3 nm PbS NPs (Figure 4.3). In this case, *d/a* = 0.25 and the AFM and cross-sectional TEM images show that the majority of the 9.3 nm NPs reside at the air/polymer interface. Interestingly, not all the NPs are expelled to the film surface as some NPs are located in the middle of the P4VP(PDP)$_1$ microdomains (Figure 4.3b).

When the NPs are larger than the interstitial sites, it becomes more energetically favorable to expel the NPs to the surfaces to avoid entropic penalty (ΔS_{con}) and maximize the enthalpic gain ($\Delta H_{ligand/air}$) from covering the surface with a layer of NPs that have lower surface tension.[18, 24] At lower loading, the NPs preferentially locate on top of parallel P4VP(PDP)$_{1.7}$ cylinders at the air/polymer interface due to favorable ligand-polymer interactions, forming single 1-D NP chains. As the particle loading increases, localizing the NPs much larger than the interstitial sites requires compression of the comb blocks. Thus, the NPs cover the entire film surface and form 2-D lattices of NPs to lower the surface tension of the film similar to those observed at air/liquid interface and to thin films NP/polymer blends.[20, 29, 30] Similar phenomenon

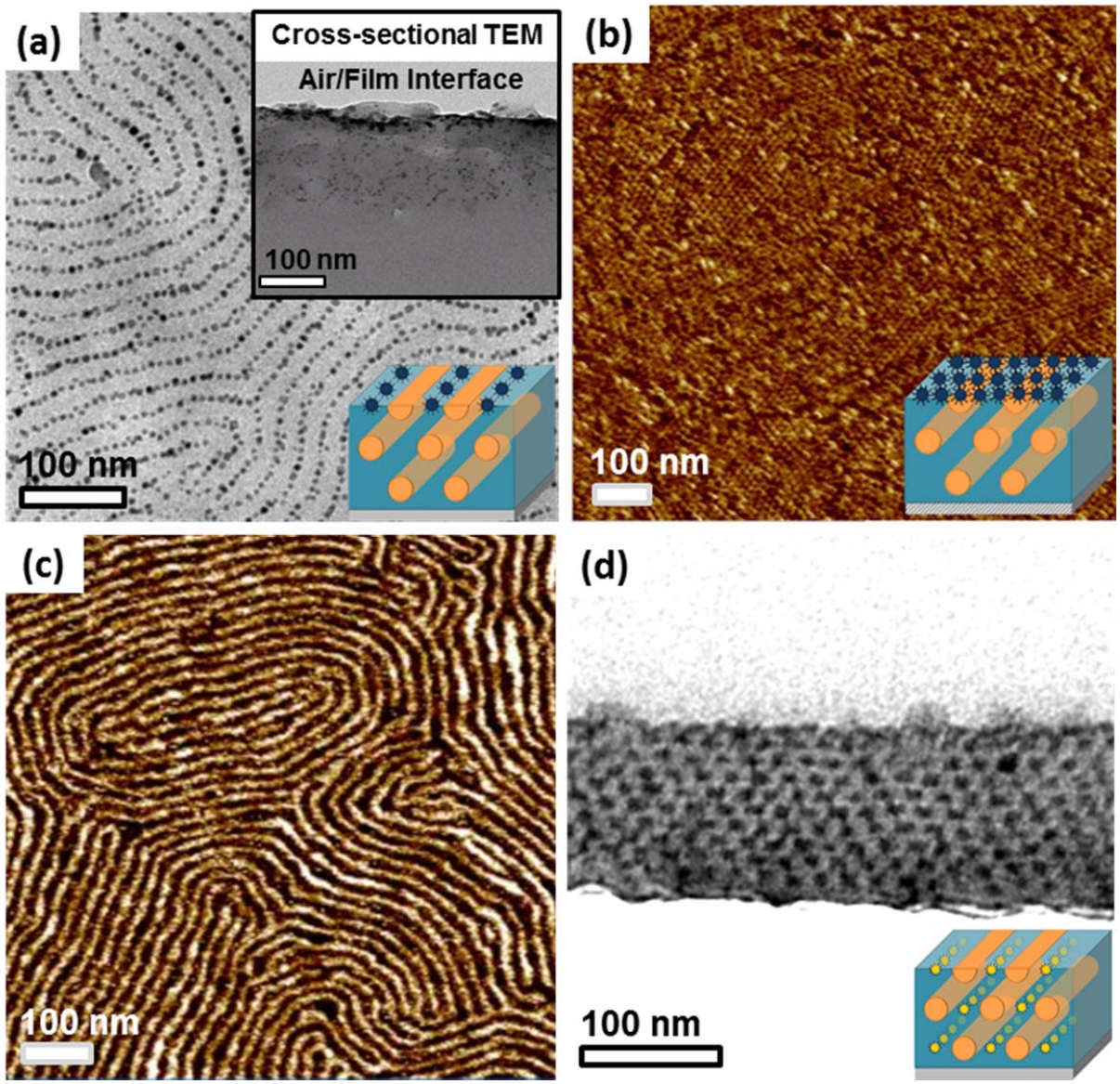

Figure 4.2. (a) Top-view TEM image of a ~180 nm thin film of PS(19 kDa)-*b*-P4VP(5.2 kDa)$(PDP)_{1.7}$ containing 9.3 nm PbS NPs at f = 5 vol %. The corresponding cross-sectional TEM image is shown in the inset. (b) AFM image showing 2-D arrays of 9.3 nm NPs formed at the air/polymer interface when f = 10 vol%. (c) and (d) show the AFM and cross-sectional TEM images of a similar film containing 7.4 nm PbS NPs at f = 5 vol%, respectively, showing hexagonally-packed 3D NP chains parallel to the surface.

is also observed in the lamellar counterpart as it is too entropically costly for the lamellar supramolecules with $d \sim 22$ nm to accommodate the 9.3 nm NPs in the interior of the film. In lamellar supramolecular thin films, however, the activation energy barrier for NP inter-domain diffusion remains large in the layered structure, making it energetically unfavorable for the NPs in the microdomains to diffuse to the air/polymer interface during solvent annealing. Hence, some 9.3 nm NPs are kinetically trapped in the P4VP(PDP)$_1$. These results confirm that the NPs are expelled to the surface when $d/a \geq 0.25$ in thin films of supramolecular nanocomposites. This threshold appears to be lower than that of NP/BCP blend ($d/a \geq 0.3$) and is indicative of the rigidity of the comb blocks.

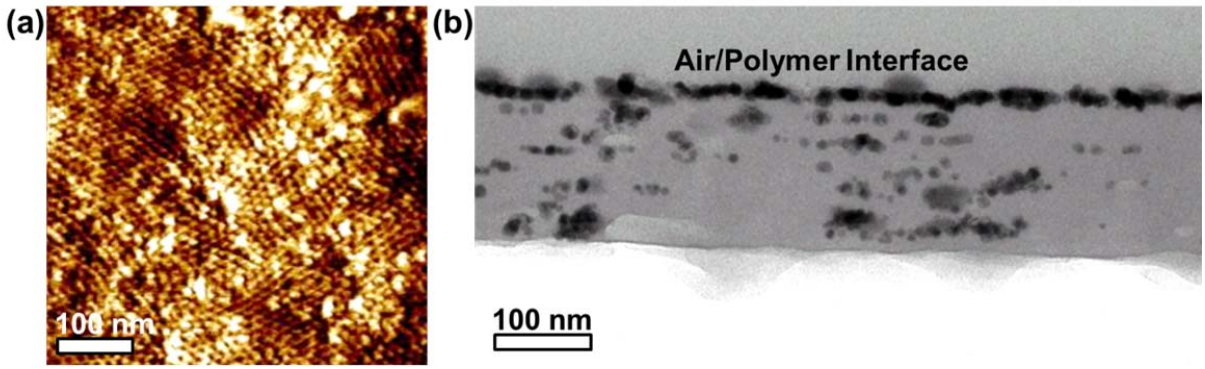

Figure 4.3. (a) AFM and (b) cross-sectional TEM images of a ~200 nm thin film of PS(40 kDa)-*b*-P4VP(5.6 kDa)(PDP)$_1$ containing 9.3 nm PbS NPs at $f = 10$ vol %. The majority of the 9.3 nm NPs reside at the air/polymer interface. Some NPs are kinetically trapped in the P4VP (PDP)$_1$ microdomains due to the layered structure provided by the lamellar morphology. Unlike that in the cylindrical supramolecular nanocomposite in Figure 4.2, the activation energy barrier for NP inter-domain diffusion remains large in parallel lamellar structure, making it energetically unfavorable for the NPs in the film to diffuse to the air/polymer interface during solvent annealing.

When the NP size was reduced to 5.7 nm, different NP assemblies were observed. At $d/a = 0.17$, the ~5.7 nm Au NPs not only segregate to the interstitial regions, but also disperse in the P4VP(PDP)$_{1.7}$ matrix. When $f = 1.5$ vol%, most of the ~5.7 nm NPs were seen localized at the interstitial sites, similar to the ~7.4 nm NPs, and dispersed in the cylindrical P4VP(PDP)$_{1.7}$ matrix (Figure 4.4a). When $f = 3$ vol%, the NPs formed 3-D connected and distorted rectangular networks (Figure 4.4b). However, the ~5.7 nm NPs are not homogeneously distributed in the middle of the P4VP(PDP)$_{1.7}$ matrix. In some regions, the NPs form a lamellae-like morphology with a tilt angle of ±55° relative to the substrate (Figure 4.4a). We speculate that once the NPs are dispersed in the cylindrical matrix, they will disrupt molecular packing of the P4VP(PDP)

comb block, lowering the chain rigidity and entropy associated with chain deformation. This effectively lowers the activation energy barrier for additional NPs to be solubilized into the region, resulting in the packing of the NPs in a certain direction with respect to the substrate. When the volume fraction of the NP increases, the entire P4VP(PDP)$_{1.7}$ matrix is occupied and the NPs are uniformly distributed in the middle of the comb blocks, leading to the formation of a distorted 3-D rectangular network of NPs in thin films to maximize S_{trans}.

These results show that the entropic contributions to the co-assemblies of NPs and cylindrical supramolecules in thin films can be tuned using NPs of different sizes. This allows us to precisely control the spatial organizations of not only a single kind but also two different species of inorganic NPs independently, opening opportunities to simultaneously obtain 2-D and 3-D NP assemblies in thin films. Figure 4.5a and 4.5b show the AFM image and cross-sectional TEM images of a ~200 nm thin film of nanocomposite containing ~7.4 nm Au NPs at f_{Au} = 2.5 vol% and ~9.0 nm PbSe NPs at f_{Au} = 7.5 vol%. The ~9.0 nm PbSe NPs resided at the air/polymer interface, forming 2-D hexagonally-packed NP 2-D arrays at the air/polymer interface (Figure 4.5a); while the ~7.4 nm Au NPs formed 3-D NP arrays inside the film shown in the cross-sectional TEM image (Figure 4.5b). Similarly, a mixture of ~5.7 nm Au and ~9.0 nm PbSe NPs can be co-assembled in thin films as shown in Figures 4.6a and 4.6b. Again, the ~9.0 nm PbSe NPs formed 2D NP arrays at the air/polymer interface and the Au NPs sequestered in the middle of the P4VP(PDP)$_{1.7}$ matrix formed distorted 3-D rectangular network of NPs. Au NPs first occupy the interstitial sites in the interior of the film as shown in the region where the NP loading is lower (Figure 4.6b). Thus, the observed morphologies are essentially additive NP assemblies of each nanocomposite based on single type of NP.

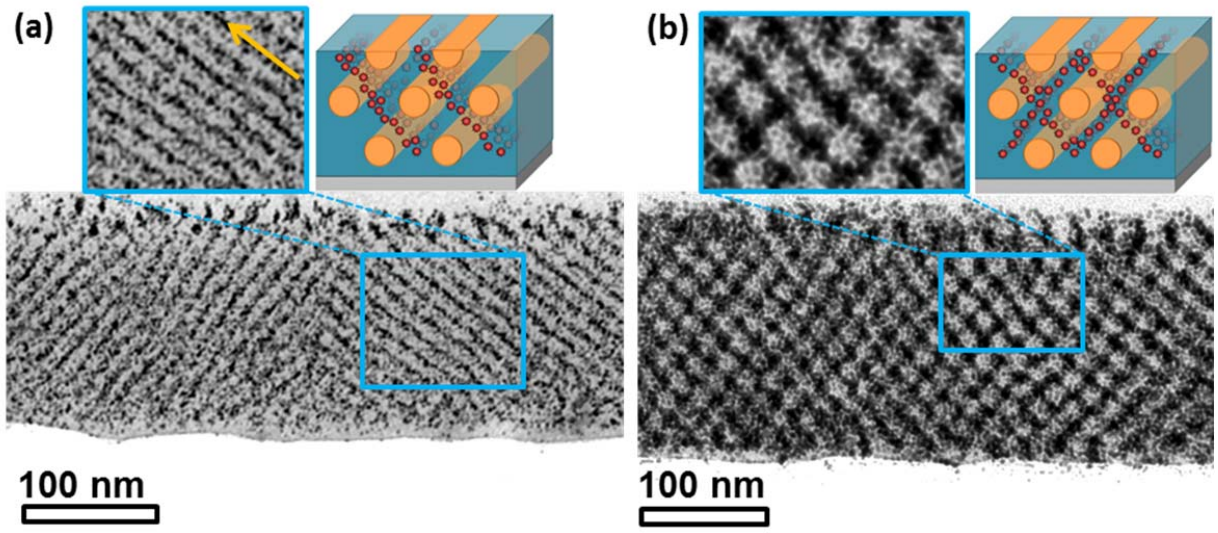

Figure 4.4. (a) and (b) show the cross-sectional TEM images of ~180 nm thin films of PS(19 kDa)-*b*-P4VP(5.2 kDa)$(PDP)_{1.7}$ containing 5.7 nm Au NPs at (a) f = 1.5 vol % and (b) f = 3 vol %. The ~5.7 nm NPs segregated to the interstitial sites and occupied the entire cylindrical matrix, forming 3-D NP network in thin film as f increased.

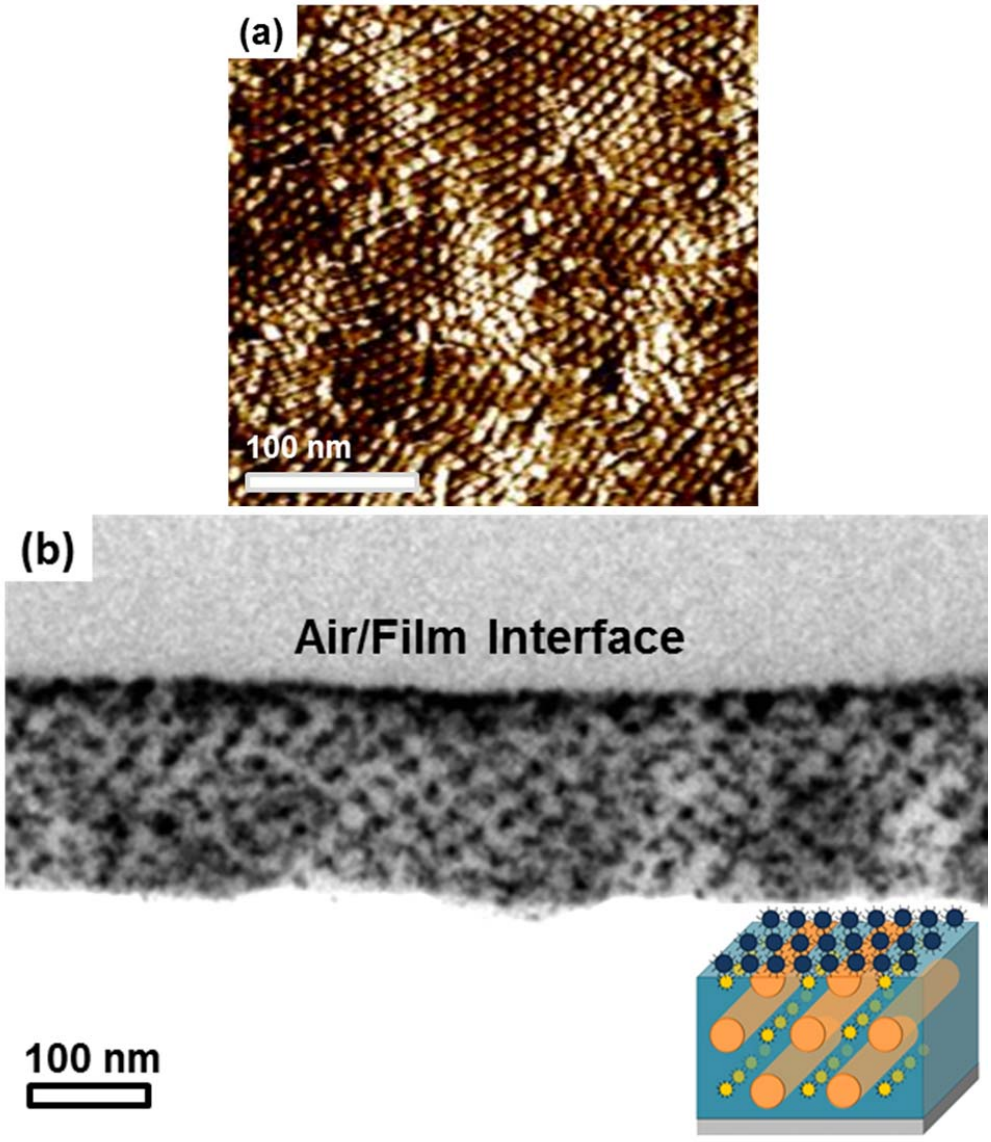

Figure 4.5. (a) and (b) show the AFM and cross-sectional TEM images of a ~200 nm thin film of PS(19 kDa)-*b*-P4VP(5.2 kDa)$(PDP)_{1.7}$ containing 2.5 vol% of ~7.4 nm Au and 7.5 vol% of ~9.0 nm PbSe NPs. The hybrid arrays of NPs are composed of 2D lattice of ~9.0 nm PbSe NPs on the surface and 3D hexagonal lattice of ~7.4 nm Au NPs chains in the interior of the film.

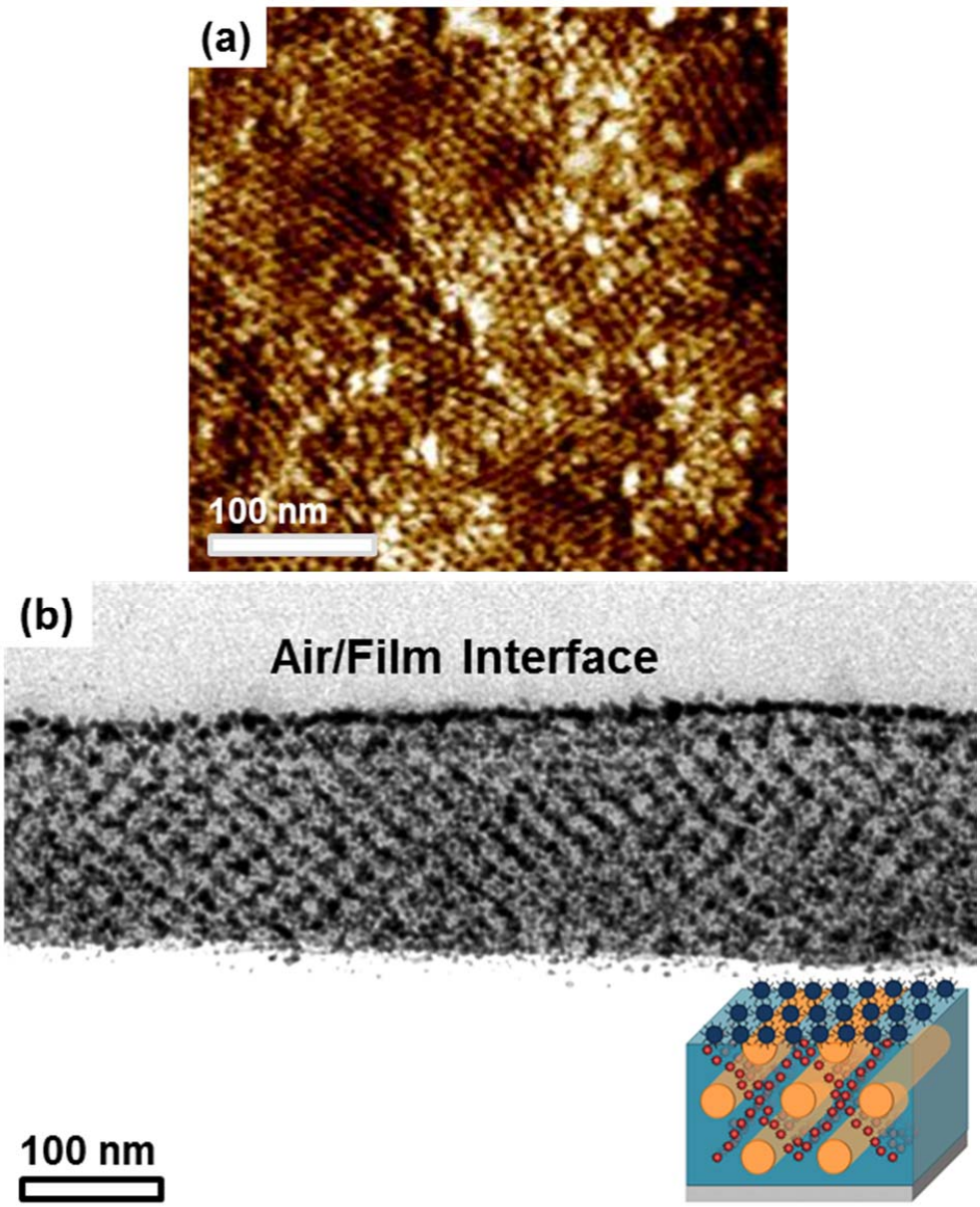

Figure 4.6. (a) and (b) show the AFM and cross-sectional TEM images of a ~200 nm thin film of PS(19 kDa)-*b*-P4VP(5.2 kDa)$(PDP)_{1.7}$ containing 2.5 vol% of ~5.7 nm Au and 7.5 vol% of ~9.0 nm PbSe NPs. The morphology is the superposition of ~5.7 nm Au and ~9.3 nm PbS NP assemblies.

Similar results were observed in the nanocomposite thin films containing both ~7.4 nm Au and ~5.5 nm PbS NPs (Figures 4.7). All the NPs were sequestered in the film interior and no

surface aggregation of NP was observed. Based on the experimental results and qualitative understanding of the thermodynamic of the supramolecular nanocomposite thin films, it is reasonable to speculate that 7.4 nm NPs should preferentially occupy the interstitial sites. Once the interstitial sites are occupied, 5.5 nm NPs should mainly distribute in the matrix. This could lead to hierarchical assemblies of two different particles with high spatial precision. When f_{Au} = f_{PbS} = 2.5 vol%, NPs preferentially filled up the interstitial regions (Figure 4.7a). Energy dispersive X-ray analysis (EDX) was used to map the NP spatial distribution, but could only confirm the presence of both Au and PbS NP in thin films due to the low signal (Figure 4.8). Based on the TEM images, the NPs dispersed in the matrix appear to be the small 5.5 nm NPs. As f_{PbS} increased to 5 vol% with f_{Au} fixed (2.5 vol%), there were more NPs, presumably the smaller 5.5 nm NPs, in the P4VP(PDP)$_{1.7}$ matrix that formed distorted 3-D rectangular network of NPs (Figure 4.7b). This speculation is further backed up by the GISAXS measurements on a series of PS(19 kDa)-*b*-P4VP(5.2 kDa)(PDP)$_{1.7}$ supramolecular thin films containing fixed amount of 7.4 nm Au (2.5 vol%) but different volume fractions of 5.5 nm PbS NPs (Figure 4.9). In the GISAXS patterns, the Bragg spots corresponding to the hexagonally packed Au NP chains in the film are clearly observed when $f_{Au} > f_{PbS}$. As f_{PbS} increases, the intensity of these Bragg peaks becomes weaker and smeared as the smaller PbS NPs packed in the P4VP(PDP)$_{1.7}$ matrix begin to contribute more to the scattering intensity. The results indirectly indicate that the majority of the 5.5 nm PbS NPs are not located in the interstitial sites where the 7.4 nm Au NPs reside. While present studies showed some promises, further optimization of polydispersity in NP size is needed to improve selectivity to obtain ideal assemblies as schematically shown in Figure 4.7. Furthermore, we do see great needs to perform theoretical studies to provide useful guidance.

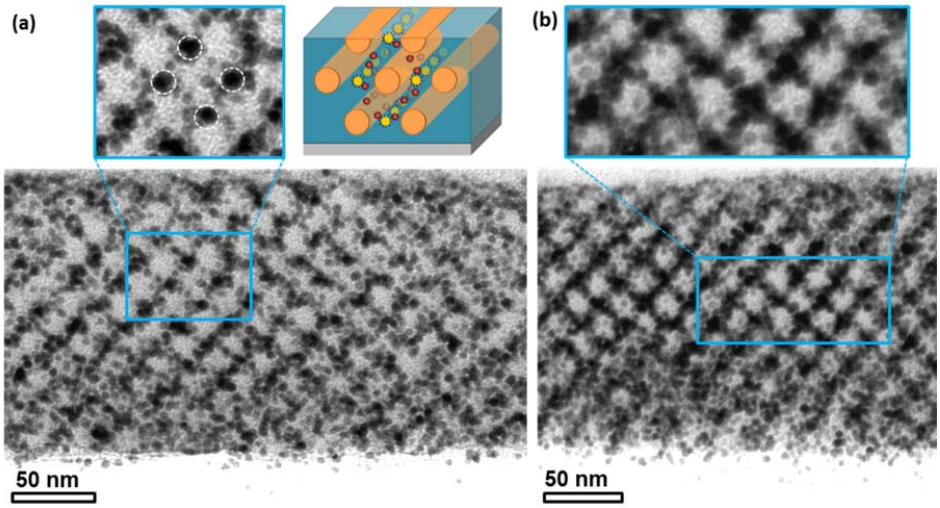

Figure 4.7. Cross-sectional TEM images of ~200 nm thin films of PS(19 kDa)-*b*-P4VP(5.2 kDa)(PDP)$_{1.7}$ containing 2.5 vol% of ~7.4 nm Au and (a) 2.5 vol% and (b) 5 vol% of ~5.5 nm

PbS NPs, respectively. The Au and PbS NPs predominantly located in the interstitial sites and the smaller PbS NPs began to occupy the entire P4VP(PDP)$_{1.7}$ matrix as f_{PbS} increased from 2.5 to 5 vol%

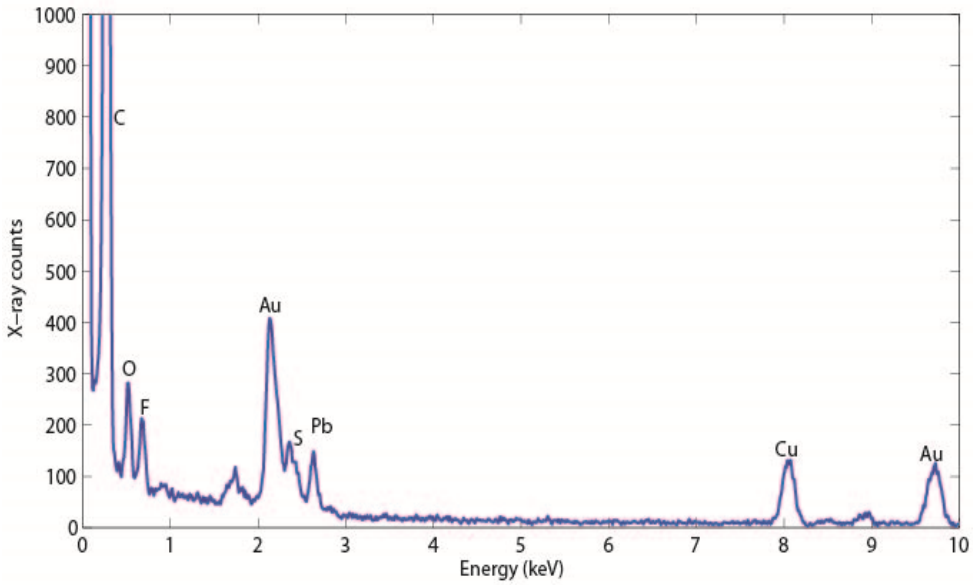

Figure 4.8. Energy Dispersive X-ray (EDX) spectrum of the PS(19 kDa)-*b*-P4VP(5.2 kDa)(PDP)$_{1.7}$ supramolecular thin film containing 2.5 vol% of ~7.4 nm Au NPs and 5 vol% of ~5.5 nm PbS NPs. The results suggest that both Au and PbS NPs are present in the P4VP (PDP)$_{1.7}$ matrix.

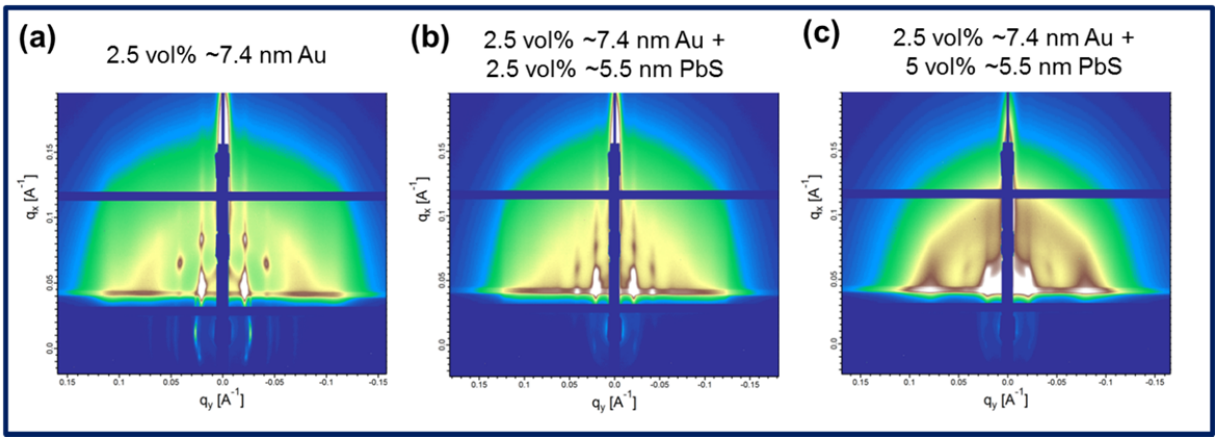

Figure 4.9. GISAXS patterns of three PS(19 kDa)-*b*-P4VP(5.2 kDa)(PDP)$_{1.7}$ supramolecular thin films containing (a) only 2.5 vol% of 7.4 nm Au, (b) 2.5 vol% of 7.4 nm Au and 2.5 vol% of 5.5 nm PbS, and (c) 2.5 vol% of 7.4 nm Au and 5 vol% of 5.5 nm PbS NPs, respectively. The Bragg spots corresponding to the hexagonally packed Au NP chains in the film are clearly

observed when $f_{Au} > f_{PbS}$. As f_{PbS} increases, the intensity of these Bragg peaks becomes weaker and smeared as the smaller PbS NPs packed in the P4VP(PDP)$_{1.7}$ matrix begin to contribute more to the scattering intensity. The results indirectly indicate that the majority of the 5.5 nm PbS NPs are not located in the interstitial sites where the 7.4 nm Au NPs reside.

§ 4.3 Conclusion

In summary, we conducted a systematic study on the effect of NP size (*d/a* ratio) on the NP assemblies in thin films of cylindrical nanocomposites and assess entropic contribution to the phase behavior of cylindrical nanocomposites in thin films. The observations suggest that the rigid comb blocks in the BCP-based supramolecules are sensitive to the chain deformation upon NP incorporation, allowing us to generate 1-D chains, 2-D lattices, and 3-D arrays and networks of NPs in thin films regardless of the chemical composition of the NPs. This gives us a useful tool to achieve co-assemblies of NP mixtures with controlled spatial organization of the hybrid arrays of NPs in thin films, which may provide a platform for one to systematically investigate their unique physical properties for plasmonic, energy storage, energy harvesting, electronic, and memory storage devices.

§ 4.4 Experimental section

4.4.1 Nanoparticle synthesis

The Au NPs were synthesized using the method reported by Peng *et al*.[31] The PbS NPs were synthesized using the method reported by Cademartiri *et al*.[32] The PbSe NPs were synthesized using the method reported by Liu *et al*.[33]

4.4.2 Sample preparation

PS(19,000)-*b*-P4VP(5,200) (PDI = 1.09) and PS(40,000)-*b*-P4VP(5,600) (PDI = 1.10) were purchased from Polymer Source, Inc. 3-*n*-pentadecylphenol (95%) was purchased from Acros. Chloroform was purchased from Fisher. All chemicals were used as received. Blends of supramolecules and nanoparticles were prepared as described previously. Thin films were prepared by spin-coating the mixed solutions onto silicon wafers or polystyrene brush modified silicon wafer at spinning speeds ranging from 1000 to 3000 rpm. Sample thicknesses were measured using a Filmetrics F20 interferometer. For solvent annealing, samples were annealed using 300 μL of $CHCl_3$ injected inside a 250 mL top-capped jar at 22.5°C. Once the film thickness of the nanocomposite thin film reached 145-150% of its original thickness, the jar was opened and the $CHCl_3$ vapor inside the jar was allowed to freely evaporate.

4.4.3 Atomic force microscopy

Atomic force microscopy was performed on a Veeco Dimension 3100 with a Nanoscope III controller and a Quadrex extension box. The spring constant of the cantilever was 10 − 130 N m^{-1} with a resonant frequency in the range of 300–500 kHz. The set point for auto tune was ~1.5 V. The set-point amplitude was 90% of the free vibration value.

4.4.4 Transmission electron microscopy

PS-*b*-P4VP(PDP)$_r$ thin films were spun cast on polystyrene-coated sodium chloride (NaCl) disks in a manner similar to those on silicon substrates. After solvent annealing, films were floated off the substrate onto a pool of water. Thin films were retrieved with carbon film coated copper grids. The top-view TEM images were collected on a FEI Tecnai 12 transmission electron microscope at an accelerating voltage of 120 kV. To prepare the cross-section of a nanocomposite thin film, the sample was first prepared on NaCl disk. Then, the thin film was floated off from the substrate on the surface of a pool of water. An epoxy block (Araldite 502, Electron Microscopy Sciences) was used to catch the film such that the sample is on top of the epoxy block with the air-polymer interface in contact with the top of the epoxy block. The epoxy along with the sample were cured at 60°C for at least 4 hours to ensure good contact between the epoxy and the nanocomposite thin film. Thin sections, ~60 nm in thickness, were microtomed using an RMC MT-X Ultramicrotome (Boeckler Instruments) and picked up on copper TEM grids on top of water. Again, the cross-sectional TEM images were collected using a FEI Tecnai 12 transmission electron microscope at an accelerating voltage of 120 kV.

4.4.5 Grazing incidence small angle X-ray scattering

GISAXS experimental measurements were made at beamline 7.3.3 at the ALS in Lawrence Berkeley National Laboratory and at beamline 8-ID-E the APS in Argonne National Laboratory. X-ray wavelengths of 1.687 Å and 1.240 Å were used at APS, and ALS, respectively. The incident angle was fixed to be 0.2°. The scattering intensity distribution was captured by a Pilatus 1M detector at ALS and APS. The intensities (I) are plotted with respect to q, where $q = (4\pi/\lambda) \sin(\theta/2)$, λ is the wavelength of the incident X-ray beam, and θ is the scattering angle.

4.4.6 Energy Dispersive Spectroscopy

EDX measurements were recorded on a FEI monochromated F20 UT Tecnai instrument operated at 200 kV with a field emission gun, Gatan Enfina electron spectrometer and EDAX EDX detector.

Chapter 5
Assembly Kinetics in Supramolecular Nanocomposite Thin Films during Solvent Annealing

Functional nanocomposites containing nanoparticles of different chemical compositions may exhibit new properties and are in demand to meet the growing material needs for advanced technology. To this end, it is imperative to simultaneously achieve structural control over multiple length scales and to develop rapid, scalable fabrication to limit degradation of nanoparticle properties due to exposure to processing environment and for compatibility with nanomanufacturing. In previous chapters, the thermodynamics in the co-assembly of supramolecules and NPs has been thoroughly studied, which enables structural tailoring of the multidimensional nanoparticle assembly in supramolecular nanocomposites. To realize the supramolecular approach for practical applications, the processing of the nanocomposite needs to be optimized by understanding the kinetic pathway of the co-assembly. Here we show that the assembly kinetics of supramolecular nanocomposite in thin films is governed by the energetic cost arising from the excess interfacial area due to defects, the chain mobility, and the activation energy for inter-domain diffusion. By controlling the solvent and small molecule fractions in the film during solvent annealing, the assembly kinetics and pathway can be precisely tailored to produce hierarchically structured thin films of supramolecular nanocomposites in minutes. The mechanism shown is applicable to supramolecules with a wide range of molecular weights and it provides fundamental guidance for the design of manufacture-friendly processing techniques for scalable nanofabrication of nanocomposite thin films using draw coating, ink-jet printing, and roll-to-roll processing.

§ 5.1 Introduction

Developments in colloidal particle synthesis enable one to engineer nanoparticles (NPs) with controlled size, shape, and chemical composition.[1-7] Numerous studies have demonstrated the significant impact of NP-based materials in life sciences, microelectronics, light manipulation, energy harvesting and storage.[8-10] Co-assemblies of NPs and organic building blocks clearly hold promise for generating nanocomposites using different elements on the periodic table that combine the advantages of both families of building blocks.[11-15] To fulfill these promises, at least two requirements must be satisfied. One is to control the spatial arrangement of NPs spanning multiple length scales in a reproducible manner, so as to modulate inter-particle coupling and the collective properties of nanocomposites.[16-21] The other is to understand and manipulate the kinetics of the assembly process to ensure compatibility with existing fabrication infrastructures. To be relevant, the fabrication process must be rapid, completed within a few minutes to minimize degradation of NP properties due to exposure to the processing environment and for compatibility with nanomanufacturing.[22]

In comparison to many current approaches such as DNA and controlled solvent evaporation, block copolymers (BCPs) provide scalable platforms to obtain nanoscopic organization of NPs, but require favorable NP-polymer interactions to achieve NP dispersion, and it remains difficult to control inter-particle ordering within BCP microdomains.[14,23-25]

Additionally, their self-assembly processes typically require tens of minutes or hours to complete and can lead to degradation of inherent optoelectronic properties of the NPs. Thermal annealing alone or in conjunction with solvent annealing has been used to accelerate the assembly process, but is not suitable for temperature sensitive NPs.[26,27]

BCP-based supramolecules are constructed by non-covalently attaching small molecules to polymer side chains. The presence of small molecules eliminates the need to modify either the NP ligand or polymer for NP incorporation and improve inter-particle ordering within BCP microdomains. 1-, 2- and 3-D NP arrays can be obtained in thin films of supramolecular nanocomposites via solvent annealing for a range of NPs or NP mixtures.[17,19,20,28,29] Kinetically, the presence of small molecules also provides unique opportunities to manipulate the energy landscape of the assembly process and to accelerate the assembly kinetics so that inherent properties of NPs can be maintained and continuous thin film processing techniques can be implemented for the device fabrication. However, the supramolecular nanocomposite has at least 5 components during solvent annealing, making it extremely challenging to manipulate the assembly process.

Here, we systematically analyzed the thermodynamics and kinetics of self-assembly in thin films of supramolecular nanocomposite upon exposure to solvent vapor. The assembly kinetics depends on the energetic penalty of the excess interfacial area due to defects, the chain mobility, and the activation energy for inter-domain diffusion. It is the solvent content in the film, f_s, during solvent annealing, rather than the swelling rate, which governs the ordering. By controlling f_s and the amount of unbound small molecules in the nanocomposite during solvent annealing, a marked acceleration in the assembly process can be achieved to generate hierarchically structured nanocomposite thin films in minutes. Moreover, the amount of solvent required for optimized ordered structure in the film was found to be related to the molecular weight of the supramolecule following a power law. In addition, by simply tailoring the solvent removal rate during the annealing process, the 3-D structure of the nanocomposite can be precisely engineered. These studies provide key insights for manipulating the kinetics as well as the morphology of the NP assembly in nanocomposites, enabling the scalable fabrication of functional thin films with tunable properties via manufacturing-friendly processing techniques such as draw coating, ink-jet printing, and roll-to-roll processing.

§ 5.2 Results and Discussion

The supramolecular nanocomposite is a blend of ~5 nm Au NPs capped with 1-dodecanethiol and the supramolecule, PS(19 kDa)-*b*-P4VP(5.6 kDa)$(PDP)_{1.7}$, prepared by hydrogen-bonding 3-pentadecylphenol (PDP) to the 4VP units of a BCP, polystyrene-*b*-poly-4-vinylpyridine (PS-*b*-P4VP) at a PDP:4VP ratio of 1.7.[30] In thin film after solvent annealing using chloroform, it forms hexagonally-packed 3-D NP arrays where the Au NPs are selectively located at the interstitial sites in the P4VP(PDP) matrix (Figure 5.1).[29] During solvent annealing,

there are 5 components in the film: BCP, NP, PDP small molecule, 1-dodecanethiol ligand, and $CHCl_3$ solvent molecule. To fully understand the kinetics of the NP assemblies in supramolecular nanocomposites during solvent annealing, we systematically studied the effects of the solvent content, small molecule loading, and the molecular weight of the BCP-based supramolecule on the kinetic pathway of the co-assembly of NPs and supramolecules in thin films, which will be discussed in detail in the following sections.

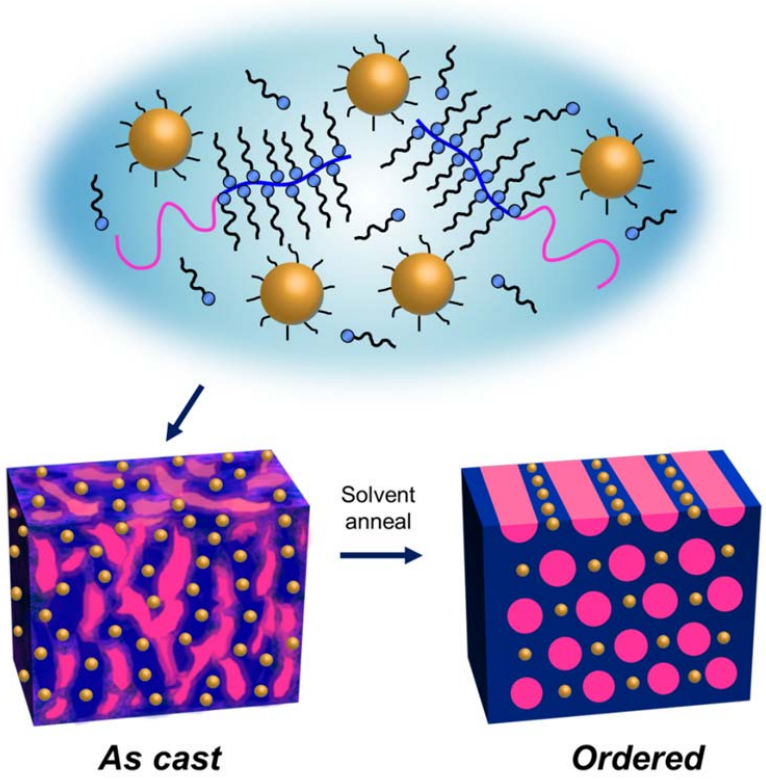

Figure 5.1. Schematic drawing of the morphologies in as-cast and ordered nanocomposite films post-solvent annealing. The supramolecular nanocomposite contains cylindrical BCP-based supramolecules and NPs. The as-cast film has small grains of poorly-ordered microdomains. After solvent annealing, the hierarchically ordered nanocomposite thin film has 3-D NP arrays packed in a distorted hexagonal lattice parallel to the surface.

5.2.1 Effect of solvent volume fraction on the assembly kinetics

Experimentally, the kinetic pathway was first captured by observing the morphological evolvement in the supramolecular nanocomposite thin film under different solvent annealing conditions. Figure 5.2 shows the AFM images of the ~70 nm films containing PS(19 kDa)-*b*-

P4VP(5.6 kDa)$(PDP)_{1.7}$ and 0.5 vol% of ~5 nm Au NPs solvent annealed using three different annealing profiles. All three films were annealed for 15 minutes and f_s was determined by monitoring the film thickness *in situ* using an interferometer. After spin casting, nanoscopic

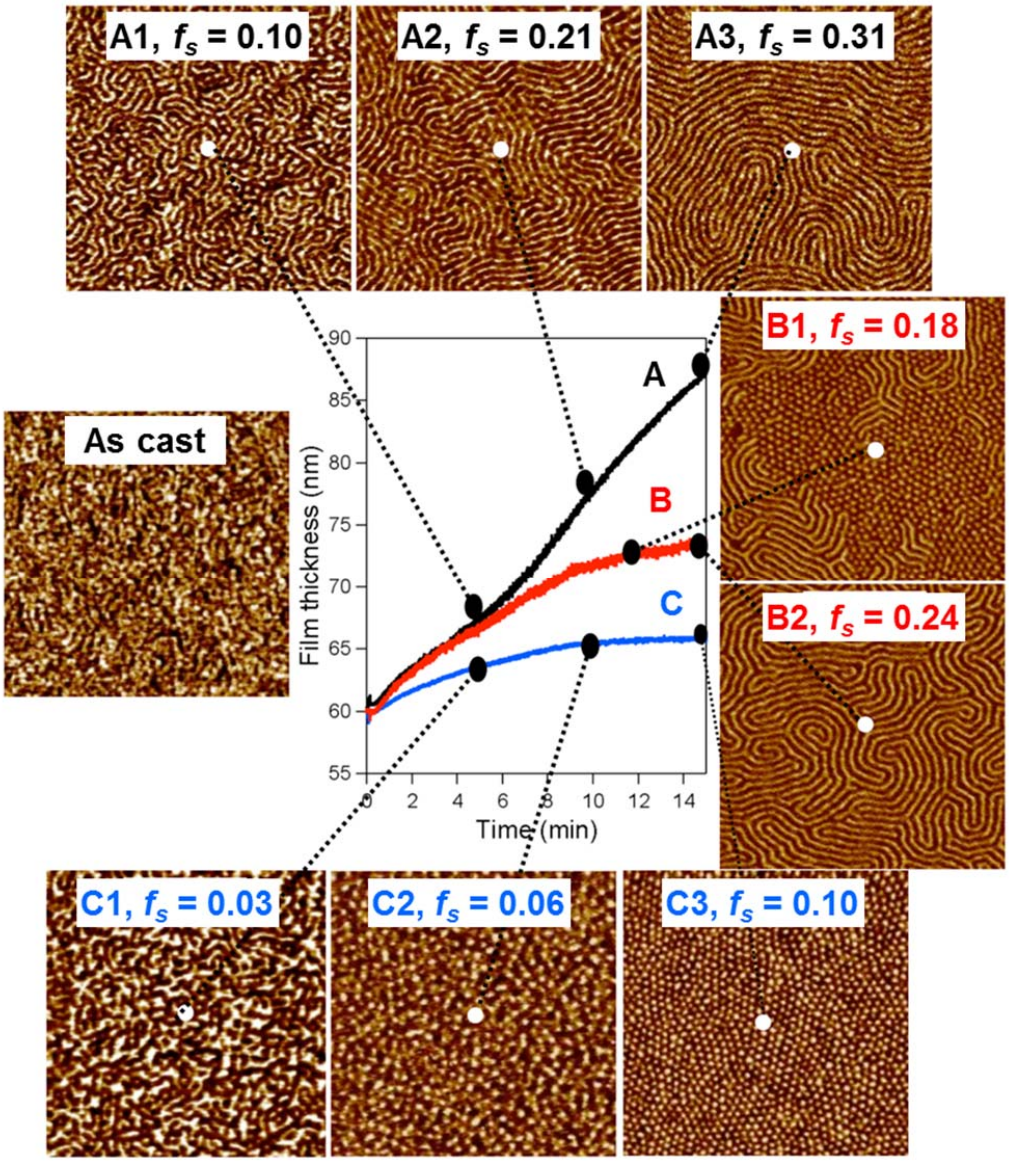

Figure 5.2. Surface morphology of supramolecular nanocomposite thin film as a function of f_s. AFM phase images of ~70 nm thin films of a blend of PS(19 kDa)-*b*-P4VP(5.6 kDa)$(PDP)_{1.7}$ and 0.5 vol% of ~5 nm Au NPs that were solvent annealed under chloroform vapor using three different annealing profiles. The film thickness profile during solvent annealing is shown in the panel at the center. The morphology of the film was characterized *ex situ* at different f_s under solvent treatments A, B, and C. The AFM images are 1 μm x 1 μm scans.

features with poor lateral order were observed on the film surface. Under solvent treatment A, the supramolecules formed ordered in-plane cylindrical morphology at f_s = 0.21. Further increasing the annealing time led to larger grain size. A different kinetic pathway was observed under solvent treatment B where a mixture of cylinders oriented normal and parallel to the surface coexisted in the film. The growth of the parallel cylindrical domains dominated at f_s = 0.24 and homogeneous morphology was observed across the surface. Unlike that observed under solvent treatments A and B, only perpendicular cylinders were seen in the early stage of morphological development under solvent treatment C. When the annealing was terminated at f_s = 0.10, the ordering of the hexagonally packed perpendicular cylinders became optimized and the NPs formed 2-D hexagonal grids in the P4VP(PDP)$_{1.7}$ matrix at the air/polymer interface (Figure A.4.1). The *ex situ* AFM results clearly demonstrate that the orientation of the microdomain/NP arrays is dependent on f_s. To further confirm the correlation between f_s and the kinetic pathway of the co-assembly, we next characterized the 3-D morphology of the nanocomposite thin film annealed under solvent treatment A.

Figure 5.3b-e show the cross-sectional TEM images of the films quenched at f_s = 0, 0.13, 0.23, and 0.31, respectively. The diffusion coefficient of $CHCl_3$ in polymer is ~10^{-12} m^2/s.[31,32] The solvent molecules are distributed uniformly in the film for the timescale considered here. The as-spun film was microphase-separated with a poorly ordered structure (Figure 5.3b). The excess interface resulting from defects resulted in a sufficient thermodynamic driving force to form ordered nanostructure, provided the components are mobile. Initially, a nanostructure normal to the film surface developed at f_s = 0.13 (Figure 5.3c). This can be attributed to the solvent gradient field normal to the surface during spin casting. Upon further annealing at f_s = 0.23, the supramolecule locally arranged itself and formed distorted hexagonally packed cylinders oriented parallel to the surface and the NPs are ordered within the P4VP(PDP) matrix (Figure 5.3d).[33] With time, the grain size of the in-plane hexagonal lattice increased from the film surface, resulting in highly ordered hexagonally packed 3-D NP arrays parallel to the surface throughout the film (Figure 5.3e). The results in Figure 5.2 and 5.3 nicely capture the self-assembly pathway of supramolecular nanocomposites in thin films and can be described in terms of the thermodynamics and kinetics in a qualitative manner. Figure 5.4 shows the energy landscape of the assembly process for two solvent fractions $f_{s,\,low}$ and $f_{s,\,high}$. $G_{as\ cast}$ and $G_{ordered}$ refer to the overall energy of the as-cast film and that of the ordered one. Overall, the main driving force for the structural evolution, *i.e.*, the energy difference, ΔG, between the as-cast and ordered films, is to minimize the interfacial area at the defects. ΔG can be approximated as $\gamma \Delta A$, where γ is the interfacial energy between PS and P4VP(PDP)$_{1.7}$/NPs and ΔA is the interfacial area due to the defect. $\gamma = \frac{kT}{a^2}\sqrt{\frac{\chi_{eff}}{6}}$, and $\chi_{eff} = \chi_o(1 - f_s)$, where χ_{eff} and χ_o are the Flory-Huggins interaction parameters of the supramolecule with and without solvent, respectively.[34] As $f_{s,}$ increases, the energetic cost of defects and the thermodynamic driving force to form ordered structure decreases, and thus may lead to a lower assembly rate following the Arrhenius equation.

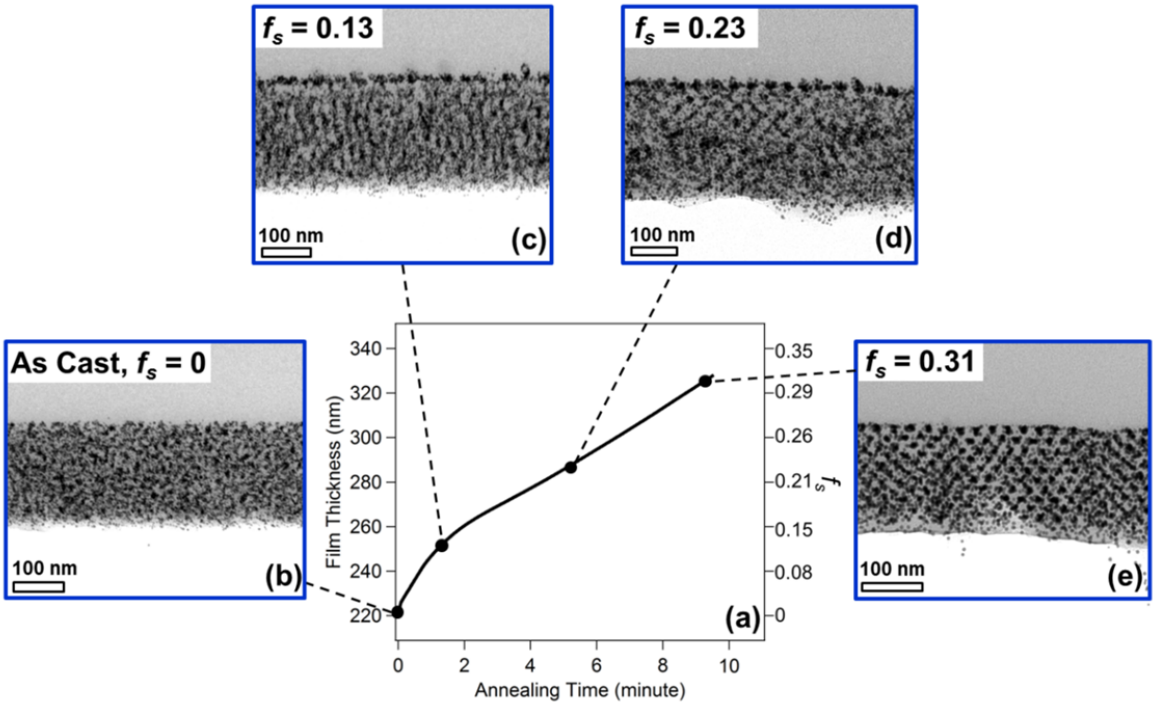

Figure 5.3. Structural evolvement of supramolecular nanocomposite thin film as a function of f_s. Cross-sectional TEM images of ~220 nm thin film of a blend of PS(19 kDa)-*b*-P4VP(5.6 kDa)$(PDP)_{1.7}$ and 3 vol% of ~5 nm Au NPs that has been solvent annealed under chloroform vapor at different f_s. The film thickness profile during solvent annealing is shown in (a). The film was characterized at f_s = (b) 0, (c) 0.13, (d) 0.23, and (e) 0.31, respectively.

Kinetically, the formation of the nanostructure requires the re-arrangement of material in the nanocomposite. The diffusion rate depends on the chain mobility and the energy barrier, ΔE_a, for the inter-domain diffusion. The presence of solvent lowers the T_g of the supramolecule, which is estimated to be 34.7, 13.4, and 0°C at f_s = 0.13, 0.23, and 0.31, respectively.[35] The chain mobility of the supramolecule increases as a function f_s. The diffusion constant of the supramolecular nanocomposite should be similar to that of supramolecule or BCP. At the interface between two blocks, a diffusing chain experiences a uniform potential when diffusing parallel to the interface but a periodic potential for perpendicular diffusion, resulting in an anisotropy in the diffusion coefficients parallel to the interface D_{para} and normal to the interface D_{perp}.[36-38] D_{perp} follows a hindered diffusion mechanism and is expressed as $D_{perp} \sim exp(-\Delta E_a)$. ΔE_a is proportional to χ_{eff} the enthalpic penalty for pulling one block through the other domain.[39] The anisotropic diffusion explains the assembly pathway observed in the cross-sectional TEM images in Figure 5.3. At low f_s, D_{para} is higher than D_{perp} due to the high χ_{eff} and the nanocomposite forms cylinders perpendicular to the surface. As f_s increases, χ_{eff} decreases, so the

inter-domain diffusion is less costly, allowing the supramolecule and NPs to rearrange and form ordered parallel cylindrical morphology.

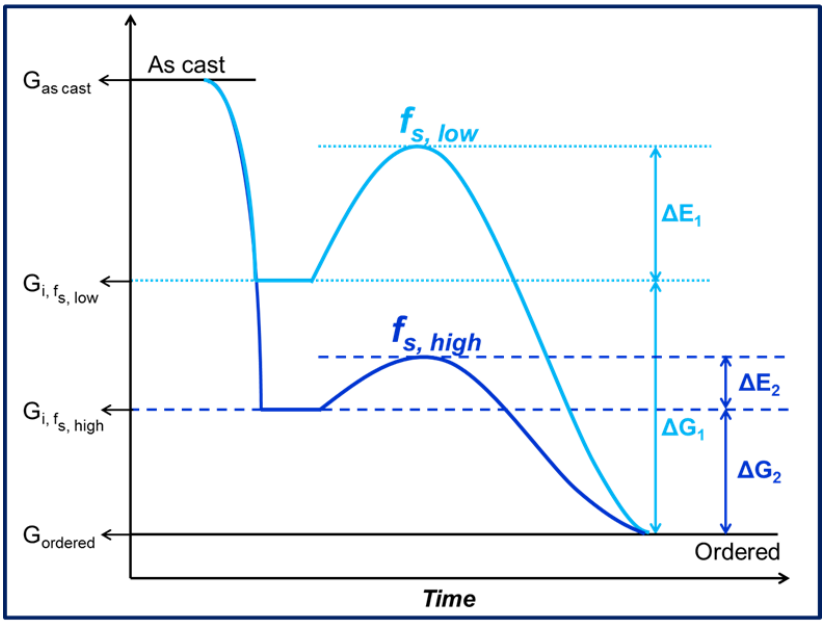

Figure 5.4. The free energy diagram that describes the assembly pathways of a supramolecular nanocomposite thin film during solvent annealing. The as-cast film has the largest value of free energy $G_{as\ cast}$ due to interfacial energy associated with defects. The energy difference between the as-cast and ordered states ΔG is the thermodynamic driving force of the assembly process. As the solvent enters the film, the free energy reduces since the solvent mediates energy cost of defects and is a function of f_s. ΔE corresponds to the activation energy barrier for the supramolecular nanocomposite to order.

Thus, the apparent assembly rate and the pathway in the supramolecular nanocomposite thin film reflect a balance between ΔG, the mobility of the supramolecules, and ΔE_a, all of which depend on f_s. Modulating f_s during solvent annealing enables control over the assembly kinetics and pathway in the system. Figure 5.5 shows the *in situ* GISAXS studies and the corresponding AFM data of~200 nm thin films of PS(19 kDa)-*b*-P4VP(5.6 kDa)$(PDP)_{1.7}$/5 nm Au NP blend that underwent three different solvent treatments. The experimental set-up of the in situ study is shown in Figure A.4.2. The ordering in the as-cast film was poor, as evidenced by the broad Bragg peak and the structure had an overall vertical alignment biased by the solvent field during spin casting. Upon exposure to the solvent under solvent treatment A where f_s was increased from 0-0.23 in 10 min, the GISAXS pattern A1 at f_s = 0.12 shows a diffraction ring from the nanostructure (Figure 5.5b). The corresponding AFM image shows the cylindrical microdomains with different orientations with respect to the interface. When f_s was between 0.13 and 0.23, there were two spots of increasing intensity along the first Bragg rod, indicating that the

cylindrical microdomains were beginning to align parallel to the surface. At f_s = 0.23, the scattering pattern corresponds to hexagonally-packed NP arrays oriented parallel to the surface. Under solvent treatment B where f_s was increased from 0 - 0.31 in 10 min, the film was allowed to reach a higher f_s. In GISAXS pattern B3 at f_s = 0.25 (Figure 5.5c), higher order peaks in the diffraction pattern are seen which shows the completion of the re-orientation of the cylindrical microdomains and the formation of distorted hexagonally packed NP arrays parallel to the surface. Further annealing (f_s = 0.31) led to a larger grain size of the in-plane morphology evidenced by a set of sharper Bragg diffraction peaks in the GISAXS pattern and the improved long-range order seen in the AFM image corresponding to B4. However, when 0.31 < f_s < 0.35 under solvent treatment C, the GISAXS patterns and the corresponding AFM images indicate that the ordered structure deteriorated and became disordered at high f_s (Figure 5.5d). When f_s = 0.4, the GISAXS pattern at C4 is dominated by the "correlation hole" effect and no clear structure factor features are observed.

(a)

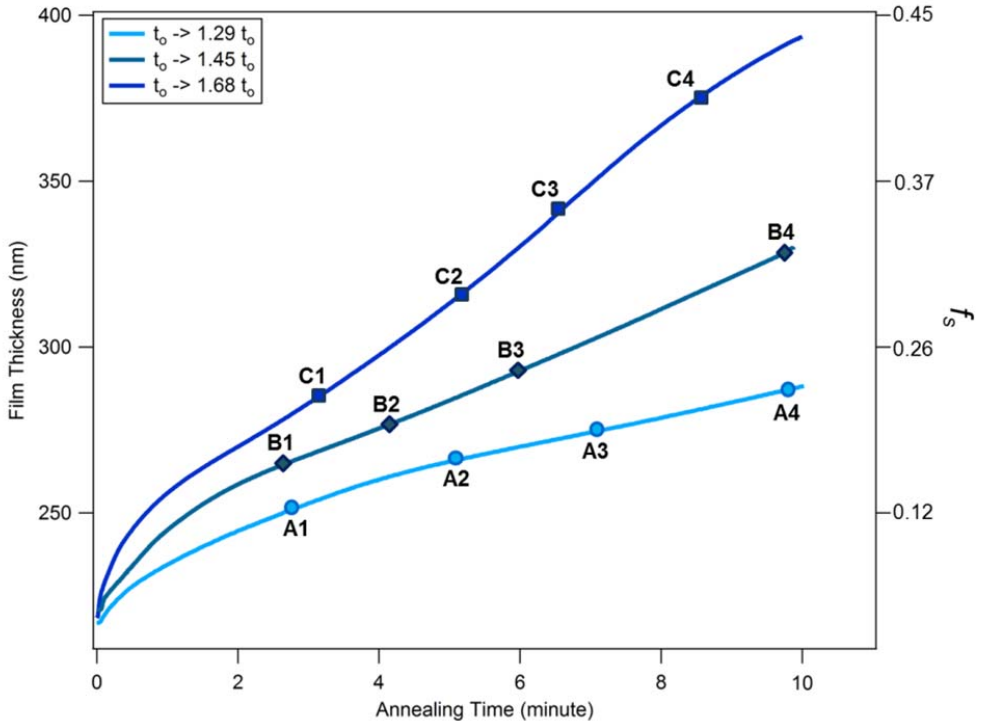

(b)

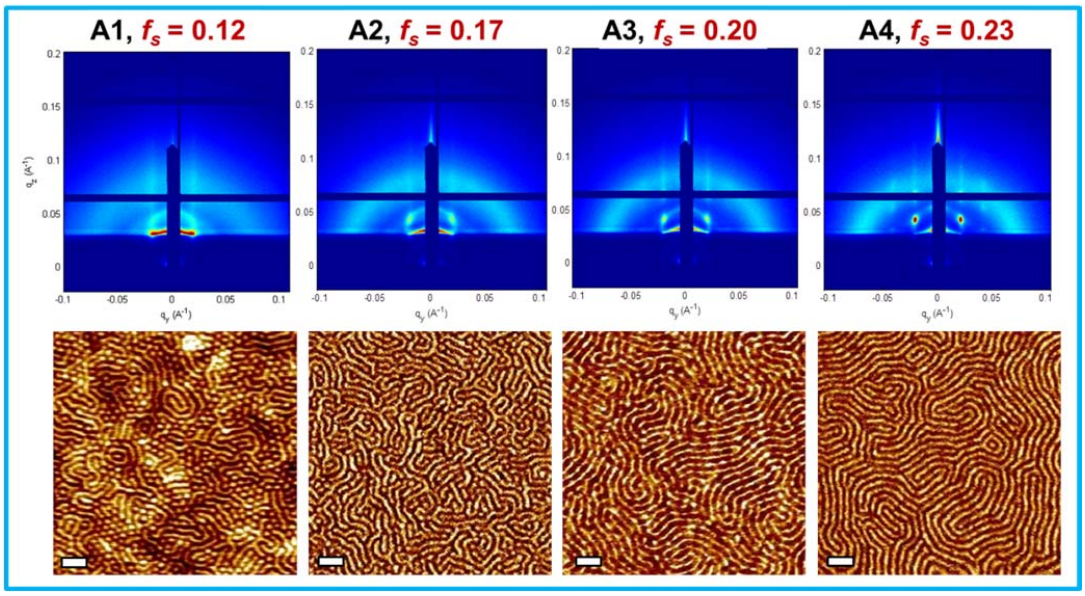
A1, f_s = 0.12
A2, f_s = 0.17
A3, f_s = 0.20
A4, f_s = 0.23

(c)

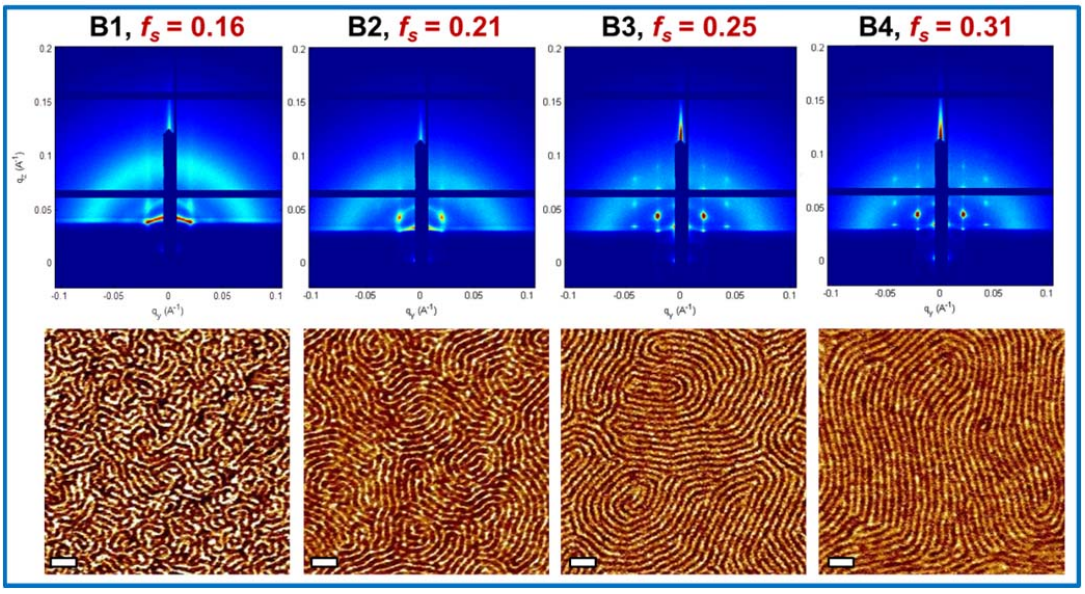
B1, f_s = 0.16
B2, f_s = 0.21
B3, f_s = 0.25
B4, f_s = 0.31

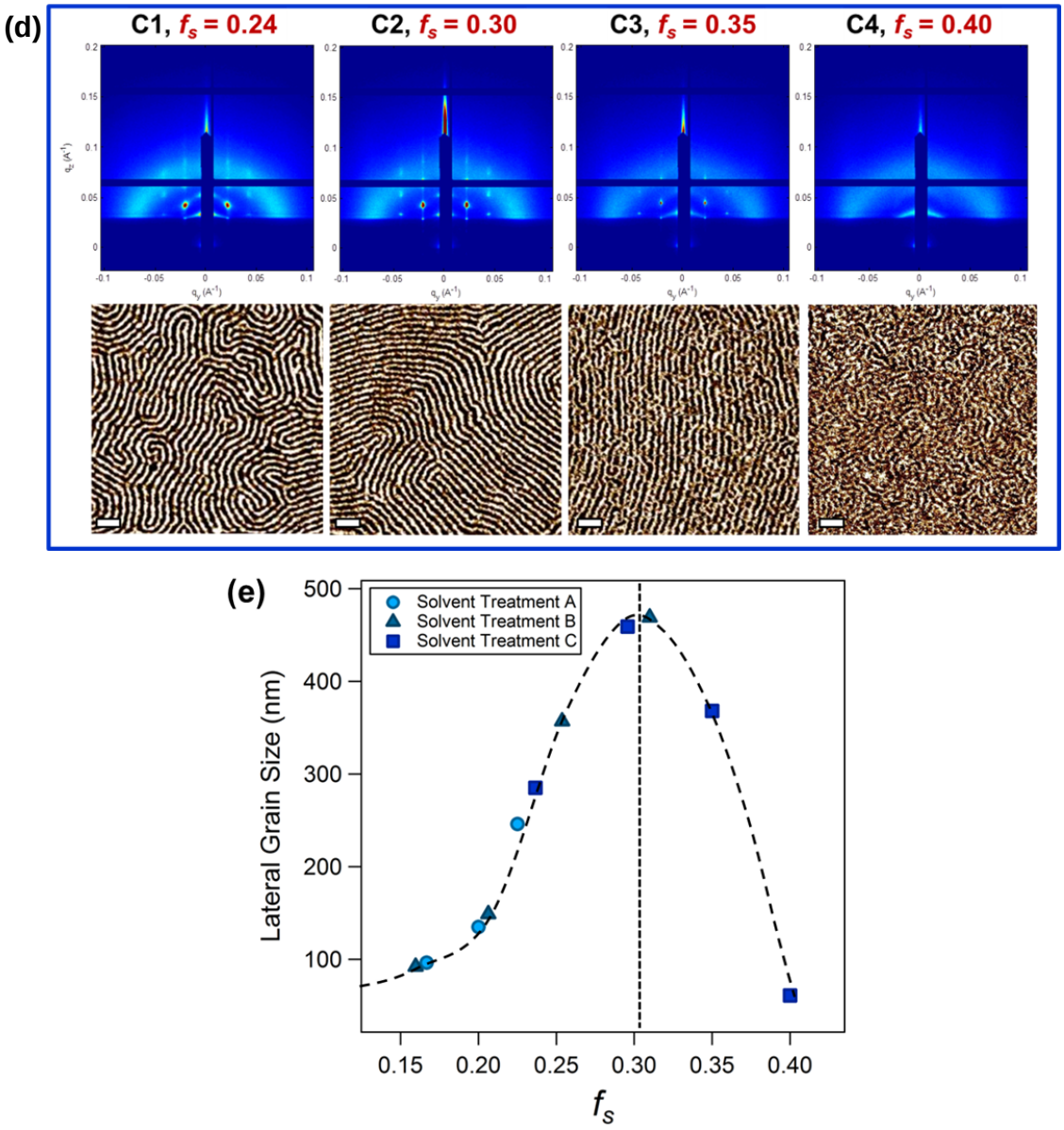

Figure 5.5. *In-situ* GISAXS studies on the assembly pathway and kinetics of supramolecular nanocomposite thin films. (a) Film thickness vs. time profiles of the ~220 nm thin films containing PS(19 kDa)-*b*-P4VP(5.6 kDa)$(PDP)_{1.7}$ supramolecules and 3 vol% of ~5 nm Au NPs annealed under different solvent treatments during *in situ* GISAXS measurements. Solvent treatments A, B, and C allowed the three nanocomposite thin films to reach f_s = 0.23, 0.31, and 0.40 in 10 minutes, respectively. The GISAXS patterns and the corresponding AFM phase images during solvent treatments A, B, and C at the points indicated in (a) are shown in panels (b), (c), and (d), respectively. (e) The plot of the grain size as a function of f_s, showing that the ordered nanostructure is optimized at f_s = 0.31 before undergoing order-disorder transition at f_s > 0.31. The dotted line is intended as a visual guide to further elucidate the trend in the grain size change. Scale bar = 100 nm.

At low f_s (e.g., f_s < 0.12), ΔG is large and so is ΔE_a. D_{perp} is lower than D_{para}, allowing only short-range diffusion along the interface to improve the perpendicular morphology at intermediate f_s (e.g., 0.12 < f_s < 0.23), the presence of solvent lowers the ΔE_a to make D_{perp} appreciable. As f_s approaches an optimal value, in this case f_s = 0.31, the nanocomposite orders rapidly. At high f_s (e.g., f_s > 0.31), ΔG decreases significantly and assemblies with high defect density or in disordered state were observed even though the increased chain diffusion and lowered ΔE_a should facilitate the defect annihilation. The lateral grain size for each nanocomposite thin film was estimated using the Scherrer equation and plotted in Figure 5.5e as a function of f_s. All results fall on one master curve and the largest grain size, ~ 0.47 μm, is obtained at f_s = 0.31.

In addition to f_s, the swelling rate is another parameter during the solvent treatments. A series of *in situ* GISAXS studies were conducted to reach a specific f_s at different swelling rates and the grain size was plotted against annealing time for each f_s (Figure 5.6a). The results show a

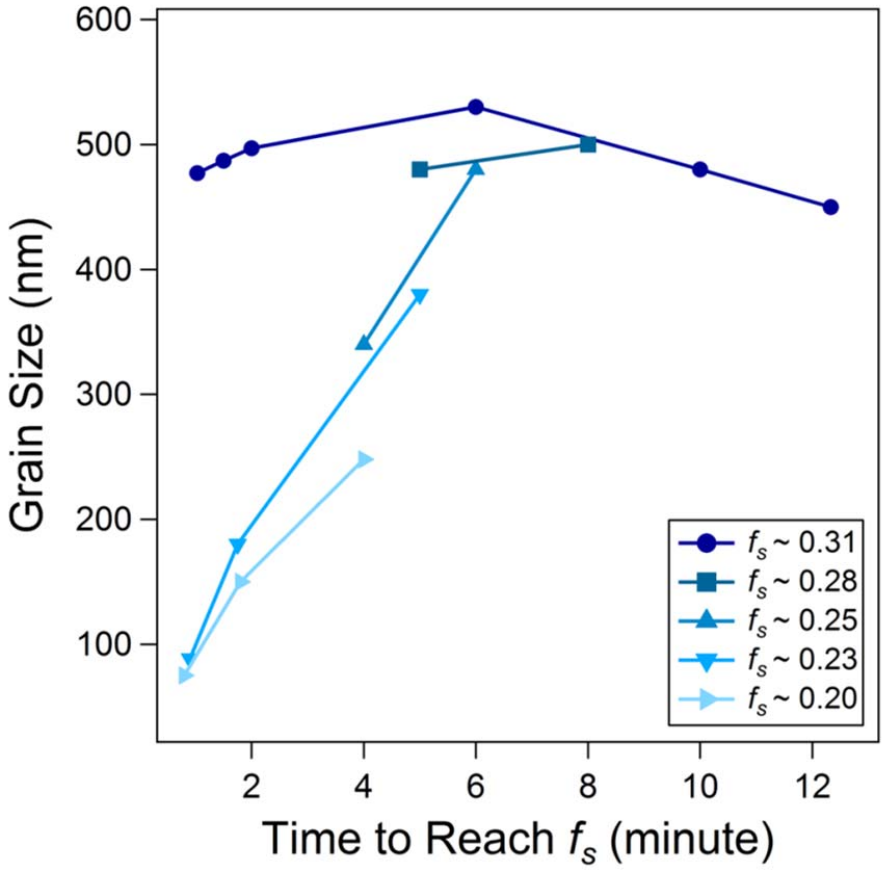

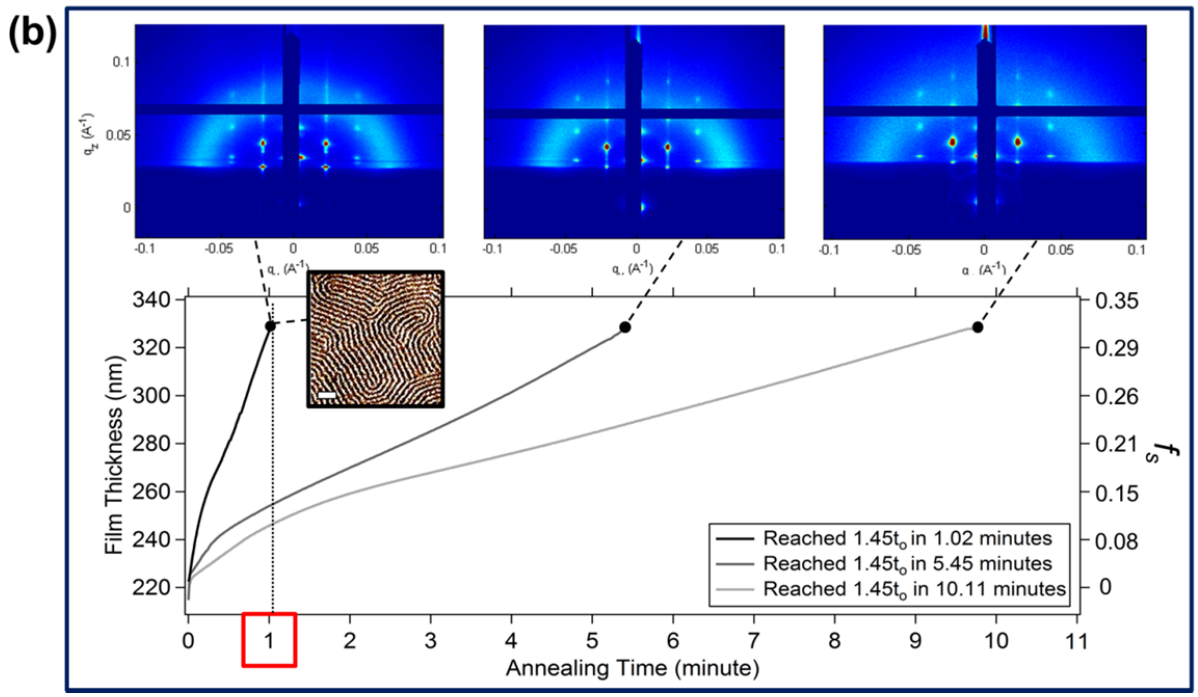

Figure 5.6. Effects of swelling rate on the assembly kinetics of supramolecular nanocomposite thin films. A series of *in situ* GISAXS studies were conducted on six identical ~220 nm PS(19 kDa)-*b*-P4VP(5.6 kDa)$(PDP)_{1.7}$ thin films containing 3 vol% of ~5 nm Au nanoparticles (a) The grain size of the nanostructure was plotted against the required annealing time to reach five different values of f_s. (b) The GISAXS patterns of three identical thin films solvent annealed with different different swelling rates. Hierarchically structured nanoparticle assemblies can be readily obtained in 1 minute. Scale bar = 100 nm.

time-f_s superposition phenomenon. The system needs longer annealing time to reach an ordered state at relatively low f_s as the assembly rate is facilitated by ΔG but limited by ΔE_a and chain mobility. Near the optimal f_s, the grain growth rate is very fast initially due to the dominant driving force but eventually experiences retardation as a result of the competition between the kinetic terms and ΔG. The results indicate that f_s determines the assembly rate and the solvent entry rate plays a minimal role in the assembly kinetics. Similar grain sizes of the optimized nanostructure were observed in the film that reached the same f_s at three different swelling rates during annealing (Figure 5.6b). Ordered films of hierarchically structured supramolecular nanocomposite can be readily obtained in one minute by simply controlling the solvent content in the film during annealing.

5.2.2 Effect of small molecule loading on the assembly kinetics

The fundamental mechanism used for supramolecular nanocomposite thin films may also be applicable to other BCP-based systems. However, to achieve the assembly within the absolute time scale presented here, *i.e.* one minute, which is required to be compatible with current film processing techniques and on-line continuous fabrication, the following factors are unique to supramolecular systems and need to be taken into consideration to design the nanocomposite. Small molecules were shown to control inter-particle ordering, incorporate functionalities, and modulate the local environment of NPs.[28] Here, the presence of PDP modulates the thermodynamics and kinetics and facilitates the fast assembly process during solvent annealing. PDP molecules form hydrogen bonds with P4VP to change the polymer chain architecture from coil to comb and reduce chain entanglement. According to the FTIR results, the hydrogen bond between 4VP and PDP is not disrupted with the presence of $CHCl_3$ solvent molecules in the film (Figure A.4.3). Unbound PDP molecules act as a plasticizer to modulate chain mobility and their spatial arrangement influences χ_{eff}. In addition, since PDP has a higher solubility in $CHCl_3$ than the supramolecule, it can act as a solvent absorber to make the entire film swell faster than those with a lesser amount of or no unbound PDP. Thus, the supramolecular system gains mobility rapidly.

To experimentally validate the role of the small molecule in the assembly kinetics, we conducted a systematic study using four supramolecules (SP1 to SP4) that have similar total molecular weights (M_n), the same weight fraction of comb block (f_{comb}), but different 4VP:PDP ratios and volume fractions of free PDP (Table 5.1). SP1 and SP2, which consist of symmetric BCPs, require fewer PDPs attached on the P4VP side chains to reach f_{comb} = 0.72. To have the same f_{comb} in SP3 and SP4, more PDP molecules need to be loaded into the P4VP blocks as SP3 and SP4 consist of asymmetric BCPs. All four films were annealed together and reached f_s = 0.31 during solvent annealing. After annealing, the macroscopic orientation of the cylindrical microdomain was found to be dependent on the amount of unbound small molecules in the film. Figures 5.7a-d show the AFM images of the ~70 nm films of SP1, SP2, SP3, and SP4 after solvent annealing, respectively. For SP1 and SP2, the supramolecules formed hexagonally

Table 5.1

	PS M_n	*P4VP M_n*	*f_{comb}*	*f_{PS}*	*PDP:4VP Ratio*
SP1	11.8 kDa	15.0 kDa	0.72	0.44	**0.4: 1**
SP2	12.0 kDa	9.5 kDa	0.72	0.56	**0.7: 1**
SP3	24.0 kDa	9.5 kDa	0.72	0.72	**2.0: 1**
SP4	19.0 kDa	5.2 kDa	0.72	0.79	**2.5: 1**

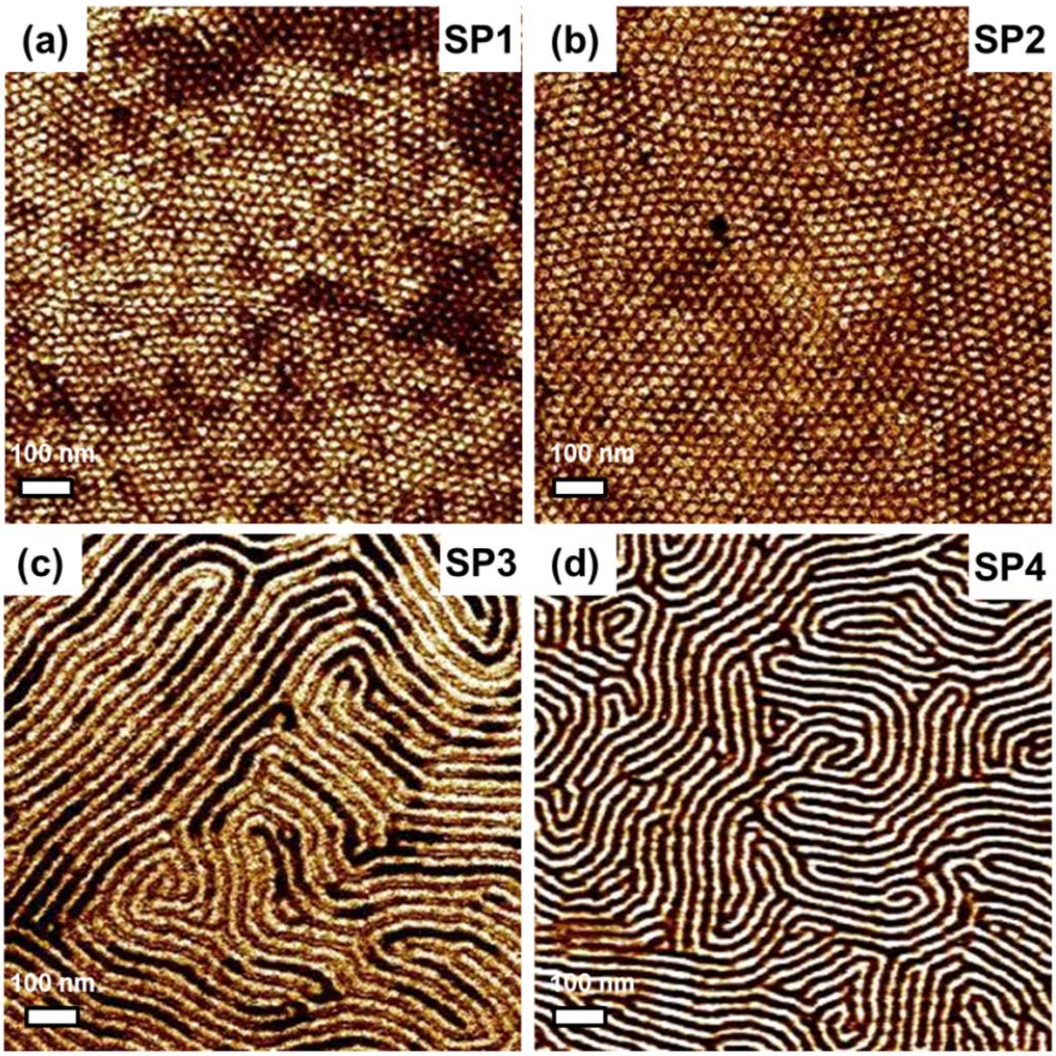

Figure 5.7. AFM phase images of the ~70 nm thin films containing (a) SP1, (b) SP2, (c) SP3, and (d) SP4 supramolecules, respectively. All the films reached t = 1.45 t_o during solvent annealing. The results show that SP1 and SP2 remained in non-equilibrium state whereas the supramolecules with more unbound PDP, SP3 and SP4, formed parallel morphology and reached thermodynamic equilibrium state in the film under the same annealing condition.

packed PS cylinders in P4VP(PDP) matrix oriented normal to the surface (Figure 5.7a and 5.7b). In contrast, SP3 and SP4 formed parallel cylindrical morphology under the same annealing condition (Figure 5.7c and 5.7d). The results indicate that the free PDPs may significantly affect the χ_{eff} and ΔE_a and consequently, the assembly kinetics to form parallel cylindrical morphology. To further confirm the observation, we conducted *in situ* GISAXS on a ~160 nm nanocomposite thin film containing SP2 supramolecule and 3 vol% of ~3.5 nm Au NPs during solvent annealing (Figure 5.8a). The *in situ* GISAXS data shows that the reorientation process began at f_s = 0.3 with no sign of ordered parallel morphology in the film until f_s reached = 0.38. Similar

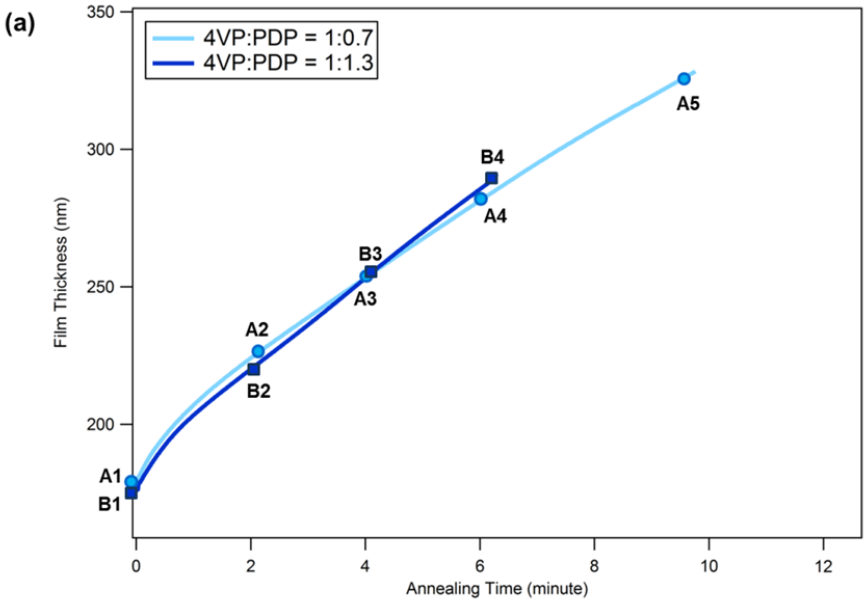
(a)
4VP:PDP = 1:0.7
4VP:PDP = 1:1.3
Film Thickness (nm)
Annealing Time (minute)
A1
B1
A2
B2
A3
B3
A4
B4
A5

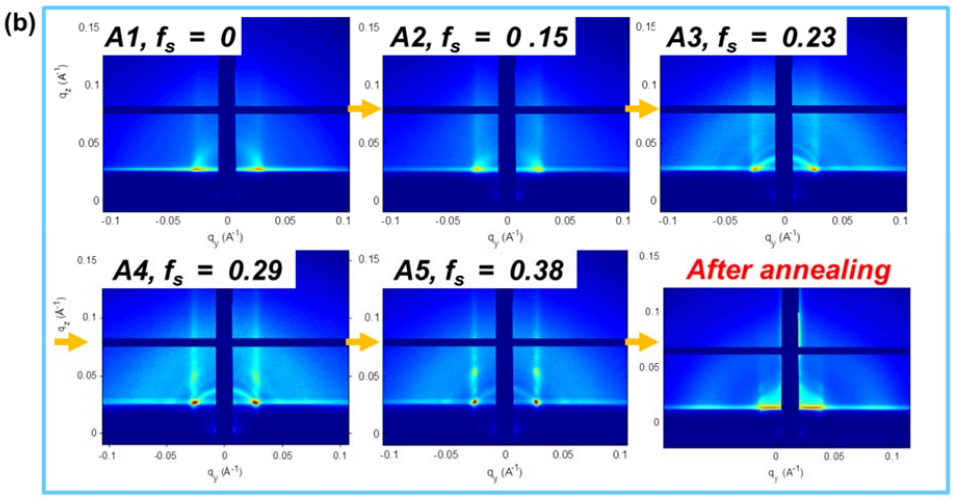
(b)
A1, f_s = 0
A2, f_s = 0 .15
A3, f_s = 0.23
A4, f_s = 0.29
A5, f_s = 0.38
After annealing

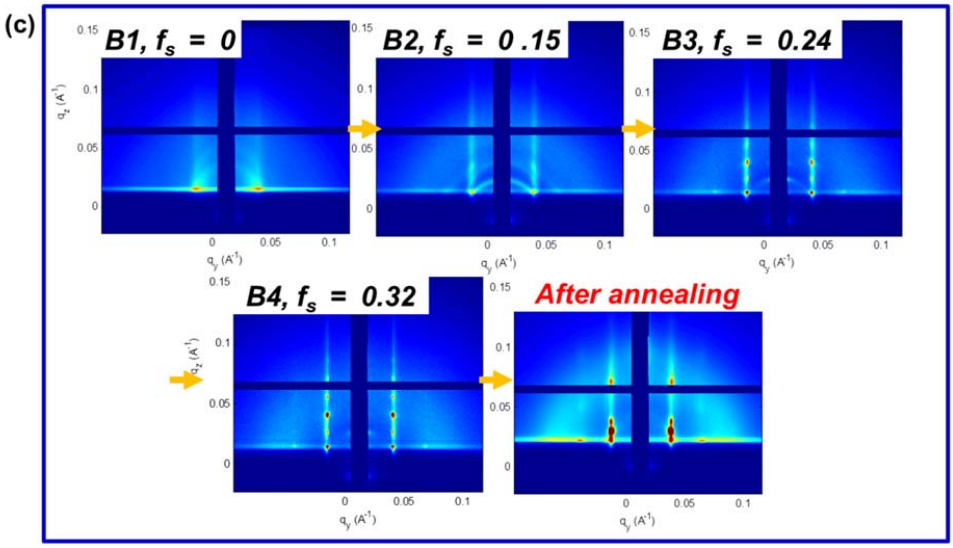
(c)
B1, f_s = 0
B2, f_s = 0 .15
B3, f_s = 0.24
B4, f_s = 0.32
After annealing

Figure 5.8. (a) Film thickness *vs.* time profile during the *in situ* GISAXS measurements on two ~160 nm supramolecular nanocomposite thin films containing PS(12 kDa)-*b*-P4VP(9.5 kDa)$(PDP)_{0.7}$ (film A) and PS(12 kDa)-*b*-P4VP(9.5 kDa)$(PDP)_{1.3}$ (film B), respectively. Both films have 3 vol% of ~3.5 nm Au NPs. (b) and (c) show the *in situ* GISAXS data of film A and film B, respectively. Film A, which has less free PDP, did not reach optimized parallel morphology before f_s = 0.38, whereas film B underwent microdomain reorientation and formed ordered parallel morphology at f_s = 0.32. The results show that the unbound PDP effectively facilitates assembly kinetics in supramolecular nanoocmposite thin films.

experiment was carried out on the nanocomposite thin film containing 3 vol% of ~3.5 nm Au NPs and a supramolecule, PS(12 kDa)-*b*-P4VP(9.5 kDa)$(PDP)_{1.3}$, which is similar to SP2 but with PDP:4VP > 1. Unlike SP2, this supramolecule formed ordered parallel morphology at f_s = 0.32 (Figure 5.8b). This, again, proves that the amount of unbound PDP in the system significantly affects the assembly kinetics in supramolecular nanocomposite thin films.

When PDP: 4VP ratio < 1, there is only a trace amount of PDP in PS domains regardless of f_s. Therefore, χ_{eff} between the two blocks stays large during solvent annealing. This makes the excursions of the chain segments into the foreign phase strongly enthalpic unfavorable so the interface between the two blocks remains sharp (Figure 5.9a). The anisotropy between D_{perp} and D_{para} leads to short-range diffusion parallel to the interface between the two blocks. As a result, the cylindrical microdomains oriented normal to the surface become the long-lived non-equilibrium state. Thus, the reorientation of microdomains happens at f_s > 0.3 and the assembly kinetics is slowed down in the supramolecular nanocomposite thin films with less unbound small molecules.

When PDP: 4VP ratio > 1, the amount of PDP in PS domains depends on f_s. Kinetically, at high f_s, the free PDPs become solubilized in PS domains, effectively mediating χ_{eff}, thereby lowering ΔE_a for diffusion normal to the interface (Figure 5.9b). In this case, the supramolecule can easily diffuse into the neighboring domains with little enthalpic penalty. In addition, the PDP molecules in PS domains plasticize the polymer chains to enhance the mobility of the supramolecule. Thus, the perpendicular nanostructure can no longer sustain and the parallel morphology develops and becomes optimized as f_s increases. As the PDP: 4VP ratio is varied, the chain architecture changes, which directly affects the diffusion constant of the supramolecule (Figure 5.9). Theoretical calculation may potentially enable us to elucidate the effect of chain architecture on the diffusion and understand the combinatorial effect of PDP loading on the assembly kinetics in the supramolecular nanocomposite system.

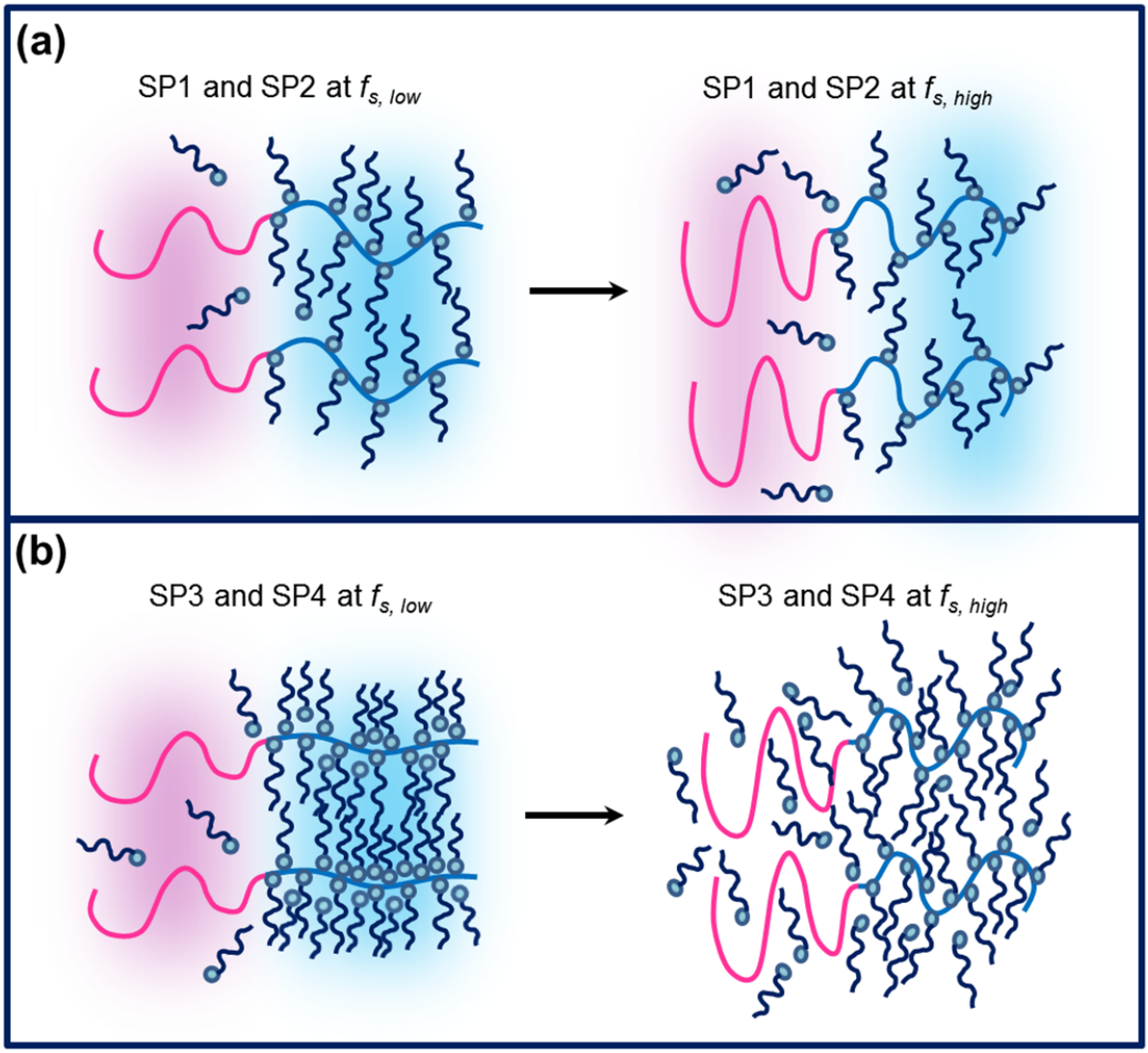

Figure 5.9. (a) and (b) schematically illustrate the distribution of free PDP and chain conformation during solvent annealing when PDP:4VP < 1 and > 1, respectively. Unbound PDP small molecules become solubilized in PS domains as f_s increases, mediating the interactions between the two blocks, thereby facilitating the assembly kinetics during annealing.

5.2.3 Effect of supramolecule molecular weight on the assembly kinetics

In addition to f_s and the small molecule volume fraction, the assembly kinetics of the supramolecular nanocomposite is also greatly dependent on the molecular weight of the supramolecule (M_n). To qualitatively investigate the effect of M_n on the kinetic pathway in the co-assembly, we conducted *in situ* GISAXS experiments on the nanocomposites consisting of 3 vol% of ~5 nm Au NPs and three supramolecules of different M_n. The supramolecules used (P1,

P2, and P3) have the same weight fraction of comb block and similar PDP:4VP ratios, but different M_n (Table 5.2). Figures A.4.4a, 5.5c, and A.4.4b show the *in situ* GISAXS data of the supramolecular nanocomposites containing P1, P2, and P3, respectively. As M_n increases, the threshold f_s for the reorientation of microdomain also rises. Moreover, the f_s required for the formation of ordered parallel nanostructure ($f_{s,\ ordered}$) increases as a function of M_n, which were found to be 0.23, 0.31, and 0.43 for P1, P2, and P3 supramolecular nanoocmposites, respectively (Table 5.2). In melt or concentrated solution, low molecular weight polymer chains moves independently. The diffusion of high molecular weight chains, however, may be retarded by chain entanglements. To investigate if the assembly kinetics of high M_n supramolecules is affected by chain entanglements, the morphological evolvement in a supramolecular nanocomposite containing a high molecular weight BCP (P4 in Table 5.2) was studied (Figure A.4.5). In this case, the molecular weight of the PS block (50 kDa) is larger than the critical molecular weight for entanglements (M_c) for PS (35 kDa). Interestingly, the kinetic pathway in this particular supramolecular nanocomposite is similar to that shown previously. The parallel morphology was optimized at f_s = 0.55 and an order-disorder transition occurred when f_s > 0.58. Plotting the values of $f_{s,\ ordered}$ for all four supramolecular nanocomposites against N reveals that $f_{s,\ ordered} \sim N^{0.05}$as shown in Figure 5.10.

According to the Mark-Houwink equation, the intrinsic viscosity $[\eta]$ of a polymer in a dilute solution is related to its viscosity-average molar mass following the equation $[\eta] = KM_v^a$, where K and a are characteristic constants for a given system. Theoretically, $[\eta] \sim M$ and $[\eta] \sim M^{3\nu-1}$ based on the Zimm and Rouse models, respectively. The diffusion mechanism of the supramolecule may not follow Zimm or Rouse model exactly since the supramolecules have non-Gaussian chain conformations and are not in a dilute solution during annealing. However, these relationships can help us qualitatively decipher the experimental results. As the molecular weight of the supramolecule increases, the viscosity of the polymer chains rises so the diffusion coefficient decreases. In addition, the activation energy barrier for inter-domain diffusion rises and the chain mobility decreases accordingly with increasing M_n. In order for the nanocomposites containing long supramolecules to achieve ordered in-plane morphology following the kinetic pathway shown in the previous sections, more solvent is required to mediate χ_{eff} and plasticize the polymer chains. Empirically, $f_{s,\ ordered}$ rises with increasing N following a power law behavior with an exponent ~0.05. When the molecular weight is larger than the critical molecular weight for entanglement, the supramolecules may follow a different diffusion mechanism. However, in this case, P4 undergoes a kinetic pathway similar to P1, P2, and P3. We speculate that the comb-like structure of the P4VP(PDP) chain may have prevented chain entanglements and raised M_c in supramolecular nanocomposites. To confirm this hypothesis, in-depth study on the assembly kinetics of high M_n supramolecules is required and is still under investigation.

Table 5.2

	PS M_n	*P4VP M_n*	*N*	*PDP: 4VP Ratio*	f_{comb}	$f_{s,\ ordered}$
P1	13.8 kDa	3.5 kDa	166	1.8: 1	0.62	**0.23**
P2	19.0 kDa	5.2 kDa	232	1.7: 1	0.62	**0.31**
P3	33.0 kDa	8.0 kDa	393	1.9: 1	0.62	**0.43**
P4	50.0 kDa	17.0 kDa	643	1.8:1	0.62	**0.55**

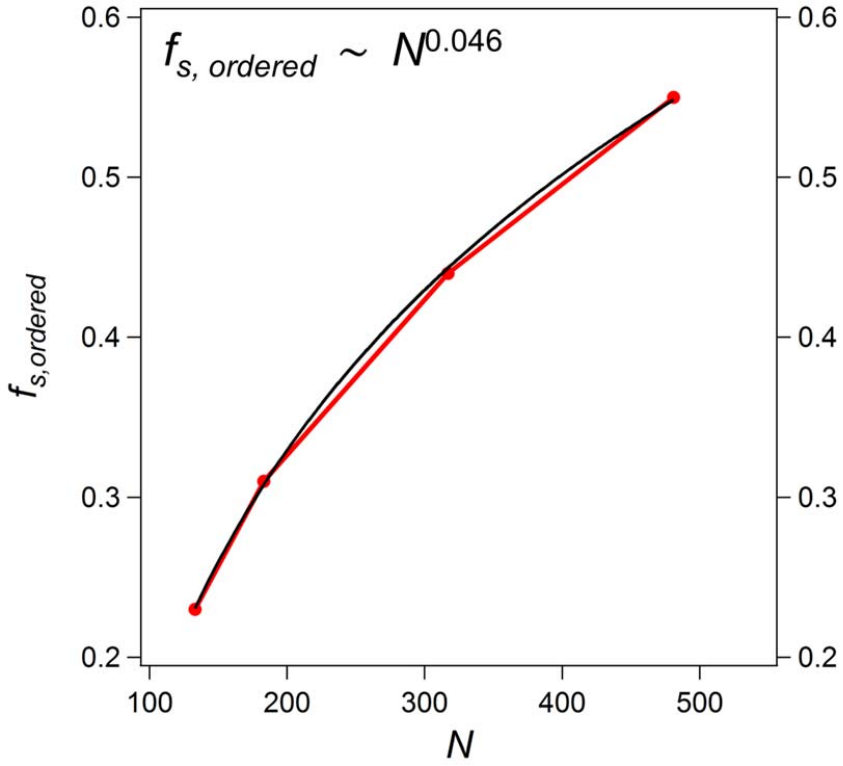

Figure 5.10. The empirical results of $f_{s,\ ordered}$ were plotted against N for the four supramolecules used. The increase in $f_{s,\ ordered}$ with increasing N follows a power law behavior with an exponent ~0.05 empirically. This indicates that the longer the supramolecule, the slower the assembly kinetics during solvent annealing.

5.2.4 Effect of solvent removal rate on the final morphology of supramolecular nanocomposite thin film

So far, the assembly kinetics of the supramolecular nanocomposite has been discussed during solvent annealing. It is important to stress that the method of conversion of the swollen state to the final dried state is critical in determining the final morphology of the nanocomposites. In traditional BCP systems, the effects of solvent removal rate on lateral ordering, macroscopic orientation, and domain spacing have been extensively investigated. By controlling the solvent removal rates, highly ordered BCP microdomains can be generated in bulk/thin films.[40-45] In addition, the solvent concentration gradient generated during rapid solvent removal can bias the macroscopic orientation of the BCP microdomains in thin films through the formation of an ordering front.[45-47] The "collapse" of the film during solvent removal can induce changes in the dimensions of microphase-separated structure and the macroscopic alignment of the domains.[48,49] As the film dries, both dynamic and thermodynamic considerations come into play and they clearly depend on the specific system being explored. In the supramolecular system studied here, the mobility of the supramolecules in a microphase separated environment, the chain architecture of the supramolecules, and the spatial distribution of the small molecules are altered upon solvent removal. Understanding the effect of solvent removal rate (*SRR*) on the morphology of the supramolecular nanocomposite thin film will provides fundamental guidance for the design of manufacture-friendly processing techniques for scalable nanofabrication of nanocomposite thin films.

Here, the morphology of a ~200 nm supramolecular nanocomposite thin film containing 3 vol% of ~3.5 nm Au NPs and PS(13.8 kDa)-*b*-P4VP(3.5 kDa)$(PDP)_{1.8}$ was monitored *in situ* by GISAXS during solvent annealing/evaporation. When f_s reached 0.23, the ordered parallel nanostructure was optimized. To remove the solvent in the film, controlled N_2 flow was employed to achieve fast (300 nm/min), intermediate (11 nm/min), and slow (0.5 nm/min) *SRRs* (Figure 5.11). The *in situ* GISAXS patterns of the films that underwent fast, intermediate, and slow *SRRs* are shown in Figure A.4.6, A.4.7, and A.4.8, respectively. All three supramolecular nanocomposites had similar morphology with 3-D hexagonally packed in-plane NP arrays in the films based on the GISAXS patterns. Moreover, the lateral ordering of the nanostructure improved with decreasing *SRR*. When *SRR* = 0.5 nm/min, the long-range order of the NP arrays was optimized as the 4^{th} order peaks in both the q_y and q_z directions can be seen in the GISAXS pattern. In addition, the lateral periodicity *a* of the nanocomposite during solvent annealing/removal was analyzed as a function of f_s (Figure A.4.6 to A.4.8). As the solvent entered the films, *a* began to decrease. It started to increase when the solvent escaped from the films. The larger the *SRR*, the smaller the *a* in the dried films (Table 5.3). To quantify the relationship between *a* and f_s, all the data points were plotted in a log-log manner as shown in Figure 5.12. The fitting of the data reveals that *a* increases with increasing supramolecule concentration following a power law behavior with an exponent of 0.62. Lastly, the 3-D structures of the supramolecular nanocomposites were analyzed by simulating the 2-D GISAXS patterns after solvent removal (Figure 5.13). The distortion factors of the films that underwent intermediate and slow solvent removal are larger than that for the fast *SRR*. This leads to a larger

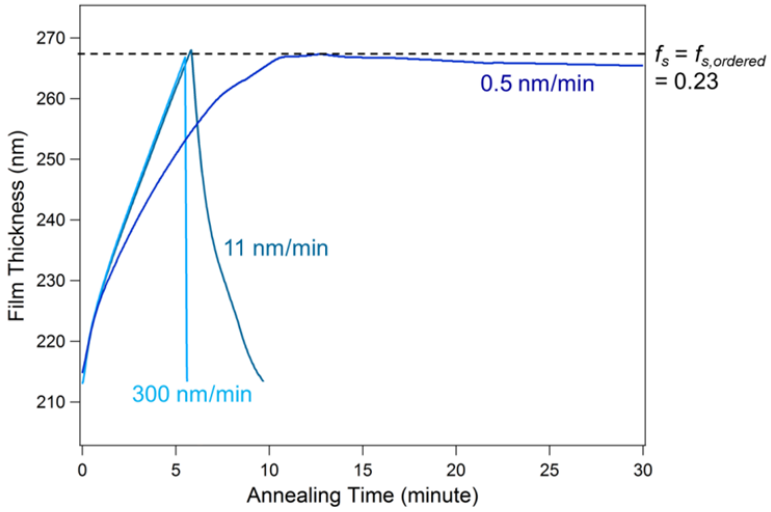

Figure 5.11. Thickness profiles as a function of annealing time measured during *in situ* GISAXS experiments. The ~200 nm supramolecular nanocomposite thin films consist of 3 vol% of ~3.5 nm Au NPs and PS(13.8 kDa)-*b*-P4VP(3.5 kDa)$(PDP)_{1.8}$. After reaching the optimized f_s value during solvent annealing, the films underwent three different solvent removal profiles with fast, intermediate, and slow solvent removal rates.

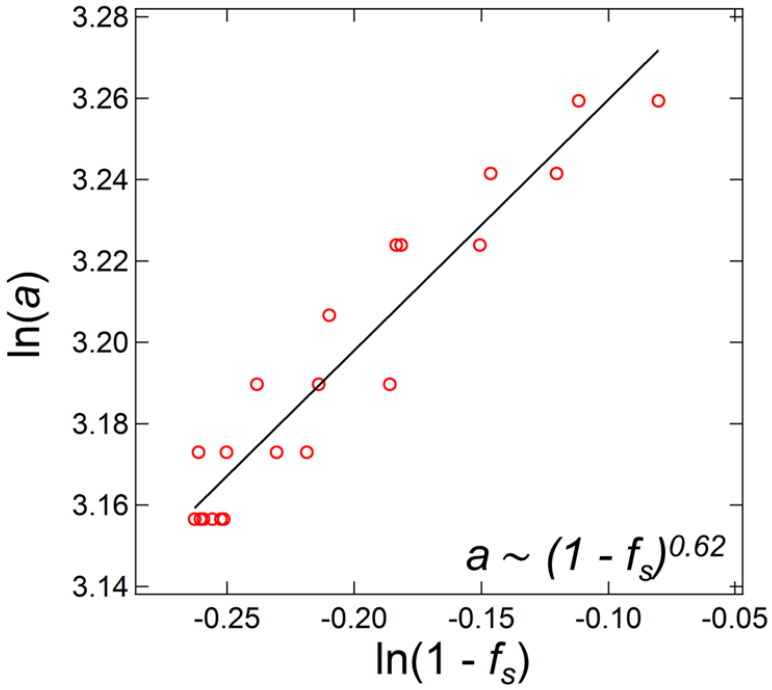

Figure 5.12. Log-log plot of *a vs*. (1-f_s). All the data points were taken during the solvent removal process of the *in situ* GISAXS measurements. The best linear fit of the data points gives a power law relationship between *a* and (1-f_s) with an exponent of 0.62.

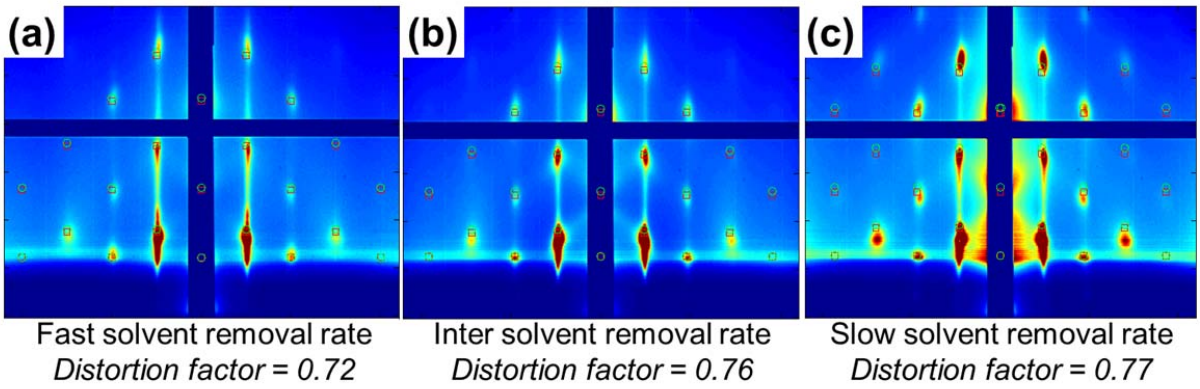

Figure 5.13. Simulated 2-D GISAXS patterns of the three ~200 nm supramolecular nanocomposite thin films that underwent (a) fast, (b) intermediate, and (c) slow solvent removal. The strong vertical solvent field during rapid solvent removal induced a large vertical compressive force in the film, leading to a more distorted hexagonal lattice of 3-D NP arrays in the nanocomposite that experienced instantaneous solvent removal.

Table 5.3

	Fast Solvent Removal Rate	***Intermediate Solvent Removal Rate***	***Slow Solvent Removal Rate***
Lateral Lattice Constant, *a*	25.13 nm	26.18 nm	26.51 nm
Vertical Lattice Constant, *c*	32.21 nm	34.46 nm	35.36 nm
Unit Cell Area	**1619 nm^2**	**1804 nm^2**	**1875 nm^2**

packing density of the supramoelcules and the NPs in the hexagonal unit cell when *SRR* is large (Table 5.3).

During spin casting, the small molecules crystallize in the P4VP(PDP) comb blocks, leading to a relatively large lateral periodicity in the nanostructure. As the solvent enters the film, more unbound small molecules become solubilized in the PS domains (Figure 5.14). The solvent together with the PDP small molecules mediate the interfacial interactions and markedly lower χ_{eff}, resulting in a change in the conformation of both PS and P4VP(PDP) chains to increase the interfacial area between the two blocks (Figure 5.14). Moreover, the solvent molecules disrupt the crystalline structure of the comb blocks, decreasing the average contour length of P4VP(PDP) chains. Therefore, *a* decreases as a function of f_s in the annealing process. As the solvent leaves the swollen film at a small *SRR*, χ_{eff} gradually rises, forcing the small molecules in PS domains to diffuse back to the P4VP(PDP) blocks and crystallize with the comb blocks,

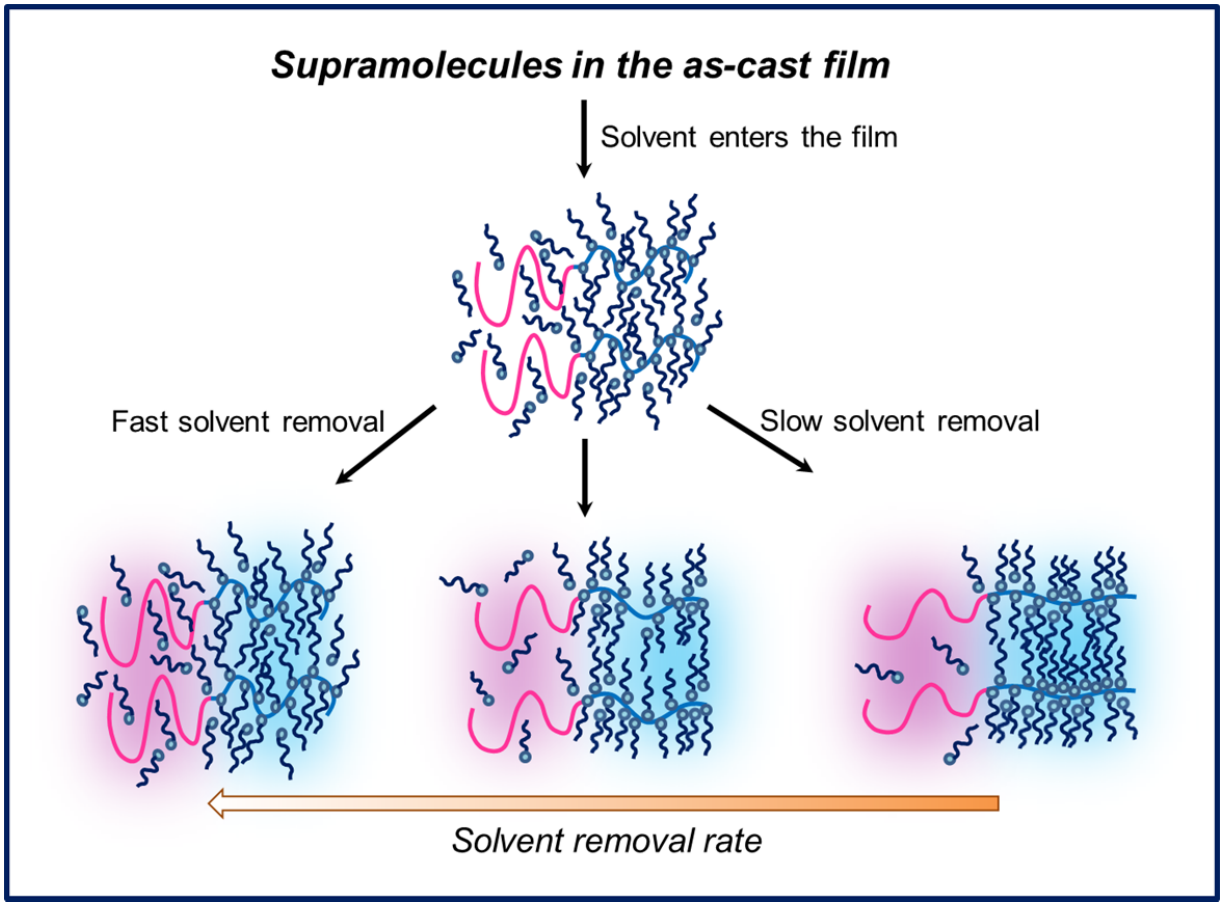

Figure 5.14. Schematics of the chain conformations and small molecule distributions in a supramolecular nanocomposite thin film during solvent annealing and after solvent removal.

leading to an increase in a as f_s decreases. Furthermore, the short-range diffusion during a slow solvent removal process enables the supramolecules to recover the coil-comb conformation and accommodate the changes in film thickness to reach a local equilibrium state where the distortion factor of the 3-D NP assemblies is ~0.76 (Figure 5.14). The rearrangement of the supramolecules, small molecules, and the NPs further improves the lateral as well as the vertical ordering during slow solvent removal, yielding an optimized 3-D nanostructure in the dried film.

On the contrary, a fast solvent removal process may kinetically arrests the chains conformations of the supramolecules at $f_{s,\,ordered}$, resulting in a lateral periodicity smaller than that in the local equilibrium (Figure 5.14). Moreover, the vertical compressive force induced during rapid solvent removal results in a decrease of the lattice constant in the vertical direction. This leads to a more distorted hexagonal lattice of the 3-D NP arrays and a larger packing density of the supramolecules in the film compared to that when *SRR* is small. The empirical results gives a power law relationship between a and $(1\text{-}f_s)$ with an exponent of 0.62, which is consistent with that predicted in case of intermediate segregation.[49,50] By carefully tuning the amount of solvent

in the film during solvent annealing/removal, the lateral lattice constant of the 3-D NP assembly in the supramolecular nanocomposite can be precisely tailored based on the relationship presented in Figure 5.12. The desired lattice constant can be realized in the dried film without affecting the overall morphology of the nanocomposite by tuning the solvent removal rate. This gives us a useful tool to precisely control the 3-D nanostructure of the NP assembly, and thereby the physical property in supramolecular nanocomposites for structure-property correlation studies and the fabrication of various NP-based devices.

§ 5.3 Conclusion

In summary, these studies show a comprehensive study of the assembly kinetics in the nanocomposite thin films during solvent annealing. The interplay between the energetic driving forces and kinetic pathways can be precisely tailored by simply controlling solvent and small molecule loadings in nanocomposite thin films to achieve a fast ordering of hierarchically structured 3-D NP assemblies over macroscopic distances. Furthermore, the overall morphology of the nanocomposite is not affected by fast solvent removal after annealing. The mechanism shown is applicable to supramolecules with a wide range of molecular weights and it provides fundamental guidance for the design of manufacture-friendly processing techniques for scalable nanofabrication of nanocomposite thin films. Since the supramolecular approach is compatible with nanoparticles of different chemical compositions and can lead to a library of nanoparticle assemblies, present studies clearly open a viable approach to fabricate a new family of nanocomposite-based devices using blade coating, ink-jet printing, and dynamic zone annealing.

§ 5.4 Experimental section

5.4.1 Sample preparation

PS(19 kDa)-*b*-P4VP(5.2 kDa) (PDI = 1.09), PS(13.8 kDa)-*b*-P4VP(3.5 kDa) (PDI = 1.09), PS(12 kDa)-*b*-P4VP(9.5 kDa) (PDI = 1.09), PS(33 kDa)-*b*-P4VP(8 kDa) (PDI = 1.10), and PS(50 kDa)-*b*-P4VP(17 kDa) (PDI = 1.15) were purchased from Polymer Source, Inc. 3-n-Pentadecylphenol (95%) was purchased from Acros. Chloroform was purchased from Fisher. All chemicals were used as received. The Au NPs were synthesized using the method reported by Peng *et al*.[28]. Blends of supramolecules and NPs were prepared as described previously. Thin films were prepared by spin-coating the mixed solutions onto silicon wafers (200 nm thermal oxide/Si) with spinning speeds ranging from 1000 to 3000 rpm. For solvent annealing, samples were annealed using $CHCl_3$ injected inside a 250 mL Teflon chamber at room temperature. The amount of solvent injected was varied from 0.3 to 2 mL to tailor the swelling rate. The thickness of the film was monitored using Filmetrics F20 as a function of annealing time. Once the film

thickness of the nanocomposite thin film reached the desired value, the chamber was opened and the $CHCl_3$ vapor was allowed to freely evaporate.

5.4.2 Fourier transform infrared spectroscopy

The FT-IR sample was prepared by placing the supramolecule solution in a liquid cell or dropping a 100 μL supramolecule solution onto a NaCl plate and allowing the film to air-dry. IR spectra were recorded in transmission with a Bruker spectrometer model Vector 33.

5.4.3 Transmission electron microscopy

To prepare the cross section of a nanocomposite thin film, the sample was floated off from the substrate on the surface of a pool of 5 vol% HF solution. An epoxy block (Araldite 502, Electron Microscopy Sciences) was used to catch the film such that the sample is on top of the epoxy block with the air/polymer interface in contact with the epoxy block. The epoxy along with the sample were cured at 60 °C for at least 4 h to ensure good contact between the epoxy and the nanocomposite thin film. Thin sections, ~50 nm in thickness, were microtomed using an RMC MT-X ultramicrotome (Boeckler Instruments) and picked up on copper TEM grids on top of water. The cross-sectional TEM images were collected using a FEI Tecnai 12 transmission electron microscope at an accelerating voltage of 120 kV.

5.4.4 Atomic force microscopy

Atomic force microscopy (AFM) was performed on a Veeco Dimension 3100 equipped with a NanoScope IIIa controller and Quadrex signal processor. The spring constant of the cantilever was 10-130 N/m with a resonant frequency in the range of 204-497 kHz. The set point for auto tune was 2.5 V. The set-point amplitude was 90% of the free vibration value.

5.4.5 *In situ* grazing incidence small angle X-ray scattering

Grazing incidence small-angle X-ray scattering (GISAXS) measurements were made at beamline 8-ID-E in Advanced Photon Source in Argonne National Laboratory. X-ray wavelength of 1.687 Å was used and the scattering spectra were collected on a Pilatus 1M detector during solvent annealing at an incident angle larger than the critical angle of the Si substrate, usually around 0.25°. With $CHCl_3$ vapor in the annealing chamber, the exposure time was chosen to be shorter than 5 s to avoid serious beam damage on the film. Line averaged intensities were reported as I vs. q, where $q = (4\pi/\lambda) \sin(\theta/2)$, λ is the wavelength of incident X-rays, and θ is the scattering angle.

Chapter 6
Macroscopic Alignment of 3-D Nanoparticle Assemblies in Thin Films via Topographically Patterned Surfaces

As shown in previous chapters, hierarchically structured 3-D nanoparticle assemblies with random lateral orientation can be generated over macroscopic distances using the supramolecular approach. To effectively harness the physical properties of supramolecular nanocomposites for various optical and energy devices, it is requisite to control the macroscopic alignment of the 3-D nanoparticle assemblies over large area. Here, we present simple yet versatile routes to control the macroscopic alignment of supramolecular nanocomposite thin films using faceted and lithographically patterned surfaces. On the saw-toothed substrates, nanoparticle arrays aligned normal to the ridge direction with orientation parameters of up to 0.92, are fabricated in 200 nm thick nanocomposites. The 3-D nanostructure of the supramolecular nanocomposite on the faceted substrate is similar to that on a flat surface where 1-D nanoparticle chains form a distorted hexagonal lattice with a distortion factor of ~0.75. On lithographic trench patterns, not only the 2-D lateral alignment, but also the 3-D structure of the 3-D nanoparticle assemblies can be precisely controlled in nanocomposites with film thicknesses < 350 nm when the ratio of the trench width to the lateral periodicity of the nanocomposite < 10. Moreover, by varying the solvent annealing condition, the spatial distribution of small molecules may be tailored to alter the macroscopic orientation of the nanoparticle arrays/microdomains on lithographic patterns. Our studies show that either faceted or lithographically patterned surfaces are effective in guiding nanoparticle assemblies parallel and normal to the substrate surface over large area, which provides a powerful platform for the investigation of emerging structure-property relationships in functional nanocomposites, paving the way for the realization of next-generation devices.

§ 6.1 Introduction

Nanocomposites containing ordered 3-D arrays of nanoparticles (NPs) exhibit unique collective properties due to quantum confinement in individual particles as well as inter-particle coupling.[1-4] Hierarchically structured 3-D NP assemblies with long-range order can lead to a new family of functional materials with tunable collective properties for a wide range of applications including nanoelectronics, plasmon-enhanced solar cells, plasmonic waveguides, photonic crystals, and memory storage. To pave the way for next-generation devices, there are critical needs for a versatile platform to precisely control the spatial organization of NPs over multiple length scales for structure-property correlation studies. Among many approaches, block copolymers (BCPs)[5-10] or BCP-based supramolecules[11-13] provide effective structural frameworks to assemble NPs over macroscopic distances. Although the NP assemblies can be precisely controlled locally, the grains of 3-D NP assemblies tend to be randomly oriented, making it difficult to achieve control over directional macroscopic properties. Various methods using external fields, [14-18] epitaxial assembly,[19-21] graphoepitaxy,[22-25] and faceted substrates[26,27] have been developed to control the macroscopic alignment of BCP microdomains in thin films. However, most studies focus on films that have a thickness of only one or two periods of the

BCP morphology. For nanocomposites it is highly desirable to direct 3-D NP assemblies of much thicker films.

Here, we show that by using saw-toothed faceted or lithographically patterned substrates, thin films of supramolecular nanocomposites containing 3-D NP arrays with long-range order can be readily obtained. NP arrays, aligned normal to the ridge direction of the saw-toothed substrate with orientation parameters of up to 0.92, are fabricated in films with thicknesses, t, < 200 nm on saw-toothed sapphire substrate with an average pitch size ~5 times of the periodicity of the supramolecular nanocomposite. The 3-D nanostructure of the supramolecular nanocomposite on the faceted substrate is similar to that on a flat surface where 1-D NP chains form a distorted hexagonal lattice with a distortion factor of ~0.75. Substrates containing lithographically patterned trenches are also employed to impose lateral confinement on the supramolecular nanocomposite. Highly aligned 3-D NP arrays with orientation parameters > 0.86 can be achieved in films with t < 350 nm on a trench pattern that is 50 nm in depth and 125 nm in width. As the ratio of the trench width to the lateral periodicity of the nanocomposite increases above 11, the long-range order of the NP arrays deteriorates. The trench pattern also affects the spatial organization of the 3-D NP arrays normal to the surface and the distortion factor of the hexagonal lattice is 0.87 as opposed to 0.75 observed in the same films on a saw-toothed surface or a flat substrate. Lastly, the preliminary results show that varying solvent annealing condition alters the NP arrays/microdomains to orient parallel or perpendicular to the trench direction on lithographic patterns. Our studies show that either faceted or lithographically patterned surfaces are effective in guiding NP assemblies parallel and normal to the substrate surface and can lead to hierarchically structured nanocomposite thin films with tunable directional properties over macroscopic distances to meet material needs for a wide range of NP-based devices.

§ 6.2 Results and discussion

6.2.1 Directed assembly of supramolecular nanocomposite thin film on saw-toothed sapphire substrates

Saw-toothed faceted substrates, generated by a thermal reconstruction of the surface of a miscut single crystal,[26,28,29] provide a simple approach to direct the macroscopic alignment of BCP microdomains and NP assemblies in thin films over arbitrarily large area. The triangular grooves comprising the saw-toothed surface impose packing constraints on the coil-comb supramolecules, which result in an orientation of the cylindrical microdomains and the NP arrays normal to the ridge direction to minimize the entropic penalties associated with chain packing and the incommensurability between the pitch of the saw-toothed pattern and the lateral period of the supramolecular nanocomposite.[27] Figure 6.1a shows atomic force microscopy (AFM) image of the surface of the saw-toothed substrate used with an average pitch (λ) and amplitude of ~140 nm and ~15 nm, respectively. Figure 6.1b shows the AFM image of a ~36 nm thin film

containing a blend of polystyrene(19 kDa)-*block*-poly(4-vinylpyridine)(5.2 kDa) (PS(19,000)-*b*-P4VP(5,200)(PDP)$_{1.7}$) and 3 vol% of 5 nm Au NPs on the faceted substrate. On the faceted substrate, the Au NPs follow the alignment of the supramolecules and form densely-packed unidirectional NP chains oriented in the plane of the substrate, perpendicular to the saw-toothed pattern.

The grazing incidence small angle X-ray scattering (GISAXS) pattern of the same film at $\Psi = 0°$, where Ψ is the angle between the X-ray direction and the direction of the 1-D NP chains, shows multiple orders of scattering in the q_y or in-plane direction from the highly oriented and aligned NP arrays, (Figure 6.1c). When the sample is rotated, increasing Ψ, the Bragg peaks weaken and broaden. The integral of the scattering intensity of the first-order peak was determined for $-30° < \Psi < 30°$, yielding an orientation parameter $S = 0.92$ (Figure 6.1d), indicating the exceptionally high degree of orientation of NP arrays over a large area (the footprint of the x-ray beam on the sample is ~3 cm). When t is increased to 82 nm, the 3-D NP arrays are still highly aligned normal to the ridge direction (Figure 6.1e and 6.1f) and order is present at $t = 182$ nm (Figure A.5.1). However, the long-range order of the NP arrays breaks down when $t > 240$ nm under the solvent annealing condition used here.

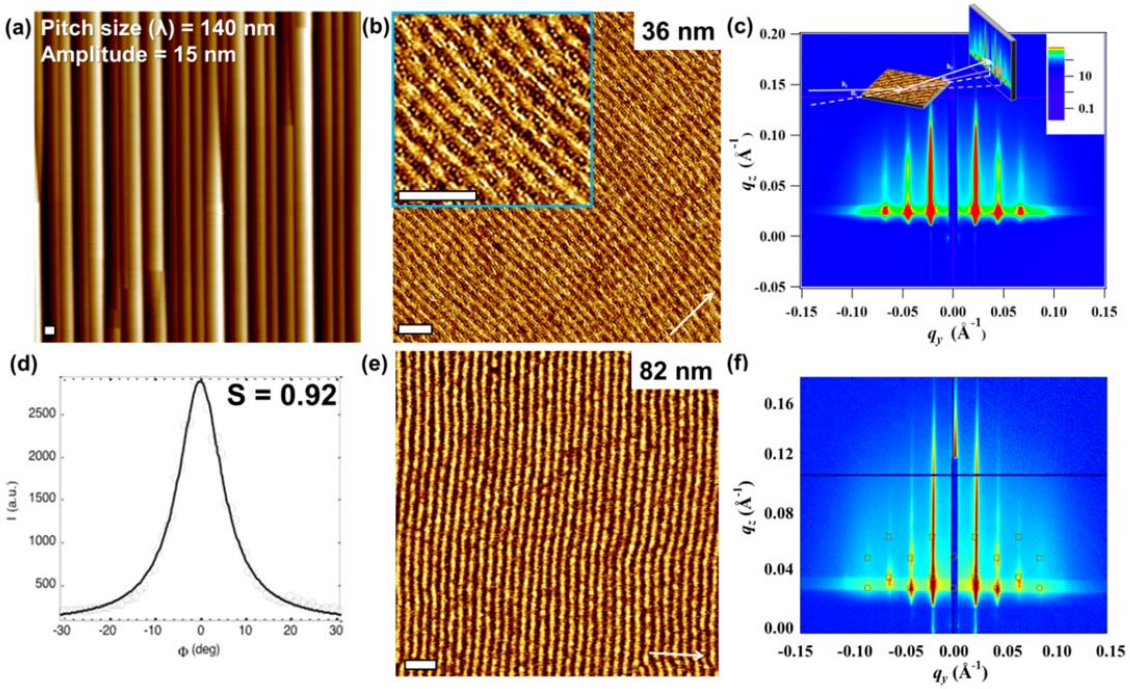

Figure 6.1. (a) AFM image of the faceted substrate used for the directed NP assembly. (b) AFM image and (c) GISAXS pattern of a ~36 nm thin film containing PS(19,000)-*b*-P4VP(5,200)(PDP)$_{1.7}$ and 3 vol% ~5 nm Au NPs on the faceted substrate in (a). The arrow indicates the ridge direction. The NP chains are aligned perpendicular to the facets. (d) The integral of the scattering intensity yields an orientation parameter $S \sim 0.92$. (e) AFM and (f) GISAXS data of an 82 nm thick film. The distortion factor of the hexagonal lattice of the 3-D NP arrays is ~0.75 from a simulation of the peak positions in the GISAXS pattern in (f). Scale bar = 100 nm.

In bulk, the supramolecular nanocomposite used here forms a hexagonally packed cylindrical morphology where the NP chains assemble at the vertices of a non-distorted hexagon.[11] In thin film, the hexagonal lattice of the NP chains becomes distorted in the vertical direction due to solvent removal.[12] To investigate the 3-D structure of the supramolecular nanocomposite thin films on the saw-toothed substrate, the diffraction peak positions in the GISAXS pattern were simulated using a model containing real space basis wave vectors for a distorted hexagonal lattice, orequivalently a rhombic lattice, of in-plane cylinders (Figure 6.1f).[12] The distortion factor of the lattice is defined as $c/(\sqrt{3}a)$, where c and a are the vertical and lateral lattice constants, respectively, *i.e.* a distortion factor of 1 indicates a hexagonally coordinated arrangement of the NP chains.[12] The average lattice constants of the thin films on a flat surface were measured and calculated by analyzing the GISAXS patterns of a series of samples for $30 < t < 200$ nm annealed under the same conditions (see A.5.2 and A.5.3).[12] The average values of a and c are 33.3 ± 1.1 nm and 44.2 ± 1.1 nm, respectively, with a distortion factor of 0.77 ± 0.04. The simulation of the GISAXS pattern of the same nanocomposite thin film on a saw-toothed substrate gives a lattice distortion factor of ~0.76 with a and c around 33.2 and 43.68 nm, respectively, similar to those on a flat substrate (Figure 6.1f). The cylindrical microdomains and the NP arrays orient normal to the ridge direction to minimize the entropic penalties associated with chain packing in the triangular grooves and the incommensurability between the λ and a.[27] Thus the shallow triangular grooves of the faceted substrate can lead to long-range order, but do not affect the distorted hexagonal packing of 1-D NP chains.

6.2.2 Directed assembly of supramolecular nanocomposite thin film on lithographically-patterned surfaces

Lithographic patterns are routinely used to guide the macroscopic and local patterning of BCP microdomains and their period, depth and mesa width can be more readily controlled than the topography of a single crystal saw-toothed substrate. To test the feasibility of the approach, we first deposited ~30-35 nm thin films of PS(19,000)-*b*-P4VP(5,200)$(PDP)_{1.7}$ in rectangular trenches with the same trench height (~50 nm) but different trench widths, L (Figure 6.2). In Figure 6.2, it is observed that the trench walls guide the macroscopic alignment of the parallel cylinders regardless of the L/a value when $L/a < 11$. The small molecules effectively mediate the polymer/substrate interfacial interactions. The P4VP$(PDP)_{1.7}$ matrix preferentially wets the trench walls, guiding the unidirectional assembly of the cylindrical microdomains in every trench. Unlike those on the saw-toothed substrate, the microdomains orient parallel to the trenches. In addition, no morphological change is observed when L/a deviates from integral values. Unlike that in the BCP systems, the incommensurability effect seems to play a minimal role as the supramolecules can accommodate the modulation of trench width, possibly due to their unique chain architecture. This is further confirmed by using supramolecules with different molecular weights (Figure A.5.4). As L/a reaches above 20, the long-range order of the microdomains breaks down as the confinement provided by the trenches becomes insignificant.

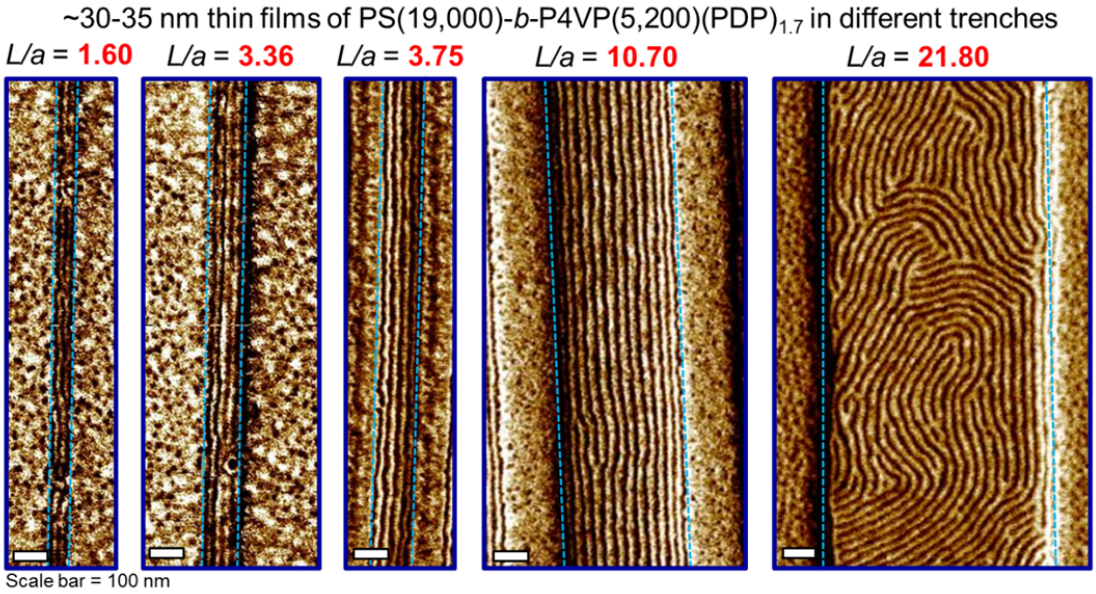

Figure 6.2. AFM images of ~30-35 nm thin films of PS(19,000)-*b*-P4VP(5,200)(PDP)$_{1.7}$ in rectangular trenches with the same trench height (~50 nm) but different trench widths, *L*. The trench walls guide the macroscopic alignment of the parallel cylinders regardless of the *L/a* value when $L/a < 11$. As *L/a* reaches above 20, the long-range order of the microdomains breaks down as the lateral confinement provided by the trenches becomes insignificant.

Next, we deposited a ~45 nm supramolecular nanocomposite thin film containing PS(19,000)-*b*-P4VP(5,200)(PDP)$_{1.7}$ and 3 vol% of ~5 nm Au NPs on a Si wafer with 50 nm deep and 125 nm wide trench patterns with 210 nm period (called "P1") (Figure 6.3). The width and periodicity of the trench pattern were characterized by AFM and GISAXS (see A.5.5). Dense arrays of highly aligned 1-D chains of Au NPs are clearly seen conforming to the unidirectional cylindrical microdomains in the AFM image (Figure 6.3a). To characterize the macroscopic alignment of the NP arrays, rotation GISAXS was conducted on the sample with Ψ ranging from 0° to 90° (Figure 6.3b-c). Bragg rods corresponding to the up to the 4th order can be clearly seen when $\Psi = 0°$. As the sample is rotated away from the beam, higher order Bragg peaks weaken and gradually disappear. This is confirmed by the q_y linecut at $q_z = 0.024$ Å^{-1} for each GISAXS pattern (Figure 6.3b). Figure 6.3c shows the dependence of the scattering intensity of the first-order peak on Ψ. Here, *S* is found to be 0.93, characteristic of highly-aligned cylindrical microdomains and NP arrays confined in the lithographic trenches. When $t < 50$ nm, the P4VP(PDP)$_{1.7}$ blocks wet the trench walls and align the NP chains along the trench direction. This macroscopic alignment further propagates throughout the entire channel when the supramolecules gain enough mobility during solvent annealing.

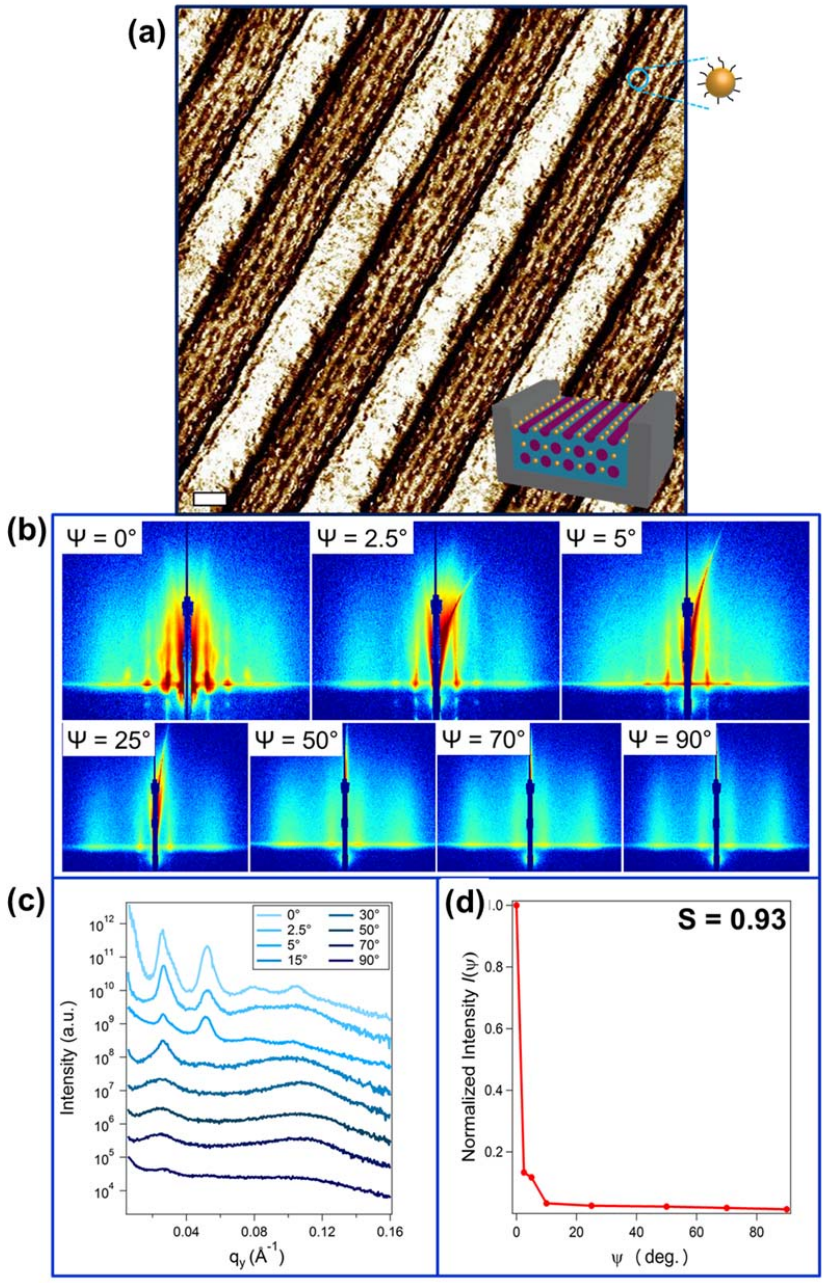

Figure 6.3. (a) AFM of the ~45 nm supramolecular nanocomposite thin films containing PS(19,000)-*b*-P4VP(5,200)(PDP)$_{1.7}$ and 3 vol% ~5 nm Au NPs deposited on P1. Dense arrays of highly aligned 1-D chains of Au NPs are clearly seen conforming to the unidirectional cylindrical microdomains. (b) GISAXS patterns of the sample at different Ψ. Higher order Bragg peaks can be observed at $\Psi = 0°$ and the peaks weaken as Ψ increases. (c) The q_y linecut at q_z = 0.0236 Å^{-1} for each GISAXS pattern in (b). (d) The dependence of the scattering intensity of the first-order peak on Ψ. Here, S is found to be 0.93, characteristic of highly-aligned cylindrical microdomains and NP arrays confined in the lithographic trenches. Scale bar = 100 nm.

Similar supramolecular nanocomposites with thicker film thicknesses were deposited on the same lithographic pattern to investigate the effect of t on the long-range order of the NP arrays. Figure 6.4a and 6.4b show the AFM images of the ~70 nm films containing PS(19,000)-*b*-P4VP(5,200)$(PDP)_{1.7}$ and a blend of the supramolecules and 5 vol% of ~8 nm PbSe NPs deposited on P1, respectively. The profiles below the AFM images demonstrate the intensity of pixels along the white dotted lines, which suggest a larger lateral periodicity of the microdomains on the mesas than that on the trenches. Figure 6.5a and 6.5b show the AFM images of the nanocomposite thin films containing PS(19,000)-*b*-P4VP(5,200)$(PDP)_{1.7}$ and 5 vol% ~8 nm PbSe NPs on P1 with t = 110 and 210 nm, respectively. The long-range order in up to 10 layers of NP chains is preserved even though the majority of the film is not confined in the trenches. The defect density begins to increase as t reaches 210 nm. For films with t > 350 nm, the long-range order of the NP assembly is no longer preserved under the solvent annealing

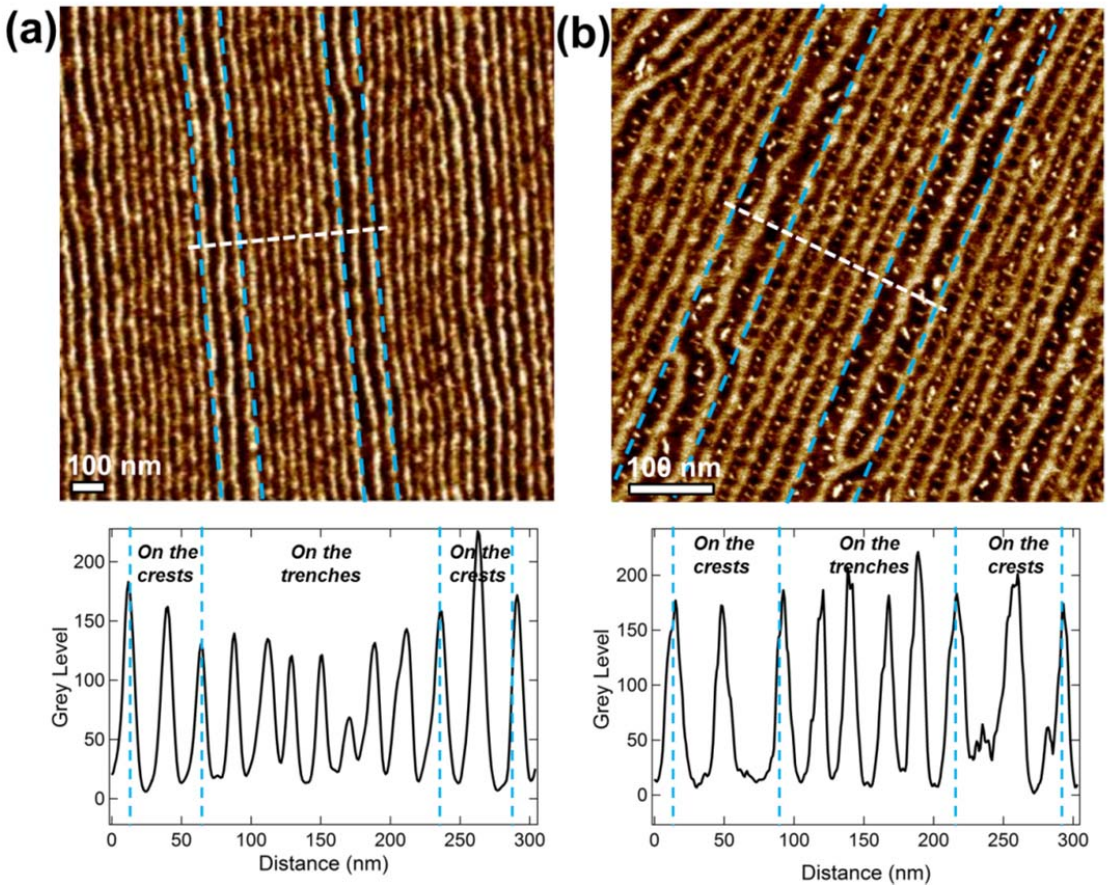

Figure 6.4. (a) and (b) show the AFM images of the ~70 nm films containing PS(19,000)-*b*-P4VP(5,200)$(PDP)_{1.7}$ and a blend of the supramolecules and 5 vol% of ~8 nm PbSe NPs deposited on P1, respectively. The profiles below the AFM images demonstrate the intensities of pixels along the white dotted lines, which suggest a larger lateral periodicity of the microdomains on the mesas than that on the trenches.

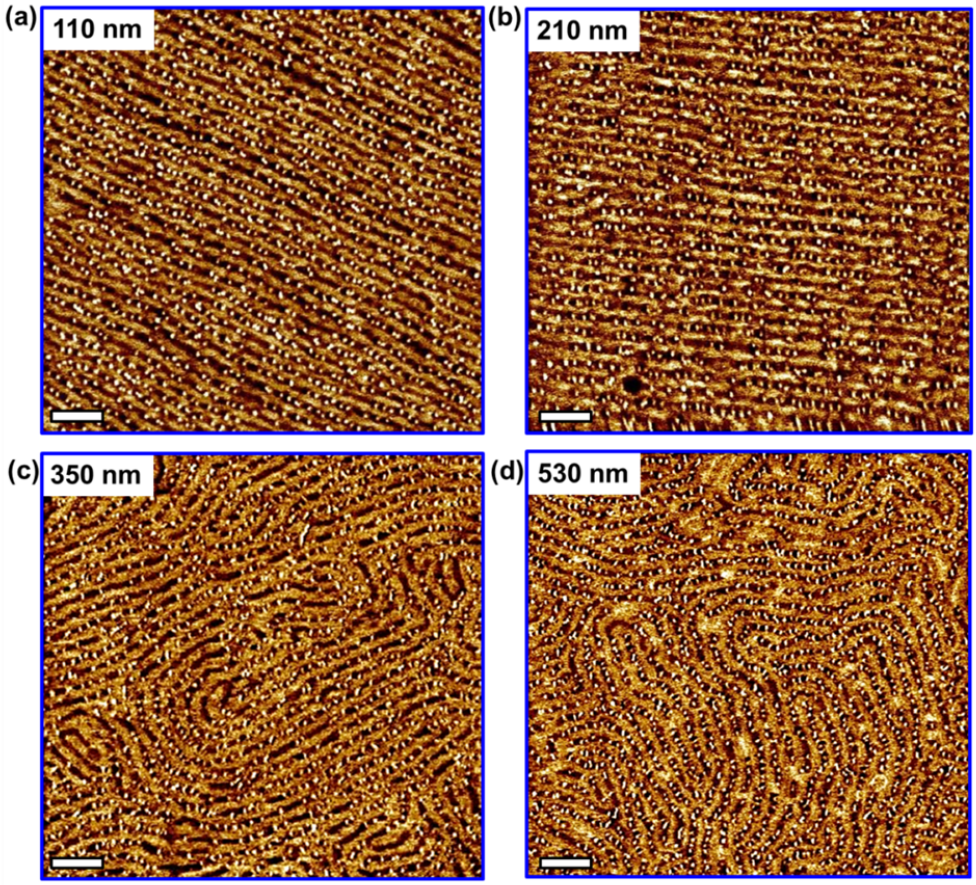

Figure 6.5. AFM images of thin films containing PS(19,000)-*b*-P4VP(5,200)(PDP)$_{1.7}$ and 10 vol% ~8 nm PbSe NPs deposited on P1 (trench width L = 125 nm, trench period 210 nm) with t = (a) 110, (b) 210, (c) 350, and (d) 530 nm. The 8 nm NPs were chosen for AFM imaging purposes.[13] The alignment of the microdomains confined in the trenches extends throughout the entire film thickness when $t \leq 210$ nm, yielding a dense array of 3-D NP arrays covering the complete surface over macroscopic distances. As $t > 300$ nm, the long-range order can no longer be maintained. Scale bar = 100 nm.

condition used here (Figure 6.5c and 6.5d). To probe the macroscopic alignment of the supramolecular nanocomposite thin film over large area, rotation GISAXS was conducted on the ~210 nm nanocomposite thin film shown in Figure 6.5b (L = 125 nm) (Figure 6.6). According to the GISAXS results, S of the ~210 nm supramolecular nanocomposite thin film was found to be ~0.92, confirming that the long-range lateral order of the nanocomposite film is still maintained at t = 210 nm.

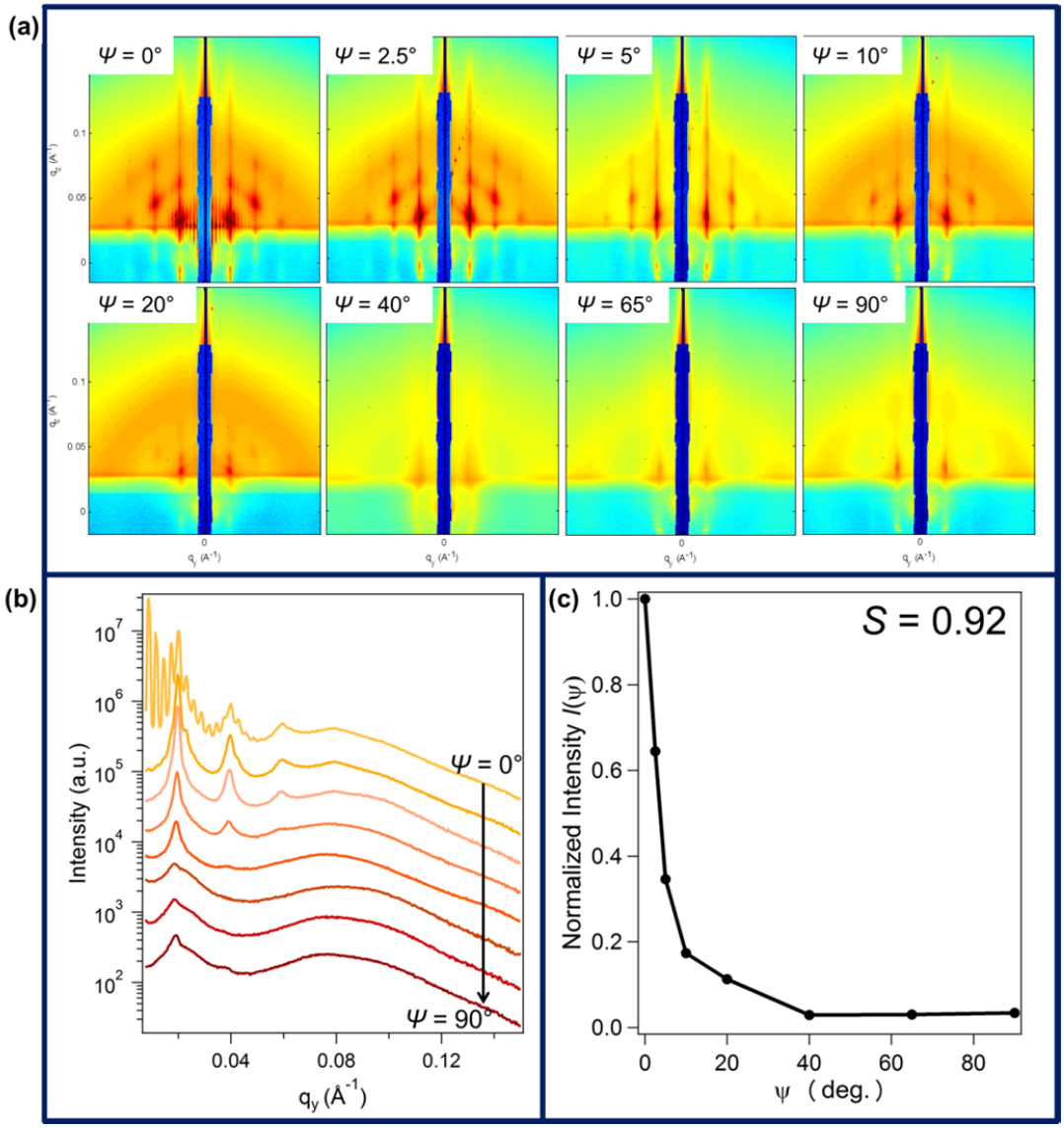

Figure 6.6. (a) GISAXS patterns and (b) q_y linecut at q_z = 0.0236 Å^{-1} of the ~210 nm thick supramolecular nanocomposite thin film containing PS(19,000)-*b*-P4VP(5,200)(PDP)$_{1.7}$ and 3 vol% ~5 nm Au NPs deposited on P1 (L = 125 nm) at different Ψ. Higher order Bragg peaks can be observed at Ψ = 0° and the peaks weaken as Ψ increases. (c) The scattering intensity of the first-order peak as a function of Ψ with S ~0.92, characteristic of highly ordered 3-D NP arrays.

When t = 70 nm, there are more than two layers of parallel cylinders that are not confined in the trenches when the long-range order of the nanocomposite is optimized at f_s = 0.31 during solvent annealing. At the moment the film deswells at the beginning of solvent removal, the fluidic supramolecules residing on the crests flow into the trenches, imposing a tensile stress and compressive stress on the cylindrical domains on the mesas and in the trenches, respectively.

Hence, the lateral periodicity of the supramolecules on the mesas becomes larger than that in the channels and the difference can be as large as 13 nm according to the analysis of the AFM images (Figure 6.4). This observation is corroborated by the result in Figure 6.4b with marker particles (8 nm PbSe NPs). Unlike those in the P4VP(PDP)$_{1.7}$ blocks on the trenches, the 1-D NP chains become undulated in the domains on the mesas. When the cylinders are under tensile stress along the short axis, more free volume may be generated among supramolecules. The NPs can move to these regions and form NP chains with less defined inter-particle ordering. This result confirms that the modulation of lateral periodicity in Figure 6.4a is real and is not simply caused by the tapping angle of the AFM tip. As there are only few layers of cylinders on the crests during solvent annealing, the flow force is not sufficient to induce any change of microdomain orientation and the overall alignment remains parallel to the trench direction. This holds true when the ratio of mesa width to trench width is small. As the crest becomes three times wider than the trench, the mass on the mesa significantly increases. The mass transport from the mesas to the trenches during solvent removal leads to a coexistence of microdomains aligned parallel and perpendicular to the trench direction as shown in Figure A.5.6. The results reveal that the flow of the supramolecules on rectangular trenches induces modulation of lateral periodicity of the microdomains without affecting the macroscopic alignment of the nanocomposite when the film barely covers the pattern. As t increases to above 110 nm, more than 50 vol% of the film is not confined in the trenches during solvent annealing. Therefore, the macroscopic alignment of the supramolecular nanocomposite on the pattern becomes less affected by the fluid dynamics of the supramolecules. Under the solvent annealing condition used here, the cylindrical microdomains/NP chains in the trenches align parallel to the trench direction, which further induces the macroscopic alignment of the microdomains beyond the channels with a constant lateral periodicity across the surface. At t > 350 nm, the confinement effect dissipates as the majority of the film is no longer confined in the trenches. Hence, the long-range order of the NP arrays breaks down and the supramolecular nanocomposite assumes fingerprint patterns similar to that observed on a flat substrate.

The 3-D structure of the 210 nm supramolecular nanocomposite thin film on P1 was further characterized by simulating the GISAXS pattern at $\Psi = 0°$. a and c of the hexagonal lattice of NP arrays are 31.5 and 47.5 nm, respectively and the distortion factor is ~0.87 (Figure 6.7a). In comparison to the same films on a flat surface, NP assemblies on the lithographic pattern yield an increase in c of 7% but a decrease in a of 6% (Figure 6.7b). Similar experiments and analysis were also conducted on two supramolecular nanocomposites on P1 with t around 350 and 530 nm (see A.5.7). The results reveal that the distortion factor remains around 0.82 though the orientation parameter drops as t increases.

When confined in the trenches with L = 125 nm, the average L/a ratio is 3.75. The supramolecular nanocomposites confined in the channels are compressed laterally to accommodate the incommensurability between L and a, which constrains a to be 31.5 nm to minimize the strain, giving 4 unit cells per trench. To keep the area and the packing density constant, c increases from 44.2 to 47.5 nm. This results in a larger distortion factor (0.87) and, hence, a less distorted hexagonal lattice of the 3-D NP arrays compared to those on a flat surface

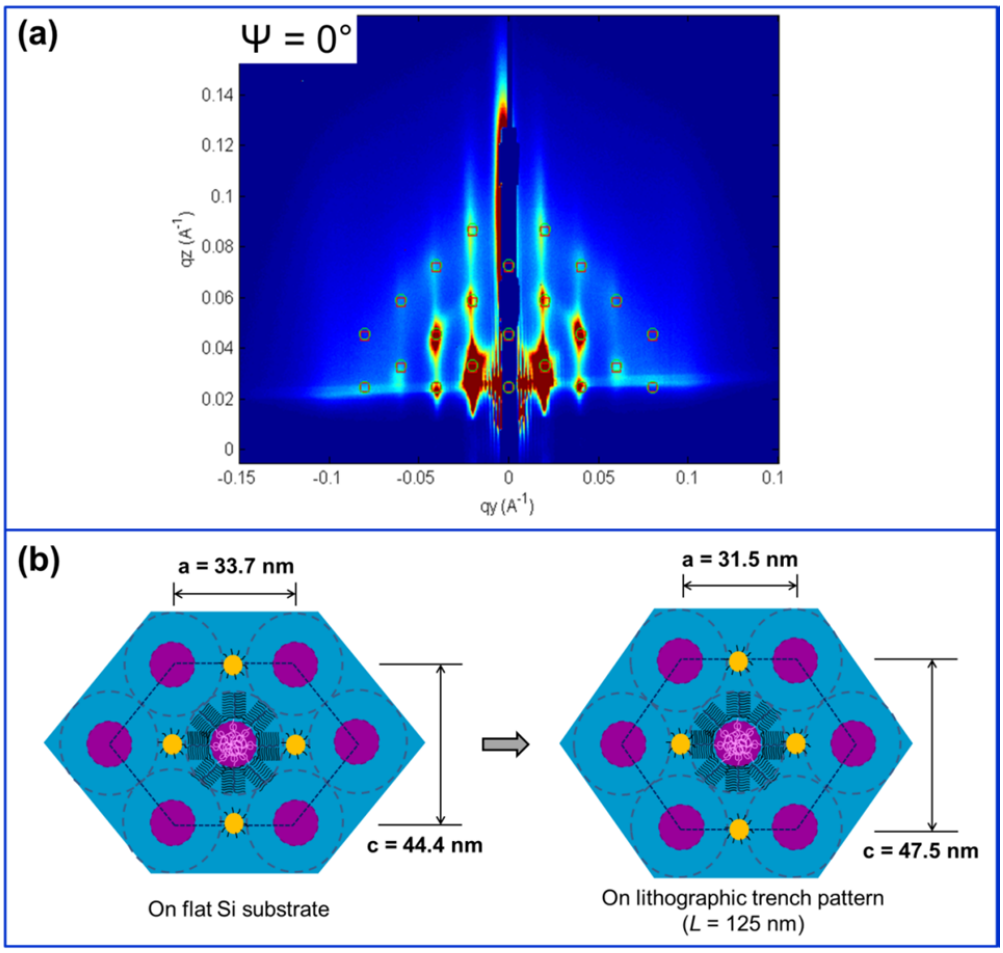

Figure 6.7. (a) GISAXS pattern of the ~210 nm supramolecular nanocomposite thin film at Ψ = 0° and the simulation of the Bragg spots corresponding to the in-plane hexagonally packed 3-D NP arrays with a distortion factor ~0.87. (b) Schematic drawing of the packing of the cylindrical supramolecules and the NPs in a distorted hexagonal lattice on a flat substrate in comparison to that on the lithographic trench pattern. In the schematics, the purple circles, the blue background, and the yellow circles represent the PS cylinders, the P4VP(PDP) matrix, and the NPs, respectively. The dark blue dotted line outlines a single hexagonal lattice cell.

when L/a = 3.75. The NP arrays and the supramolecules adjust their spatial organization to accommodate the increase of the distortion factor in the trenches and further induce the 3-D nanostructure throughout the entire film thickness. At this point, it is still unclear why the 3-D structure can prevail in a 530 nm thick film. Further investigation is required to elucidate the underlying physical reasons for this phenomenon.

To confirm that the change of the 3-D structure in the nanocomposite thin films is induced by the lateral confinement provided by the lithographic trenches, the effect of L/a was further studied for the ~200 nm film. Figure 6.8a-c show the AFM and GISAXS images at Ψ =

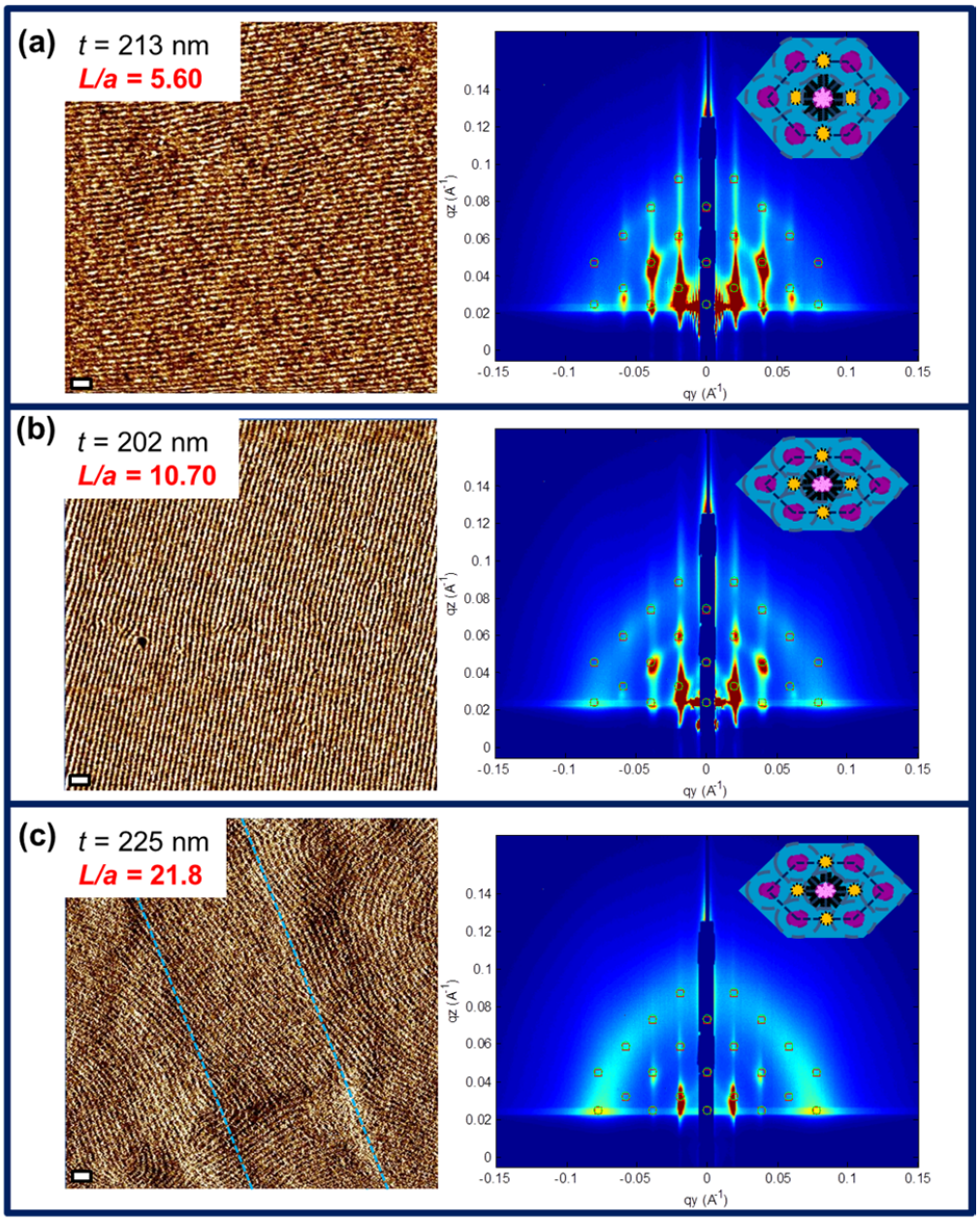

Figure 6.8. AFM and GISAXS images of the ~200 nm supramolecular nanocomposite thin films containing PS(19,000)-*b*-P4VP(5,200)$(PDP)_{1.7}$ and 3 vol% ~5 nm Au NPs deposited on lithographic trenches with (a) L = 186 nm, (b) L = 356 nm, and (c) L = 725 nm. The simulated 2-D GISAXS patterns were taken at $\Psi = 0°$. The long-range order breaks down at $L/a > 20$. The simulation of the GISAXS patterns reveals that the hexagonal lattice of the 3-D NP arrays in the nanocomposite becomes less distorted when $L/a < 5$. With $L/a > 10$, the lateral confinement from the trench walls is no longer effective so the 3-D structure in the film becomes similar to that on flat substrate. Scale bar = 100 nm.

0° of the ~200 nm films containing PS(19,000)-*b*-P4VP(5,200)$(PDP)_{1.7}$ and 3 vol% ~5 nm Au NPs deposited on lithographic patterns with L = 186 nm (L/a = 5.6), 356 nm (L/a = 10.7), and 725 nm (L/a = 21.8), respectively. When L/a is smaller than 11, the macroscopic alignment of the microdomains and NP arrays is maintained. The long-range order of the assembly breaks down when L/a > 20. Rotation GISAXS experiments were conducted on these samples and the order parameters are listed in Table 6.1. To characterize the 3-D structures in the nanocomposite thin films on different trenches, the GISAXS patterns were simulated as shown in Figure 6.8 and the calculated distortion factor for each film is listed in Table 6.1. The results reveal that the hexagonal lattice of the 3-D NP arrays is less distorted when L/a is small. As L/a increases to above 10, the distortion factor of the 3-D NP assemblies drops to 0.76, which is similar to that on a flat Si substrate.

Table 6.1

	L/a = 3.75	***L/a = 5.60***	***L/a = 10.70***	***L/a = 21.80***
t	210 nm	213 nm	202 nm	225 nm
S	0.92	0.91	0.87	0.59
a	31.5 nm	31.8 nm	32.4 nm	33.0 nm
c	47.5 nm	45.2 nm	42.6 nm	43.4 nm
Distortion Factor	0.87	0.82	0.76	0.76

When L/a < 10, the strain induced by the incommensurability between L and a needs be accommodated over a smaller number of cylindrical micordomains. This leads to laterally compressed supramolecules and a decrease of a by at least 6% in the trenches. The decrease in a further induces an increase in c so the packing density remains constant in each hexagonal unit cell. The 3-D structure in the channels direct the assembly throughout the entire film thickness, resulting in a larger distortion factor in the ~200 nm film when L/a < 10. As L/a becomes larger, the extra strain energy induced by the confinement can be easily dissipated by a small change in a or via defect formation in every trench. As the incommensurability effect becomes insignificant at large L/a ratios, the supramolecules assume the packing configuration similar to that on a flat substrate with distortion factor around 0.76. Figure 6.9 and Table 6.2 summarize the GISAXS patterns and the simulated 3-D structures of the NP assemblies in ~200 nm nanocomposite thin films deposited on different topographic surfaces. Unlike the flat or faceted substrate, lithographic trenches impose lateral confinement on the supramolecular nanocomposite, inducing a change in the lateral as well as the vertical lattice constants of the 3-D NP assemblies. By using lithographic trench patterns with different geometric dimensions, the 3-D structure of supramolecular nanocomposite thin films can be precisely tailored, especially when L/a < 10 in this particular system.

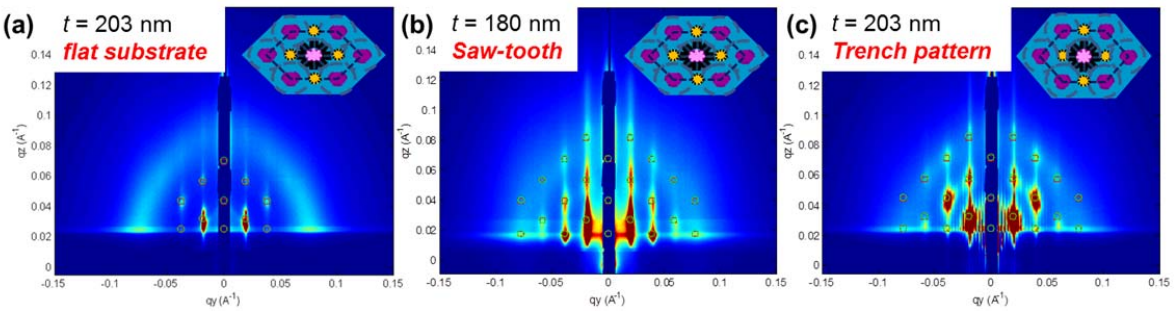

Figure 6.9. Simulated GISAXS patterns of ~200 nm films containing PS(19,000)-*b*-P4VP(5,200)(PDP)$_{1.7}$ and 3 vol% ~5 nm Au NPs deposited on flat Si substrate, saw-toothed sapphire substrate (λ = 140 nm, Ψ = 0°), and lithographically patterned surface (L = 125 nm, Ψ = 0°). The 3-D hexagonally packed NP arrays on flat and faceted substrates share similar vertical as well as lateral lattice constants whereas the ones on lithographic trench pattern are packed into a less distorted hexagonal lattice with a distortion factor as large as 0.87. This suggests that 3-D structure of the NP assemblies in the supramolecular nanocomposite can be tailored using lithographically patterned substrates.

Table 6.2

	On flat Si	***On saw-tooth pattern***	***On lithographic trenches (L/a = 3.75)***
t	203 nm	180 nm	210 nm
a	33.3 nm	33.2 nm	31.5 nm
c	44.2 nm	43.7 nm	47.5 nm
Distortion Factor	0.77	0.76	0.87

So far, the discussion has focused on the 3-D structure of the supramolecular nanocomposites on lithographic patterns. As shown previously, the trenches effectively guide the macroscopic alignment of the microdomains when L/a is small. In addition to the lateral confinement provided by the trench walls, our preliminary data shows that the macroscopic alignment of the nanocomposite can be significantly altered by solvent annealing. Figure 6.10 shows the AFM image of a ~40 nm film containing PS(19,000)-*b*-P4VP(5,200)(PDP)$_{1.7}$ and 3 vol% ~5 nm Au NPs confined in the trenches with L = 125 nm. During solvent annealing, t reached 115% of its original film thickness (f_s = 0.13) before the termination of the annealing. Four rows of hexagonally packed perpendicular PS cylinders are observed in each channel. In this case, the trench walls direct the long-range order of the cylindrical domains, leading to closed-packed, defect-free perpendicular nanostructures extending across the trench. By simply

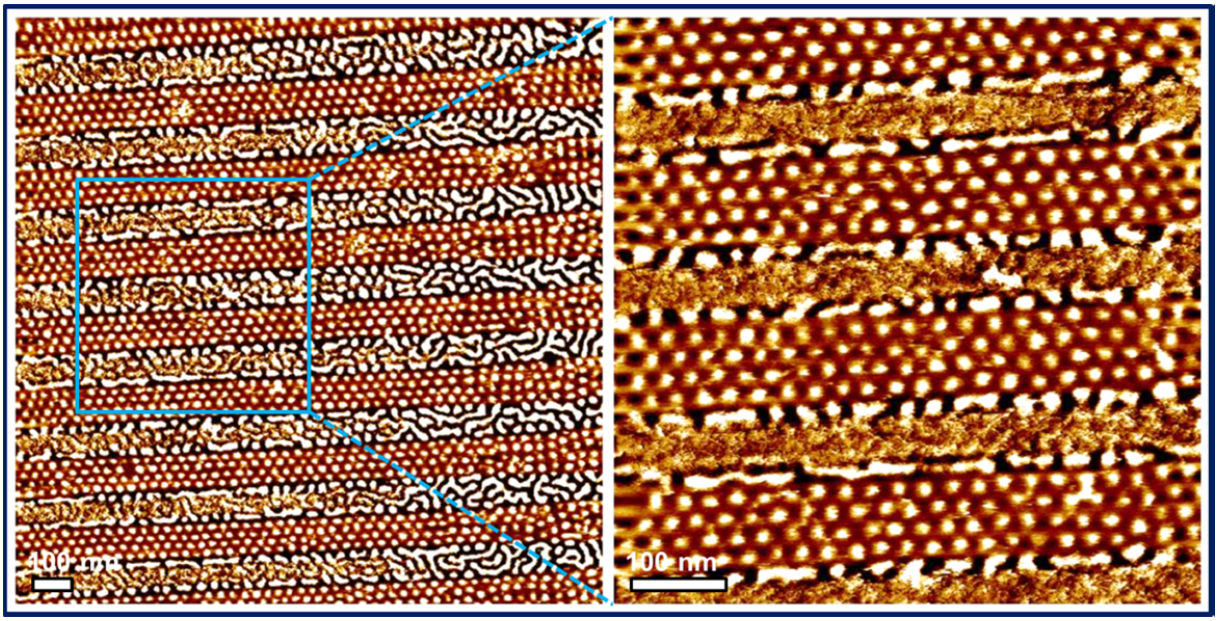

Figure 6.10. AFM image of the a ~40 nm film containing PS(19,000)-*b*-P4VP(5,200)$(PDP)_{1.7}$ and 3 vol% ~5 nm Au NPs confined in the trenches with L = 125 nm. The solvent was removed from the film at f_s = 0.13 during solvent annealing. The trench walls impose lateral confinement on the supramolecules, leading to four rows of defect-free hexagonally packed perpendicular cylinders over micrometer scales in every trench.

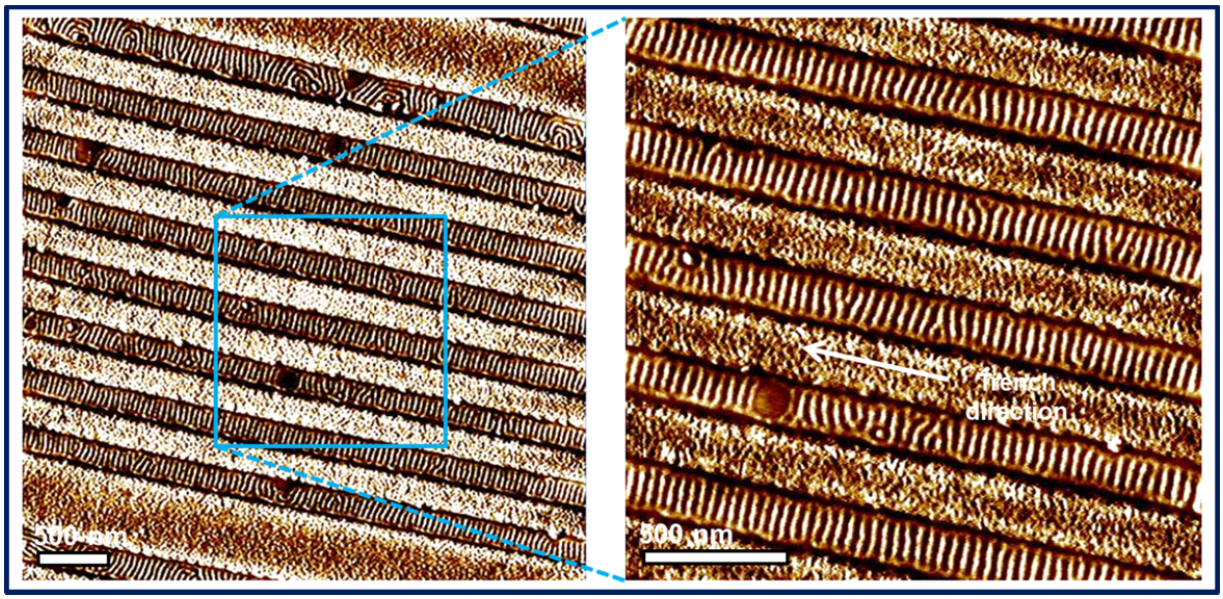

Figure 6.11. AFM image of a ~40 nm film of PS(19,000)-*b*-P4VP(5,200)$(PDP)_{1.7}$ confined in the trenches with L = 125 nm (L/a = 3.75). During solvent annealing, the film swelled to > 145% of its original film thickness (f_s > 0.3). After solvent annealing, the cylinders no longer align along the trench direction. Instead, they become oriented normal to the trench walls.

varying the solvent content in the film during annealing, the macroscopic orientation of the NP arrays/micrdomains can be controlled to be in-plane or out-of-plane. This is consistent with that observed in the previous chapter.

At f_s = 0.3, the supramolecular nanocomposite confined in the lithographic trenches align parallel to the trench direction, forming unidirectional NP arrays in the channels. At higher f_s, the supramolecules may find a new energy minimum and form cylindrical domains oriented normal to the trench direction. Figure 6.11 shows the AFM image of a ~40 nm film of PS(19,000)-*b*-P4VP(5,200)$(PDP)_{1.7}$ confined in the trenches with L = 125 nm. During solvent annealing, the film swelled to > 145% of its original film thickness (f_s > 0.3). Unlike that shown previously, the cylindrical microdomains are oriented perpendicular to the trench direction (Figure 6.11). The P4VP(PDP) chains still wet the SiO_2/Si trench walls, guiding the macroscopic alignment of one neighboring PS cylinder along the trench direction. However, this alignment does not propagate into the channel. Instead, both PS and P4VP(PDP) domains interface with the PS cylinder and orient 90° to the trench walls, forming stair-like structure in each channel.

When a BCP film is confined between two infinite, parallel plates with significant mismatch between the plat separation distance and the equilibrium periodicity of the microdomains, a vertical morphology may be realized in the film to effectively eliminate the entropic penalty from chain deformation.[30] As demonstrated previously, the supramolecules can usually accommodate the incommensurability between L and a by chain stretching/compression without inducing any change of microdomain orientation. In the trenches, the P4VP(PDP) chains form a brush layer on the trench walls due to their favorable interactions with the native oxide layer on Si. At high f_s during solvent annealing, some unbound PDP small molecules are solubilized in the PS blocks and they become more uniformly distributed in the film. The PDP as well as the solvent molecules effectively neutralize the thin PS layer next to the P4VP(PDP) chains pinned on the trench walls. This makes it much less energetically costly to generate extra PS/P4VP(PDP) interfacial area to align the microdomains perpendicular to the PS layer to alleviate the entropic penalty from laterally confined supramolecules.

This hypothesis is supported by two pieces of evidence. According to a series of AFM images taken *ex situ* as a function of f_s/annealing time, semicircular rings of cylinders, which are highlighted in Figure A.5.8, appear in the trenches as f_s goes above 0.3. They alter the alignment of the neighboring supramolecules, acting as growth fronts for the microdomains oriented normal to the trench direction. This confirms that the interfacial interactions between the two blocks are mediated by the solvent and PDP small molecules, leading to the reorientation of the microdomains from parallel to perpendicular to the trench direction at high f_s. In addition, the role of the incommensurability effect was investigated by annealing the supramolecular thin film deposited on a substrate with trenches of different L. Under the same solvent annealing condition, the supramolecules confined in the trenches with L = 200 nm form cylinders oriented normal to the trench walls whereas they align parallel to the trench direction in the channels that have L > 400 nm (Figure A.5.9).

The microdomains oriented normal to the trench walls in the channels may further guide the macroscopic alignment of the supramolecules beyond the trench volumes in a thicker film. Figure 6.12a-c show the AFM images of the ~140 nm PS(19,000)-*b*-P4VP(5,200)$(PDP)_{1.7}$ films

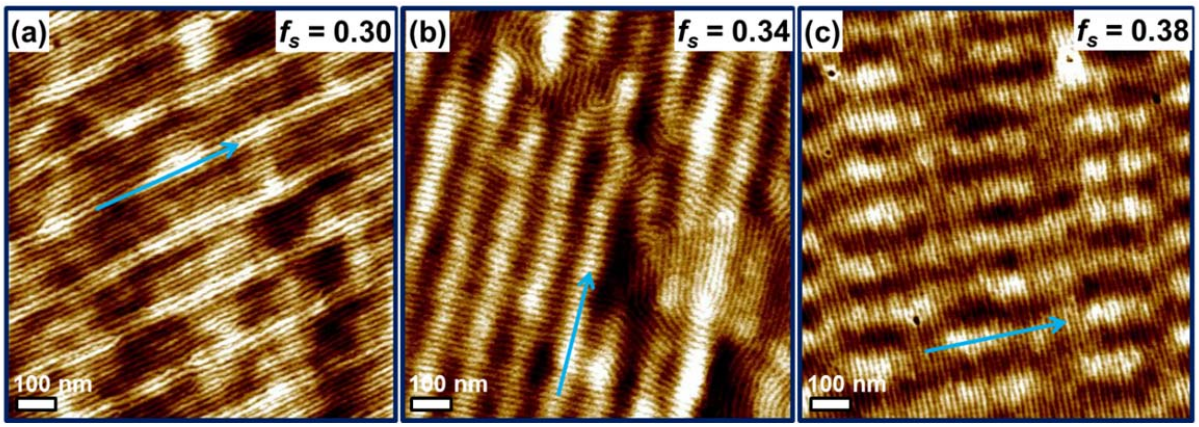

Figure 6.12. (a), (b), and (c) show the AFM images of the ~140 nm PS(19,000)-*b*-P4VP(5,200)$(PDP)_{1.7}$ films on P1 (L = 125 nm) that were swollen to 143% (f_s = 0.30), 152% (f_s = 0.34), and 160% (f_s = 0.38) of its original film thickness during solvent annealing, respectively. The blue arrow indicates the trench direction. At f_s = 0.30, the cylindrical microdomains align parallel to the trench direction. As f_s increases, the cylinders undergo a reorientation that switches the alignment to be perpendicular to the trenches.

on P1 (L = 125 nm) that are swollen to 143% (f_s = 0.30), 152% (f_s = 0.34), and 160% (f_s = 0.38) of its original film thickness during solvent annealing, respectively. Unidirectionally aligned cylinders along the trench direction are observed at f_s = 0.30 (Figure 6.12a). As the film reaches a higher swelling ratio during annealing, some cylinders become oriented perpendicular to the trench direction (Figure 6.12b). Two configurations of macroscopic alignment coexist and are in competition with each other. At f_s larger than 0.3, small grains of the cylinders oriented normal to the trenches grow into larger ones, covering the majority of the surface area (Figure 6.12c). In some regions, however, the microdomains oriented parallel to the trenches can still be observed (Figure A.5.10). This indicates that the two local energy minimums have similar energy levels and the final morphology of the film is dependent on the kinetic pathway during solvent annealing.

The *ex situ* AFM results were further validated by the *in situ* GISAXS measurements on similar supramolecular nanocomposite thin films on P1 with the X-ray beam parallel and perpendicular to the trench direction (see A.5.11 and A.5.12). When the X-ray beam is parallel to the trenches, the Bragg spots corresponding to the hexagonally packed in-plane 3-D NP arrays aligned parallel to the trench direction reach highest intensity at f_s = 0.3 during solvent annealing (Figure A.5.11). Between f_s = 0.3 and 0.35, these Bragg spots weaken and the structure factor from the inter-particle ordering becomes dominant. When f_s reaches 0.39, the scattering from the

3-D NP arrays disappears and only the Bragg peaks corresponding to the inter-particle distance in the microdomains are present in the GISAXS pattern. At $f_s > 0.4$, order-disorder transition occurs in the nanocomposite. The *in situ* results indicate that the reorientation of the microdomains/NP arrays happen between $f_s = 0.3$ and 0.35, which is consistent with that shown in Figure 6.12. Similar *in situ* experiments were conducted on the same nanocomposite thin film on P1 with the X-ray beam aligned perpendicular to the trench direction (Figure A.5.12). In this case, an opposite trend was observed. At $f_s = 0.3$, sharp Bragg peaks corresponding to the inter-particle distance in the NP arrays are seen in the GISAXS pattern, suggesting a perpendicular orientation of the microdomains with respect to the X-ray beam. At $f_s = 0.33$, the 2-D scattering pattern corresponding to the aligned 3-D NP arrays instantaneously show up and it becomes optimized at $f_s = 0.38$. This indicates that the cylindrical microdomains reorient to align normal to the trench direction at $f_s > 0.3$.

These results corroborate the observation that the solvent annealing condition alters the local energy minimum, and therefore the preferred macroscopic alignment of the surpamolecules on lithographic trench patterns. At high f_s, the cylindrical domains undergo a reorientation from parallel to perpendicular orientation with respect to the trench walls in the channels. This further induces a switch of the macroscopic alignment of the microdomains throughout the entire film thickness. By tailoring the swelling ratio of the film on lithographic trenches with relatively small L/a, not only the NP chains aligned parallel or normal to the trench direction alone, but also mixtures of both orientations may be fabricated in supramolecular nanocomposite thin films. To gain further control over the solvent annealing processing condition, in-depth investigation using *in situ* GISAXS is required and is currently under investigation.

§ 6.3 Conclusion

In summary, macroscopically aligned 3-D NP arrays can be achieved by guided assembly of supramolecular nanocomposite thin films using faceted substrates and lithographic trench patterns. The long-range order of more than 10 layers of NP chains in thick nanocomposite films can be preserved over macroscopic distances. Moreover, the lateral confinement is effective for trench patterns with widths < ~10 times the lateral periodicity of the supramolecular nanocomposite. By varying the solvent annealing condition, the spatial distribution of small molecules may be tailored to alter the orientation of the NP arrays/microdomains in local equilibrium. In addition, the lateral confinement provided by the trench walls may allow further structural tailoring of the 3-D NP arrays in the supramolecular nanocomposite by changing the c/a ratio of the unit cell of the structure. Present studies provide simple yet versatile routes to obtain macroscopically aligned hierarchical NP assemblies with tunable 3-D structures for the investigation of structure-property relationships in this new family of functional materials. This provides a powerful platform to test theoretical predictions of nanocomposite properties to ultimately harness the emerging macroscopic responses in functional nanocomposites for various applications.

§ 6.4 Experimental section

6.4.1 Sample preparation

PS(19 kDa)-*b*-P4VP-(5.2 kDa) (PDI = 1.09) and 3-n-Pentadecylphenol were dissolved together in $CHCl_3$ and stirred over a week to form supramolecules. PS(19 kDa)-*b*-P4VP-(5.2 kDa) (PDI = 1.09) was purchased from Polymer Source, Inc. and 3-n-Pentadecylphenol (95%) was purchased from Acros. All chemicals were used as received. Au and PbSe NPs were synthesized using the reported methods. Thin films with blends of supramolecules and NPs were prepared as described previously by spin-coating the solutions onto lithographically patterned Si wafers and faceted sapphire substrates with spinning speeds ranging from 1000 to 3000 rpm. For solvent annealing, samples were annealed for 8 minutes using 300 μL $CHCl_3$ injected into a 250 mL Teflon chamber at room temperature and 45% humidity. The films reached 150% of their original film thicknesses during solvent annealing. To terminate the annealing process, the chamber was opened and the $CHCl_3$ solvent vapor in the chamber was allowed to freely evaporate.

6.4.2 Fabrication of lithographically patterned substrates

The 50 nm deep periodic trench patterns were generated exposing a trilayer resist stack (resist/silica etch mask/antireflective coating) on an oxidized Si substrate using a Lloyd's Mirror interference lithography system with a He-Cd laser (λ = 325 nm), developing the resist, transferring the pattern into the etch mask then the ARC, and finally reactive ion etching with CF_4 plasma to transfer the pattern into the oxide. The facets were produced by thermally annealing a single crystal surface of sapphire, cut along the M-plane (a crystallographic plane that is unstable at elevated temperatures), at 1500°C for 24 h in air. The surface reconstructed to form stable crystal facets, resulting in a saw-toothed topography over the entire surface, where the orientation of the facets was in register with the underlying single crystal. No surface modification was employed on the lithographically patterned or faceted substrates.

6.4.3 Fabrication of saw-toothed patterns

Sapphire (a-Al_2O_3), cut along the M-plane, was annealed at 1300 C for 24 hours in a conventional furnace to produce the crystalline facets that form a saw-toothed pattern on the entire surface.

6.4.4 Atomic force microscopy

Atomic force microscopy was performed on a Veeco Dimension 3100 with a Nanoscope III controller and a Quadrex extension box. The spring constant of the cantilever was 10 − 130 N m^{-1} with a resonant frequency in the range of 300–500 kHz. The set point for auto tune was ~1.5 V. The set-point amplitude was 90% of the free vibration value.

6.4.5 Rotation GISAXS Measurements

Rotation GISAXS Measurements were made at beamline 7.3.3 in Advanced Light Source and beamline 8-ID-E in the Advanced Photon Source in Lawrence Berkeley National Laboratory. The angle between the direction of the X-ray beam and the direction of the microdomains, Ψ, was varied between 0° and 90°. To avoid strong scattering from the lithographic pattern at $\Psi = 0°$, the incidence angle was set to be 0.1° and the exposure time for each measurement was 0.3s for consistent data acquisition. Line averaged intensities were reported as I vs. q, where $q = (4\pi/\lambda)\sin(\theta/2)$, λ is the wavelength of incident X-rays, and θ is the scattering angle. The orientation parameter for a 2D system, S, was calculated using the following equation:[31]

$$S = 2\left(\frac{\sum I(\Psi)\cos^2(\Psi)}{\sum I(\Psi)}\right) - 1$$

where $I(\Psi)$ is the scattering intensity of the first-order peak at Ψ and the summation was done between 0° and 90°.

Afterword

Supramolecular nanocomposite thin films clearly hold great promise as an interesting class of functional materials with applications in novel electronic, optical, and magnetic devices and beyond. Research in this area often lies at the interface between many disciplines as this new class of inorganic-organic hybrid materials combines the polymer and nanomaterial fields. From a materials science and engineering point of view, structural control over the co-assembly into well-defined nanostructures is necessary to realize the full potential of each building block in the nanocomposites. Due to the unique architecture of the supramoelcule and many non-covalent interactions involved in the co-assembly, not only the enthalpic, but also the entropic contributions influence the morphology of the nanocomposite. Detailed structural characterization allowed us to decipher the complex interplay among these energetic contributions. By tailoring the chain conformation, supramolecule composition, nanoparticle size, and nanoparticle loading, a delicate balance of conformational entropy, particle/polymer enthalpic interactions, and surface energy has been achieved to generate targeted 1-D, 2-D, and even 3-D nanoparticle assemblies over multiple length scales in thin films. The fundamental knowledge gained in this dissertation lays down a solid foundation for further exploration of the energy landscape in the system. Engineering the ligand chemistry of the nanoparticles will expand the toolbox for manipulating the co-assembly, and thereby the collective properties of the supramoelcular nanocomposites.

To realize these nanocomposites for real applications, the kinetics of the co-assembly needs to be fully understood to optimize processing parameters for manufacturing-friendly roll-to-roll nanofabrication. Preliminary results demonstrate that the diffusion coefficient and the thermodynamic driving force for defect elimination can be precisely tuned to facilitate the assembly of highly ordered nanoparticle arrays by simply controlling solvent and small molecule fractions in the nanocomposites during solvent annealing. In order to translate the developed processing technique from lab bench to plant, the processing parameters need to be optimized. Toward this end, *in situ* scattering is a very powerful tool used to deduce the kinetic pathway and nanoparticle/polymer chain dynamics in the co-assembly. Evaluating the thermodynamics as well as the dynamics in self-assembled nanocomposites may potentially enable rapid, reproducible bottom-up fabrication of functional materials that meets industrial standards for high-volume manufacturing.

We are only in the initial stages of these studies and there is a lot of potential waiting to be harnessed in the years to come. While the results are encouraging, a lot remains to be done in order to provide materials solutions that can facilitate the necessary advances in nanocomposite-based devices to become performance and cost competitive with existing technologies. As small molecule synthesis and polymer synthetic methodology advance and become more mainstream, exciting new opportunities will emerge for the fabrication of next-generation smart nanocomposites that have multiple functionalities, stimuli-responsiveness, and tunable physical properties. As we approach these milestones, and as the supramolecular approaches mature, computational design and simulation will become more important than ever to provide insights into the assembly process for the rational design of supramolecular nanocomposite thin films with functionality as desired. It is my hope that the readers take this work as an inspiration to further advance this rising field and implement it in the fabrication of advanced functional materials.

Appendix

A.1 Supporting Information for Chapter 2

A.1.1 Nanoparticle size analysis:

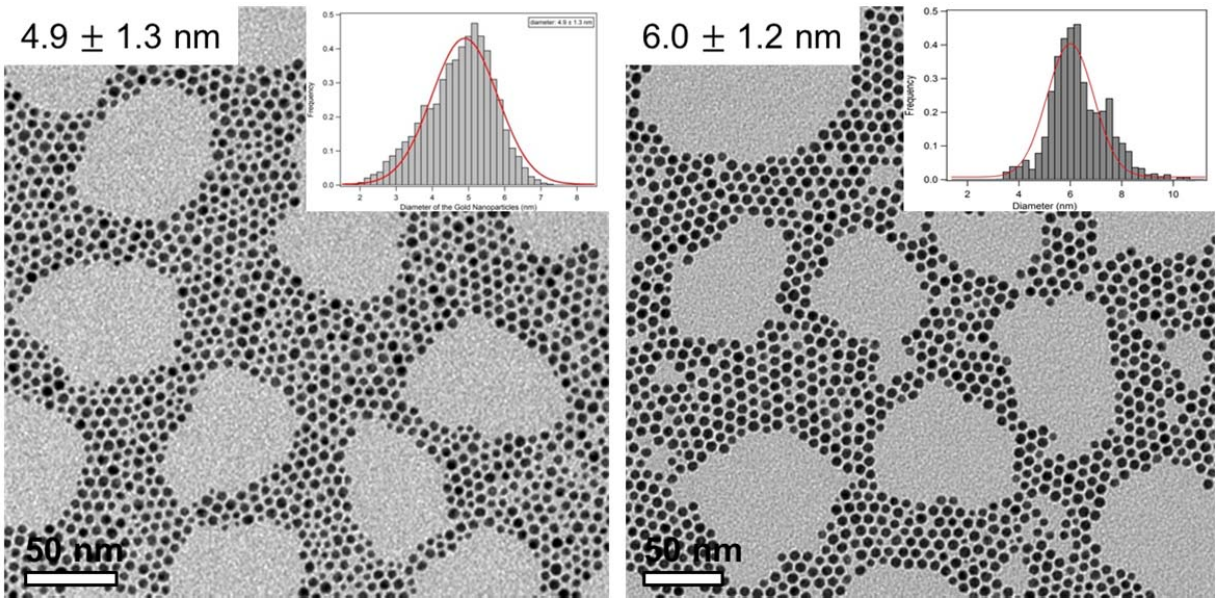

A.1.1. TEM images of the two batches of Au nanoparticles used. The average core diameters of the nanoparticles were found to be around 4.9 ± 1.3 nm and 6.0 ± 1.2 nm by image analysis using ImageJ.

A.1.2

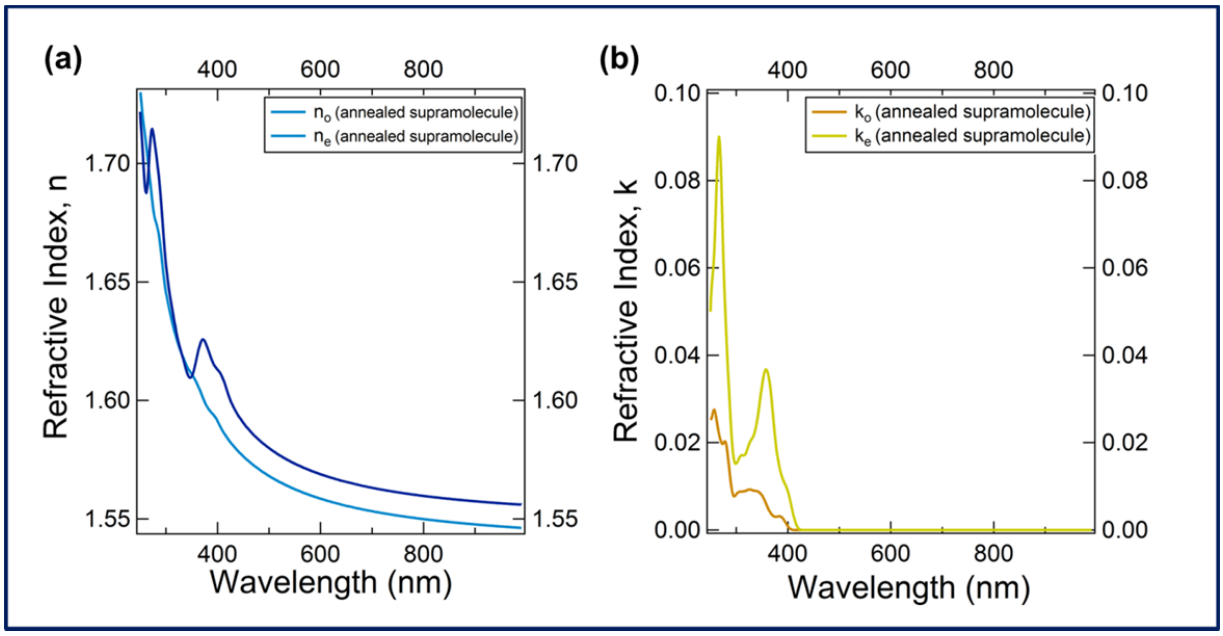

A.1.2. Experimentally measured complex refractive indices of the annealed supramolecular thin film containing PS(19 kDa)-*b*-P4VP(5.6 kDa)$(PDP)_{1.7}$ alone. The wavelength dependence of the real part and the imaginary part of the refractive indices are plotted from 250 nm to 1000 nm in (a) and (b), respectively. $n_o + ik_o$ and $n_e + ik_e$ represent the in-plane and out-of-plane components of the complex refractive indices, respectively. Weak wavelength dependence of n and k is observed from 450 to 600 nm, confirming that the optical anisotropy of the annealed cylindrical nanocomposite thin film shown in Figure 2.8 arises from the hierarchically ordered Au nanoparticles in the film.

A.1.3

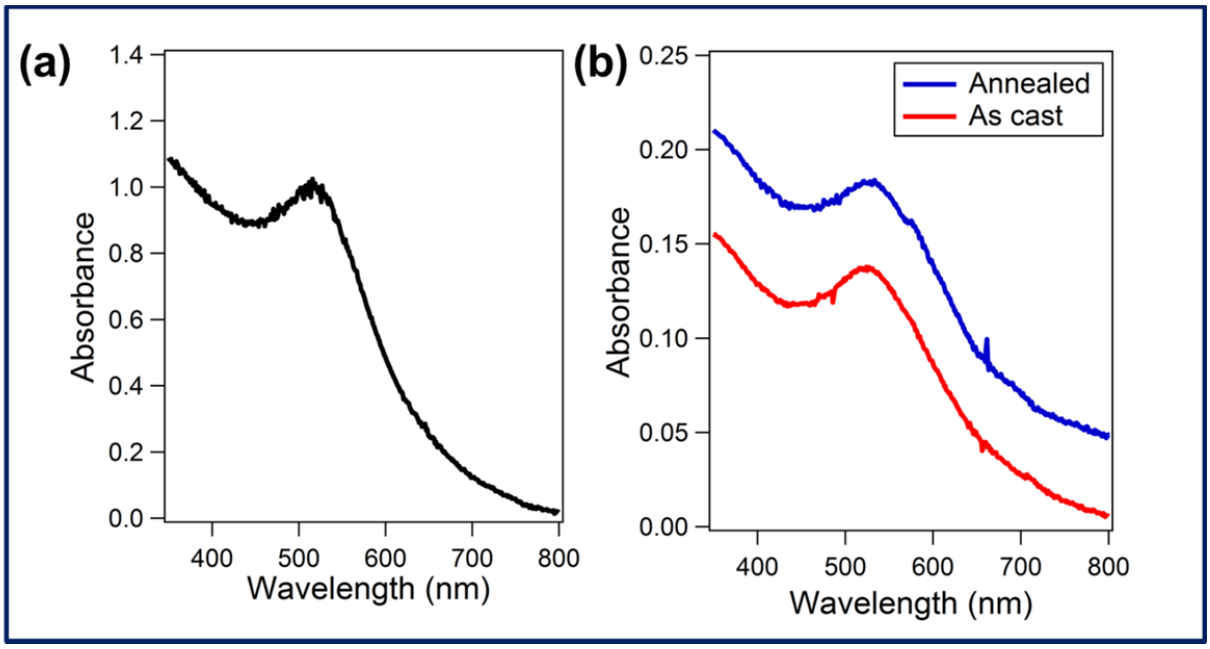

A.1.3. UV-Vis spectra of (a) the dilute solution of ~4.9 nm Au nanoparticles in $CHCl_3$ and (b) the as-cast and annealed cylindrical supramolecular nanocomposite thin films containing PS(19 kDa)-*b*-P4VP(5.6 kDa)$(PDP)_{1.7}$. and 3 vol% of 5 nm Au nanoparticles. The as-cast and annealed supramolecular nanocomposite thin films both have absorption peaks at 525 nm, similar to that of the Au nanoparticles alone. This indicates that the unique optical properties of the annealed film shown in Figure 2.8 originate from the collective macroscopic response of the hierarchically structure nanoparticle assembly instead of the plasmonic coupling between individual Au nanoparticles.

A.2 Supporting Information for Chapter 3

A.2.1 Nanoparticle size analysis:

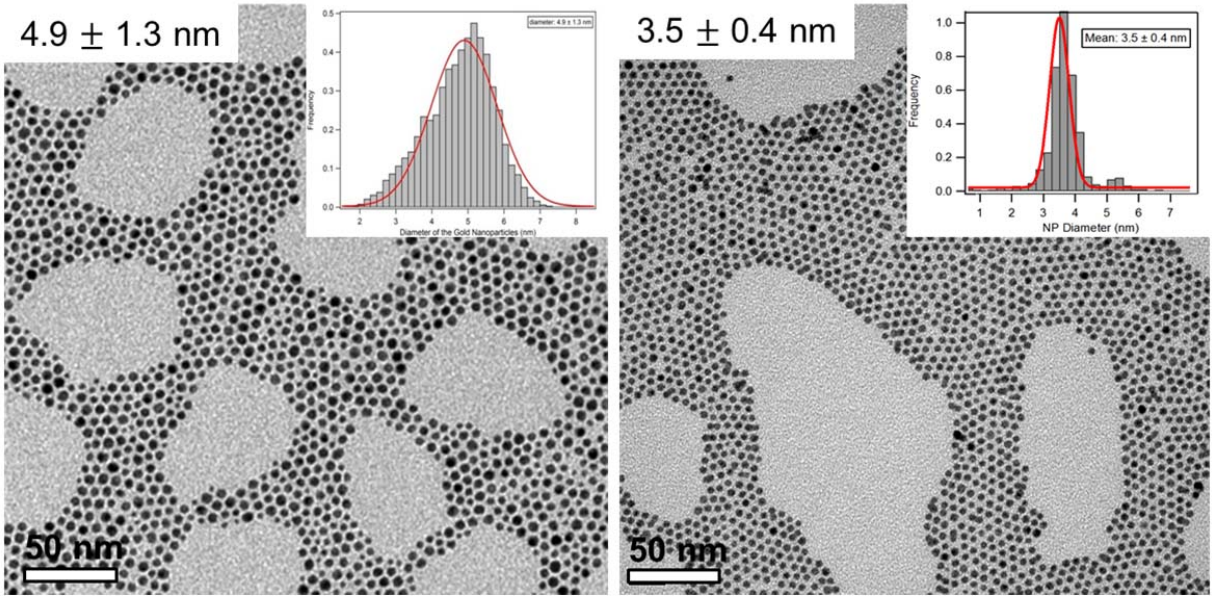

A.2.1. TEM images of the two batches of Au nanoparticles used. The average core diameters of the nanoparticles were found to be around 4.9 ± 1.3 nm and 3.5 ± 0.4 nm by image analysis using ImageJ.

A.2.2

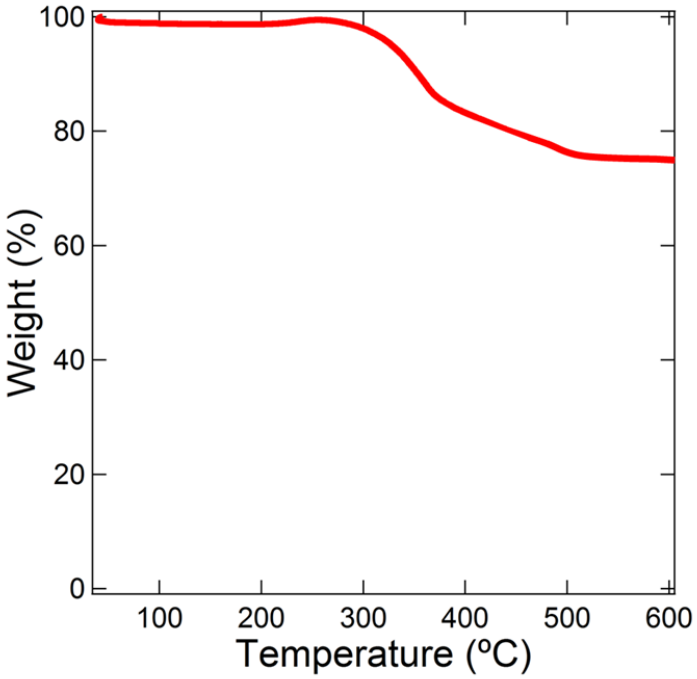

A.2.2. TGA profile of the Au nanoparticles dried from a ~1 wt% solution in $CHCl_3$. 24 wt% of the entire mass is from 1-dodecanethil ligands, which were completely carbonized after heating the sample to above 600 °C. This suggests that the Au core only accounts for 76 wt% of the contents in the nanoparticle solution.

A.2.3

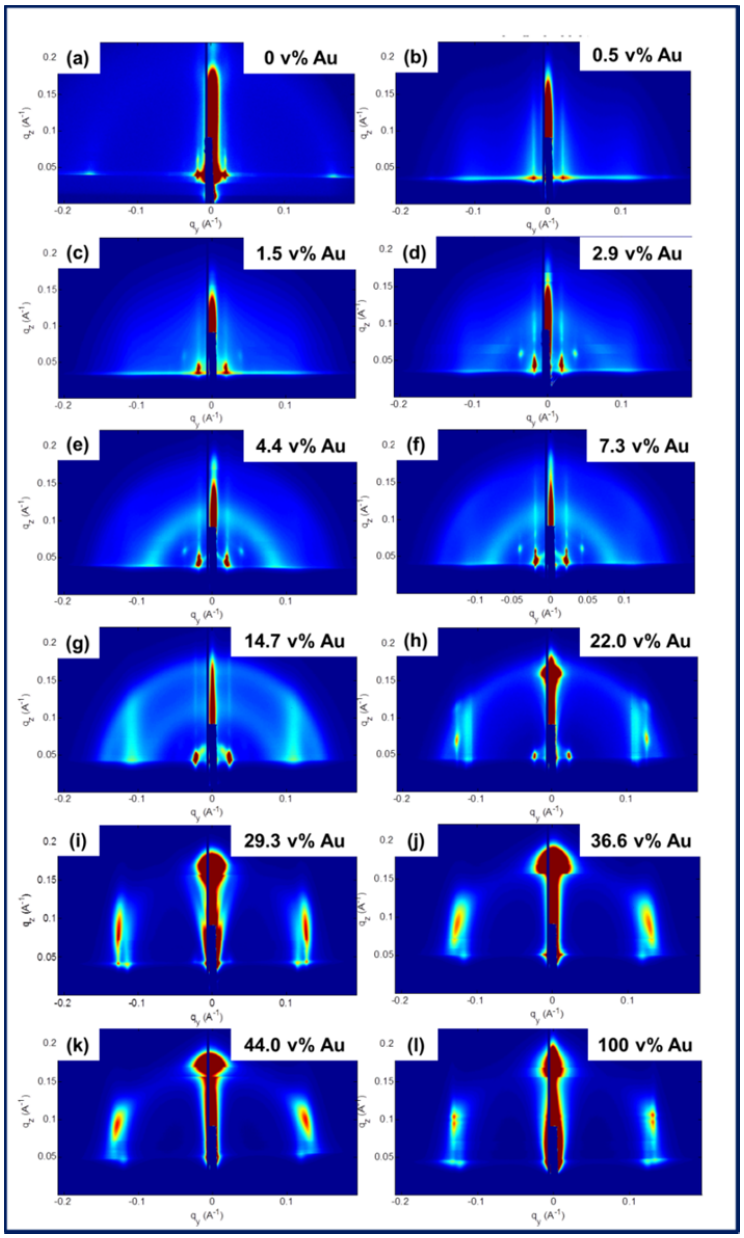

A.2.3. GISAXS patterns of the supramolecular thin films containing PS(19 kDa)-*b*-P4VP(5.2 kDa)$(PDP)_{1.7}$ and (a) 0, (b) 0.5, (c) 1.5, (d) 2.9, (e) 4.4, (f) 7.3, (g) 14.7, (h) 22.0, (i) 29.3, (j) 36.6, (k) 44.0, and (l) 100 vol% of ~4.9 nm Au nanoparticles. The GISAXS patterns were taken at incident angles around 0.21°, 0.22°, 0.22°, 0.22°, 0.22°, 0.23°, 0.24°, 0.27°, 0.29°, 0.31°, 0.35°, and 0.40°, respectively.

A.2.4

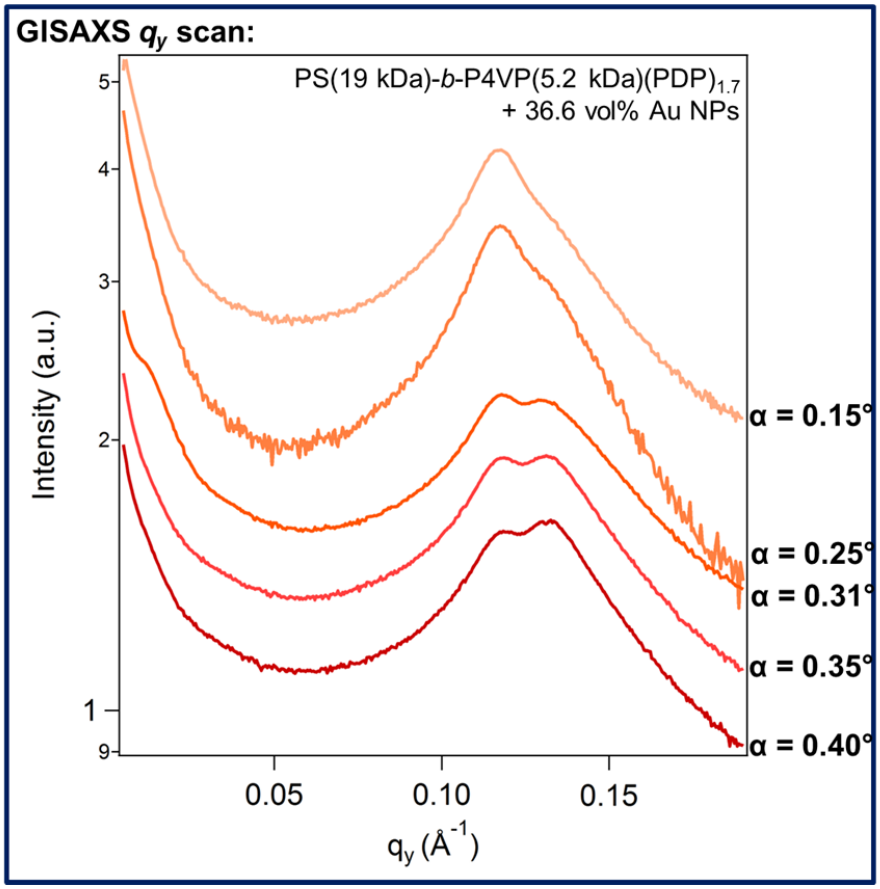

A.2.4. GISAXS q_y scans at 0.15°, 0.25°, 0.31°, 0.35°, and 0.40° for the supramolecular thin film containing PS(19 kDa)-*b*-P4VP(5.2 kDa)(PDP)$_{1.7}$ and 36.6 vol% of ~4.9 nm Au nanoparticles. When the incident angle is small, only the Bragg peak at q_y = 0.12 Å^{-1} can be seen on the q_y scans. As the incident angle increases, a second peak at q_y = 0.13 Å^{-1} begins to show up with increasing intensity. This indicates that the inter-particle distances in the *h.c.p.* nanoparticle lattices near the surface and in the interior of the film are different, which are around 5.4 and 4.8 nm, respectively.

A.2.5

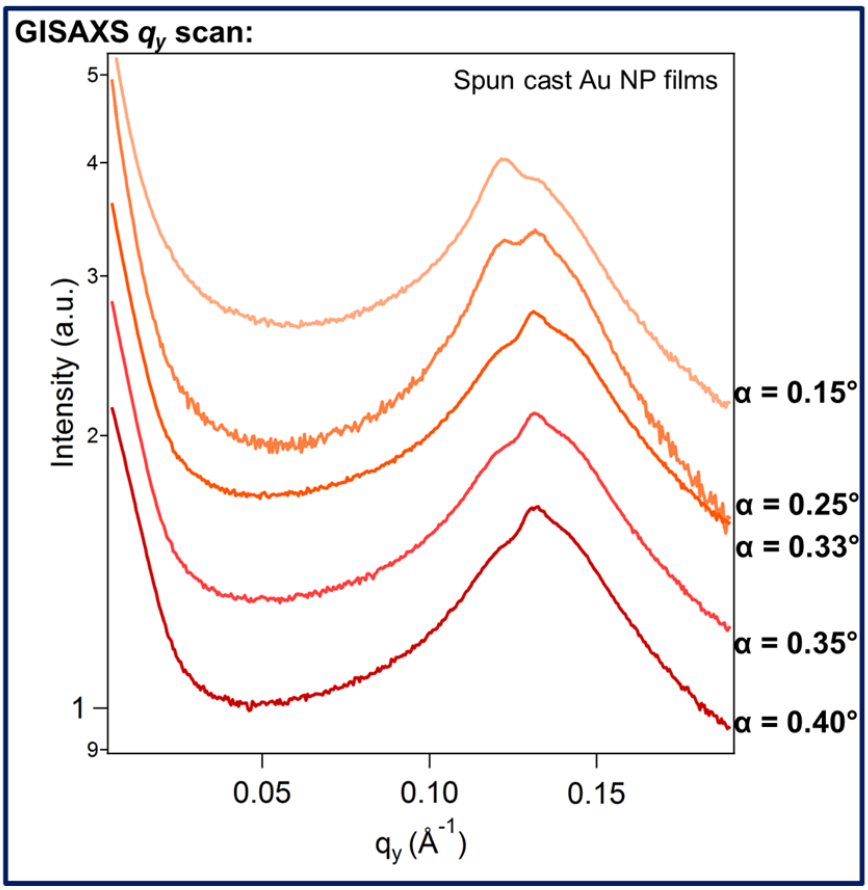

A.2.5. GISAXS q_y scans at 0.15°, 0.25°, 0.33°, 0.35°, and 0.40° for the spun cast film of ~4.9 nm nanoparticles. When the incident angle is small, the Bragg peak at q_y = 0.12 Å^{-1} has the highest intensity on the q_y scans. As the incident angle increases, this peak gradually weekends and the one at q_y = 0.13 Å^{-1} becomes more and more pronounced. This indicates that the inter-particle distances in the *h.c.p*. nanoparticle lattices near the surface and in the interior of the nanoparticle film are different, which are around 5.1 and 4.8 nm, respectively.

A.2.6

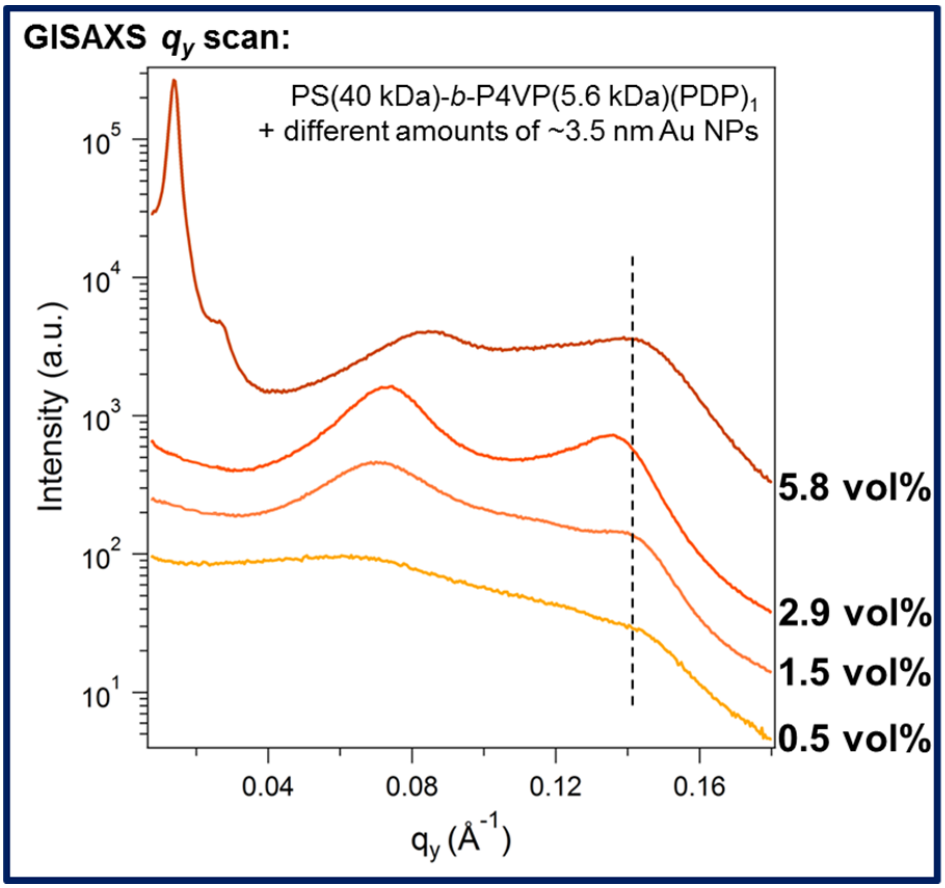

A.2.6. GISAXS q_y scans of the ~200 nm PS(40 kDa)-*b*-P4VP(5.6 kDa)(PDP)$_1$ supramolecular thin films containing 0.5, 1.5, 2.9, and 5.8 vol% of ~3.5 nm Au nanoparticles. All the GISAXS patterns were taken at incident angles around 0.22°. The nanoparticles induce lamella-to-cylinder morphological transition in the film between 2.9 and 5.8 vol%. In addition, the Bragg peak corresponding to the periodicity of the P4VP(PDP)$_1$ lamellae becomes stronger as the nanoparticle loading increases. This suggests that the 3.5 nm nanoparticles may reside in the middle of the microdomains as well as the comb blocks, forming hierarchical nanoparticle assemblies in each P4VP(PDP)$_1$ domain.

A.2.7

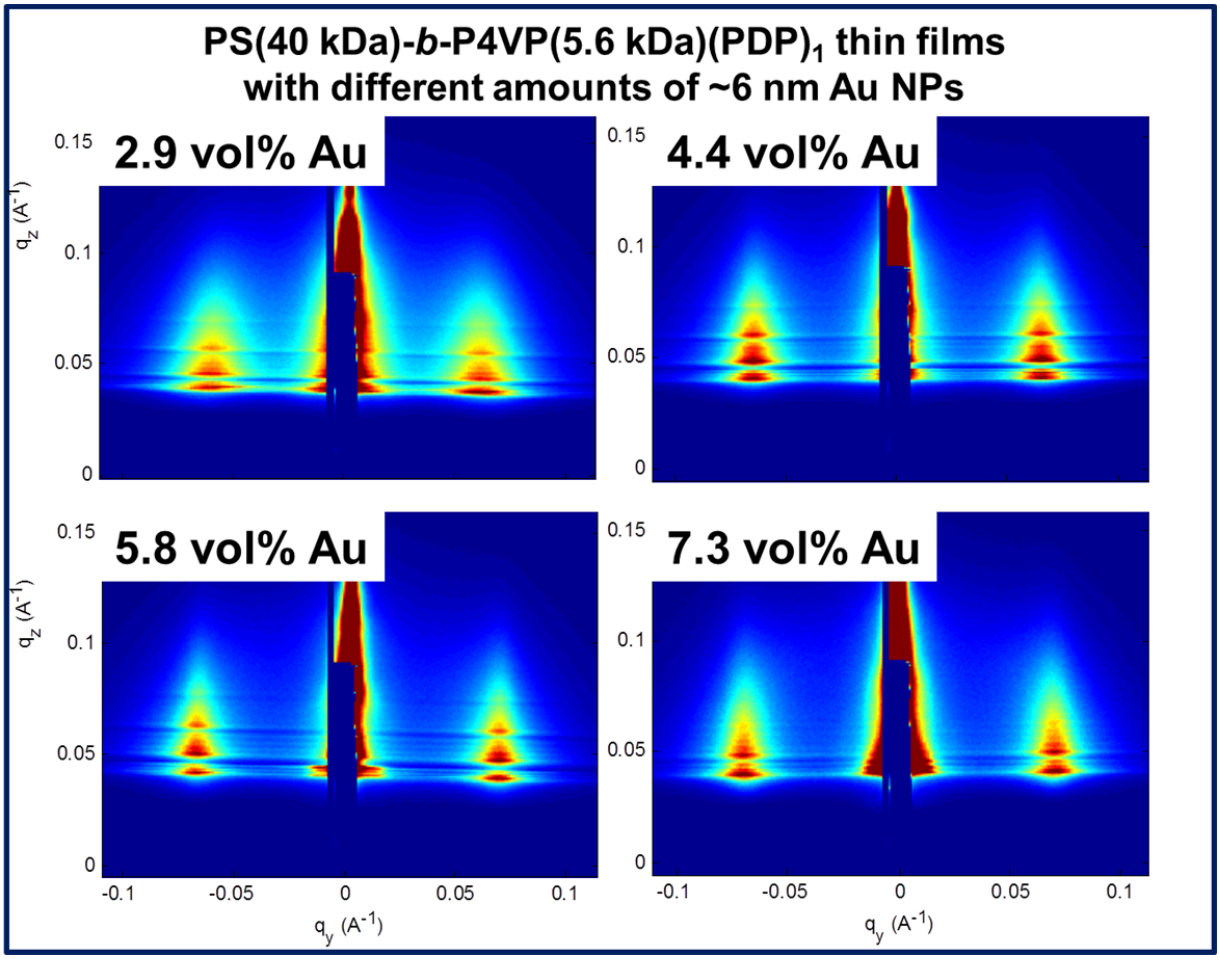

A.2.7. GISAXS patterns of the ~200 nm supramolecular thin film containing PS(40 kDa)-*b*-P4VP(5.6 kDa)(PDP)$_1$ and 2.9, 4.4, 5.8, and 7.3 vol% of ~6.0 nm Au nanoparticles. No Bragg peaks corresponding to the periodicity of the P4VP(PDP)$_1$ lamellae and parallel cylindrical morphology can be seen on the GISAXS pattern. Unlike the 3.5 nm Au nanoparticles, the 6 nm Au nanoparticles mainly reside in the middle of the P4VP(PDP)$_1$ microdomains. Hence, no lamella-to-cylinder morphological transition is induced in the film when the nanoparticle loading reaches above 7.3 vol%.

A.3 Supporting Information for Chapter 4

A.3.1 Nanoparticle size analysis:

The nanoparticle size (*d*) includes both the nanoparticle core size and the ligand shell thickness. It is determined by directly measuring the center-to-center interparticle distances on the TEM images using ImageJ. The *d/a* ratio is calculated using the lateral periodicity of the supremolecule (*a*), where *a* = 33 nm. Figure A.3.1.1. shows an example measurement of nanoparticle size using ImageJ. Table 4.1 summarizes the measured nanoparticle size and calculated *d/a* ratio for each nanoparticle batch. Figures A.3.1.1 to A.3.1.7 show the TEM images and nanoparticle size analysis for all nanoparticles used. *Note*: the nanoparticle size in the distribution histogram corresponds to the core size alone.

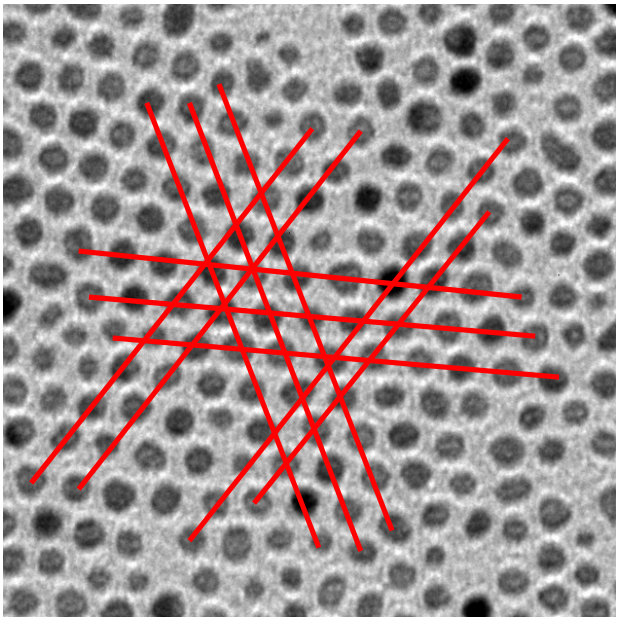

A.3.1.1. Example measurement of center-to-center interparticle distance using ImageJ.

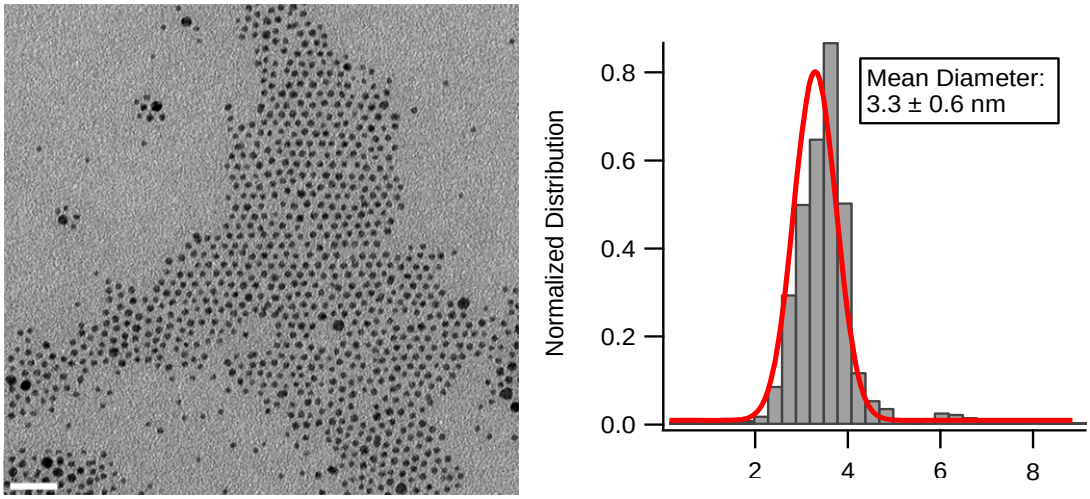

A.3.1.2. TEM image (left) and the nanoparticle core size distribution (right) of 5.7 nm Au nanoparticles.

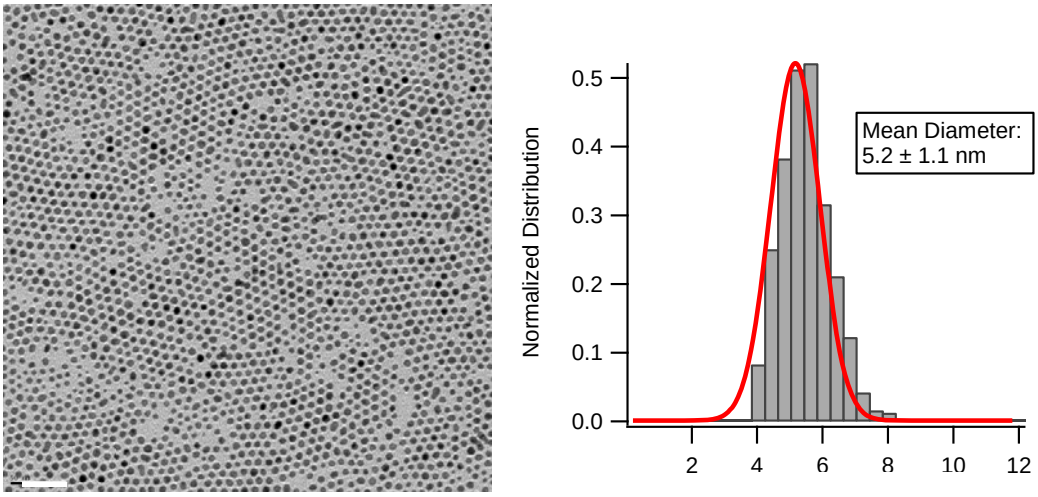

A.3.1.3. TEM image (left) and the nanoparticle core size distribution (right) of 7.4 nm Au nanoparticles.

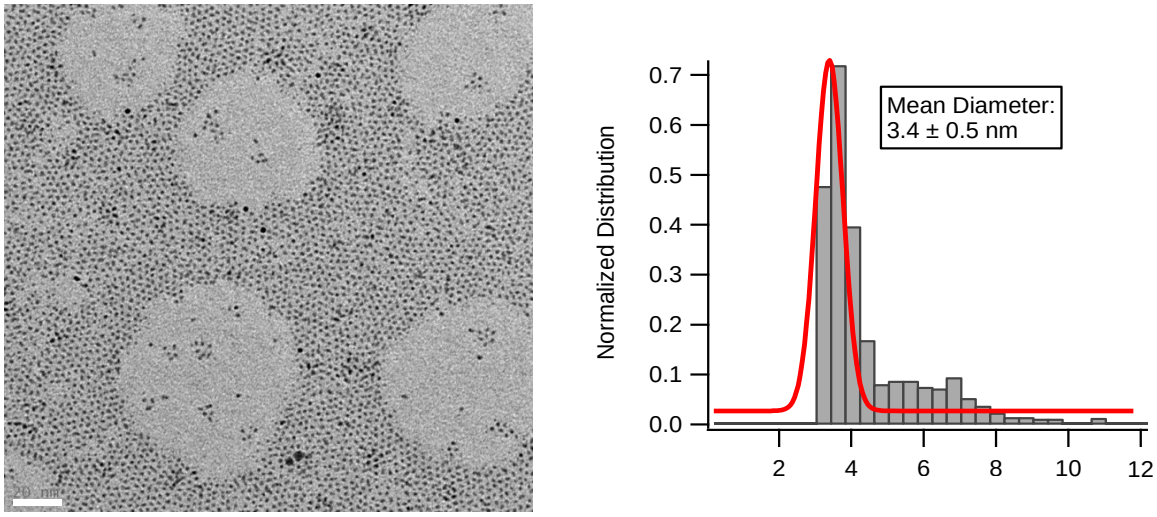

A.3.1.4. TEM image (left) and the nanoparticle core size distribution (right) of 5.5 nm PbS nanoparticles.

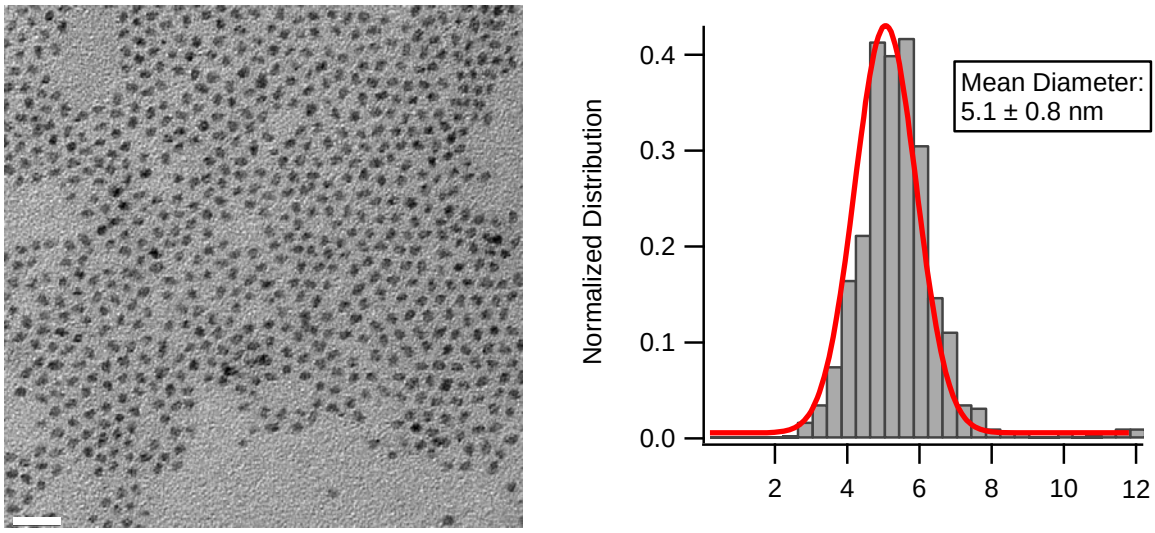

A.3.1.5. TEM image (left) and the nanoparticle core size distribution (right) of 7.4 nm PbS nanoparticles.

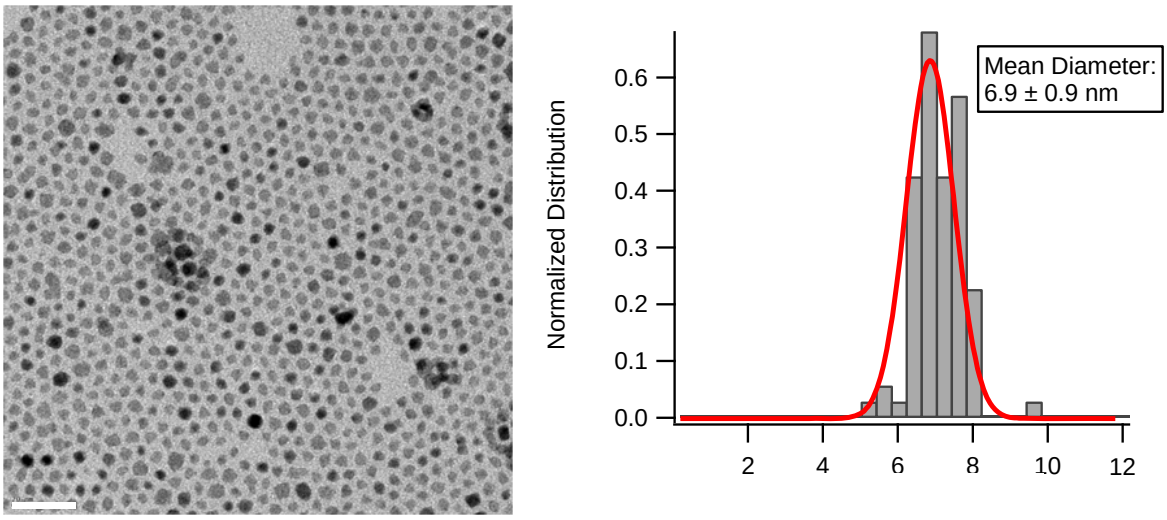

A.3.1.6. TEM image (left) and the nanoparticle core size distribution (right) of 9.3 nm PbS nanoparticles.

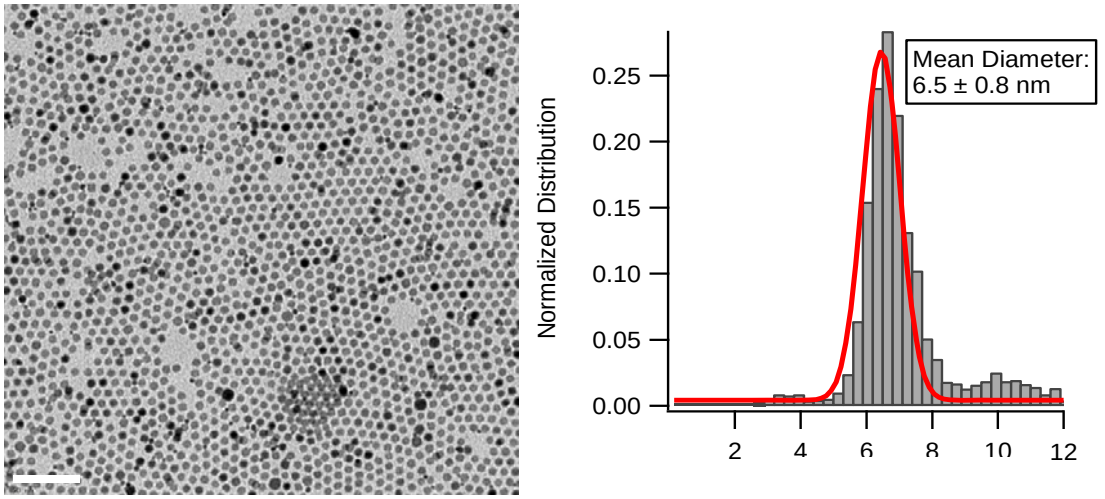

A.3.1.7. TEM image (left) and the nanoparticle core size distribution (right) of 9.0 nm PbSe nanoparticles.

A.4 Supporting Information for Chapter 5

A.4.1

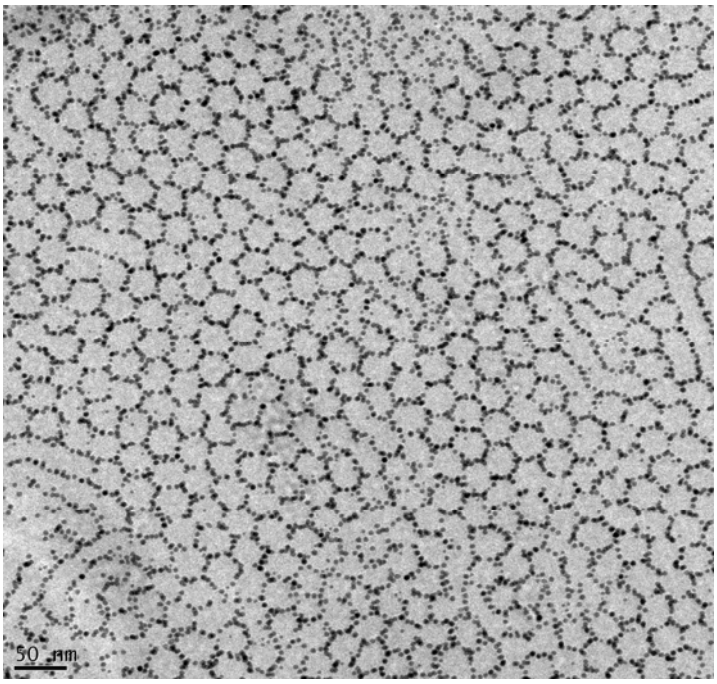

A.4.1. Top-view TEM image of a ~70 nm film containing PS(19 kDa)-*b*-P4VP(5.6 kDa)$(PDP)_{1.7}$ and 0.5 vol% of ~5 nm Au nanoparticles. During solvent annealing, the film was swollen to 111% of its original film thickness (f_s = 0.1) before solvent removal. The cylinderical domains were oriented normal to the surface after annealing, in which the nanoparticles formed 2-D hexagonal grid in the P4VP$(PDP)_{1.7}$ matrix at the air/polymer interface.

A.4.2

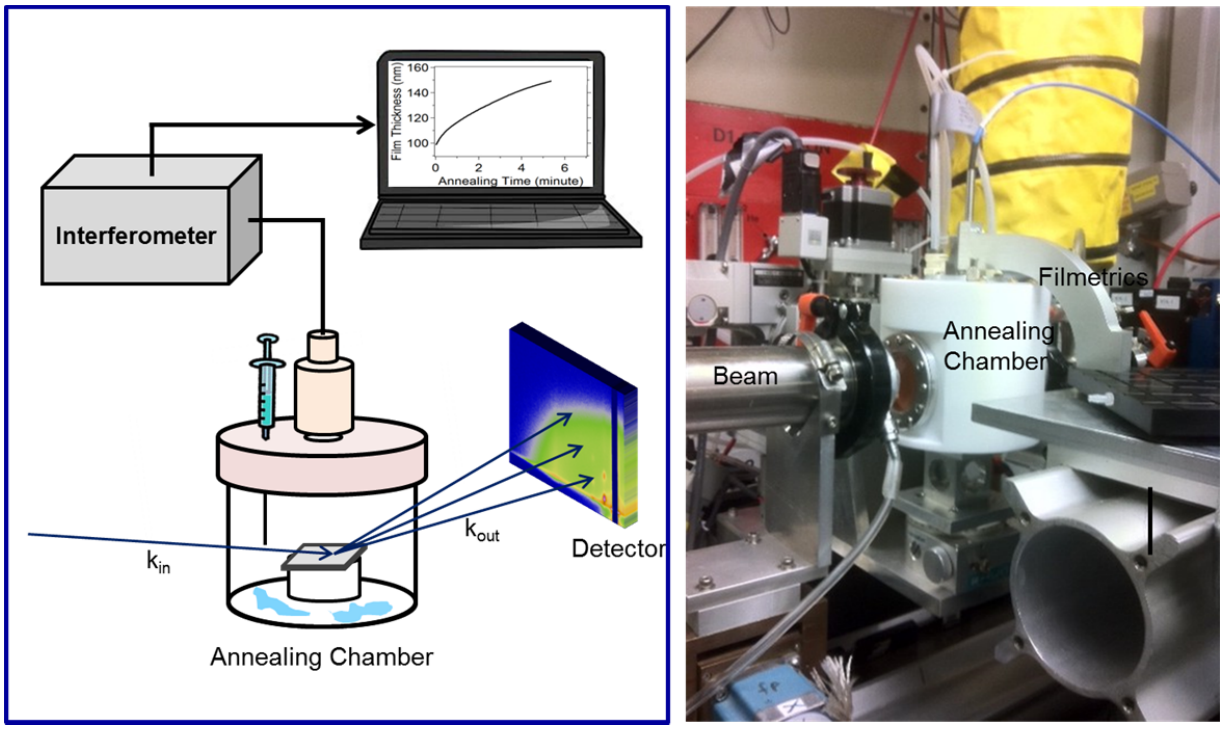

A.4.2. Experimental set-up for *in situ* GISAXS measurements during solvent annealing. The nanocomposite thin film is placed on a sample stage in a home-made Teflon chamber. After solvent injection, the film thickness is monitored *in situ* by an interferometer, a Filmetrics F20 in this case. To remove the solvent, a N_2 supply and an outlet tube is connected to the chamber.

A.4.3

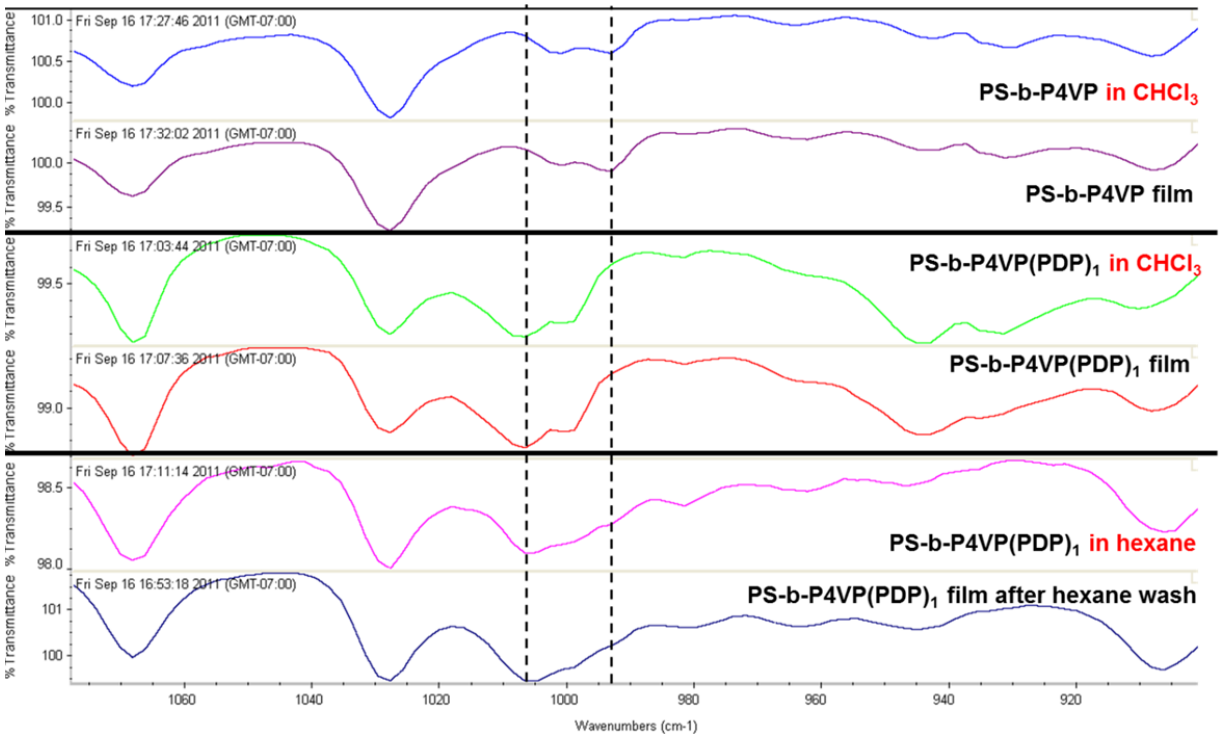

A.4.3. FTIR spectra of PS(19 kDa)-*b*-P4VP(5.6 kDa) alone and PS(19 kDa)-*b*-P4VP(5.6 kDa)$(PDP)_{1.7}$ supramolecules in dried thin films, in $CHCl_3$, and in hexane. Free pyridine group in the PS-*b*-P4VP thin film contribute to the absorption at 993cm^{-1}. The hydrogen-bonded pyridine groups have absorption at 1005-1010 cm^{-1}. As seen upon hydrogen bonding to the PDP, the absorption at 993 cm^{-1} disappeared, and the integrity of the supramolecule in $CHCl_3$, was confirmed.

A.4.4

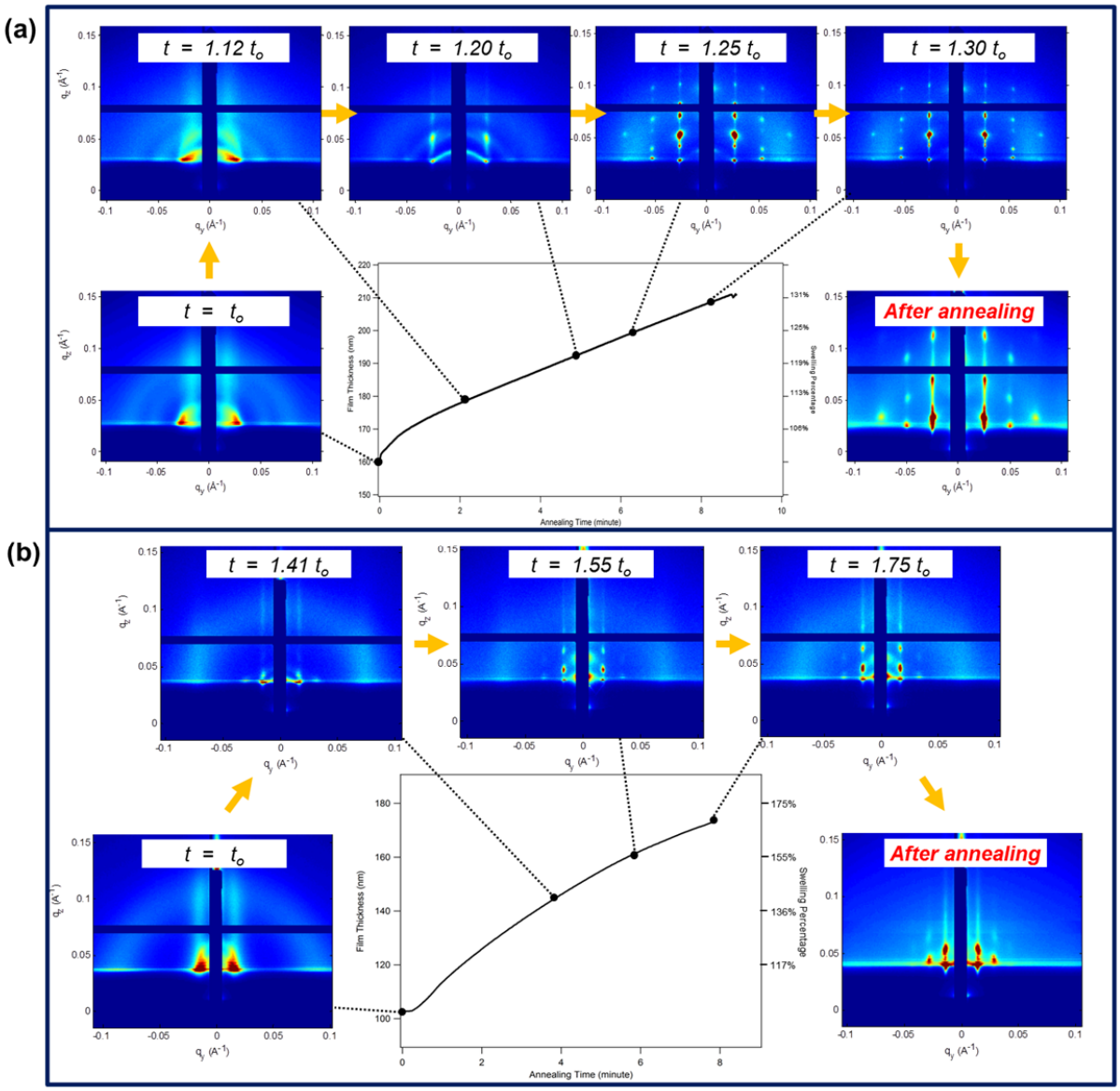

A.4.4. (a) and (b) show the *in situ* GISAXS measurements of two supramolecular nanocomposite thin films containing PS(13.8 kDa)-*b*-P4VP(3.5 kDa)$(PDP)_{1.8}$ and PS(33 kDa)-*b*-P4VP(8 kDa)$(PDP)_{1.9}$, respectively. Both films contain 3 vol% of Au nanoparticles. The results show that both films reached ordered parallel morphology when f_s reached $f_{s,\ ordered}$, which rises with increasing M_n. The overall kinetic pathway is not influenced as PDP: 4VP > 1 in both films.

A.4.5

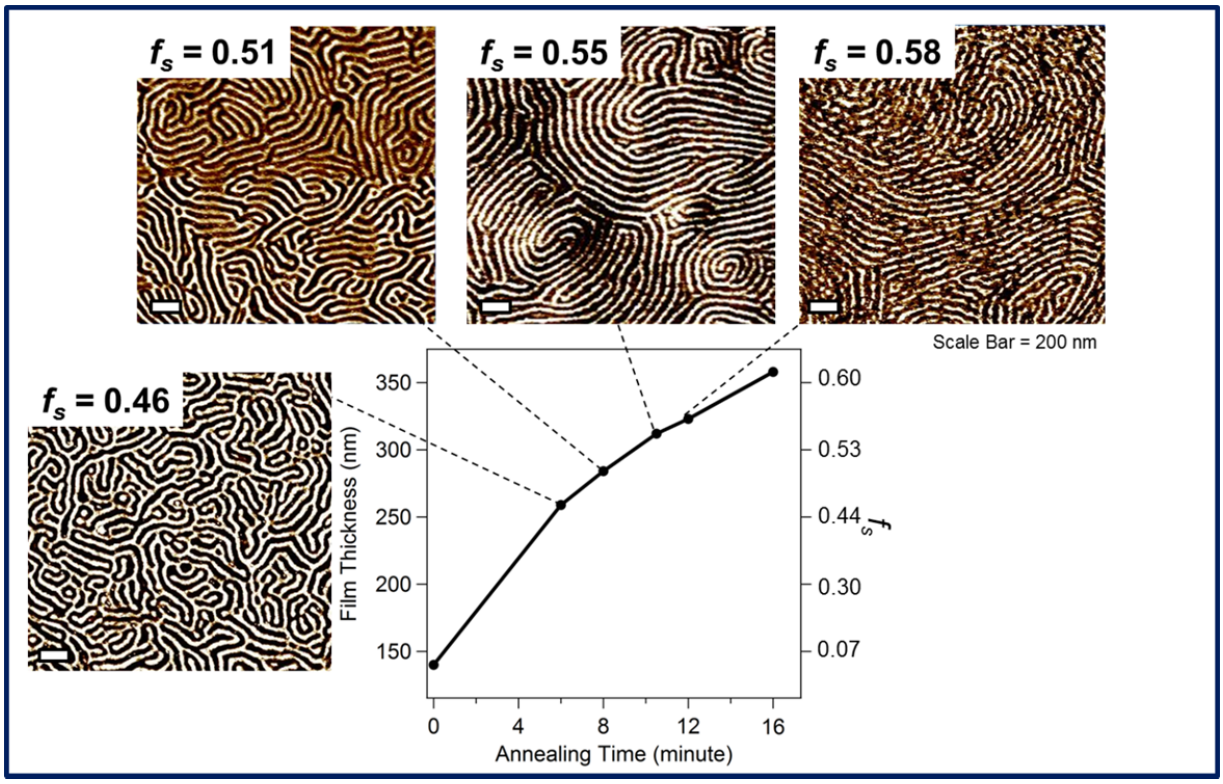

A.4.5. *Ex situ* AFM images of the ~200 nm supramolecular nanocomposite thin films containing PS(50 kDa)-*b*-P4VP(17 kDa)$(PDP)_{1.8}$ and 3 vol% ~5 nm Au nanoparticles taken at different annealing time/f_s during solvent annealing. The morphology of the nanocomposite is optimized at $f_{s,\ ordered}$ = 0.55 and an order-disorder transition begins to occur at f_s = 0.58. Although the molecular weight of the PS blocks is larger than the critical molecular weight for entanglements, the supramolecular nanocomposite still undergoes a kinetic pathway similar to that for low molecular weight supramolecules.

A.4.6

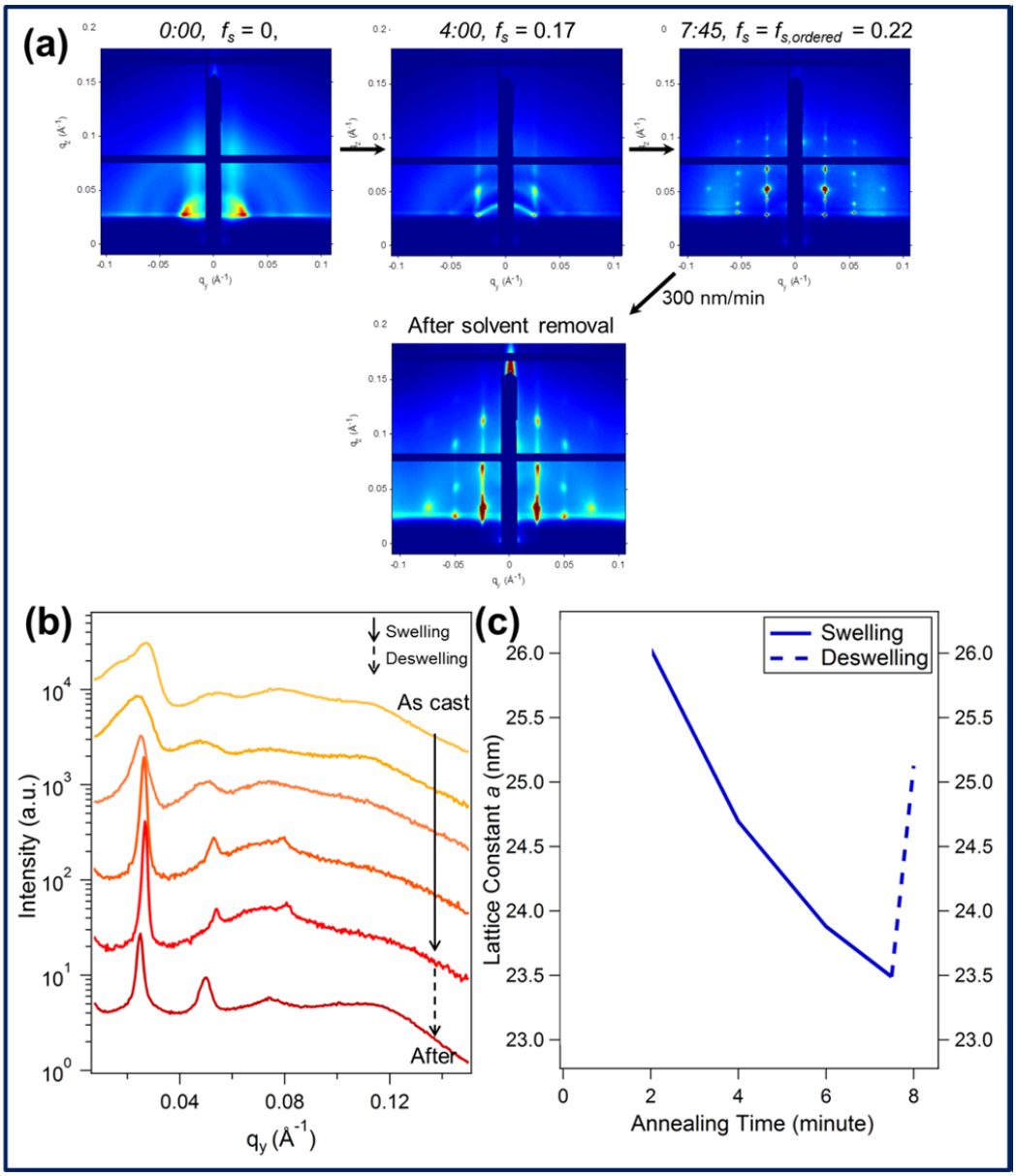

A.4.6. (a) *In situ* GISAXS measurements on a ~200 nm supramolecular nanocomposite thin film containing PS(13.8 kDa)-*b*-P4VP(3.5 kDa)$(PDP)_{1.8}$ and 3 vol% ~3.5 nm Au nanoparticles underwent rapid solvent removal (*SRR* = 300 nm/min) during solvent annealing. The q_y scans of the GISAXS patterns are plotted in (b). The position of the 1st order Bragg peak gives the lateral periodicity of the nanocomposite, which is plotted against annealing time in (c). *a* decreases when the solvent enters the film and it increases during solvent removal. After solvent escapes the film at a rate of 300 nm/min, the lateral periodicity becomes smaller than the original value.

A.4.7

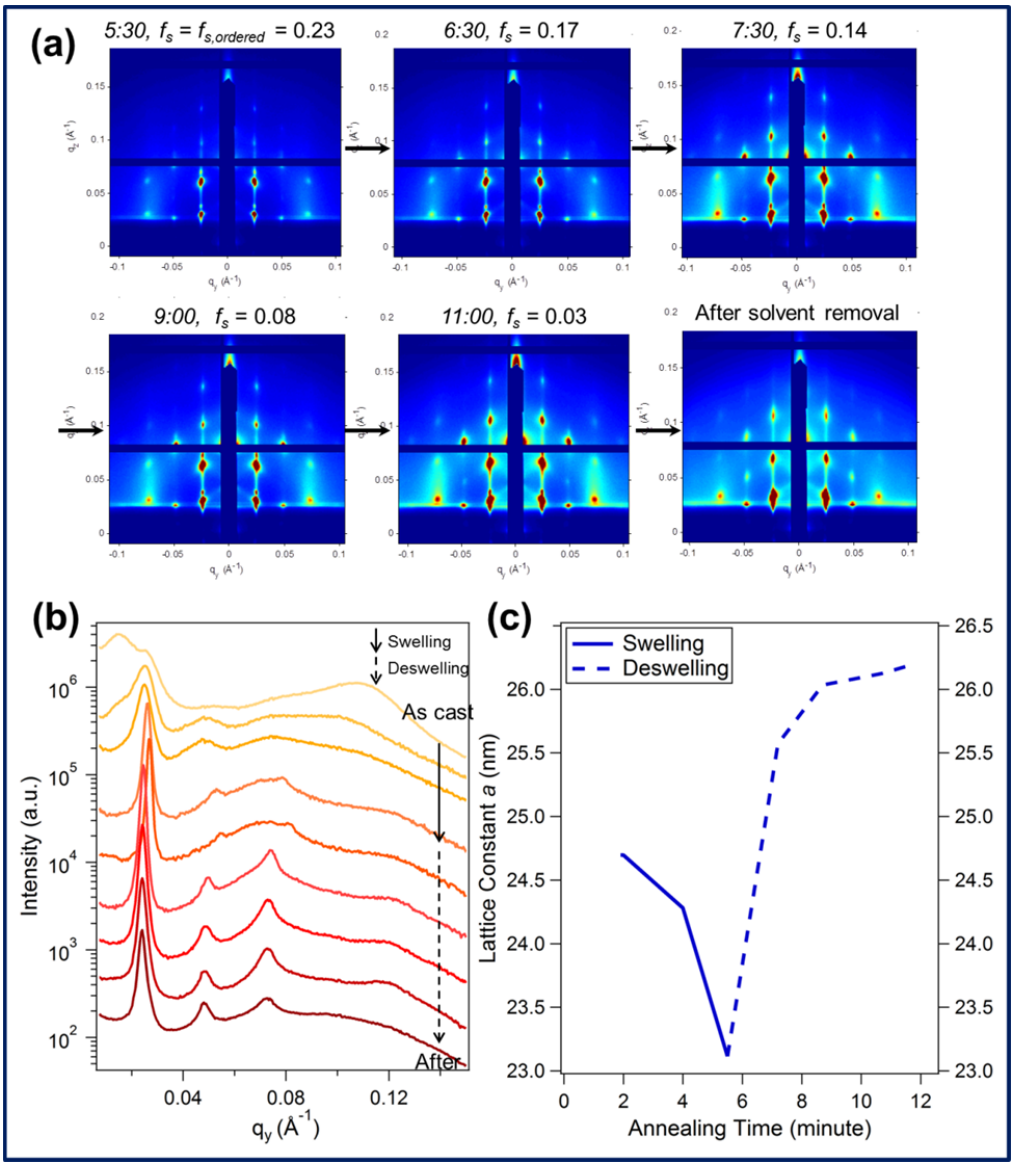

A.4.7. (a) *In situ* GISAXS measurements on a ~200 nm supramolecular nanocomposite thin film containing PS(13.8 kDa)-*b*-P4VP(3.5 kDa)$(PDP)_{1.8}$ and 3 vol% ~3.5 nm Au nanoparticles underwent intermediate solvent removal (*SRR* = 11 nm/min) during solvent annealing. The q_y scans of the GISAXS patterns are plotted in (b). The position of the 1st order Bragg peak gives the lateral periodicity of the nanocomposite, which is plotted against annealing time in (c). *a* decreases when the solvent enters the film and it increases during solvent removal. After solvent escapes the film at a rate of 11 nm/min, the lateral periodicity becomes slightly larger than that before solvent annealing.

A.4.8

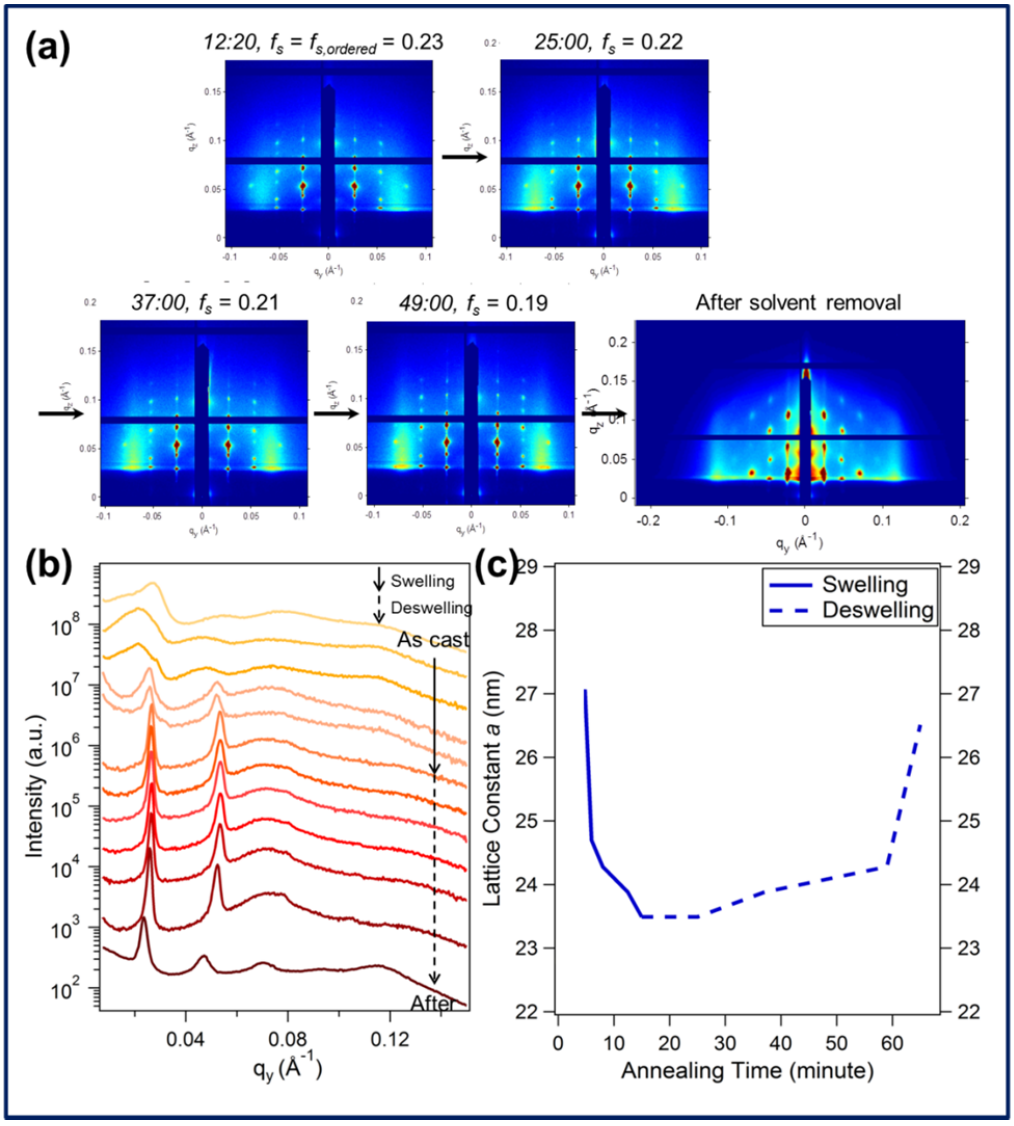

A.4.8. (a) *In situ* GISAXS measurements on a ~200 nm supramolecular nanocomposite thin film containing PS(13.8 kDa)-*b*-P4VP(3.5 kDa)$(PDP)_{1.8}$ and 3 vol% ~3.5 nm Au nanoparticles underwent slow solvent removal (*SRR* = 0.5 nm/min) during solvent annealing. The q_y scans of the GISAXS patterns are plotted in (b). The higher order peaks up to the 4th order can be seen in both q_y and q_z directions, characteristic of a highly order nanoparticle arrays in the films. The position of the 1st order Bragg peak gives the lateral periodicity of the nanocomposite, which is plotted against annealing time in (c). *a* decreases when the solvent enters the film and it increases during solvent removal. After solvent escapes the film at a rate of 0.05 nm/min, the lateral periodicity becomes comparable to the original value.

A.5 Supporting Information for Chapter 6

A.5.1

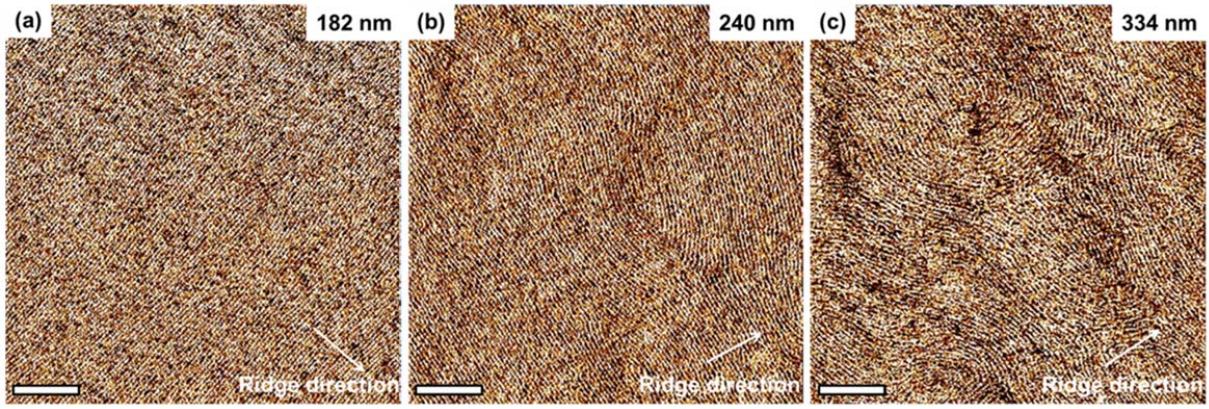

A.5.1. AFM images of three supramolecular nanocomposite thin films containing 3 vol% ~5 nm Au nanoparticles on the same faceted substrate with film thicknesses (*t*) around (a) 182 nm, (b) 240 nm, and (c) 334 nm. The arrow in each image indicates the ridge direction of the saw-toothed pattern. When *t* = 182 nm, the supramolecules and the nanoparticle arrays orient normal to the facets with exceptional long-range order. However, as *t* increases, the supramolecular nanocomposite begins to have random lateral orientation as the saw-toothed pattern becomes effectively screened by the relatively thick films on the facets. Scale bar = 500 nm.

A.5.2 Analysis of the lateral lattice parameter (*a*) of the 3-D hexagonally packed in-plane nanoparticle chains in cylindrical supramolecular nanocomposite thin films:

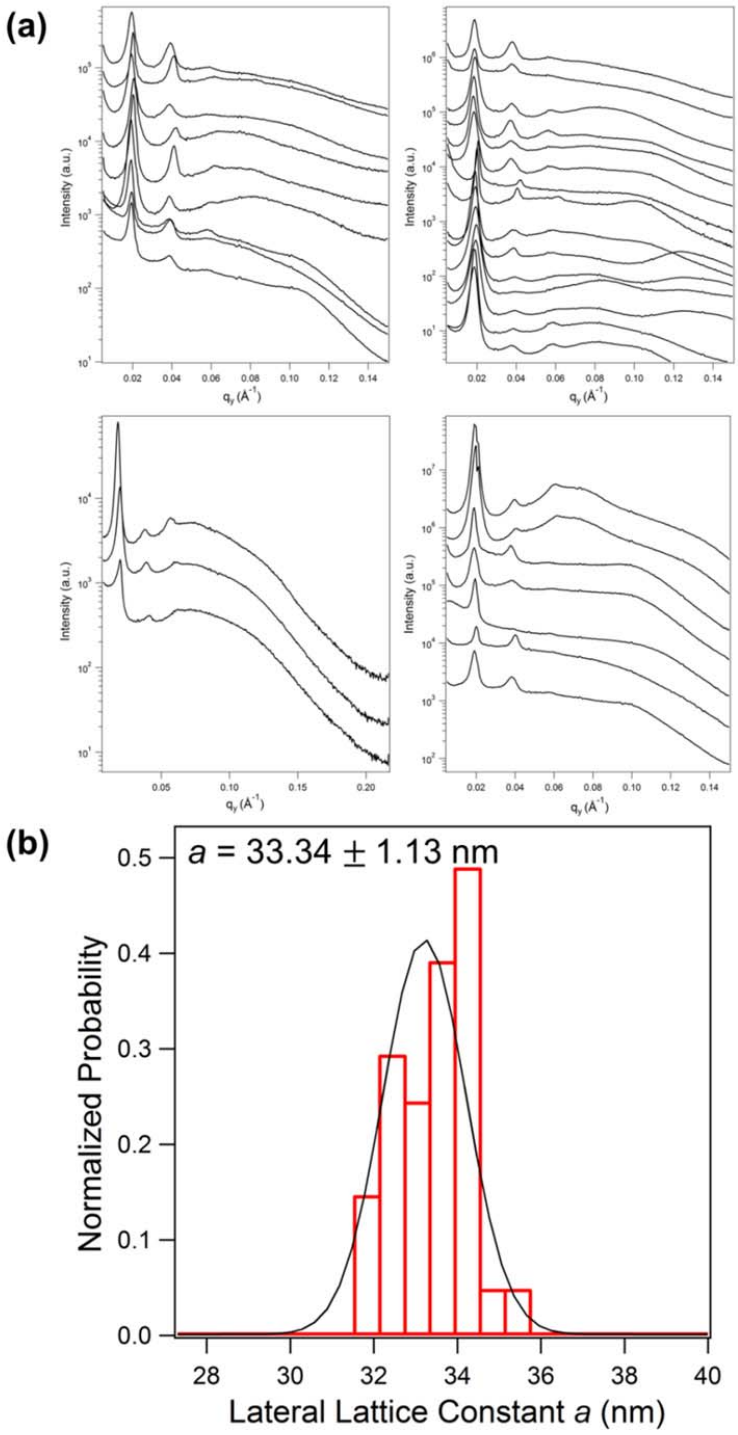

A.5.2. (a) GISAXS q_y linecuts of 34 ~200 nm supramolecular nanocomposite thin films containing PS(19,000)-*b*-P4VP(5,200)(PDP)$_{1.7}$ and 3 vol% ~5 nm Au nanoparticles on Si wafer. The data was obtained from four separate synchrotron beamtimes. All the supramolecular nanocomposite thin films were solvent annealed under similar condition without controlled solvent removal. The distribution of the lateral periodicity, *a*, of the supramolecular nanocomposite is 33.3 $\pm$ 1.1 nm and is shown in the histogram in (b) and tabulated in Table A.5.1. When the supramolecular nanocomposite is deposited on P1 and P2, the values of *L/a* are 3.8 $\pm$ 0.1 and 10.7 $\pm$ 0.4, respectively.

Table A.5.2. Distribution of *a* based on the data in Figure A.5.2.

Data Source	Distribution of *a* (nm)	Average *a* (nm)
Data set #1	31.5 – 33.3	32.5 $\pm$ 0.9
Data set #2	30.8 – 34.9	33.5 $\pm$ 1.2
Data set #3	31.5 – 34.5	33.2 $\pm$ 1.7
Data set #4	32.2 – 33.5	32.9 $\pm$ 0.6
Average	**30.8 – 34.9**	**33.3 $\pm$ 1.1**

A.5.3 Analysis of the vertical lattice parameter (*c*) of the 3-D hexagonally packed in-plane nanoparticle chains in cylindrical supramolecular nanocomposite thin films:

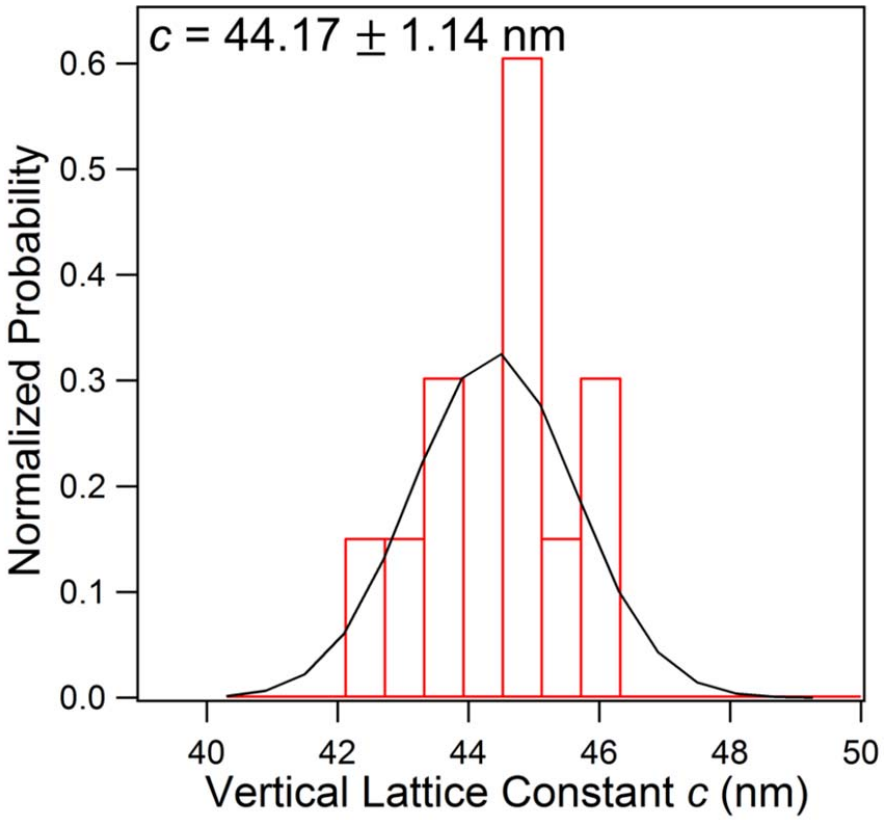

A.5.3. Histogram of the calculated lattice constants *c* of the hexagonally packed 3-D nanoparticle arrays in 11 ~200 nm supramolecular nanocomposite thin films containing PS(19,000)-*b*-P4VP(5,200)$(PDP)_{1.7}$ and 3 vol% ~5 nm Au nanoparticles on flat Si wafer. All the supramolecular nanocomposite thin films were solvent annealed under similar condition without controlled solvent removal. The lattice constants were obtained based on the simulation of the GISAXS patterns and tabulated in Table A.5.3. Fitting the histogram by a Gaussian curve yields the distribution of *c*, which is 44.2 ± 1.1 nm.

Table A.5.3. Vertical lattice constants, *c*, of the hexagonally packed 3-D nanoparticle arrays in 11 ~200 nm supramolecular nanocomposite thin films on flat Si wafer. Simulating the GISAXS patterns of the samples gives the distortion parameters of the hexagonal lattice of the 3-D nanoparticle arrays for the calculation of *c*.

Sample No.	*a* (nm)	*c* (nm)	Distortion parameter	Total area in a hexagonal lattice cell (nm^2)
1	33.3	45.6	0.79	1519.1
2	34.1	44.3	0.75	1510.5
3	31.9	43.0	0.78	1371.3
4	31.9	45.8	0.83	1459.3
5	34.9	42.3	0.70	1477.6
6	34.9	43.5	0.72	1519.8
7	33.3	44.4	0.77	1480.7
8	33.3	42.7	0.74	1423.0
9	34.0	44.7	0.76	1518.1
10	31.6	44.9	0.82	1416.4
11	33.0	44.6	0.78	1472.1
Average	**33.3 $\pm$ 1.2**	**44.2 $\pm$ 1.1**	**0.77 $\pm$ 0.04**	**1469.8 $\pm$ 49.0**

A.5.4

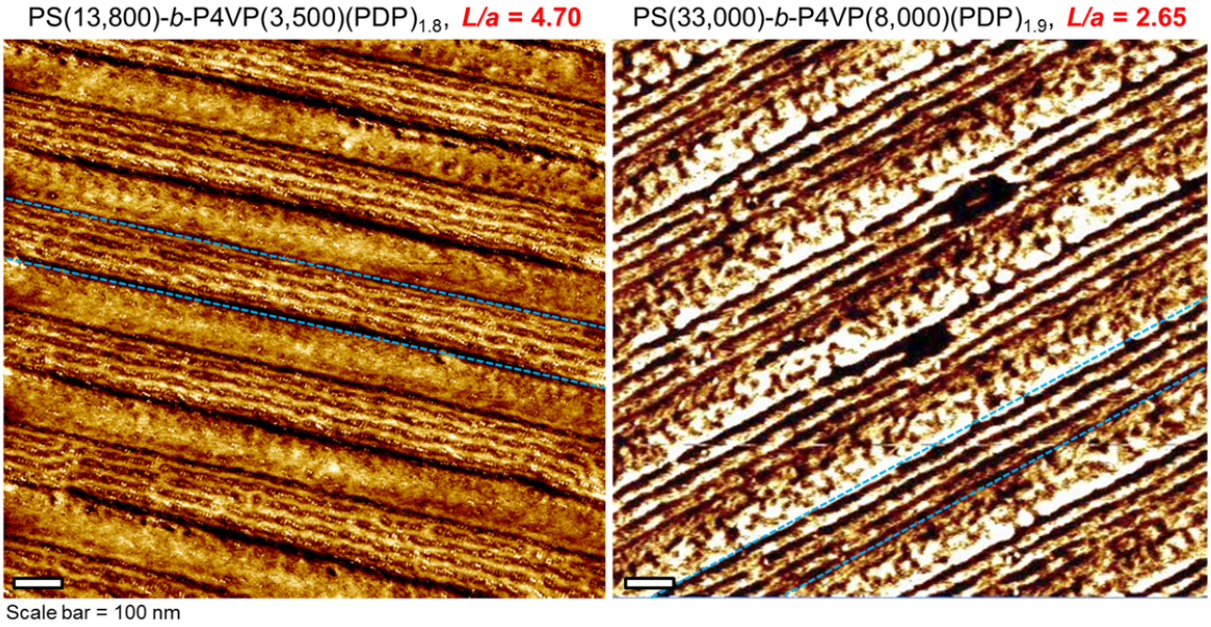

A.5.4. AFM images of the ~40 nm supramolecular thin films containing PS(13,800)-*b*-P4VP(3,500)(PDP)$_{1.8}$ (left) and PS(33,000)-*b*-P4VP(8,000)(PDP)$_{1.9}$ (right) confined in lithographic trenches with L = 125 nm. In both cases, the trench walls guide the macroscopic alignment of the cylindrical microdomains over micrometer scale even though the L/a ratios are not integral values. The results indicate that the supramolecules can accommodate the strain energy generated by the incommensurability between the trench width and the lateral periodicity of the supramolecules.

A.5.5 Characterization of the trench width (*L*) of the lithographic trench patterns:

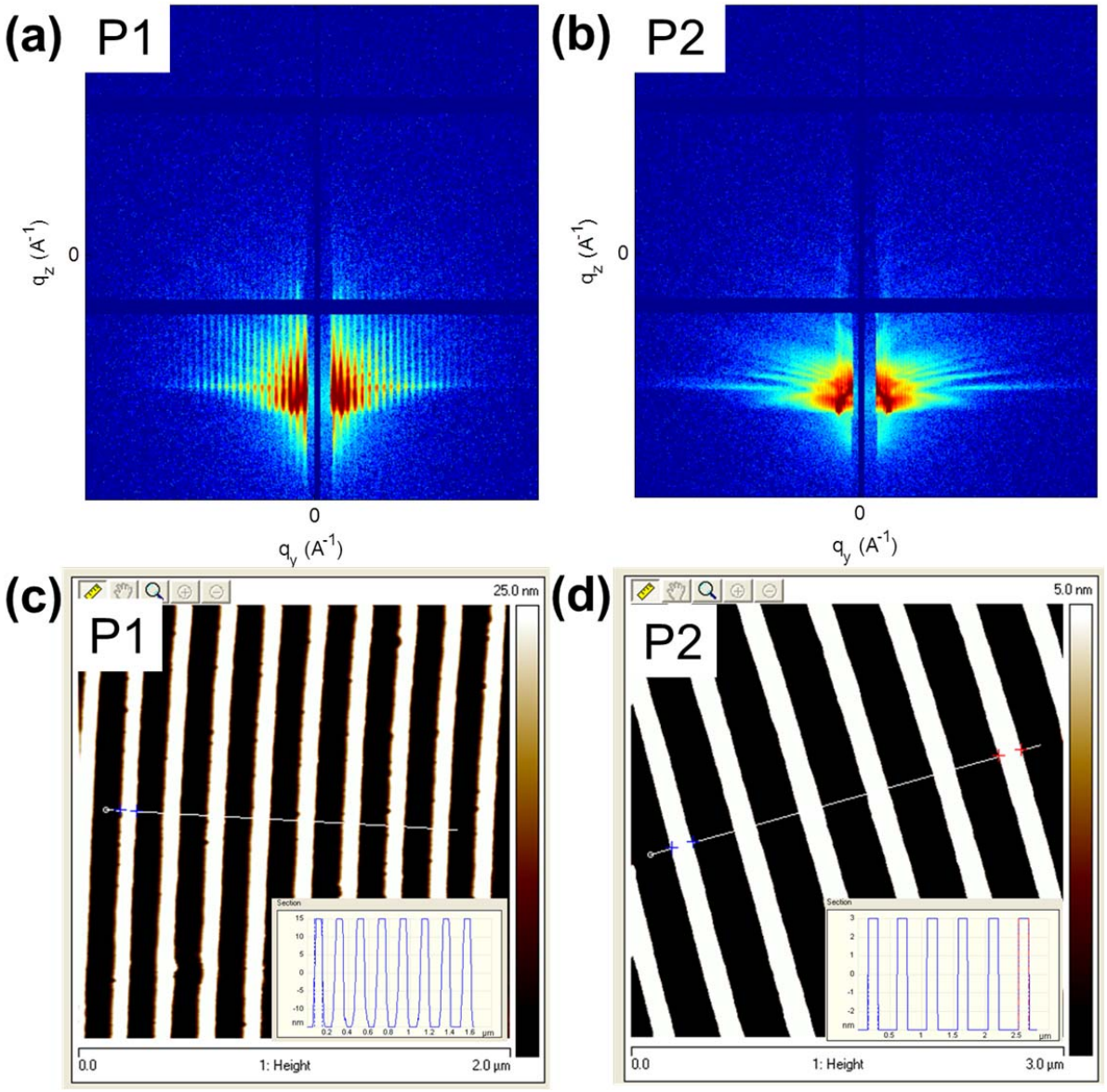

A.5.5. (a) and (b) show the GISAXS patterns of the lithographic patterns P1 and P2, respectively. The q_y linecuts of the GISAXS patterns were analyzed, giving the periodicities of the two trench patterns P_1 and P_2, which are 211 and 511 nm, respectively. (c) and (d) show the image analysis of the AFM images of P1 and P2, which yields the average mesa widths of the two patterns (M_1 = 86 nm and M_2 = 155 nm). With the periodicities and the mesa widths of P1 and P2, the trench widths, *L*, of the two lithographic patterns were calculated and listed in Table S3.

Table A.5.5. Characteristics of the two lithographic patterns used to control the long-range order of supramolecular nanocomposite thin films.

	Periodicity, *P*	**Mesa Width, *M***	**Trench Width, *L* = (*P* – *M*)**
P1	211 nm	86 nm	125 nm
P2	511 nm	155 nm	356 nm
P3	936 nm	211 nm	725 nm

A.5.6

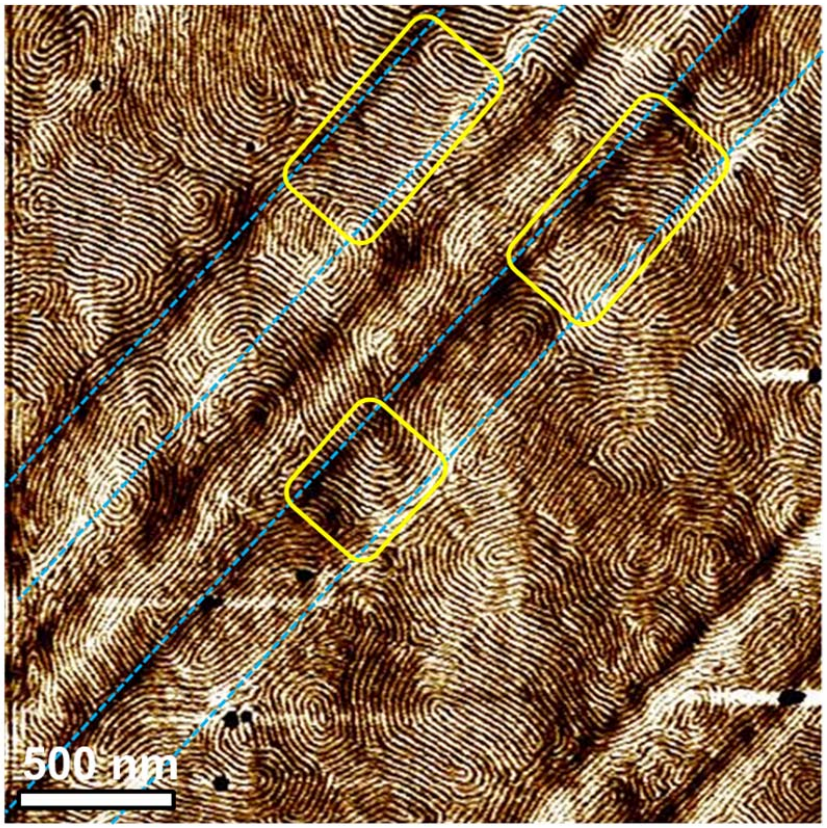

A.5.6. AFM images of the ~60 nm PS(19,000)-*b*-P4VP(5,200)(PDP)$_{1.7}$ supramolecular thin film deposited on lithographic trenches that have L = 460 nm. The blue dotted lines outline the positions of the trench walls. Cylindrical microdomains oriented perpendicular to the trench direction are observed in the highlighted regions, which may be caused by the flow of the supramolecules from the 1100 nm wide mesas into the channels. This piece of data suggests that the fluid dynamics of the supramolecules may disrupt the macroscopic alignment of the microdomains during solvent annealing when the mesas are much wider than the trenches.

A.5.7

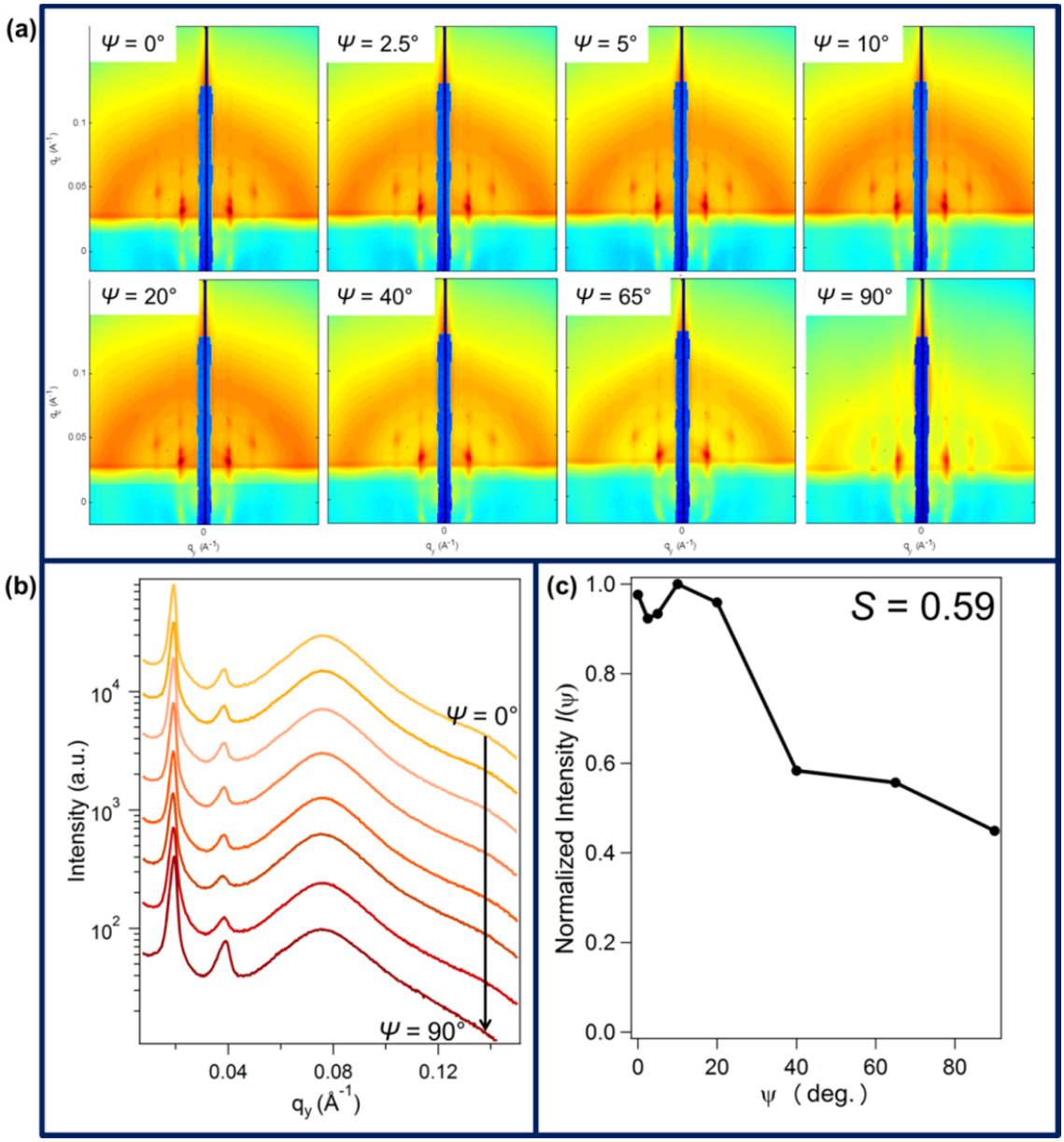

A.5.7.1. (a) GISAXS patterns of the ~530 nm thick supramolecular nanocomposite thin film containing PS(19,000)-*b*-P4VP(5,200)$(PDP)_{1.7}$ and 3 vol% ~5 nm Au nanoparticles deposited on P1 measured at different Ψ. All the 2-D GISAXS patterns are identical regardless of Ψ. (b) The q_y linecut at $q_z = 0.0236$ Å^{-1} for each GISAXS pattern in (a). (c) The dependence of the scattering intensity of the first-order peak on Ψ. Here, S is found to be 0.65, indicating that the cylindrical microdomains and nanoparticle arrays assume poor long-range ordering on the lithographic trenches.

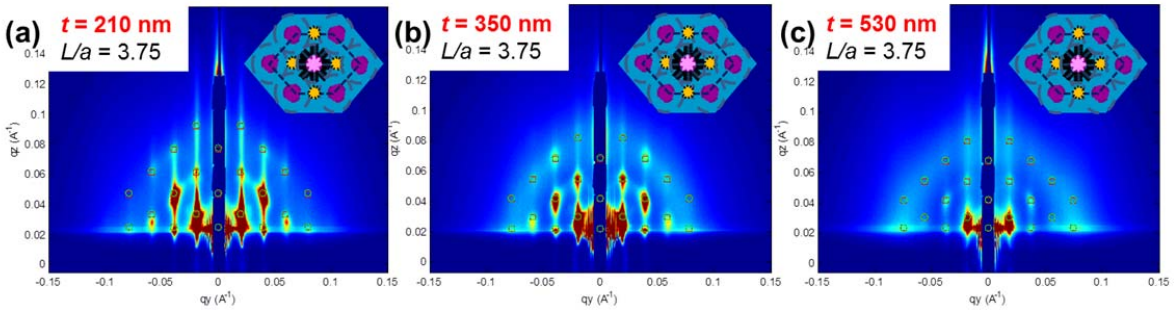

A.5.7.2. (a) GISAXS patterns (Ψ = 0°) of the supramolecular nanocomposite thin films containing PS(19,000)-*b*-P4VP(5,200)$(PDP)_{1.7}$ and 3 vol% ~5 nm Au nanoparticles deposited on the same lithographic trench pattern with film thicknesses around (a) 210 nm, (b) 350 nm, and (c) 530 nm. The simulation of the GISAXS patterns reveals that all three samples have similar 3-D structure in the films. The distortion factors of the hexagonally packed in-plane nanoparticle chains were found to be > 0.8 regardless of the film thickness. This indicates that the lateral confinement provided by the trenches effectively tailor the 3-D morphology of the supramolecular nanocomposite that can prevail throughout the entire film thickness.

Table A.5.7. Summary of the orientation parameters and the distortion factors of the 3-D nanoparticle assemblies in supramolecular nanocomposite thin films with different film thicknesses deposited on the same lithographic trench pattern (P1). Unlike the lateral alignment of the nanoparticle arrays, the 3-D structure in the film is not thickness dependent.

	t = 210 nm	**t = 350 nm**	**t = 530 nm**
S	0.92	0.88	0.65
a	31.19 nm	31.77 nm	32.99 nm
c	44.30 nm	44.57 nm	46.86 nm
Distortion Factor	0.87	0.81	0.82

A.5.8.

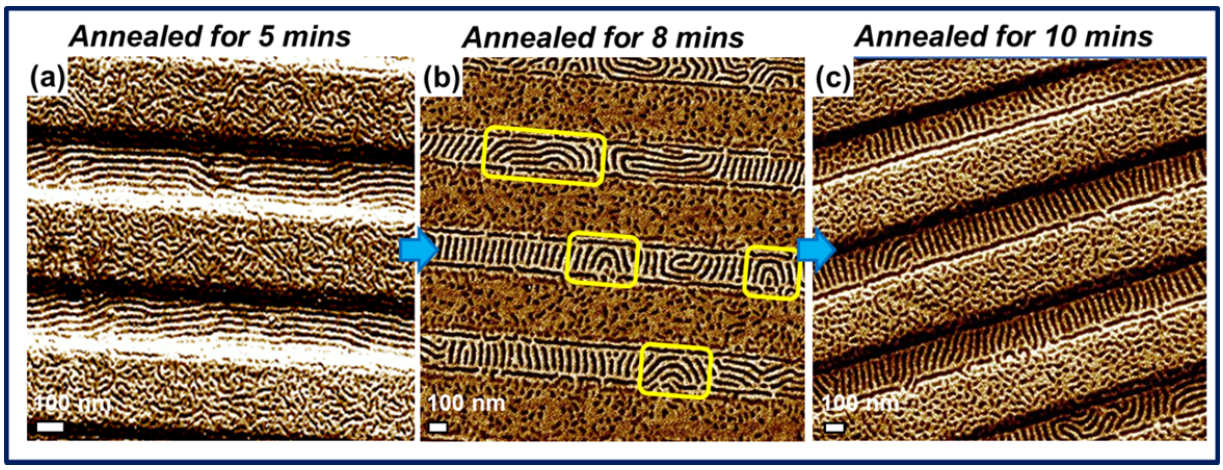

A.5.8. AFM images of the ~40 nm PS(19,000)-*b*-P4VP(5,200)(PDP)$_{1.7}$ supramolecular thin films confined in lithographic trenches with L = 200 nm. Same amount of solvent was injected into the annealing chamber but the annealing time was varied so the films could reach different swelling ratios during the annealing process. After 5 minutes of solvent annealing, the cylindrical domains still aligned parallel to the trench direction. The microdomains underwent a reorientation from parallel to perpendicular to the trench walls after 8 minutes of solvent annealing under this particular annealing condition shown here.

A.5.9

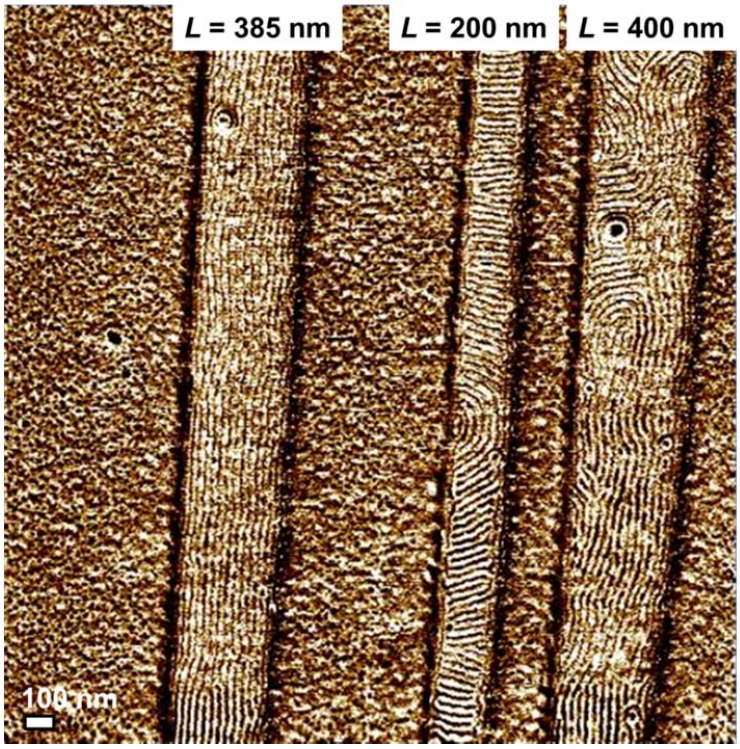

A.5.9. AFM images of the ~40 nm PS(19,000)-*b*-P4VP(5,200)$(PDP)_{1.7}$ supramolecular thin film confined in lithographic trenches with L = 200, 385, and 400 nm. During solvent annealing, the film was significantly swollen to reach t > 145% of its original film thickness. After solvent annealing, the cylinders in the smallest trench are oriented normal to the trench walls whereas the ones in the larger trenches align parallel to the trench direction. When L/a is small, the strain generated in the supramolecules due to the incommensurability between L and a is relatively larger than that in a wider trench. At high f_s during solvent annealing, the interfacial interactions between the two blocks become mediated. Therefore, it becomes both enthalpically and entropically favorable to orient the microdomains normal to the trench walls when L/a is relatively small.

A.5.10

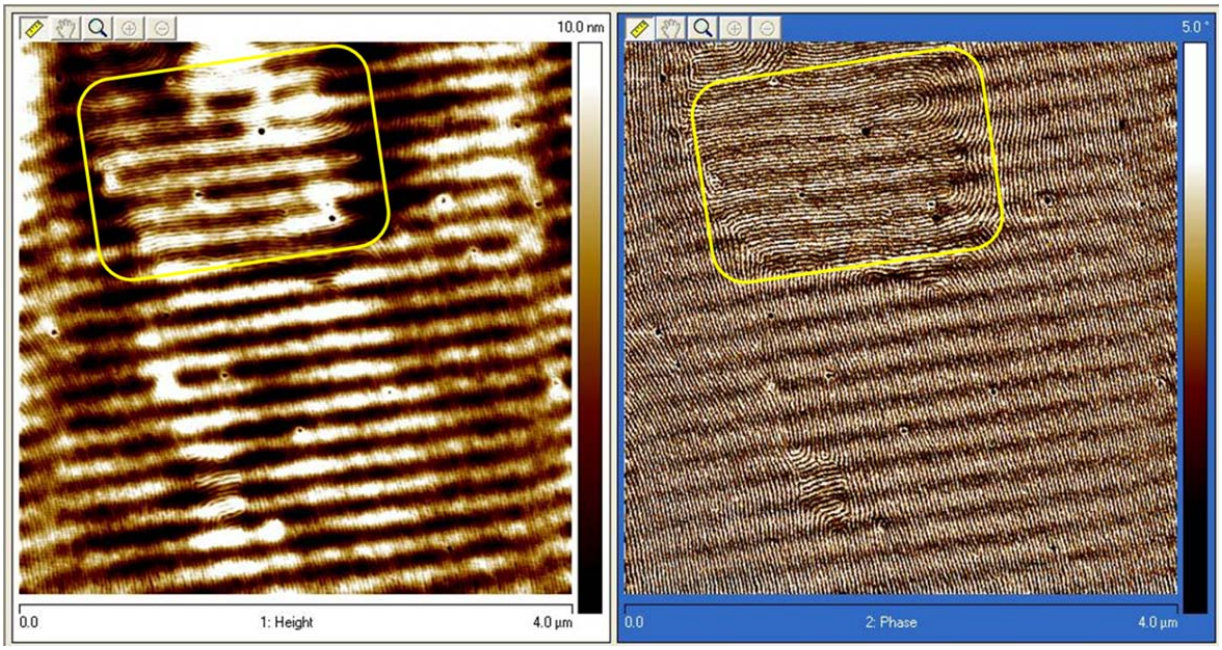

A.5.10. AFM images of the ~140 nm thick PS(19,000)-*b*-P4VP(5,200)$(PDP)_{1.7}$ supramolecular thin film deposited on lithographic trenches that have L = 125 nm. At f_s = 0.38, solvent annealing was terminated and the cylindrical microdomains were found to orient normal to the trench walls. In some regions, however, the cylinders still align parallel to the trench direction. This indicates that the two local energy minimums have similar energy levels and the final morphology of the film is dependent on the kinetic pathway during solvent annealing.

A.5.11

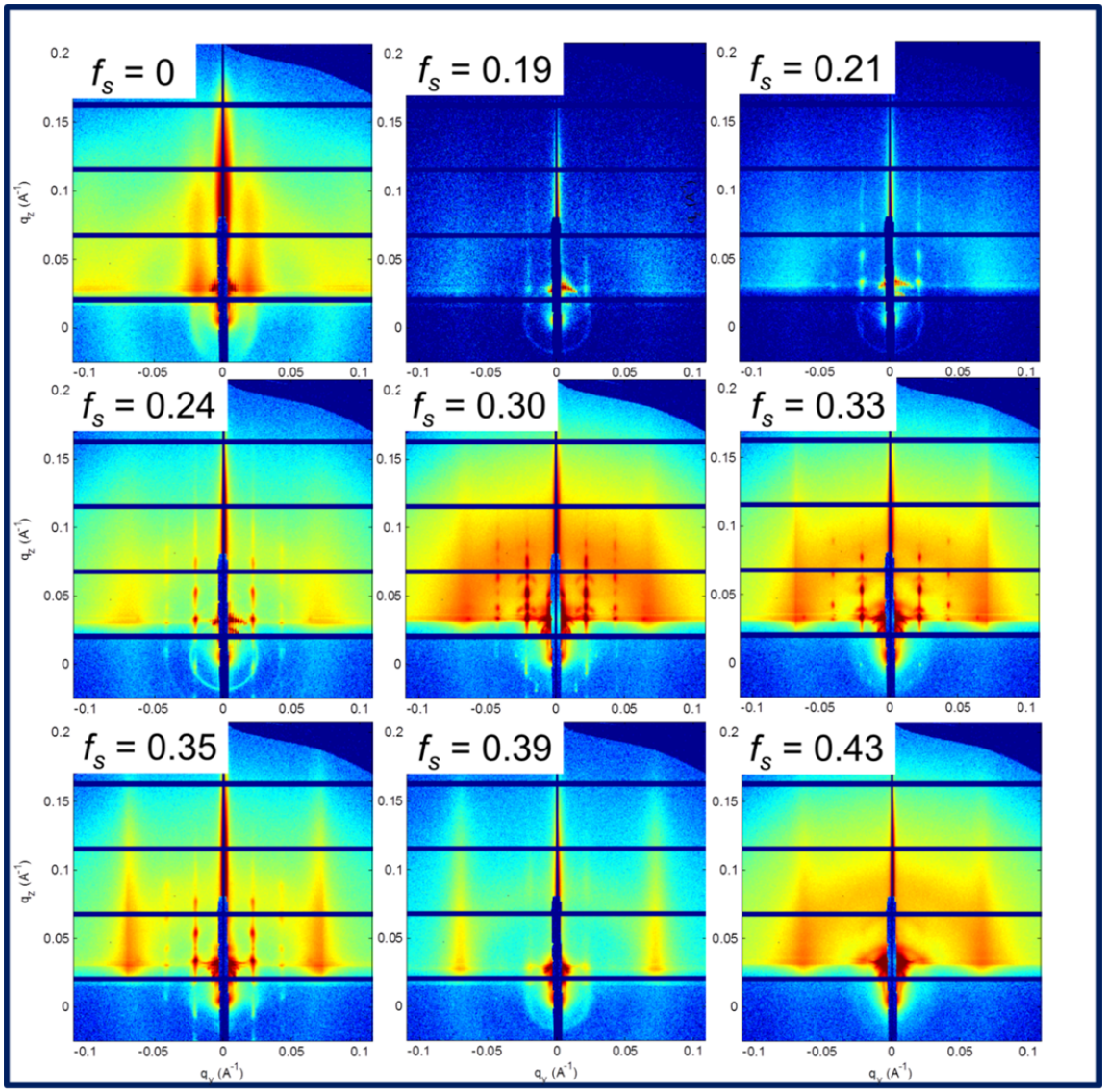

A.5.11. *In situ* GISAXS patterns of a ~140 nm supramolecular nanocomposite thin film containing PS(19,000)-*b*-P4VP(5,200)$(PDP)_{1.7}$ and 3 vol% of 5 nm Au nanoparticles taken at different f_s with the X-ray beam parallel to the trench direction. The Bragg spots corresponding to the hexagonally packed in-plane 3-D nanoparticle arrays aligned parallel to the trench direction reach highest intensity at $f_s = 0.3$ and gradually weaken at $f_s > 0.3$. On the contrary, the structure factor from the inter-particle ordering becomes more and more dominant as a function of f_s. At $f_s > 0.4$, order-disorder transition occurs in the nanocomposite. The *in situ* results indicate that the microdomains/nanoparticle arrays reorient from parallel to normal to the trench walls between $f_s = 0.3$ and 0.35, which is consistent with that shown in Figure 6.12.

A.5.12

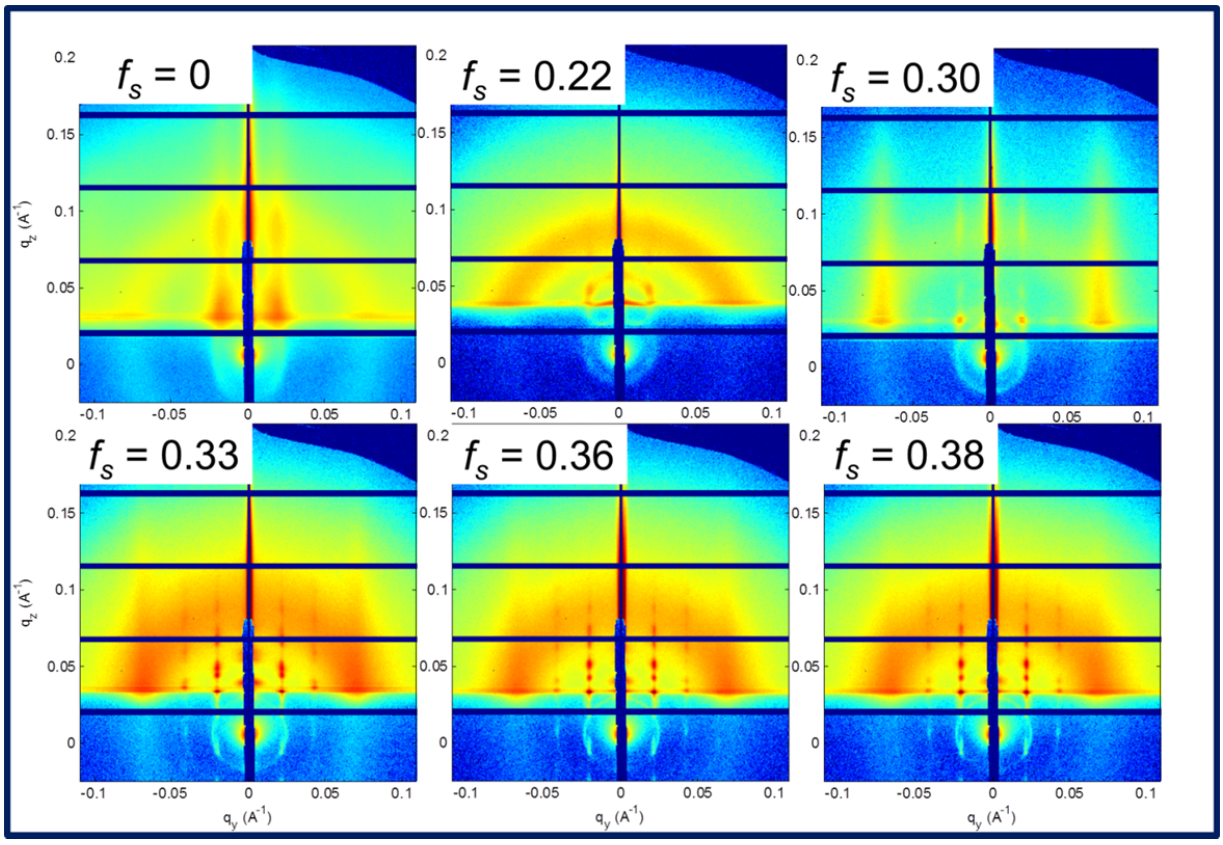

A.5.12. *In situ* GISAXS patterns of a ~140 nm supramolecular nanocomposite thin film containing PS(19,000)-*b*-P4VP(5,200)$(PDP)_{1.7}$ and 3 vol% of 5 nm Au nanoparticles taken at different f_s with the X-ray beam perpendicular to the trench direction. At f_s = 0.3, sharp Bragg peaks corresponding to the inter-particle distance in the nanoparticle arrays are seen in the GISAXS pattern, suggesting a perpendicular orientation of the microdomains with respect to the X-ray beam. At f_s = 0.33, the 2-D scattering pattern corresponding to the aligned 3-D nanoparticle arrays instantaneously show up and it becomes optimized at f_s = 0.38. This indicates that the cylindrical microdomains reorient to align normal to the trench direction at f_s > 0.3, which is consistent with that observed in Figure 6.12 and Figure A.5.11.

References

Chapter 1

(1) Kingery, W. D.; Vandiver, P. *Ceramic Masterpieces. Art, Structure, Technology.*; Free Press: New York, 1986.
(2) Choi, C. L.; Alivisatos, A. P. *Annu. Rev. Phys. Chem.* **2010**, *61*, 369-389.
(3) Talapin, D. V.; Lee, J.-S.; Kovalenko, M. V.; Shevchenko, E. V. *Chem. Rev.* **2010**, *110*, 389-458.
(4) Peng, X.; Wickham, J.; Alivisatos, A. P. *J. Am. Chem. Soc.* **1998**, *120*, 5343-5344.
(5) Manna, L.; Milliron, D. J.; Meisel, A.; Scher, E. C.; Alivisatos, A. P. *Nat. Mater.* **2003**, *2*, 382-385.
(6) Talapin, D. V.; Nelson, J. H.; Shevchenko, E. V.; Aloni, S.; Sadtler, B.; Alivisatos, A. P. *Nano Lett.* **2007**, *7*, 2951-2959.
(7) Luther, J. M.; Zheng, H.; Sadtler, B.; Alivisatos, A. P. *J. Am. Chem. Soc.* **2009**, *131*, 16851-16857.
(8) Luther, J. M.; Jain, P. K.; Ewers, T.; Alivisatos, A. P. *Nat. Mater.* **2011**, *10*, 361-366.
(9) Alivisatos, A. P.; Johnsson, K. P.; Peng, X. G.; Wilson, T. E.; Loweth, C. J.; Bruchez, M. P.; Schultz, P. G. *Nature* **1996**, *382*, 609-611.
(10) Mirkin, C. A.; Letsinger, R. L.; Mucic, R. C.; Storhoff, J. J. *Nature* **1996**, *382*, 607-609.
(11) Talapin, D. V.; Murray, C. B. *Science* **2005**, *310*, 86-89.
(12) Elteto, K.; Lin, X. M.; Jaeger, H. M. *Phys. Rev. B* **2005**, *71*, 205412-1-5.
(13) Schmid, G.; Simon, U. *Chem. Comm.* **2005**, *36*, 697-710.
(14) Bigioni, T. P.; Lin, X. M.; Nguyen, T. T.; Corwin, E. I.; Witten, T. A.; Jaeger, H. M. *Nat. Mater.* **2006**, *5*, 265-270.
(15) Mueggenburg, K. E.; Lin, X.-M.; Goldsmith, R. H.; Jaeger, H. M. *Nat. Mater.* **2007**, *6*, 656-660.
(16) Nykypanchuk, D.; Maye, M. M.; van der Lelie, D.; Gang, O. *Nature* **2008**, *451*, 549-552.
(17) Baker, J. L.; Widmer-Cooper, A.; Toney, M. F.; Geissler, P. L.; Alivisatos, A. P. *Nano Lett.* **2010**, *10*, 195-201.
(18) Grzelczak, M.; Vermant, J.; Furst, E. M.; Liz-Marzan, L. M. *ACS Nano* **2010**, *4*, 3591-3605.
(19) Gao, Y.; Tang, Z. *Small* **2011**, *7*, 2133-2146.

(20) Nie, Z.; Petukhova, A.; Kumacheva, E. *Nat. Nanotechnol.* **2010**, *5*, 15-25.
(21) Cheng, J. Y.; Ross, C. A.; Chan, V. Z. H.; Thomas, E. L.; Lammertink, R. G. H.; Vancso, G. J. *Adv. Mater.* **2001**, *13*, 1174-1178.
(22) Ling, X. Y.; Phang, I. Y.; Maijenburg, W.; Schonherr, H.; Reinhoudt, D. N.; Vancso, G. J.; Huskens, J. *Angew. Chem. Int. Ed.* **2009**, *48*, 983-985.
(23) Shipway, A. N.; Katz, E.; Willner, I. *Chemphyschem* **2000**, *1*, 18-52.
(24) Xia, Y. N.; Gates, B.; Yin, Y. D.; Lu, Y. *Adv. Mater.* **2000**, *12*, 693-713.
(25) Zhirnov, V. V.; Herr, D. J. C. *Computer* **2001**, *34*, 34-43.
(26) Lopes, W. A.; Jaeger, H. M. *Nature* **2001**, *414*, 735-738.
(27) Bockstaller, M. R.; Lapetnikov, Y.; Margel, S.; Thomas, E. L. *J. Am. Chem. Soc.* **2003**, *125*, 5276-5277.
(28) Hawker, C. J.; Russell, T. P. *MRS Bull.* **2005**, *30*, 952-966.
(29) Kim, B. J.; Chiu, J. J.; Yi, G. R.; Pine, D. J.; Kramer, E. J. *Adv. Mater.* **2005**, *17*, 2618-2622.
(30) Lin, Y.; Boker, A.; He, J. B.; Sill, K.; Xiang, H. Q.; Abetz, C.; Li, X. F.; Wang, J.; Emrick, T.; Long, S.; Wang, Q.; Balazs, A.; Russell, T. P. *Nature* **2005**, *434*, 55-59.
(31) Chiu, J. J.; Kim, B. J.; Kramer, E. J.; Pine, D. J. *J. Am. Chem. Soc.* **2005**, *127*, 5036-5037.
(32) Warren, S. C.; DiSalvo, F. J.; Wiesner, U. *Nat. Mater.* **2007**, *6*, 156-161.
(33) Warren, S. C.; Messina, L. C.; Slaughter, L. S.; Kamperman, M.; Zhou, Q.; Gruner, S. M.; DiSalvo, F. J.; Wiesner, U. *Science* **2008**, *320*, 1748-1752.
(34) Huang, E.; Rockford, L.; Russell, T. P.; Hawker, C. J. *Nature* **1998**, *395*, 757.
(35) Xu, T.; Kim, H. C.; DeRouchey, J.; Seney, C.; Levesque, C.; Martin, P.; Stafford, C. M.; Russell, T. P. *Polymer* **2001**, *42*, 9091-9095.
(36) Thurn-Albrecht, T.; DeRouchey, J.; Russell, T. P.; Jaeger, H. M. *Macromolecules* **2000**, *33*, 3250-3253.
(37) Kim, S. H.; Misner, M. J.; Xu, T.; Kimura, M.; Russell, T. P. *Adv. Mater.* **2004**, *16*, 226-231.
(38) Thurn-Albrecht, T.; Schotter, J.; Kastle, C. A.; Emley, N.; Shibauchi, T.; Krusin-Elbaum, L.; Guarini, K.; Black, C. T.; Tuominen, M. T.; Russell, T. P. *Science* **2000**, *290*, 2126-2129.
(39) Bockstaller, M. R.; Mickiewicz, R. A.; Thomas, E. L. *Adv. Mater.* **2005**, *17*, 1331-1349.
(40) Haryono, A.; Binder, W. H. *Small* **2006**, *2*, 600-611.
(41) Mayer, A. B. R. *Polymer. Adv. Tech.* **2001**, *12*, 96-106.
(42) Sankaran, V.; Cummins, C. C.; Schrock, R. R.; Cohen, R. E.; Silbey, R. J. *J. Am. Chem. Soc.* **1990**, *112*, 6858-6859.
(43) Cummins, C. C.; Beachy, M. D.; Schrock, R. R.; Vale, M. G.; Sankaran, V.; Cohen, R. E. *Chem. Mater.* **1991**, *3*, 1153-1163.
(44) Chan, Y. N. C.; Craig, G. S. W.; Schrock, R. R.; Cohen, R. E. *Chem. Mater.* **1992**, *4*, 885-894.
(45) Chan, Y. N. C.; Schrock, R. R.; Cohen, R. E. *J. Am. Chem. Soc.* **1992**, *114*, 7295-7296.
(46) Chan, Y. N. C.; Schrock, R. R.; Cohen, R. E. *Chem. Mater.* **1992**, *4*, 24-27.
(47) Cummins, C. C.; Schrock, R. R.; Cohen, R. E. *Chem. Mater.* **1992**, *4*, 27-30.
(48) Hashimoto, T.; Harada, M.; Sakamoto, N. *Macromolecules* **1999**, *32*, 6867-6870.
(49) Arora, H.; Du, P.; Tan, K. W.; Hyun, J. K.; Grazul, J.; Xin, H. L.; Muller, D. A.; Thompson, M. O.; Wiesner, U. *Science* **2010**, *330*, 214-219.
(50) Du, P.; Li, M. Q.; Douki, K.; Li, X. F.; Garcia, C. R. W.; Jain, A.; Smilgies, D. M.; Fetters, L. J.; Gruner, S. M.; Wiesner, U.; Ober, C. K. *Adv. Mater.* **2004**, *16*, 953-957.

(51) Simon, P. F. W.; Ulrich, R.; Spiess, H. W.; Wiesner, U. *Chem. Mater.* **2001**, *13*, 3464-3486.
(52) Templin, M.; Franck, A.; DuChesne, A.; Leist, H.; Zhang, Y. M.; Ulrich, R.; Schadler, V.; Wiesner, U. *Science* **1997**, *278*, 1795-1798.
(53) Kim, H. C.; Jia, X.; Stafford, C. M.; Kim, D. H.; McCarthy, T. J.; Tuominen, M.; Hawker, C. J.; Russell, T. P. *Adv. Mater.* **2001**, *13*, 795-797.
(54) Cha, M.-A.; Shin, C.; Kannaiyan, D.; Jang, Y. H.; Kochuveedu, S. T.; Ryu, D. Y.; Kim, D. H. *J. Mater. Chem.* **2009**, *19*, 7245-7250.
(55) Peng, J.; Mao, C.; Kim, J.; Kim, D. H. *Macromol. Rapid Commun.* **2009**, *30*, 1857-1861.
(56) Kim, S. H.; Misner, M. J.; Yang, L.; Gang, O.; Ocko, B. M.; Russell, T. P. *Macromolecules* **2006**, *39*, 8473-8479.
(57) Garcia, C.; Zhang, Y. M.; DiSalvo, F.; Wiesner, U. *Angew. Chem. Int. Ed.* **2003**, *42*, 1526-1530.
(58) Nedelcu, M.; Lee, J.; Crossland, E. J. W.; Warren, S. C.; Orilall, M. C.; Guldin, S.; Huettner, S.; Ducati, C.; Eder, D.; Wiesner, U.; Steiner, U.; Snaith, H. J. *Soft Matter* **2009**, *5*, 134-139.
(59) Docampo, P.; Guldin, S.; Stefik, M.; Tiwana, P.; Orilall, M. C.; Huettner, S.; Sai, H.; Wiesner, U.; Steiner, U.; Snaith, H. J. *Adv. Funct. Mater.* **2010**, *20*, 1787-1796.
(60) Chai, J.; Huo, F.; Zheng, Z.; Giam, L. R.; Shim, W.; Mirkin, C. A. *Proc. Natl. Acad. Sci. U.S.A.* **2010**, *107*, 20202-20206.
(61) Oh, M.; Mirkin, C. A. *Angew. Chem. Int. Ed.* **2006**, *45*, 5492-5494.
(62) Thompson, R. B.; Ginzburg, V. V.; Matsen, M. W.; Balazs, A. C. *Science* **2001**, *292*, 2469-2472.
(63) Balazs, A. C.; Emrick, T.; Russell, T. P. *Science* **2006**, *314*, 1107-1110.
(64) Lee, J. Y.; Thompson, R. B.; Jasnow, D.; Balazs, A. C. *Phys. Rev. Lett.* **2002**, *89*, 155503-1-4.
(65) Lee, J. Y.; Shou, Z. Y.; Balazs, A. C. *Macromolecules* **2003**, *36*, 7730-7739.
(66) Lauter-Pasyuk, V.; Lauter, H. J.; Ausserre, D.; Gallot, Y.; Cabuil, V.; Kornilov, E. I.; Hamdoun, B. *Physica B* **1997**, *241*, 1092-1094.
(67) Lauter-Pasyuk, V.; Lauter, H. J.; Ausserre, D.; Gallot, Y.; Cabuil, V.; Hamdoun, B.; Kornilov, E. I. *Physica B* **1998**, *248*, 243-245.
(68) Shenhar, R.; Norsten, T. B.; Rotello, V. M. *Adv. Mater.* **2005**, *17*, 657-669.
(69) Fogg, D. E.; Radzilowski, L. H.; Blanski, R.; Schrock, R. R.; Thomas, E. L. *Macromolecules* **1997**, *30*, 417-426.
(70) Xu, C.; Ohno, K.; Ladmiral, V.; Composto, R. J. *Polymer* **2008**, *49*, 3568-3577.
(71) Kim, B. J.; Bang, J.; Hawker, C. J.; Kramer, E. J. *Macromolecules* **2006**, *39*, 4108-4114.
(72) Kim, B. J.; Bang, J.; Hawker, C. J.; Chiu, J. J.; Pine, D. J.; Jang, S. G.; Yang, S.-M.; Kramer, E. J. *Langmuir* **2007**, *23*, 12693-12703.
(73) Chiu, J. J.; Kim, B. J.; Yi, G.-R.; Bang, J.; Kramer, E. J.; Pine, D. J. *Macromolecules* **2007**, *40*, 3361-3365.
(74) Sides, S. W.; Kim, B. J.; Kramer, E. J.; Fredrickson, G. H. *Phys. Rev. Lett.* **2006**, *96*, 250601.
(75) Akcora, P.; Liu, H.; Kumar, S. K.; Moll, J.; Li, Y.; Benicewicz, B. C.; Schadler, L. S.; Acehan, D.; Panagiotopoulos, A. Z.; Pryamitsyn, V.; Ganesan, V.; Ilavsky, J.; Thiyagarajan, P.; Colby, R. H.; Douglas, J. F. *Nat. Mater.* **2009**, *8*, 354-359.
(76) Jayaraman, A.; Schweizer, K. S. *Macromolecules* **2009**, *42*, 8423-8434.

(77) Nair, N.; Jayaraman, A. *Macromolecules* **2010**, *43*, 8251-8263.
(78) Martin, T. B.; Seifpour, A.; Jayaraman, A. *Soft Matter* **2011**, *7*, 5952-5964.
(79) Warren, S. C.; Messina, L. C.; Slaughter, L. S.; Kamperman, M.; Zhou, Q.; Gruner, S. M.; DiSalvo, F. J.; Wiesner, U. *Science* **2008**, *320*, 1748-1752.
(80) Jang, S. G.; Kramer, E. J.; Hawker, C. J. *J. Am. Chem. Soc.* **2012**, *133*, 16986-16996.
(81) Lin, Y.; Daga, V. K.; Anderson, E. R.; Gido, S. P.; Watkins, J. J. *J. Am. Chem. Soc.* **2011**, *133*, 6513-6516.
(82) Jang, S. G.; Khan, A.; Hawker, C. J.; Kramer, E. J. *Macromolecules* **2012**, *45*, 1553-1561.
(83) Lee, J. Y.; Shou, Z.; Balazs, A. C. *Phys. Rev. Lett.* **2003**, *91*, 136103.
(84) Huh, J.; Ginzburg, V. V.; Balazs, A. C. *Macromolecules* **2000**, *33*, 8085-8096.
(85) Lee, J. Y.; Thompson, R. B.; Jasnow, D.; Balazs, A. C. *Macromolecules* **2002**, *35*, 4855-4858.
(86) Spontak, R. J.; Shankar, R.; Bowman, M. K.; Krishnan, A. S.; Hamersky, M. W.; Samseth, J.; Bockstaller, M. R.; Rasmussen, K. Ø. *Nano Lett.* **2006**, *6*, 2115-2120.
(87) Zehner, R. W.; Lopes, W. A.; Morkved, T. L.; Jaeger, H.; Sita, L. R. *Langmuir* **1998**, *14*, 241-244.
(88) Binder, W. H.; Kluger, C.; Straif, C. J.; Friedbacher, G. *Macromolecules* **2005**, *38*, 9405-9410.
(89) Thurn-Albrecht, T.; Steiner, R.; DeRouchey, J.; Stafford, C. M.; Huang, E.; Bal, M.; Tuominen, M.; Hawker, C. J.; Russell, T. *Adv. Mater.* **2000**, *12*, 787-791.
(90) Misner, M. J.; Skaff, H.; Emrick, T.; Russell, T. P. *Adv. Mater.* **2003**, *15*, 221-224.
(91) Zhang, Q. L.; Xu, T.; Butterfield, D.; Misner, M. J.; Ryu, D. Y.; Emrick, T.; Russell, T. P. *Nano Lett.* **2005**, *5*, 357-361.
(92) Li, Q.; He, J.; Glogowski, E.; Li, X.; Wang, J.; Emrick, T.; Russell, T. P. *Adv. Mater.* **2008**, *20*, 1462-1466.
(93) Kang, H.; Detcheverry, F. A.; Mangham, A. N.; Stoykovich, M. P.; Daoulas, K. C.; Hamers, R. J.; Mueller, M.; de Pablo, J. J.; Nealey, P. F. *Phys. Rev. Lett.* **2008**, *100*, 148303.
(94) Park, S. C.; Kim, B. J.; Hawker, C. J.; Kramer, E. J.; Bang, J.; Ha, J. S. *Macromolecules* **2007**, *40*, 8119-8124.
(95) Li, D.; Lee, J. Y.; Kim, D. H. *J. Colloid Interface Sci.* **2011**, *354*, 585-591.
(96) Meli, L.; Li, Y.; Lim, K. T.; Johnston, K. P.; Green, P. F. *Macromolecules* **2007**, *40*, 6713-6720.
(97) Arceo, A.; Meli, L.; Green, P. F. *Nano Lett.* **2008**, *8*, 2271-2276.
(98) Meli, L.; Arceo, A.; Green, P. F. *Soft Matter* **2009**, *5*, 533-537.
(99) Green, P. F. *Soft Matter* **2011**, *7*, 7914-7926.
(100) Gupta, S.; Zhang, Q. L.; Emrick, T.; Balazs, A. C.; Russell, T. P. *Nat. Mater.* **2006**, *5*, 229-233.
(101) Kim, J.; Green, P. F. *Macromolecules* **2010**, *43*, 10452-10456.
(102) Yoo, M.; Kim, S.; Jang, S. G.; Choi, S.-H.; Yang, H.; Kramer, E. J.; Lee, W. B.; Kim, B. J.; Bang, J. *Macromolecules* **2011**, *44*, 9356-9365.
(103) Li, D.; He, Q.; Cui, Y.; Li, J. *Chem. Mater.* **2007**, *19*, 412-417.
(104) Chai, J.; Buriak, J. M. *Acs Nano* **2008**, *2*, 489-501.
(105) Li, D.; Cui, Y.; Wang, K.; He, Q.; Yan, X.; Li, J. *Adv. Funct. Mater.* **2007**, *17*, 3134-3140.
(106) Li, D.; He, Q.; Cui, Y.; Wang, K.; Zhang, X.; Li, J. *Chem. Eur. J.* **2007**, *13*, 2224-2229.

(107) Shevchenko, E. V.; Talapin, D. V.; Kotov, N. A.; O'Brien, S.; Murray, C. B. *Nature* **2006**, *439*, 55-59.
(108) Shevchenko, E. V.; Ringler, M.; Schwemer, A.; Talapin, D. V.; Klar, T. A.; Rogach, A. L.; Feldmann, J.; Alivisatos, A. P. *J. Am. Chem. Soc.* **2008**, *130*, 3274-3275.
(109) Sohn, B. H.; Choi, J. M.; Yoo, S. I.; Yun, S. H.; Zin, W. C.; Jung, J. C.; Kanehara, M.; Hirata, T.; Teranishi, T. *J. Am. Chem. Soc.* **2003**, *125*, 6368-6369.
(110) Acharya, H.; Sung, J.; Sohn, B.-H.; Kim, D. H.; Tamada, K.; Park, C. *Chem. Mater.* **2009**, *21*, 4248-4255.
(111) Acharya, H.; Sung, J.; Bae, I.; Kim, T.; Kim, D. H.; Park, C. *Chem. Eur. J.* **2012**, *Early View*.
(112) Haridas, M.; Basu, J. K. *Nanotechnology* **2010**, *21*, 415202.
(113) Haridas, M.; Tripathi, L. N.; Basu, J. K. *Appl. Phys. Lett.* **2011**, *98*, 063305.
(114) Ruokolainen, J.; Saariaho, M.; Ikkala, O.; ten Brinke, G.; Thomas, E. L.; Torkkeli, M.; Serimaa, R. *Macromolecules* **1999**, *32*, 1152-1158.
(115) Ruokolainen, J.; ten Brinke, G.; Ikkala, O. *Adv. Mater.* **1999**, *11*, 777-780.
(116) Kosonen, H.; Valkama, S.; Hartikainen, J.; Eerikainen, H.; Torkkeli, M.; Jokela, K.; Serimaa, R.; Sundholm, F.; ten Brinke, G.; Ikkala, O. *Macromolecules* **2002**, *35*, 10149-10154.
(117) Kosonen, H.; Valkama, S.; Ruokolainen, J.; Torkkeli, M.; Serimaa, R.; ten Brinke, G.; Ikkala, O. *Eur. Phys. J. E Soft Matter* **2003**, *10*, 69-75.
(118) Polushkin, E.; van Ekenstein, G. A.; Dolbnya, I.; Bras, W.; Ikkala, O.; ten Brinke, G. *Macromolecules* **2003**, *36*, 1421-1423.
(119) van Ekenstein, G. A.; Polushkin, E.; Nijland, H.; Ikkala, O.; ten Brinke, G. *Macromolecules* **2003**, *36*, 3684-3688.
(120) Valkama, S.; Ruotsalainen, T.; Nykanen, A.; Laiho, A.; Kosonen, H.; ten Brinke, G.; Ikkala, O.; Ruokolainen, J. *Macromolecules* **2006**, *39*, 9327-9336.
(121) ten Brinke, G.; Ruokolainen, J.; Ikkala, O. In *Hydrogen Bonded Polymers*; Binder, W., Ed. 2007; Vol. 207, p 113-177.
(122) Ikkala, O.; Knaapila, M.; Ruokolainen, J.; Torkkeli, M.; Serimaa, R.; Jokela, K.; Horsburgh, L.; Monkman, A.; ten Brinke, G. *Adv. Mater.* **1999**, *11*, 1206-1210.
(123) Ikkala, O.; ten Brinke, G. *Chem. Comm.* **2004**, 2131-2137.
(124) de Moel, K.; Maki-Ontto, R.; Stamm, M.; Ikkala, O.; ten Brinke, G. *Macromolecules* **2001**, *34*, 2892-2900.
(125) van Zoelen, W.; ten Brinke, G. *Soft Matter* **2009**, *5*, 1568-1582.
(126) van Zoelen, W.; Asumaa, T.; Ruokolainen, J.; Ikkala, O.; ten Brinke, G. *Macromolecules* **2008**, *41*, 3199-3208.
(127) Tung, S.-H.; Kalarickal, N. C.; Mays, J. W.; Xu, T. *Macromolecules* **2008**, *41*, 6453-6462.
(128) Kao, J.; Tingsanchali, J.; Xu, T. *Macromolecules* **2011**, *44*, 4392-4400.
(129) van Zoelen, W.; Polushkin, E.; ten Brinke, G. *Macromolecules* **2008**, *41*, 8807-8814.
(130) Nandan, B.; Vyas, M. K.; Boehme, M.; Stamm, M. *Macromolecules* **2010** *43*, 2463-2473.
(131) Zhao, Y.; Thorkelsson, K.; Mastroianni, A. J.; Schilling, T.; Luther, J. M.; Rancatore, B. J.; Matsunaga, K.; Jinnai, H.; Wu, Y.; Poulsen, D.; Fréchet, J. M. J.; Paul Alivisatos, A.; Xu, T. *Nat. Mater.* **2009**, *8*, 979-985.
(132) Thorkelsson, K.; Rancatore, B. J.; Mauldin, C. E.; Luther, J. M.; Poulsen, D.; Freacutechet, J. M. J.; Alivisatos, A. P.; Ting, X. *Proceedings 2010 10th IEEE International*

Conference on Nanotechnology and Joint Symposium with Nano Korea 2010 KINTEX (IEEE-NANO 2010) **2010**, 51-5.
(133) Kato, T.; Frechét, J. M. J. *Macromolecules* **1989**, *22*, 3818-3819.
(134) Ruokolainen, J.; Torkkeli, M.; Serimaa, R.; Vahvaselka, S.; Saariaho, M.; tenBrinke, G.; Ikkala, O. *Macromolecules* **1996**, *29*, 6621-6628.
(135) Chen, H. L.; Ko, C. C.; Lin, T. L. *Langmuir* **2002**, *18*, 5619-5623.
(136) Chao, C. Y.; Li, X. F.; Ober, C. K.; Osuji, C.; Thomas, E. L. *Adv. Funct. Mater.* **2004**, *14*, 364-370.
(137) Chao, C. Y.; Li, X. F.; Ober, C. K. *Pure and Appl. Chem.* **2004**, *76*, 1337-1343.
(138) Osuji, C. O.; Chao, C. Y.; Ober, C. K.; Thomas, E. L. *Macromolecules* **2006**, *39*, 3114-3117.
(139) de Wit, J.; van Ekenstein, G. A.; Polushkin, E.; Kvashnina, K.; Bras, W.; Ikkala, O.; ten Brinke, G. *Macromolecules* **2008**, *41*, 4200-4204.
(140) Korhonen, J. T.; Verho, T.; Rannou, P.; Ikkala, O. *Macromolecules* **2010**, *43*, 1507-1514.
(141) Gopinadhan, M.; Majewski, P. W.; Beach, E. S.; Osuji, C. O. *ACS Macro Lett.* **2012**, *1*, 184-189.
(142) Würthner, F.; Chen, Z.; Hoeben, F. J. M.; Osswald, P.; You, C.-C.; Jonkheijm, P.; Herrikhuyzen, J. V.; Schenning, A. P. H. J.; van der Schoot, P. P. A. M.; Meijer, E. W.; Beckers, E. H. A.; Meskers, S. C. J.; Janssen, R. A. J. *J. Am. Chem. Soc.* **2004**, *126*, 10611-8.
(143) Sary, N.; Richard, F.; Brochon, C.; Leclerc, N.; Lévêque, P.; Audinot, J.-N.; Berson, S.; Heiser, T.; Hadziioannou, G.; Mezzenga, R. *Adv. Mater.* **2010**, *22*, 763-8.
(144) Rancatore, B. J.; Mauldin, C. E.; Tung, S.-H.; Wang, C.; Hexemer, A.; Strzalka, J.; Fréchet, J. M. J.; Xu, T. *ACS Nano* **2010**, *4*, 2721-2729.
(145) Rancatore, B. J.; Mauldin, C. E.; Fréchet, J. M. J.; Xu, T. *Macromolecules* **2012**, *45*, 8292-8299.

Chapter 2

(1) Alivisatos, A. P.; Johnsson, K. P.; Peng, X. G.; Wilson, T. E.; Loweth, C. J.; Bruchez, M. P.; Schultz, P. G. *Nature* **1996**, *382*, 609.
(2) Mirkin, C. A.; Letsinger, R. L.; Mucic, R. C.; Storhoff, J. J. *Nature* **1996**, *382*, 607.
(3) Talapin, D. V.; Murray, C. B. *Science* **2005**, *310*, 86.
(4) Bigioni, T. P.; Lin, X. M.; Nguyen, T. T.; Corwin, E. I.; Witten, T. A.; Jaeger, H. M. *Nat. Mater.* **2006**, *5*, 265.
(5) Elteto, K.; Lin, X. M.; Jaeger, H. M. *Phys. Rev. B: Condens. Matter* **2005**, *71*, 205412.
(6) Nykypanchuk, D.; Maye, M. M.; van der Lelie, D.; Gang, O. *Nature* **2008**, *451*, 549.
(7) Baker, J. L.; Widmer-Cooper, A.; Toney, M. F.; Geissler, P. L.; Alivisatos, A. P. *Nano Lett.* **2010**, *10*, 195.
(8) Mueggenburg, K. E.; Lin, X.-M.; Goldsmith, R. H.; Jaeger, H. M. *Nat. Mater.* **2007**, *6*, 656.
(9) Choi, C. L.; Alivisatos, A. P. *Annu. Rev. Phys. Chem.* **2010**, *61*, 369.
(10) Schmid, G.; Simon, U. *Chem. Commun.* **2005**, *36*, 697.
(11) Gao, Y.; Tang, Z. *Small* **2011**, *7*, 2133.
(12) Quinten, M.; Leitner, A.; Krenn, J. R.; Aussenegg, F. R. *Opt. Lett.* **1998**, *23*, 1331.
(13) Brongersma, M. L.; Hartman, J. W.; Atwater, H. A. *Phys. Rev. B.* **2000**, *62*, 16356.
(14) Maier, S. A.; Kik, P. G.; Atwater, H. A.; Meltzer, S.; Harel, E.; Koel, B. E.; Requicha, A. A. G. *Nat. Mater.* **2003**, *2*, 229.
(15) Wang, H.; Levin, C. S.; Halas, N. J. *J. Am. Chem. Soc.* **2005**, *127*, 14992.
(16) Chen, C.-F.; Tzeng, S.-D.; Chen, H.-Y.; Lin, K.-J.; Gwo, S. *J. Am. Chem. Soc.* **2008**, *130*, 824.
(17) Tan, S. J.; Campolongo, M. J.; Luo, D.; Cheng, W. *Nat. Nanotechnol.* **2011**, *6*, 268.
(18) Redl, F. X.; Cho, K. S.; Murray, C. B.; O'Brien, S. *Nature* **2003**, *423*, 968.
(19) Shevchenko, E. V.; Talapin, D. V.; Kotov, N. A.; O'Brien, S.; Murray, C. B. *Nature* **2006**, *439*, 55.
(20) Tian, M.; Xiaoshan, K.; Huanjun, C.; Tao, W.; Hoi-Lam, T.; Kok-Wai, C.; Ji-Yao, C.; Jianfang, W. *Angew. Chem. Int. Ed.* **2008**, *47*, 9685.
(21) Zanella, M.; Gomes, R.; Povia, M.; Giannini, C.; Zhang, Y.; Riskin, A.; Van Bael, M.; Hens, Z.; Manna, L. *Adv. Mater.* **2011**, *23*, 2205.
(22) Cheng, J. Y.; Ross, C. A.; Chan, V. Z. H.; Thomas, E. L.; Lammertink, R. G. H.; Vancso, G. J. *Adv. Mater.* **2001**, *13*, 1174.
(23) Cheng, J. Y.; Ross, C. A.; Thomas, E. L.; Smith, H. I.; Vancso, G. J. *Appl. Phys. Lett.* **2002**, *81*, 3657.
(24) Ling, X. Y.; Phang, I. Y.; Maijenburg, W.; Schonherr, H.; Reinhoudt, D. N.; Vancso, G. J.; Huskens, J. *Angew. Chem. Int. Ed.* **2009**, *48*, 983.
(25) Bockstaller, M. R.; Mickiewicz, R. A.; Thomas, E. L. *Adv. Mater.* **2005**, *17*, 1331.
(26) Mackay, M. E.; Tuteja, A.; Duxbury, P. M.; Hawker, C. J.; Horn, B. V.; Guan, Z.; Chen, G.; Krishnan, R. S. *Science* **2006**, *311*, 1740.
(27) Akcora, P.; Liu, H.; Kumar, S. K.; Moll, J.; Li, Y.; Benicewicz, B. C.; Schadler, L. S.; Acehan, D.; Panagiotopoulos, A. Z.; Pryamitsyn, V.; Ganesan, V.; Ilavsky, J.; Thiyagarajan, P.; Colby, R. H.; Douglas, J. F. *Nat. Mater.* **2009**, *8*, 354.

(28) Zhao, Y.; Thorkelsson, K.; Mastroianni, A. J.; Schilling, T.; Luther, J. M.; Rancatore, B. J.; Matsunaga, K.; Jinnai, H.; Wu, Y.; Poulsen, D.; Frechet, J. M. J.; Alivisatos, A. P.; Xu, T. *Nat. Mater.* **2009**, *8*, 979.
(29) Chan, Y. N. C.; Schrock, R. R.; Cohen, R. E. *Chem. Mater.* **1992**, *4*, 24.
(30) Yue, J.; Sankaran, V.; Cohen, R. E.; Schrock, R. R. *J. Am. Chem. Soc.* **1993**, *115*, 4409.
(31) Warren, S. C.; Messina, L. C.; Slaughter, L. S.; Kamperman, M.; Zhou, Q.; Gruner, S. M.; DiSalvo, F. J.; Wiesner, U. *Science* **2008**, *320*, 1748.
(32) Haryono, A.; Binder, W. H. *Small* **2006**, *2*, 600.
(33) Balazs, A. C.; Emrick, T.; Russell, T. P. *Science* **2006**, *314*, 1107.
(34) Chiu, J. J.; Kim, B. J.; Kramer, E. J.; Pine, D. J. *J. Am. Chem. Soc.* **2005**, *127*, 5036.
(35) Kim, B. J.; Bang, J.; Hawker, C. J.; Kramer, E. J. *Macromolecules* **2006**, *39*, 4108.
(36) Jang, S. G.; Khan, A.; Dimitriou, M. D.; Kim, B. J.; Lynd, N. A.; Kramer, E. J.; Hawker, C. J. *Soft Matter*, *7*, 6255.
(37) Jang, S. G.; Kramer, E. J.; Hawker, C. J. *J. Am. Chem. Soc.*, *133*, 16986.
(38) Thompson, R. B.; Ginzburg, V. V.; Matsen, M. W.; Balazs, A. C. *Science* **2001**, *292*, 2469.
(39) Lee, J. Y.; Thompson, R. B.; Jasnow, D.; Balazs, A. C. *Phys. Rev. Lett.* **2002**, *89*, 155503.
(40) Lee, J. Y.; Shou, Z. Y.; Balazs, A. C. *Macromolecules* **2003**, *36*, 7730.
(41) Jayaraman, A.; Schweizer, K. S. *Macromolecules* **2009**, *42*, 8423.
(42) Martin, T. B.; Seifpour, A.; Jayaraman, A. *Soft Matter* **2011**, *7*, 5952.
(43) Nair, N.; Jayaraman, A. *Macromolecules* **2010**, *43*, 8251.
(44) Bockstaller, M. R.; Lapetnikov, Y.; Margel, S.; Thomas, E. L. *J. Am. Chem. Soc.* **2003**, *125*, 5276.
(45) Listak, J.; Bockstaller, M. R. *Macromolecules* **2006**, *39*, 5820.
(46) Thorkelsson, K.; Mastroianni, A. J.; Ercius, P.; Xu, T. *Nano Lett.* **2012**, *12*, 498.
(47) Li, Q.; He, J.; Glogowski, E.; Li, X.; Wang, J.; Emrick, T.; Russell, T. P. *Adv. Mater.* **2008**, *20*, 1462.
(48) Kim, J.; Green, P. F. *Macromolecules*, *43*, 10452.
(49) Meli, L.; Li, Y.; Lim, K. T.; Johnston, K. P.; Green, P. F. *Macromolecules* **2007**, *40*, 6713.
(50) Gupta, S.; Zhang, Q. L.; Emrick, T.; Balazs, A. C.; Russell, T. P. *Nat. Mater.* **2006**, *5*, 229.
(51) Meli, L.; Arceo, A.; Green, P. F. *Soft Matter* **2009**, *5*, 533.
(52) Yoo, M.; Kim, S.; Jang, S. G.; Choi, S.-H.; Yang, H.; Kramer, E. J.; Lee, W. B.; Kim, B. J.; Bang, J. *Macromolecules*, *44*, 9356.
(53) Hasegawa, H.; Hashimoto, T. *Macromolecules* **1985**, *18*, 589.
(54) Huang, E.; Rockford, L.; Russell, T. P.; Hawker, C. J. *Nature* **1998**, *395*, 757.
(55) Fasolka, M. J.; Mayes, A. M. *Annu. Rev. Mater. Res.* **2001**, *31*, 323.
(56) Xu, T.; Hawker, C. J.; Russell, T. P. *Macromolecules* **2005**, *38*, 2802.
(57) Lin, Y.; Boker, A.; He, J. B.; Sill, K.; Xiang, H. Q.; Abetz, C.; Li, X. F.; Wang, J.; Emrick, T.; Long, S.; Wang, Q.; Balazs, A.; Russell, T. P. *Nature* **2005**, *434*, 55.
(58) Lee, J. Y.; Shou, Z.; Balazs, A. C. *Phys. Rev. Lett.* **2003**, *91*.
(59) Kim, G.; Libera, M. *Macromolecules* **1998**, *31*, 2569.
(60) Kim, S. H.; Misner, M. J.; Russell, T. P. *Adv. Mater.* **2004**, *16*, 2119.

(61) Rubinstein, M.; Colby, R. H. *Polymer Physics*; Oxford University Press: New York, 2003.
(62) Tung, S.-H.; Kalarickal, N. C.; Mays, J. W.; Xu, T. *Macromolecules* **2008**, *41*, 6453.
(63) Kao, J.; Tingsanchali, J.; Xu, T. *Macromolecules* **2011**, *44*, 4392.
(64) Son, J. G.; Chang, J.-B.; Berggren, K. K.; Ross, C. A. *Nano Lett.* **2011**, *11*, 5079.
(65) Jung, Y. S.; Ross, C. A. *Adv. Mater.* **2009**, *21*, 2540.
(66) Ikkala, O.; ten Brinke, G. *Chem. Commun.* **2004**, 2131.
(67) Peng, S.; Lee, Y.; Wang, C.; Yin, H.; Dai, S.; Sun, S. *Nano Res.* **2008**, *1*, 229.
(68) van Zoelen, W.; Asumaa, T.; Ruokolainen, J.; Ikkala, O.; ten Brinke, G. *Macromolecules* **2008**, *41*, 3199.
(69) van Zoelen, W.; Polushkin, E.; ten Brinke, G. *Macromolecules* **2008**, *41*, 8807.
(70) Lee, B.; Park, I.; Yoon, J.; Park, S.; Kim, J.; Kim, K. W.; Chang, T.; Ree, M. *Macromolecules* **2005**, *38*, 4311.
(71) Tate, M. P.; Urade, V. N.; Kowalski, J. D.; Wei, T. C.; Hamilton, B. D.; Eggiman, B. W.; Hillhouse, H. W. *J. Phys. Chem. B* **2006**, *110*, 9882.
(72) Stein, G. E.; Kramer, E. J.; Li, X.; Wang, J. *Macromolecules* **2007**, *40*, 2453.
(73) Saariaho, M.; Subbotin, A.; Szleifer, I.; Ikkala, O.; ten Brinke, G. *Macromolecules* **1999**, *32*, 4439.

Chapter 3

(1) Colvin, V. L.; Schlamp, M. C.; Alivisatos, A. P. *Nature* **1994**, *370*, 354.
(2) Murray, C. B.; Kagan, C. R.; Bawendi, M. G. *Science* **1995**, *270*, 1335.
(3) Murray, C. B.; Kagan, C. R.; Bawendi, M. G. *Annu. Rev. Mater. Sci.* **2000**, *30*, 545.
(4) Talapin, D. V.; Murray, C. B. *Science* **2005**, *310*, 86.
(5) Luther, J. M.; Law, M.; Beard, M. C.; Song, Q.; Reese, M. O.; Ellingson, R. J.; Nozik, A. J. *Nano Lett.* **2008**, *8*, 3488.
(6) Nakanishi, H.; Walker, D. A.; Bishop, K. J. M.; Wesson, P. J.; Yan, Y.; Soh, S.; Swaminathan, S.; Grzybowski, B. A. *Nat. Nanotechnol.* **2011**, *6*, 740.
(7) Koh, W.-k.; Saudari, S. R.; Fafarman, A. T.; Kagan, C. R.; Murray, C. B. *Nano Lett.* **2011**, *11*, 4764.
(8) Kovalenko, M. V.; Scheele, M.; Talapin, D. V. *Science* **2009**, *324*, 1417.
(9) Nag, A.; Kovalenko, M. V.; Lee, J.-S.; Liu, W.; Spokoyny, B.; Talapin, D. V. *J. Am. Chem. Soc.* **2011**, *133*, 10612.
(10) Fafarman, A. T.; Koh, W.-k.; Diroll, B. T.; Kim, D. K.; Ko, D.-K.; Oh, S. J.; Ye, X.; Doan-Nguyen, V.; Crump, M. R.; Reifsnyder, D. C.; Murray, C. B.; Kagan, C. R. *J. Am. Chem. Soc.* **2011**, *133*, 15753.
(11) Scheele, M.; Hanifi, D.; Zherebetskyy, D.; Chourou, S. T.; Axnanda, S.; Rancatore, B. J.; Thorkelsson, K.; Xu, T.; Liu, Z.; Wang, L.-W.; Liu, Y.; Alivisatos, A. P. *ACS Nano* **2014**, *8*, 2532.
(12) Bockstaller, M. R.; Mickiewicz, R. A.; Thomas, E. L. *Adv. Mater.* **2005**, *17*, 1331.
(13) Balazs, A. C.; Emrick, T.; Russell, T. P. *Science* **2006**, *314*, 1107.
(14) Millo, O.; Azulay, D.; Toker, D.; Balberg, I. *Int. J. Mod. Phys. B* **2004**, *18*, 2091.
(15) Grimaldi, C.; Balberg, I. *Phys. Rev. Lett.* **2006**, *96*, 066602.
(16) Kagan, C. R.; Murray, C. B.; Nirmal, M.; Bawendi, M. G. *Phys. Rev. Lett.* **1996**, *76*, 1517.
(17) Orilall, M. C.; Wiesner, U. *Chem. Soc. Rev.* **2013**, *40*, 520.
(18) Thompson, R. B.; Ginzburg, V. V.; Matsen, M. W.; Balazs, A. C. *Science* **2001**, *292*, 2469.
(19) Bockstaller, M. R.; Lapetnikov, Y.; Margel, S.; Thomas, E. L. *J. Am. Chem. Soc.* **2003**, *125*, 5276.
(20) Chiu, J. J.; Kim, B. J.; Kramer, E. J.; Pine, D. J. *J. Am. Chem. Soc.* **2005**, *127*, 5036.
(21) Yeh, S.-W.; Wei, K.-H.; Sun, Y.-S.; Jeng, U. S.; Liang, K. S. *Macromolecules* **2003**, *36*, 7903.
(22) Yeh, S.-W.; Wei, K.-H.; Sun, Y.-S.; Jeng, U. S.; Liang, K. S. *Macromolecules* **2005**, *38*, 6559.
(23) Kim, B. J.; Chiu, J. J.; Yi, G. R.; Pine, D. J.; Kramer, E. J. *Adv. Mater.* **2005**, *17*, 2618.
(24) Park, M. J.; Char, K.; Park, J.; Hyeon, T. *Langmuir* **2006**, *22*, 1375.
(25) Chung, H.-j.; Ohno, K.; Fukuda, T.; Composto, R. J. *Nano Lett.* **2005**, *5*, 1878.
(26) Li, L.; Miesch, C.; Sudeep, P. K.; Balazs, A. C.; Emrick, T.; Russell, T. P.; Hayward, R. C. *Nano Lett.* **2011**, *11*, 1997.
(27) Jang, S. G.; Kramer, E. J.; Hawker, C. J. *J. Am. Chem. Soc.* **2011**, *133*, 16986.
(28) Lin, Y.; Daga, V. K.; Anderson, E. R.; Gido, S. P.; Watkins, J. J. *J. Am. Chem. Soc.* **2011**, *133*, 6513.
(29) Jang, S. G.; Khan, A.; Hawker, C. J.; Kramer, E. J. *Macromolecules* **2012**, *45*, 1553.

(30) Yao, L.; Lin, Y.; Watkins, J. J. *Macromolecules* **2014**, *47*, 1844.
(31) Warren, S. C.; Messina, L. C.; Slaughter, L. S.; Kamperman, M.; Zhou, Q.; Gruner, S. M.; DiSalvo, F. J.; Wiesner, U. *Science* **2008**, *320*, 1748.
(32) Lin, Y.; Boker, A.; He, J.; Sill, K.; Xiang, H.; Abetz, C.; Li, X.; Wang, J.; Emrick, T.; Long, S.; Wang, Q.; Balazs, A.; Russell, T. P. *Nature* **2005**, *434*, 55.
(33) Kim, J.; Green, P. F. *Macromolecules* **2010**, *43*, 10452.
(34) Zhao, Y.; Thorkelsson, K.; Mastroianni, A. J.; Schilling, T.; Luther, J. M.; Rancatore, B. J.; Matsunaga, K.; Jinnai, H.; Wu, Y.; Poulsen, D.; Frechet, J. M. J.; Paul Alivisatos, A.; Xu, T. *Nat. Mater.* **2009**, *8*, 979.
(35) Kao, J.; Bai, P.; Chuang, V. P.; Jiang, Z.; Ercius, P.; Xu, T. *Nano Lett.* **2012**, *12*, 2610.
(36) Kao, J.; Bai, P.; Lucas, J. M.; Alivisatos, A. P.; Xu, T. *J. Am. Chem. Soc.* **2013**, *135*, 1680.
(37) Stratford, K.; Adhikari, R.; Pagonabarraga, I.; Desplat, J. C.; Cates, M. E. *Science* **2005**, *309*, 2198.
(38) Herzig, E. M.; White, K. A.; Schofield, A. B.; Poon, W. C. K.; Clegg, P. S. *Nat. Mater.* **2007**, *6*, 966.
(39) Ruokolainen, J.; Saariaho, M.; Ikkala, O.; ten Brinke, G.; Thomas, E. L.; Torkkeli, M.; Serimaa, R. *Macromolecules* **1999**, *32*, 1152.
(40) Lin, H.; Steyerl, A.; Satija, S. K.; Karim, A.; Russell, T. P. *Macromolecules* **1995**, *28*, 1470.

Chapter 4

(1) Nie, Z.; Petukhova, A.; Kumacheva, E. *Nat. Nanotechnol.* 2010, *5*, 15.
(2) Shimizu, K. T.; Woo, W. K.; Fisher, B. R.; Eisler, H. J.; Bawendi, M. G. *Phys. Rev. Lett.* 2002, *89*, 117401.
(3) Kulakovich, O.; Strekal, N.; Yaroshevich, A.; Maskevich, S.; Gaponenko, S.; Nabiev, I.; Woggon, U.; Artemyev, M. *Nano Lett.* 2002, *2*, 1449.
(4) Govorov, A. O.; Bryant, G. W.; Zhang, W.; Skeini, T.; Lee, J.; Kotov, N. A.; Slocik, J. M.; Naik, R. R. *Nano Lett.* 2006, *6*, 984.
(5) Akimov, A. V.; Mukherjee, A.; Yu, C. L.; Chang, D. E.; Zibrov, A. S.; Hemmer, P. R.; Park, H.; Lukin, M. D. *Nature* 2007, *450*, 402.
(6) Fedutik, Y.; Temnov, V. V.; Schops, O.; Woggon, U.; Artemyev, M. V. *Phys. Rev. Lett.* 2007, *99*, 136802.
(7) Noginov, M. A.; Zhu, G.; Belgrave, A. M.; Bakker, R.; Shalaev, V. M.; Narimanov, E. E.; Stout, S.; Herz, E.; Suteewong, T.; Wiesner, U. *Nature* 2009, *460*, 1110.
(8) Gomez, D. E.; Vernon, K. C.; Mulvaney, P.; Davis, T. J. *Nano Lett.* 2009, *10*, 274.
(9) Atwater, H. A.; Polman, A. *Nat. Mater.* 2010, *9*, 205.
(10) Shevchenko, E. V.; Talapin, D. V.; Kotov, N. A.; O'Brien, S.; Murray, C. B. *Nature* 2006, *439*, 55.
(11) Shevchenko, E. V.; Ringler, M.; Schwemer, A.; Talapin, D. V.; Klar, T. A.; Rogach, A. L.; Feldmann, J.; Alivisatos, A. P. *J. Am. Chem. Soc.* 2008, *130*, 3274.
(12) Mistark, P. A.; Park, S.; Yalcin, S. E.; Lee, D. H.; Yavuzcetin, O.; Tuominen, M. T.; Russell, T. P.; Achermann, M. *ACS Nano* 2009, *3*, 3987.
(13) Kagan, C. R.; Murray, C. B.; Bawendi, M. G. *Phys. Rev. B* 1996, *54*, 8633.
(14) Haryono, A.; Binder, W. H. *Small* 2006, *2*, 600.
(15) Bockstaller, M. R.; Mickiewicz, R. A.; Thomas, E. L. *Adv. Mater.* 2005, *17*, 1331.
(16) Thompson, R. B.; Ginzburg, V. V.; Matsen, M. W.; Balazs, A. C. *Science* 2001, *292*, 2469.
(17) Huh, J.; Ginzburg, V. V.; Balazs, A. C. *Macromolecules* 2000, *33*, 8085.
(18) Lee, J. Y.; Thompson, R. B.; Jasnow, D.; Balazs, A. C. *Macromolecules* 2002, *35*, 4855.
(19) Bockstaller, M. R.; Lapetnikov, Y.; Margel, S.; Thomas, E. L. *J. Am. Chem. Soc.* 2003, *125*, 5276.
(20) Yoo, M.; Kim, S.; Jang, S. G.; Choi, S.-H.; Yang, H.; Kramer, E. J.; Lee, W. B.; Kim, B. J.; Bang, J. *Macromolecules* 2011, *44*, 9356.
(21) Lin, Y.; Boker, A.; He, J. B.; Sill, K.; Xiang, H. Q.; Abetz, C.; Li, X. F.; Wang, J.; Emrick, T.; Long, S.; Wang, Q.; Balazs, A.; Russell, T. P. *Nature* 2005, *434*, 55.
(22) Kao, J.; Bai, P.; Chuang, V. P.; Jiang, Z.; Ercius, P.; Xu, T. *Nano Lett.* 2012, *12*, 2610.
(23) Balazs, A. C.; Emrick, T.; Russell, T. P. *Science* 2006, *314*, 1107.
(24) Meli, L.; Li, Y.; Lim, K. T.; Johnston, K. P.; Green, P. F. *Macromolecules* 2007, *40*, 6713.
(25) Jang, S. G.; Kramer, E. J.; Hawker, C. J. *J. Am. Chem. Soc.* 2011, *133*, 16986.
(26) Jang, S. G.; Khan, A.; Hawker, C. J.; Kramer, E. J. *Macromolecules* 2012, *45*, 1553.
(27) Wang, Q.; Nealey, P. F.; de Pablo, J. J. *J. Chem. Phys.* 2003, *118*, 11278.
(28) Kitano, H.; Akasaka, S.; Inoue, T.; Chen, F.; Takenaka, M.; Hasegawa, H.; Yoshida, H.; Nagano, H. *Langmuir* 2007, *23*, 6404.
(29) Kim, J.; Green, P. F. *Macromolecules* 2010, *43*, 10452.

(30) Bigioni, T. P.; Lin, X. M.; Nguyen, T. T.; Corwin, E. I.; Witten, T. A.; Jaeger, H. M. *Nat. Mater.* 2006, *5*, 265.
(31) Peng, S.; Lee, Y.; Wang, C.; Yin, H.; Dai, S.; Sun, S. *Nano Research* 2008, *1*, 229.
(32) Cademartiri, L.; Bertolotti, J.; Sapienza, R.; Wiersma, D. S.; von Freymann, G.; Ozin, G. A. *J. Phys. Chem. B* 2005, *110*, 671.
(33) Liu, Y.; Gibbs, M.; Puthussery, J.; Gaik, S.; Ihly, R.; Hillhouse, H. W.; Law, M. *Nano Lett.* 2010, *10*, 1960.

Chapter 5

(1) Murray, C. B.; Norris, D. J.; Bawendi, M. G. *J. Am. Chem. Soc.* **1993**, *115*, 8706.
(2) Peng, X.; Schlamp, M. C.; Kadavanich, A. V.; Alivisatos, A. P. *J. Am. Chem. Soc.* **1997**, *119*, 7019.
(3) Manna, L.; Scher, E. C.; Alivisatos, A. P. *J. Am. Chem. Soc.* **2000**, *122*, 12700.
(4) Peng, X.; Manna, L.; Yang, W.; Wickham, J.; Scher, E.; Kadavanich, A.; Alivisatos, A. P. *Nature* **2000**, *404*, 59.
(5) Talapin, D. V.; Haubold, S.; Rogach, A. L.; Kornowski, A.; Haase, M.; Weller, H. *J. Phys. Chem. B* **2001**, *105*, 2260.
(6) Sun, Y.; Xia, Y. *Science* **2002**, *298*, 2176.
(7) Luther, J. M.; Jain, P. K.; Ewers, T.; Alivisatos, A. P. *Nat. Mater.* **2011**, *10*, 361.
(8) Lopes, W. A.; Jaeger, H. M. *Nature* **2001**, *414*, 735.
(9) Huynh, W. U.; Dittmer, J. J.; Alivisatos, A. P. *Science* **2002**, *295*, 2425.
(10) D. V. Talapin, C. B. Murray *Science* **2005**, *310*, 86.
(11) Alivisatos, A. P.; Johnsson, K. P.; Peng, X.; Wilson, T. E.; Loweth, C. J.; Bruchez, M. P.; Schultz, P. G. *Nature* **1996**, *382*, 609.
(12) Mirkin, C. A.; Letsinger, R. L.; Mucic, R. C.; Storhoff, J. J. *Nature* **1996**, *382*, 607.
(13) Templin, M.; Franck, A.; Du Chesne, A.; Leist, H.; Zhang, Y.; Ulrich, R.; Schädler, V.; Wiesner, U. *Science* **1997**, *278*, 1795.
(14) Balazs, A. C.; Emrick, T.; Russell, T. P. *Science* **2006**, *314*, 1107.
(15) Warren, S. C.; Messina, L. C.; Slaughter, L. S.; Kamperman, M.; Zhou, Q.; Gruner, S. M.; DiSalvo, F. J.; Wiesner, U. *Science* **2008**, *320*, 1748.
(16) Thompson, R. B.; Ginzburg, V. V.; Matsen, M. W.; Balazs, A. C. *Science* **2001**, *292*, 2469.
(17) Bockstaller, M. R.; Lapetnikov, Y.; Margel, S.; Thomas, E. L. *J. Am. Chem. Soc.* **2003**, *125*, 5276.
(18) F. X. Redl, K. S. Cho, C. B. Murray, S. O'Brien *Nature* **2003**, *423*, 968.
(19) Chiu, J. J.; Kim, B. J.; Kramer, E. J.; Pine, D. J. *J. Am. Chem. Soc.* **2005**, *127*, 5036.
(20) Lin, Y.; Boker, A.; He, J.; Sill, K.; Xiang, H.; Abetz, C.; Li, X.; Wang, J.; Emrick, T.; Long, S.; Wang, Q.; Balazs, A.; Russell, T. P. *Nature* **2005**, *434*, 55.
(21) E. V. Shevchenko, D. V. Talapin, N. A. Kotov, S. O'Brien, C. B. Murray *Nature* **2006**, *439*, 55.
(22) *International Technology Roadmap for Semiconductors (Emerging Research Materials)*; 2007 Edition ed.; Semiconductor Industry Association: San Jose, CA, 2007.
(23) Bockstaller, M. R.; Mickiewicz, R. A.; Thomas, E. L. *Adv. Mater.* **2005**, *17*, 1331.
(24) Mackay, M. E.; Tuteja, A.; Duxbury, P. M.; Hawker, C. J.; Horn, B. V.; Guan, Z.; Chen, G.; Krishnan, R. S. *Science* **2006**, *311*, 1740.
(25) Akcora, P.; Liu, H.; Kumar, S. K.; Moll, J.; Li, Y.; Benicewicz, B. C.; Schadler, L. S.; Acehan, D.; Panagiotopoulos, A. Z.; Pryamitsyn, V.; Ganesan, V.; Ilavsky, J.; Thiyagarajan, P.; Colby, R. H.; Douglas, J. F. *Nat. Mater.* **2009**, *8*, 354.
(26) Zhang, X.; Harris, K. D.; Wu, N. L. Y.; Murphy, J. N.; Buriak, J. M. *ACS Nano* **2010**, *4*, 7021.
(27) Park, W. I.; Kim, K.; Jang, H.-I.; Jeong, J. W.; Kim, J. M.; Choi, J.; Park, J. H.; Jung, Y. S. *Small* **2013**, *8*, 3762.

(28) Zhao, Y.; Thorkelsson, K.; Mastroianni, A. J.; Schilling, T.; Luther, J. M.; Rancatore, B. J.; Matsunaga, K.; Jinnai, H.; Wu, Y.; Poulsen, D.; Frechet, J. M. J.; Paul Alivisatos, A.; Xu, T. *Nat. Mater.* **2009**, *8*, 979.
(29) Kao, J.; Bai, P.; Chuang, V. P.; Jiang, Z.; Ercius, P.; Xu, T. *Nano Lett.* **2012**, *12*, 2610.
(30) Ikkala, O.; ten Brinke, G. *Chem. Commun.* **2004**, 2131.
(31) Crank, J.; Park, G. S. *J. Chem. Soc. Faraday Trans.* **1949**, *45*, 240.
(32) Boyer, R. F. *J. Polym. Sci.* **1950**, *5*, 139.
(33) van Zoelen, W.; Asumaa, T.; Ruokolainen, J.; Ikkala, O.; ten Brinke, G. *Macromolecules* **2008**, *41*, 3199.
(34) Li, Y.; Wang, X.; Sanchez, I. C.; Johnston, K. P.; Green, P. F. *J. Phys. Chem. B* **2006**, *111*, 16.
(35) Ruokolainen, J.; Saariaho, M.; Ikkala, O.; ten Brinke, G.; Thomas, E. L.; Torkkeli, M.; Serimaa, R. *Macromolecules* **1999**, *32*, 1152.
(36) Dalvi, M. C.; Lodge, T. P. *Macromolecules* **1993**, *26*, 859.
(37) Cavicchi, K. A.; Lodge, T. P. *Macromolecules* **2003**, *36*, 7158.
(38) Mishra, V.; Fredrickson, G. H.; Kramer, E. J. *ACS Nano* **2012**, *6*, 2629.
(39) Helfand, E. *Macromolecules* **1992**, *25*, 492.
(40) Shibayama, M.; Hashimoto, T.; Hasegawa, H.; Kawai, H. *Macromolecules* **1983**, *16*, 1427.
(41) Albalak, R. J.; Capel, M. S.; Thomas, E. L. *Polymer* **1998**, *39*, 1647.
(42) Fukunaga, K.; Elbs, H.; Magerle, R.; Krausch, G. *Macromolecules* **2000**, *33*, 947.
(43) Fukunaga, K.; Hashimoto, T.; Elbs, H.; Krausch, G. *Macromolecules* **2002**, *35*, 4406.
(44) Kimura, M.; Misner, M. J.; Xu, T.; Kim, S. H.; Russell, T. P. *Langmuir* **2003**, *19*, 9910.
(45) Kim, S. H.; Misner, M. J.; Xu, T.; Kimura, M.; Russell, T. P. *Adv. Mater.* **2004**, *16*, 226.
(46) Lin, Z. Q.; Kim, D. H.; Wu, X. D.; Boosahda, L.; Stone, D.; LaRose, L.; Russell, T. P. *Adv. Mater.* **2002**, *14*, 1373.
(47) Phillip, W. A.; Hillmyer, M. A.; Cussler, E. L. *Macromolecules* **2010**, *43*, 7763.
(48) Albert, J. N. L.; Young, W.-S.; Lewis, R. L.; Bogart, T. D.; Smith, J. R.; Epps, T. H. *ACS Nano* **2012**, *6*, 459.
(49) Gu, X.; Gunkel, I.; Hexemer, A.; Gu, W.; Russell, T. P. *Adv. Mater.* **2014**, *26*, 273.
(50) Shull, K. R. *Macromolecules* **1992**, *25*, 2122.

Chapter 6

(1) Lopes, W. A.; Jaeger, H. M. *Nature* **2001**, *414*, 735-738.
(2) Ross, C. A. *Annu. Rev. Mater. Res.* **2001**, *31*, 203-235.
(3) Maier, S. A.; Kik, P. G.; Atwater, H. A.; Meltzer, S.; Harel, E.; Koel, B. E.; Requicha, A. A. G. *Nat. Mater.* **2003**, *2*, 229-232.
(4) Talapin, D. V.; Murray, C. B. *Science* **2005**, *310*, 86-89.
(5) Thompson, R. B.; Ginzburg, V. V.; Matsen, M. W.; Balazs, A. C. *Science* **2001**, *292*, 2469-2472.
(6) Bockstaller, M. R.; Lapetnikov, Y.; Margel, S.; Thomas, E. L. *J. Am. Chem. Soc.* **2003**, *125*, 5276-5277.
(7) Lin, Y.; Boker, A.; He, J.; Sill, K.; Xiang, H.; Abetz, C.; Li, X.; Wang, J.; Emrick, T.; Long, S.; Wang, Q.; Balazs, A.; Russell, T. P. *Nature* **2005**, *434*, 55-59.
(8) Chiu, J. J.; Kim, B. J.; Kramer, E. J.; Pine, D. J. *J. Am. Chem. Soc.* **2005**, *127*, 5036-5037.
(9) Balazs, A. C.; Emrick, T.; Russell, T. P. *Science* **2006**, *314*, 1107-1110.
(10) Warren, S. C.; Messina, L. C.; Slaughter, L. S.; Kamperman, M.; Zhou, Q.; Gruner, S. M.; DiSalvo, F. J.; Wiesner, U. *Science* **2008**, *320*, 1748-1752.
(11) Zhao, Y.; Thorkelsson, K.; Mastroianni, A. J.; Schilling, T.; Luther, J. M.; Rancatore, B. J.; Matsunaga, K.; Jinnai, H.; Wu, Y.; Poulsen, D.; Frechet, J. M. J.; Paul Alivisatos, A.; Xu, T. *Nat.w Mater.* **2009**, *8*, 979-985.
(12) Kao, J.; Bai, P.; Chuang, V. P.; Jiang, Z.; Ercius, P.; Xu, T. *Nano Lett.* **2012**, *12*, 2610-2618.
(13) Kao, J.; Bai, P.; Lucas, J. M.; Alivisatos, A. P.; Xu, T. *J. Am. Chem. Soc.* **2013**, *135*, 1680-1683.
(14) Morkved, T. L.; Lu, M.; Urbas, A. M.; Ehrichs, E. E.; Jaeger, H. M.; Mansky, P.; Russell, T. P. *Science* **1996**, *273*, 931-933.
(15) Kim, S. H.; Misner, M. J.; Xu, T.; Kimura, M.; Russell, T. P. *Adv. Mater.* **2004**, *16*, 226-231.
(16) Angelescu, D. E.; Waller, J. H.; Adamson, D. H.; Deshpande, P.; Chou, S. Y.; Register, R. A.; Chaikin, P. M. *Adv. Mater.* **2004**, *16*, 1736-1740.
(17) Tang, C.; Tracz, A.; Kruk, M.; Zhang, R.; Smilgies, D.-M.; Matyjaszewski, K.; Kowalewski, T. *J. Am. Chem. Soc.* **2005**, *127*, 6918-6919.
(18) Singh, G.; Yager, K. G.; Berry, B.; Kim, H.-C.; Karim, A. *ACS Nano* **2012**, *6*, 10335-10342.
(19) Rockford, L.; Liu, Y.; Mansky, P.; Russell, T. P.; Yoon, M.; Mochrie, S. G. J. *Phys. Rev. Lett.* **1999**, *82*, 2602-2605.
(20) Kim, S. O.; Solak, H. H.; Stoykovich, M. P.; Ferrier, N. J.; de Pablo, J. J.; Nealey, P. F. *Nature* **2003**, *424*, 411-414.
(21) Stoykovich, M. P.; Muller, M.; Kim, S. O.; Solak, H. H.; Edwards, E. W.; de Pablo, J. J.; Nealey, P. F. *Science* **2005**, *308*, 1442-1446.
(22) Segalman, R. A.; Yokoyama, H.; Kramer, E. J. *Adv. Mater.* **2001**, *13*, 1152-1155.
(23) Sundrani, D.; Darling, S. B.; Sibener, S. J. *Nano Lett.* **2003**, *4*, 273-276.
(24) Cheng, J. Y.; Mayes, A. M.; Ross, C. A. *Nat. Mater.* **2004**, *3*, 823-828.
(25) Bita, I.; Yang, J. K. W.; Jung, Y. S.; Ross, C. A.; Thomas, E. L.; Berggren, K. K. *Science* **2008**, *321*, 939-943.

(26) Park, S.; Lee, D. H.; Xu, J.; Kim, B.; Hong, S. W.; Jeong, U.; Xu, T.; Russell, T. P. *Science* **2009**, *323*, 1030-1033.
(27) Hong, S. W.; Huh, J.; Gu, X.; Lee, D. H.; Jo, W. H.; Park, S.; Xu, T.; Russell, T. P. *Proc. Natl. Acad. Sci.* **2012**.
(28) Huth, M.; Ritley, K. A.; Oster, J.; Dosch, H.; Adrian, H. *Adv. Funct. Mater.* **2002**, *12*, 333-338.
(29) Gabai, R.; Ismach, A.; Joselevich, E. *Adv. Mater.* **2007**, *19*, 1325-1330.
(30) Walton, D. G.; Kellogg, G. J.; Mayes, A. M.; Lambooy, P.; Russell, T. P. *Macromolecules* **1994**, *27*, 6225-6228.
(31) Frenkel, D.; Eppenga, R. *Phys. Rev. A* **1985**, *31*, 1776-1787.